A Concise Moment Method for Unsteady Polydisperse Sprays

Vom Fachbereich Maschinenbau
an der Technischen Universität Darmstadt
zur
Erlangung des Grades eines Doktor-Ingenieurs (Dr.-Ing.)
genehmigte

D i s s e r t a t i o n

von

Dipl.-Ing. Lukas Schneider

aus Heppenheim an der Bergstraße

Berichterstatter:	Prof. Dr.–Ing. J. Janicka
Mitberichterstatter:	Prof. Dr. rer. nat. A. Sadiki
Mitberichterstatter:	Prof. Dr.–Ing. B. Weigand
Tag der Einreichung:	04. Mai 2009
Tag der mündlichen Prüfung:	08. Juli 2009

Darmstadt 2009

D 17

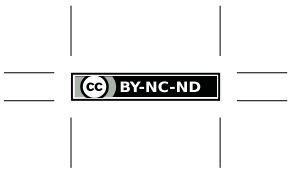

Kurzfassung der Dissertation

"Eine präzise Momenten-Methode für instationäre polydisperse Sprays"
von Lukas Schneider

Diese Arbeit behandelt die mathematische und numerische Beschreibung von instationären, polydispersen Sprays mit dem übergeordneten Ziel, das Verhalten von Verbrennungskraftmaschinen genauer und mit geringerem Rechenaufwand zu simulieren. Die wesentlichen Sprayphänomene in diesen Systemen sind der primäre und sekundäre Zerfall des Kraftstoffstrahls, die Kollision und Verdampfung von Tropfen sowie die Widerstandskraft, welche von dem meist turbulenten Gas auf die Tropfen wirkt. Dem Spray kommt dabei die Aufgabe zu, den Brennstoff im Brennraum so zu verteilen, dass am vorgesehenen Ort und zum richtigen Zeitpunkt das Brennstoff-Gas-Gemisch zündet. Aufgrund der starken Kopplung der genannten Prozesse können sich Ungenauigkeiten bei der Sprayberechnung ausbreiten oder sogar verstärken, was die Simulation der eigentlichen Verbrennung erschwert.

Das komplexe Verhalten technischer Sprays kann zwar mit direkter numerischer Simulation genau wiedergegeben werden, diese ist jedoch nicht praktikabel, da ein nicht zu rechtfertigender Rechenaufwand vonnöten ist. Stattdessen werden für die Tropfenphase so genannte Lagrange- und Euler-Methoden eingesetzt, die darauf basieren, dass Lösungen der kinetischen Spraygleichung, einer partiellen Differentialgleichung für die Verteilungsfunktion von Tropfen, angenähert werden. Obwohl die Lagrange-Methode die volle Komplexität dieser Gleichung darstellen kann, hängt ihr Rechenaufwand von der Instationarität und der Tropfenbeladung des Spraysystems ab. Bei Euler-Methoden ist dies nicht der Fall, allerdings bedürfen diese Methoden einer Weiterentwicklung, da sie meist von monomodalen Geschwindigkeitsverteilungen und vorgegebenen Größenverteilungen ausgehen. Diese Annahmen sind in technischen Sprays nicht haltbar, da sie zu unphysikalischen Tropfenkonzentrationen an Kreuzungspunkten von Spraystrahlen und zu fehlerhaften Verdampfungsraten führen.

In dieser Arbeit wird ein präziserer Eulerscher Ansatz vorgeschlagen, der die oben genannten Probleme der klassischen Euler-Methode löst. Hierzu wird die kinetische Spraygleichung in Momentengleichungen überführt, die durch einen neu entwickelten Ansatz der Verteilungsfunktion der Tropfen geschlossen werden. Dieser berücksichtigt die zeitliche und räumliche Änderung der Dispersion von Tropfengrößen und -geschwindigkeiten. Die in der Arbeit entwickelten numerischen Algorithmen folgen aus diesem Ansatz. Bei der Wahl der mathematischen und numerischen Modellierung des Sprays wurde Wert darauf gelegt, dass der Massenaustausch zwischen Tropfen und Gas genau abgebildet werden kann, da dieser Vorgang die Verbrennung entscheidend beeinflusst. Die Überprüfung der neuen Methode erfolgt mittels stationärer und instationärer, eindimensionaler und zweidimensionaler Testfälle, in denen ein polydisperses Spray verdampft, Widerstandskraft erfährt oder auf eine Wand prallt und teilweise reflektiert wird. Diese Konfigurationen sind so gewählt, dass sich zwei oder mehrere Spraystrahlen kreuzen und somit bi- oder multimodale Geschwindigkeitsverteilungen auftreten. Der Vergleich der Ergebnisse mit hoch aufgelösten Lagrange-Rechnungen zeigt, dass die neue Methode geeignet ist, den polydispersen Charakter von Sprays und das Kreuzen von Spraystrahlen genau wiederzugeben.

Summary of the thesis

"A Concise Moment Method for Unsteady Polydisperse Sprays"
by Lukas Schneider

This body of research deals with the mathematical and numerical description of unsteady polydisperse sprays. The superior objective is to simulate the behaviour of combustion engines with higher accuracy but lower computational costs. The main spray phenomena in this type of processes are the primary and secondary breakup of the fuel jet, collision and evaporation of droplets, and acceleration or deceleration of droplets due to drag forces. The purpose of the spray is to distribute the fuel in the combustion chamber such that the fuel/air mixture ignites at controllable locations and times. Errors in the modelling of just one of the above spray phenomena can spread and even amplify as the combustion simulation proceeds. This occurs due to the strong coupling between the processes involved.

Although the behaviour of technical sprays can be captured accurately with direct numerical simulation it is not applied as the computational workload would be extraordinary. Instead, methods such as Lagrange and Euler methods are used to describe the spray behaviour by approximating a solution to the kinetic spray equation, a partial differential equation for the distribution function of droplets. Although the Lagrange method captures the full complexity of this equation, it is computationally very expensive to use it for unsteady flows that have a high mass loading of droplets. The computational performance of Euler methods is independent of the unsteadiness and mass loading. However, Euler methods require further development as most of them assume the velocity distribution of droplets to be mono-modal and use presumed size distributions to describe the polydisperse character of sprays. These assumptions are not justified for technical sprays as they lead to spurious droplet concentrations at crossing points of fuel jets and inaccurate evaporation rates.

In this thesis a concise Euler method is proposed that resolves the above problems of the classical Euler methods. The kinetic spray equation is transformed into moment equations that are closed by assuming the droplet distribution function to have a specific form. However, it still takes into account the spatial and temporal changes of dispersion in size and velocity space. All numerical algorithms follow from this specification. In the choice of the mathematical and numerical model, care was taken in modelling the mass transfer between droplets and gas. It is a key feature in combustion engines because it determines the fuel/air mass fraction. To assess the abilities of the method it was extensively tested in steady and unsteady, one- and two-dimensional configurations in which a polydisperse spray was splashed, evaporated or effected by a Stokes drag force. The tests were organised in such a way that crossing of two or more spray distributions was always included and bi- or multi-modal velocity distributions were present. The comparison of the results with highly resolved Lagrangian calculations demonstrates that the polydisperse character of sprays and the crossing of spray jets can be captured accurately.

Eidestattliche Erklärung

Hiermit erkläre ich an Eides statt, dass ich die vorliegende Dissertation selbständig verfasst und keine anderen als die von mir angegebenen Hilfsmittel verwendet habe. Ich erkläre außerdem, dass ich bisher noch keinen Promotionsversuch unternommen habe.

Lukas Schneider Darmstadt, den 04. Mai 2009

Acknowledgments

My sincere gratitude goes to Prof. Dr.-Ing. Johannes Janicka, head of the institute 'Energy and Power Plant Technology' (EKT), and to Prof. Dr. rer. nat. Amsini Sadiki for their encouragement and scientific advice. I am grateful to them for their guidance but also for the freedom and trust they gave me when entering this emerging field of research. I also wish to thank Prof. Dr.-Ing. Bernhard Weigand of the Institute of Aerospace Thermodynamics at Universität Stuttgart for his willingness to take over the review of this thesis.

An undeniable portion for the success of this work is assigned to Philippe Villedieu, Associate Professor at INSA and senior scientist at ONERA/DMAE in Toulouse, and to Nechtan Le Lostec, his Ph.D. student. I appreciate their hospitality and their interest in my work. I also thank them for the highly beneficial discussions as well as their willingness to cooperate for the purpose of science.

My sincere thanks also go to Daniele Marchisio, Assistant Professor at Politecnico di Torino, and Kolumban Hutter, Professor at ETH Zürich, for the encouragement and the interesting discussions.

I am further indebted to Thomas Breitenberger, Jens Kühne, Christian Klewer, Mouldi Chrigui and Frederik Hahn for their excellent care of the computer network. Thanks also go to Larissa Moore and Kaushal Nishad for their editing of the manuscript. I am also grateful to Elisabeth Zweyrohn, Jasmin Krenzer, Simone Eisenhuth and my colleagues at EKT for their help and the good times we spend together. In particular, I thank my roommates, Desislava Dimitrova, Florian Seffrin, Mouldi Chrigui, Wahid Ahmadi and Dmitry Goryntsev for the enlightening discussions and motivating atmosphere in the office.

This body of research is the result of 3 $\frac{1}{2}$ years employment at EKT. The financial support from Technische Universität Darmstadt and SFB 568 is gratefully acknowledged.

I would certainly not be where I stand today without the continuous support, help and encouragement of my family. They have trusted and supported me tremendously during these scientific years.

A million thanks go to my wife. Despite her own long working hours and enormous workload, she supported me wherever she could. She discussed the theoretical part of the thesis with me and managed our living whenever I was hunting some bug in the code. She allowed me to fully concentrate on this work, which is an invaluable contribution. Without her, this work would have undoubtedly taken a good deal longer, if finished at all.

Lukas Schneider Darmstadt, Mai 04, 2009

To Eveline, Gerlinde, Hans, Katharina, Gregor, Doris, Karl, Beate, Falko and Anna.

'The whole is more than the sum of its parts.' (Aristotle)

Contents

Nomenclature

Some variables will have a double meaning because, if not otherwise stated, from section 3.2.3 all quantities are assumed to be dimensionless. Here, the quantities are listed with dimensions. A dash (–) at the 'Units' column indicates a dimensionless quantity. Einstein's convention of summation is used for Latin but not for Greek subscripts.

Uppercase Latin letters		**Unit**
$\mathbf{F}$	total force on a droplet	N
$\mathbf{F}_d$	drag force on a droplet	N
$\mathbf{U}_k^p$	mean droplet velocity vector in section I_k	$\mathrm{m\,s^{-1}}$
$\mathbf{U}_g$	velocity vector of the gas	$\mathrm{m\,s^{-1}}$
$\mathbf{U}_k^\alpha$	velocity abscissa for node α in section I_k	$\mathrm{m\,s^{-1}}$
$\mathcal{Q}$	breakup frequency	$\mathrm{s^{-1}}$
$\mathcal{R}_s$	heat transfer term in the dimensionless moment equations	–
$\mathcal{V}_k^d$	set of moments of the d-dimensional space in section I_k	–
$\mathcal{W}_k^\beta$	set of parameters of $\tilde{f}$ in section I_k with β nodes	–
$\mathbb{R}^d$	d-dimensional Euclidean vector space	–
$\mathbb{R}_\pm$	set of all non-negative / non-positive real numbers	–
K	evaporation rate of the droplet surface	$\mathrm{m^2 s^{-1}}$
$\mathrm{M}_{k;lmn}^{K,L,M}$	moment for surface, temperature and velocity in section I_k	–
R	rate of change of the droplet temperature	$\mathrm{K\,s^{-1}}$
$D_{k;lmn}^M$	drag term in the dimensionless moment equations	–
$D_{v\alpha}$	diffusivity of fuel vapour in air	$\mathrm{m^2 s^{-1}}$
I_k	section with index k	–
K	order of moment $\mathrm{M}_{k;lmn}^{K,L,M}$ with respect to the surface variable	–
L	order of moment $\mathrm{M}_{k;lmn}^{K,L,M}$ with respect to the temperature variable	–
M	order of moment $\mathrm{M}_{k;lmn}^{K,L,M}$ with respect to the velocity variable	–
N_s	number of finite sections	–
N_x	number of cells in direction $\mathbf{e}_x$	–
N_y	number of cells in direction $\mathbf{e}_y$	–
S_{char}	characteristic droplet surface	$\mathrm{m^2}$
V_{char}	characteristic velocity of the gas flow	$\mathrm{m\,s^{-1}}$
X_{char}	characteristic length scale of the gas flow	m

Lowercase Latin letters		**Unit**
$\dot{m}_d$	mass transfer between droplet and gas	$\mathrm{kg\,s^{-1}}$

$\mathbf{e}_i$	unit vector in i-direction	–
$\mathbf{v}$	velocity vector of droplets	$\mathrm{m\,s^{-1}}$
$\mathbf{v}_{\mathrm{rel}}$	relative velocity between droplet and gas	$\mathrm{m\,s^{-1}}$
$\mathbf{x}$	position vector	m
d_{32}	Sauter mean diameter	m
$\tilde{f}$	approximation of the NDF	$\mathrm{s^3m^{-8}K^{-1}}$
b_k	exponential parameter for $\tilde{f}$ in section I_k	$\mathrm{m^{-2}}$
c_p	specific heat capacity	$\mathrm{J\,kg^{-1}K^{-1}}$
d	number of real space dimensions	–
f	number density function	$\mathrm{s^3m^{-8}K^{-1}}$
f^+	number density function of incident droplets	$\mathrm{s^3m^{-8}}$
f^r	number density of splashed droplets	$\mathrm{s^3m^{-8}}$
g	acceleration of gravity	$\mathrm{m\,s^{-2}}$
m	mass of droplets	kg
m_d	mass of one droplet	kg
n	number density of droplets	$\mathrm{m^{-3}}$
n_k^α	quadrature weight of node α for $\tilde{f}$ in section I_k	$\mathrm{m^{-3}}$
s	droplet surface	$\mathrm{m^2}$
s_k, s_{k+1}	boundaries of section I_k	$\mathrm{m^2}$
t	time variable	s
u, v, w	velocity components in $\mathbf{e}_x$, $\mathbf{e}_y$ and $\mathbf{e}_z$ direction	$\mathrm{m\,s^{-1}}$
v_i	velocity component, equal to $\mathbf{v}\cdot\mathbf{e}_i$	$\mathrm{m\,s^{-1}}$
x, y, z	components of $\mathbf{x}$ in the directions $\mathbf{e}_x$, $\mathbf{e}_y$ and $\mathbf{e}_z$	m

Uppercase Greek letters		**Unit**
Δs_k	size of section I_k	$\mathrm{m^2}$
Δt	time step	s
Δx_i	size of the i-th cell in direction $\mathbf{e}_x$	m
Δy_j	size of the j-th cell in direction $\mathbf{e}_y$	m
Γ	collision frequency	$\mathrm{s^{-1}}$
Θ_k	temperature abscissa in section I_k	K
Θ_{char}	characteristic droplet temperature	K

Lowercase Greek letters		**Unit**
α_x	splashing parameter for v_x	–
α_y	splashing parameter for v_y	–
α_z	splashing parameter for v_z	–
β	number of quadrature nodes	–
β_d	splashing parameter for droplet partition	–
$\boldsymbol{\sigma}_U$	velocity covariance matrix	$\mathrm{m^2\,s^{-2}}$
η_g	dynamic viscosity of the gas	$\mathrm{kg\,(ms)^{-1}}$
γ	splashing parameter for mass losses	–
ρ_ℓ	mass density of the droplet liquid	$\mathrm{kg\,m^{-3}}$
ρ_g	mass density of the gas	$\mathrm{kg\,m^{-3}}$
σ_d	surface tension of a droplet	$\mathrm{N\,m^{-1}}$
τ_d	droplet response time	s

τ_g	time scale of the gas flow	s
τ_{ev}	time scale for the evaporation	s
τ_{he}	time scale for the heat transfer	s
θ	temperature of droplets	K
θ_g	temperature of the gas	K

Operators and Symbols

$\bar{(\cdot)}$	quantity in brackets is divided by $\int_{s_k}^{s_{k+1}} s^{3/2} f(s) ds$
$\delta(\cdot)$	Dirac delta function
δ_{ij}	Kronecker delta
$\mathbf{a} \cdot \mathbf{b}$	scalar product of vectors $\mathbf{a}$ and $\mathbf{b}$
$\lvert \cdot \rvert$	Euclidean norm
∇	nabla operator

Dimensionless Numbers

B_h	coefficient of heat transfer	–
B_m	coefficient of mass transfer	–
Ev	evaporation number	–
Fr	Froude number	–
He	heat transfer number	–
Kn_d	droplet Knudsen number	–
Nu	Nusselt number	–
Re_d	droplet Reynolds number	–
Sh	Sherwood number	–
St	Stokes number	–
We	Weber number	–

Abbreviations

CFD	computational fluid dynamics
DNS	direct numerical simulation
DQMoM	direct quadrature method of moments
EE	Euler-Euler
EL	Euler-Lagrange
LES	large-eddy simulation
NDF	number density function
NS	Navier-Stokes
ODE	ordinary differential equation
PDE	partial differential equation
PDF	probability density function
PTC	particle trajectory crossing
QBMoM	quadrature-based method of moments
QBSM	quadrature-based sectional method
QMoM	quadrature method of moments
SM	sectional method
SMD	Sauter mean diameter

Chapter 1

Introduction

1.1 Motivation

Industrialised societies rely heavily on fossil fuels and will do so for decades to come [3, 4]. This is due to the fact that the generation of electricity, passenger transportation, carriage of freight, the production of synthetic goods, etc. are based on the products of petroleum, natural gas or coal. These products have high specific and volumetric energy densities (see Figure 1.1) and can also be transformed into chemicals that are the basis for plastics, pharmaceutics and other synthetic products. Scientists and politicians have agreed in recent years that there is an urgent need to reduce fossil fuel consumption, in particular, in combustion systems [82, 117, 118].

The transformation of carbon fuels to energy, e.g. in vehicles, aeroplanes or power plants, causes the emission of carbon dioxide (CO_2), water (H_2O), nitrogen oxides (NO_x), carbon monoxide (CO), sulphur dioxide (SO_2), soot and uncombusted hydrocarbons (UCH). Except for the water, all these gases have negative impacts on the environment if they are emitted in large amounts. They affect the local ecosystem directly through acid rain, creation of ozone and the formation of carcinogen particles or they enhance the greenhouse effect which causes global climate changes [159]. There are also socio-economic and political arguments that are influencing the handling of fossil fuels: the expected rise in global fuel consumption, the limited resources of petroleum [4] and the concentration of petroleum and neutral gas resources in politically unstable regions [85].

While technologies based on renewable energy sources are pushed forward, one way to reduce fossil fuel consumption is the optimisation of existing combustion technologies. Since the first inventors, N.A. Otto (1832-1891), R. Diesel (1858-1913) and H.J. Pabst von Ohain (1911-1998), combustion engines have steadily been improved to exploit fuels more efficiently. However, due to the complexity of technical combustion processes, the development has always been confined to expensive and time-consuming test runs that are required to find the correlations between tuning parameters and the global characteristics of combustion engines. The most recent advances in the research on combustion engines are new combustion concepts like homogeneous charge compression ignition (HCCI) in diesel engines, controlled autoignition (CAI) in spark ignition engines [111] and concepts

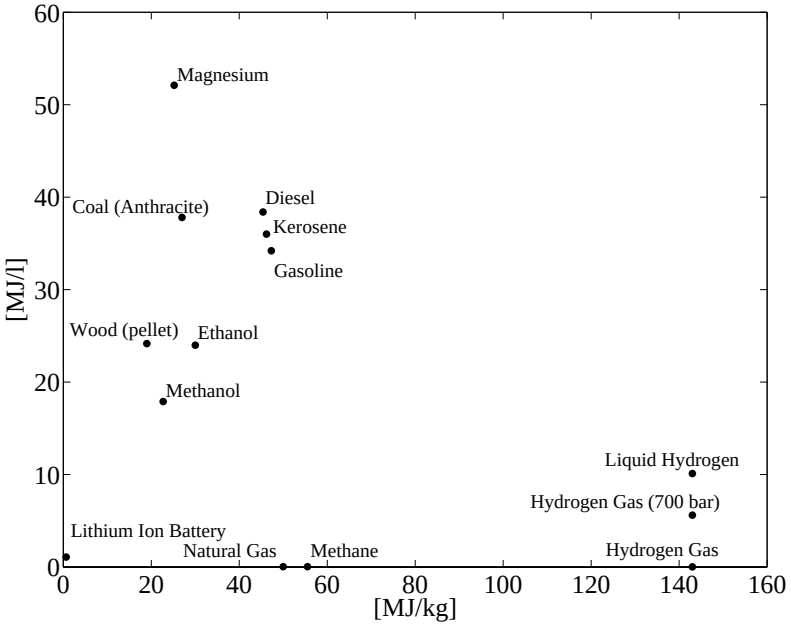

Figure 1.1: Volumetric vs. specific energy densities of selected fuels [21].

such as lean direct injection (LDI), lean premixed prevaporized (LPP) and rich burn quick quench lean burn (RQL) in aeroplane engines.[1] The main goals of these concepts are the reduction of fuel consumption, NO_x and UCH emissions and soot formation by operating under lean and homogeneous combustion conditions. At the same time, the fuel-air mixture formation needs to be controlled to ensure that stable ignition and combustion for all load and speed combinations are achieved. However, these new combustion technologies are known for their unstable combustion characteristics, in particular at partial loads [111]. These defects require further research and development.

In recent years the development of combustion technologies has been accelerated with the use of computational fluid dynamics (CFD) and massively parallelised computer systems [15, 185]. In general, CFD methods are based on physical, mathematical and numerical models of the flow phenomena. The algorithms derived from these models are transformed into program codes that allow the prediction of technical flows. These computations are quantitatively and qualitatively predictive only in a limited area of validity which has to be determined by comparisons with measurements of real physical flows. A CFD method is characterised by its area of validity, accuracy, robustness, requirements of computer resources and its performance on parallelised computer systems.

The numerical methods for the prediction of highly unsteady fuel sprays in combustion chambers using existing CFD-tools are not mature, in particular, there is a need to develop new models that are more accurate and have a faster and more robust behaviour

[1] A promising alternative to the combustion of carbon fuels in vehicles is the use of hydrogen. It has a much larger specific energy density and can be used together with fuel cells and electric motors. The biggest problems with using hydrogen in vehicles are the low efficiency of its extraction, the low volumetric energy density (see Figure 1.1) and the risk of explosion.

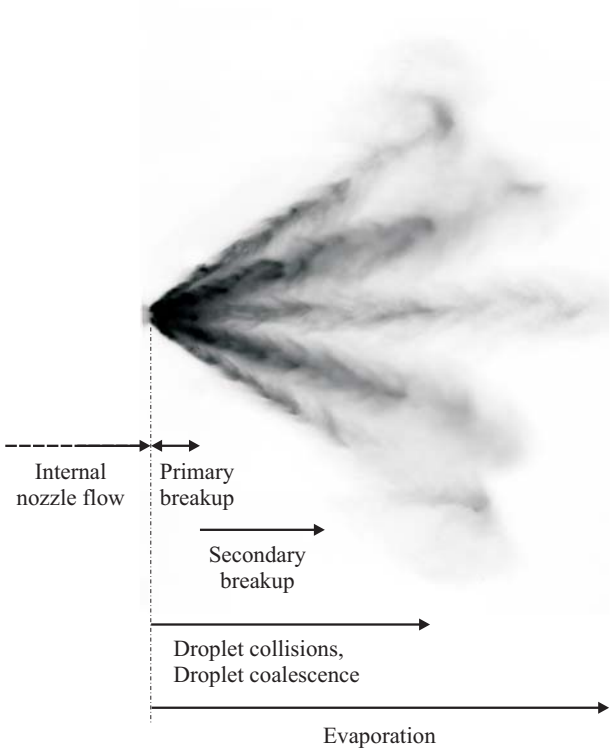

Figure 1.2: Fuel injection from a seven-hole nozzle in a car engine (shadow technique) [29].

on highly parallelised computers (cf. [39, 75, 83, 123, 137]). In the combustion concept LPP, for example, combustion instabilities are more likely to occur and hence, the standard CFD-tools for multiphase flows, which are based on Reynolds-averaged Navier-Stokes (RANS) equations, cannot capture all the relevant effects. They have to be replaced by techniques that tackle the unsteady behaviour of spray processes. The coupling of large-eddy simulations (LES) for the gas phase with a Lagrangian solver (to be specified) for the droplet phase could be one of various alternatives. The challenging task of unsteady spray flows in combustion systems will be the subject of intensive research for years to come.

In this body of research the focus is on the modelling of unsteady and polydisperse fuel sprays encountered in combustion systems. In these, the liquid fuel is injected into a combustion chamber where it atomises and forms a droplet cloud that evaporates (see Figure 1.2). The principle physical processes that must be accounted for in the droplet clouds are:

- convection of droplets,
- droplet heating and evaporation,
- acceleration or deceleration of droplets due to drag forces,
- collision and breakup of droplets,
- particle (or droplet) trajectory crossing (PTC).

The behaviour of the fuel droplets has a strong influence on the mixing of oxidiser and fuel vapour, which determines the ignition and burning processes that follow. Other dominant phenomena that increase the complexity of combustion processes are the unsteady turbulent gas flow, the high pressure and temperature, the fast chemical reactions in the flame and the complexity of the combustion chamber geometries.

The two main approaches classically used to describe multiphase flows are Euler-Lagrange (EL) and Euler-Euler (EE) methods. The EL method is usually applied in systems where (solid) particles, droplets or bubbles are dispersed in a gaseous or liquid carrier phase [33]. In this approach the continuous phase is modelled by appropriate governing equations that include additional source terms modelling the influence of the particles, droplets or bubbles on the carrier phase. The dispersed phase is treated as if it is composed of discrete entities which are 'tracked' in the computational domain. Consequently, the computational costs of the EL method are strongly linked to the mass or bubble loading in the system. In addition, the coupling between dispersed and carrier phase is done on an Eulerian level which requires the averaging of a representative sample of dispersed entities. If the sample size is too small, i.e. the number of discrete entities tracked in the system is not sufficient, the level of statistical noise reduces the quality of the computational results. This situation may arise when unsteady and fine resolved computations are conducted which require small time and spatial sampling intervals. In this work the Lagrangian approach will not be pursued. However, a highly resolved Lagrangian procedure will be used to verify the Euler method developed here.

The classical EE method assumes two (or more) phases to be interpenetrating continua [42]. For each continuum, balance equations for mass, momentum, moment of momentum, energy and additional density fields (like the diameter or volume fraction) are considered that include phase-interaction terms. The classical EE method is commonly applied in granular flows that arise in fluidised beds [48], slurry flows [87, 151] or dense droplet-gas flows [36]. It is also applied to configurations in which a liquid is moving through the pores of some solid matrix (porous materials [31]), for example, ground water transport in soils [177] or blood circulation in bones [32].

When the phases are equally distributed in the domain of interest, i.e. the separation between the phases is only moderate, the classical EE method is appropriate. However, in dispersed gas-liquid flows the particles, droplets or bubbles with intermediate Stokes numbers concentrate in regions of low gas vorticity [143]. In turbulent spray flows, for example, vacuum zones and regions of strong mass concentration form at the centre and rim of vortices, respectively (see Chapter 6). In addition, the continuum assumption, which is usually enforced in the classical EE method, has to be bent considerably in order to use classical EE methods for dispersed gas-liquid flows. If the dispersed entities are not interacting at all (Knudsen number of the dispersed phase goes to infinity) the continuum assumption breaks down completely and physical fields like pressure and stresses cannot be defined in the dispersed phase. Other critical issues in the modelling of dispersed gas-liquid systems with EE methods are:

- the choice of the turbulence model,
- the polydispersity of the dispersed phase,
- the crossing trajectory effects of droplets (see Section 2.2.4).

On the other hand, EE methods are independent of the mass or bubble loading and the coupling between dispersed and carrier phases does not require averaging over a representative sample of dispersed entities. These advantages of the EE method come into play when unstationary, turbulent, gas-liquid flows are considered and loading with dispersed entities is high.

It is expected that for unsteady spray flows an improved EE method can outperform the EL method in terms of accuracy and speedup on highly parallelised computers. However, the improved Euler method (presented in this work) differs considerably from the classical Euler methods. The main differences are the drop of the continuum assumption, the consideration of dispersion in velocity space and the rigorous consideration of polydispersity. It will be shown that this method can describe polydisperse droplet clouds that allow infinite droplet Knudsen numbers and multi-modal distributions of the droplet velocity.

1.2 Objectives and Methods

The EL method was ascertained by Apte et al. [7], Nora Okong'o et al. [115] and Sadiki et al. [145] to be the right method for turbulent spray flows in combustion systems which have low mass loadings and a moderate degree of unsteadiness. For higher droplet mass loadings and higher degrees of unsteadiness, the workload of the EL method increases considerably and the speedup using a large number of processors does not increase linearly, as is the case for simulation methods describing the gas flow [137].

In contrast, the computational performance of EE methods is similar to that of the solution methods for the gas flow [137]. Although the number of balance equations increases, the structure of the equations remains very similar to Navier-Stokes (NS) equations. However, the ability of the classical EE methods [42] to describe spray flows is very limited because, as stated above, the continuum assumption breaks down if the droplets are not interacting, the modelling of turbulence in the dispersed phase is not completely resolved [83], the polydispersity of a spray experiencing breakup, collision and evaporation is not settled [59] and the crossing trajectory effects are not captured by most Euler methods. The latter effect is most critical for dilute spray flows in a turbulent environment because it is taking place nearly everywhere in a spray system [38].

There are several concepts that lead to a mathematical model for EE methods. Most of them start from continuum balance equations and perform some sort of averaging, i.e. time, volume or ensemble averaging, to obtain mass, momentum, moment of momentum, energy, entropy, diameter and other balance equations for each phase [42]. In this work, the objective is to develop a method that allows infinite droplet Knudsen numbers for the dispersed phase. Therefore, the mathematical model for the droplet phase is not based on the continuum assumption but on the kinetic spray equation introduced by Williams [179]. It is a partial differential equation (PDE) for a general function, called number density function (NDF). The NDF can be interpreted as the probability for encountering droplets at a point with specific properties. It depends on time, position and other variables, denoted as internal variables that describe the state of a cloud of droplets. For sprays in combustion systems the internal variables of droplet velocity, size[2] and temperature are

[2]The size variable can be the diameter, surface or volume of droplets. For sprays in combustion

considered as describing the droplet phenomena of drag, gravity, evaporation, breakup, collision and heat transfer with the surrounding gas. The kinetic spray equation can be reduced to time and position dependent balance equations for moments of the NDF by applying moment transforms to it. To close the unknown terms in these equations special forms of the NDF are assumed that include various degrees of freedom to capture the spray effects.

The objective of this work is the development, implementation and validation of a new EE method for spray flows encountered in combustion systems. Besides the five spray phenomena mentioned in Section 1.1, most combustion systems are dominated by

- the turbulent gas flow,
- the mixture of fuel and air,
- the fast chemical reaction in the flame,
- the influence of the wall.

As a first step in this development, the focus is on the dispersed droplet phase which experiences the effects of:

(i) drag and gravity forces,

(ii) evaporation,

(iii) heat transfer,

(iv) particle trajectory crossing (PTC),

(v) splashing on a wall,

(vi) droplet motion in unsteady gas structures.

The breakup and collision of droplets which are of interest near the nozzle are only considered in the physical and mathematical model of the new EE method. For the numerical model and the transfer from the developed algorithms to the program code, only issues (i)-(vi) are considered. The modelling of the gas phase is set aside in order to concentrate on the critical issues in the mathematical and numerical modelling of the dispersed phase. The physical models for drag force, evaporation and heat transfer are taken from the literature.

In the development of a mathematical model for the new Eulerian approach the following questions are answered:

(i) Can the standard physical models for evaporation, drag force, breakup and collision be used?

systems the consideration of the surface is the most natural choice because it allows the control of the evaporation process.

(ii) How can the balance equations for the moments be closed and still allow the NDF to be polydisperse in size and multimodal in the velocity variable?

(iii) Can the mass and number of droplets be controlled by the model?

Question (iii) is central to the simulation of spray combustion, because the chemical reaction in the flame is determined by the mass ratio between vapour fuel and oxidiser, which is strongly related to the mass transfer from liquid to gaseous fuel.

The numerical model builds on the balance equations resulting from the mathematical model. The numerical schemes used here

(i) allow the coexistence of droplets of the same size but with different velocities at one location,

(ii) capture vacuum zones and strong mass concentrations in unsteady gas flow structures,

(iii) are able to solve a weakly hyperbolic transport system that exhibits no pressure (infinite droplet Knudsen number),

(iv) are conservative, realisable and non-oscillatory in real and size space (for convection and evaporation),

(v) are able to consider the stiff terms of drag forces,

(vi) prevent extraordinary computational costs.

These requirements cannot be met by the well-known pressure correction algorithm [50, 83] because, among other things, no pressure is defined in the equations for the dispersed phase. In this work, an explicit procedure is preferred that is based on the Strang splitting algorithm [165]. It allows the numerical modelling of the various spray phenomena independently.

In general, CFD simulations are used for the prediction of flow phenomena because they are considered as less expensive and less time consuming than experimental measurements. However, it can only be trusted in CFD predictions, if the methods are carefully verified by comparing to reference calculations in simple configurations and if they are intensively validated by comparing to experimental measurements. The verification and validation, reported for the new Eulerian approach (see Chapter 6), are based on one- and two-dimensional test cases. They help to confirm the above properties of the new mathematical and numerical model. Complex three-dimensional cases are left for future research.

1.3 State of the Scientific Knowledge

As previously mentioned, the simulation methods for sprays in technical combustion systems are not mature. However, due to ecological and socio-economic relevance, the optimisation of combustion technologies and spray research are advancing rapidly. The

overview of the existing simulation methods given here, is only a glimpse of a much broader development.

The most refined but most costly simulation techniques are direct numerical simulations (DNS) of droplets and/or spray flows. They provide a detailed model for the dynamics of the interface between the gas and liquid and the exchanges of heat and mass. Various competitive techniques are in use: the volume of fluid method (VOF) [35, 86, 147, 150], the level set method [76, 122, 155], the ghost fluid method [49] and combinations of them [40, 110]. These methods are regarded as 'microscopic' approaches to the description of spray flows because every detail of the two-phase flow is captured. The 'mesoscopic' approach describes the droplets as a cloud of point droplets for which the exchanges of mass, momentum and heat are described using a statistical point of view [106, 112, 123]. Eulerian quantities like the diameter, surface or volume of droplets and their velocity or temperature are accounted for. The equation following from this physical model is denoted as a kinetic spray equation[3] [179] and allows the modelling of all main physical processes of sprays mentioned in Section 1.1. In the following, the dispersed phase part of the classical EL and the EE methods will be outlined. It has been shown by Pai [123] that both methods can be derived from the kinetic spray equation.

Numerical Issues: Euler-Euler vs. Euler-Lagrange

The Lagrangian procedure (cf. [9, 33, 45, 113, 119, 144, 167]), also called the particle stochastic method, treats the kinetic spray equation by solving the motion of a large number of numerical particles (parcels) in a space equipped with the same variables as the NDF in the kinetic spray equation. The mean spray properties, e.g. the mean droplet velocity and mass transfer, at position $\mathbf{x}$ and time t, which are needed for the coupling with the gas phase, are obtained by averaging over a representative sample of parcels that cross a defined volume around $\mathbf{x}$ within a certain time interval including t. The sample size and the number of tracked parcels determines the level of statistical noise of the mean droplet quantities. Hence, smaller sample volumes and shorter time intervals, which are necessary for more refined and unsteady computations, require more parcels. If, additionally, a spray is injected in a hot gas environment and a large amount of droplets vanishes very close to the injection nozzle, the number of parcels must further be increased to obtain smooth mean values away from the nozzle [74]. It was further observed by Riber et al. [137] that the speedup of the EL method by increasing the number of processors is not perfect and it strongly depends on the type of computational grid (hexahedron-based or tetrahedron-based). They show that the drop in performance is not due to large communication costs but originate from the parallel load imbalance generated by the partitioning algorithm. Riber et al. [137] used the unsteady test configuration of Borée et al. [17] to compare their EL computations to experimental measurements for moderate mass loadings. They report that the overall central processing unit (CPU) and memory requirements for high-accuracy computations of the particle phase is less than the LES gas computations, indicating that with larger mass loadings the computational costs increase.

By solving the kinetic spray equation with an Euler method, balance equations for various moments of the NDF are solved at each position and time [42, 51, 123]. These

[3] This approach is similar to the description of molecules in the kinetic gas theory (cf. Boltzmann [16] and Cercignani [24]).

moments are related to average density fields of physical droplet quantities like the mean mass, number, velocity or temperature of droplets. This procedure has the advantage that, irrespective of the amount of droplets in a region, the same number of equations always has to be solved; hence in EE computations a cost is added for the dispersed phase which is independent of the mass loading. In addition, the solver of both phases can be parallelised with the same strategy [137]. In consideration of these issues, it is expected and shown by Riber et al. [137] that the speedup of the particle phase computation behaves equally well as the speedup of the gas phase computation. With this property, EE methods are assumed to outperform EL methods on massively parallelised computers, particularly, for dense and unsteady spray flows. These assumptions are the motivation for the development of the new Euler method presented in this work.

Euler Methods for Spray Flows

The classical Eulerian description of dispersed droplets has certain principle limitations. By using a two-fluid model as described in [71, 77, 83] the cloud of droplets and the ambient gas are modelled as two interacting continuous fluids. In this approach the polydisperse character of the spray can only be captured in a very crude manner because the two superposed and coupled sets of NS-like equations are not sufficient to capture the shape of the droplet size distribution which changes when drag forces, collision and breakup are present. For two-fluid methods, the droplet size distribution is commonly assumed to have a particular form, for example, the Rosin-Rammler distribution [71, 100]. To capture the polydispersity of the spray, the use of a kinetic spray equation [179] appears to be indispensable. There are several Eulerian approaches for the detailed consideration of the polydisperse character using this equation. These are the methods of moments [72], such as the quadrature method of moments (QMoM) [183] or the direct quadrature method of moments (DQMoM) [107], and the class or sectional methods [175] introduced, for example, by Gelbard et al. [63]. They will be described in more detail in Chapter 3. Other methods, like the methods of characteristics [136], the methods of weighted residuals [132] or the method of Laplace transforms [65] can also be applied to polydisperse sprays but so far, they are more popular for the description of crystallization in chemical engineering.

In this work, the sectional method (SM)[4] developed by Domelevo [41], Dufour and Villedieu [44], Gelbard et al. [63], Laurent and Massot [96] and Laurent et al. [97] is employed as basic model because, as shown in Chapter 3, it is the most robust for evaporating sprays. In this approach the size space is discretised into fixed intervals, in which balance equations for lower order moments of the NDF in size and velocity are solved for each interval. This treatment of the kinetic spray equation allows the accurate prediction of evaporation, drag, breakup and collision of sprays. There are a variety of other approaches available which are based on a fixed discretisation of the size space. For an overview and a detailed comparison of these methods (including the SM) see Vanni [175].

Unfortunately, the SM and most other Euler methods that were developed to treat the spray in size space cannot describe the dispersion of droplet velocities at one location for one droplet size. However, this is necessary to capture the crossing of two dilute sprays arising, for example, at the rim of turbulent eddies or at walls where droplets

[4]The SM is also called 'Eulerian multifluid method' by Laurent et al. [97].

are splashed. Recently, Desjardins et al. [39] (see also [56]) proposed a quadrature-based moment method (cf. [107] for quadrature methods) that overcomes this drawback by solving balance equations not only for the number, mass and momentum densities but also for the kinetic energy and other higher order velocity moments of the NDF. This method is able to describe the crossing of sprays but does not take into account the polydisperse character of sprays.

In this work, a combination of the SM developed by Dufour and Villedieu [44] and the third-order quadrature-based methods of moments (QBMoM) developed by Fox [56] and Le Lostec et al. [99] is undertaken (see Chapters 4 to 6). Both procedures are merged in a way that allows the resulting method to describe the polydisperse nature of sprays as well as the coexistence of two or more droplet velocities at one location. To this end, a new and more general approximate NDF is proposed that reduces to the approximations of Dufour and Villedieu [44] and Fox [56] or Le Lostec et al. [99] if special sets of parameters are chosen.

1.4 Structure of the thesis

This work is organised in the following way. In Chapter 2 the physical models for sprays in technical systems are addressed by *first* giving the definitions and categorisations of the main spray phenomena (Section 2.2). *Second*, the principle physical approaches to technical sprays are discussed (Section 2.3). These considerations allow the definition of the standard physical models for the droplet-gas interaction which are the models for droplet forces, evaporation and heat transfer between droplet and gas (Section 2.4). The models for the droplet-droplet interaction, which include breakup and collision, are discussed in Section 2.5. Chapter 2 ends with a new physical model for splashing processes, in which a cloud of droplets is reflected on a wall but droplets break and loss mass and momentum.

Chapter 3 deals with the mathematical model of the kinetic spray equation (Section 3.2). Due to the large number of independent variables of the general kinetic spray equation, it cannot be solved numerically or analytically unless some mathematical transformations and assumptions on the NDF are introduced. The Lagrange and Euler methods for the description of the dispersed phase start from the same kinetic spray equation but differ in the transformation of it and in the assumptions on the NDF. The Lagrange method and the different approaches to Euler methods are discussed in more detail in Section 3.3. It will be demonstrated why certain Euler methods, particularly DQMoM, are applicable to evaporating sprays only under very strong assumptions. Arguments for the inclusion of the SM of Dufour [43] and the QBMoM of Fox [56] and Le Lostec et al. [99] are also presented. The well-known mathematical models for multicomponent gas flows are the subject of Section 3.4, where the influence of the dispersed phase on the gas equations is also addressed.

In Chapter 4 the kinetic spray equation is transformed into balance equations for a chosen set of moments (Section 4.2). This system of moment equations is closed in Section 4.3 by assuming the NDF to have a form that is special to polydisperse sprays that undergo PTC. This approximate NDF is a generalisation of those employed in the SM [43] and the QBMoM [56, 99]. The parameters of the approximate NDF are determined by the

moments that are transported. The transformation between moments and parameters is discussed in detail in Section 4.4. With these considerations the mathematical model of the new Euler method is established. Chapter 4 is supplemented by a summary of all relevant equations that have to be solved for the new Euler method.

The numerical model, i.e. the numerical schemes for the PDE system proposed in Chapter 4, is addressed in Chapter 5. The PDE system is solved using the Strang splitting procedure (Section 5.2). This allows the treatment of convection, drag force, heat transfer and evaporation with independent numerical schemes. The convection problem is treated with a finite volume discretisation in real space, using the kinetic approach of Bouchut [18] (Section 5.3). The drag force problem and the heat transfer can be solved using a stiff ODE-solver (Section 5.4). For the solution of the evaporation problem, a second-order finite volume discretisation in size space is proposed that is based on a kinetic approach as well (Section 5.5). The new splashing model which is introduced in Chapter 2 is specialised to the new Euler method in Section 5.6. Chapter 5 is completed by an overview of the general algorithm of the new Euler method.

Chapter 6 is devoted to the verification, validation and application of the new Euler method to simplified spray problems. The results are compared to a semi-analytical solution and reference Lagrangian calculations. In Sections 6.2 and 6.3 the 'pure' methods, i.e. the SM and the QBMoM are verified in one- and two-dimensional configurations. The SM is also validated by comparing the results with the measurements of Wong and Chang [182]. The new Euler method is assessed in three one-dimensional (Section 6.4) and four two-dimensional (Sections 6.5 and 6.6) test configurations by comparison to highly-resolved Lagrangian calculations. The method is tested *first* in a one-dimensional setting of two crossing spray clouds that evaporate according to a d^2-law. *Second*, the sprays cross each other but are affected by a Stokes drag force, and *third*, the method is applied to a configuration where a droplet cloud is splashed on a wall. In two dimensions the new Euler method is tested in two crossing configurations of two perpendicular moving jets that are affected by evaporation and drag force. The splashing test case is also conducted in two dimensions where, in contrast to the one-dimensional splashing, a parameter for the friction on the wall is necessary. In the last test case (Section 6.6) an evaporating and non-evaporating droplet cloud is affected through Stokes drag force by a Taylor-Green gas vortex [168]. This configuration allows the testing of the new method in an unsteady configuration that is similar to turbulent gas flow structures.

Chapter 7 presents the highlights and principal conclusions of this work. Some ideas on future work are outlined in Chapter 8.

Chapter 2

Physical Models for Sprays

2.1 Introduction

Physical models constitute the first level of abstraction in the description of physical phenomena. The real nature of matters is far too complex to be entirely considered in simulation models[1]. Therefore, only the principle effects are extracted from the vast amount of information on the physical process. The simplifying assumptions of a physical model only hold true for a specific region of length and time scales. Thus it is essential to know the characteristic scales of a process before it is physically modelled.

A prominent example of a physical model is the continuum assumption for gases, liquids and solid materials. It assumes that the mean free path between molecules, clusters or ions is much smaller than the size of the entities and interstitial space can be neglected. This assumption allows the definition of physical density fields of mass, momentum, etc. at every point in the continuum body. This assumption is appropriate for most technical flows but breaks down when the length scale of interest is only a few Ångström.

A physical model allows the definition of physical quantities for the principle effects of a process and variables for determining the state and motion of a body. Part of the role of the physical model is also to find the functional dependencies between principle effects and physical variables. These functions include dimensionless numbers that can be used to characterise a physical system or to define the area of validity of a model. The dimensionless Knudsen number,

$$\mathrm{Kn} = \frac{\text{mean free path}}{\text{char. size of smallest entity}} \,, \tag{2.1}$$

for example, is used to quantify the accuracy of the continuum assumption. For small Kn the motion of a body is dominated by a large number of molecules, ions, etc. that interact heavily with each other. For large Kn the differentiation between interstitial space and structural elements becomes important and the continuum assumption does not apply.

[1] In this work, a simulation model is considered as the combination of the physical, mathematical and numerical models of a physical process. It also includes the algorithms for implementation in a program code and the optimisation of the program code on a computer system.

The physical models for sprays are outlined in the following sections. In Section 2.2 the principle effects for spray flows are introduced and global quantities are given that allow a crude categorisation of technical sprays. In the same section the polydisperse nature of sprays and the particle trajectory crossing is discussed. In Section 2.3 the various basic modelling approaches for spray flows are outlined and reasons for the physical model chosen in this work are given. In Sections 2.4 and 2.5 standard models for droplet-gas and droplet-droplet interactions are presented. Section 2.6 is devoted to a new model for the splashing of sprays on walls.

2.2 Characteristics of Sprays

A spray is a moving cloud of dispersed droplets carried in a gaseous environment. The droplets are commonly denoted as dispersed phase and the gas as carrier phase because in most cases the droplets have a definite boundary [12].[2]

2.2.1 Principle Effects of Sprays

In combustion systems the spray is generated by injecting the liquid fuel through some type of nozzle [100]. The high fuel velocity within and at the exit of nozzles, the large moment ratio of liquid to gas phase and the surrounding gas turbulence can lead to the implosion of cavitation bubbles, high levels of turbulence in the liquid and strong aerodynamic forces on the droplet surface. In car engines, for example, these effects cause an immediate primary breakup of the connected liquid phase into droplets and ligaments which form a dense spray. The droplets are usually decelerated by the ambient gas and collisions between droplets are likely. These collisions are either totally inelastic and the droplets coalesce or they separate again, forming new droplets with different momenta and sizes. In aeroplane engines, on the other hand, the liquid fuel has relative low velocities in the nozzle but is strongly accelerated in the gas flow. Therefore, the primary breakup is dominated by the strong aerodynamic forces acting on the liquid jet. The acceleration leads also to a thinning of the spray which reduces the probability of collision.

In the regime of secondary breakup (see Figure 1.2) the droplets fragment into smaller droplets. Although the velocity difference between droplets and gas is smaller than in the primary breakup regime it is sufficient to amplify the Kelvin-Helmholtz or Rayleigh-Taylor instabilities [103]. The type of breakup strongly depends on the Weber number, defined by

$$\mathrm{We} := \frac{\rho_g \left|\mathbf{v}_{\mathrm{rel}}\right|^2 \mathrm{d}}{\sigma_d} \,, \tag{2.2}$$

where ρ_g [$\mathrm{kg\,m^{-3}}$] is the mass density of the gas, d [m] a characteristic diameter of a droplet, $\mathbf{v}_{\mathrm{rel}}$ [$\mathrm{m\,s^{-1}}$] the (barycentric) velocity difference between gas and droplet and σ_d [$\mathrm{N\,m^{-1}}$] the surface tension of a droplet.

Far away from the nozzle (see Figure 1.2), the droplets reach the gas velocity, the events of collision and breakup are rare and the overall surface area of droplets is large. In

[2] In supercritical spray flows the definition of a phase has to be loosened because there is no sharp boundary, only a transition zone from the droplet to the gas.

this region the evaporation of droplets is dominant and the motion of the gas determines that of the droplets. The ability of droplets to follow the gas is high because their size is small and it is further reducing due to evaporation.

2.2.2 Categorisation of Sprays

There are various ways to categorise sprays. The simplest way to differentiate between various patterns of sprays is the geometric description of spray jets using quantities like spray penetration, spray cone angle or other geometric measures. These quantities can be gained using relatively simple measurements but cannot be used for general purposes as they are closely related to a specific type of nozzle.

A more general global quantity to categorise sprays is the total mass loading

$$Z = \frac{\dot{M}_d}{\dot{M}_g} \ , \tag{2.3}$$

which is the ratio of the overall mass flow rate of the droplet phase, $\dot{M}_d$ [kg s^{-1}], to that of the gas phase, $\dot{M}_g$ [kg s^{-1}]. Another global quantity that is useful for the characterisation of sprays is the total volume fraction of the dispersed phase in the system

$$\alpha_d = \frac{V_d}{V_{sys}} \ , \tag{2.4}$$

where V_d [m^3] is the volume of droplets and V_{sys} [m^3] is the system volume. The total mass loading and the total volume fraction are global values that are used to design combustion chambers. They give an indication of the equivalence ratio and the denseness of the spray. However, it is observed in Figure 1.2 that a fuel spray is far from being homogeneously distributed in the combustion chamber. Near the nozzle the spray is considered as very dense and far away from the nozzle it is usually regarded as dilute. Therefore, it is advantageous to introduce local dimensionless quantities to categorise sprays.

The dimensionless droplet Knudsen number, also called the droplet spacing [33],[3]

$$\mathrm{Kn}_d = \frac{\text{mean free path of droplets}}{\text{mean size of droplets}} \ , \tag{2.5}$$

is used to classify sprays or regions of sprays in terms of diluteness. This quantity is related to the collision of droplets which are more likely in dense sprays. For regions of dilute sprays, i.e. far away from the nozzle, events of collisions are rare as the droplets are small and widely distributed. The gas flow has an impact on the mean free path because droplets tend to follow the non-crossing streamlines of the gas. This indicates that the mean free path depends not only on the denseness of a spray but also on the ability of the droplets to follow the gas.

Another categorisation of sprays, which is the most suitable for simulation modelling, is based on the local dimensional numbers for the different spray phenomena which are introduced in Sections 2.5 and 2.6.

[3] An alternative definition of the droplet Knudsen number will be given in equation (2.64).

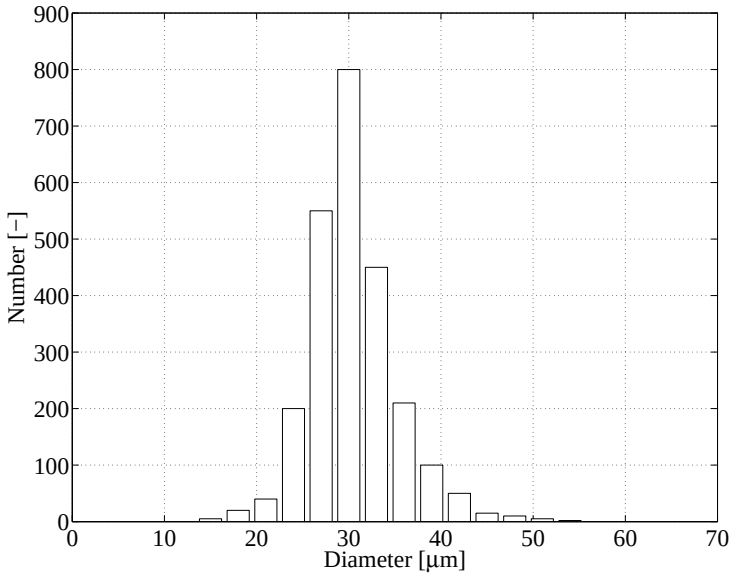

Figure 2.1: Number vs. diameter of droplets in a polydisperse spray; from experiment of Wong and Chang [182].

2.2.3 The Polydisperse Nature of Sprays

A collection of droplets is called polydisperse if it can be characterised by a broad range of shapes, sizes and masses. The atomization of liquid fuel in a technical injection device generates a spray that is polydisperse but, to be precise, the droplets also have different velocities, temperatures and rotational speeds [73, 181]. The polydispersity of a spray originates from the collision and breakup[4] of droplets in the primary and secondary breakup region (see Figure 1.2), from the evaporation of droplets in the inhomogeneous turbulent gas flow and from the drag forces that are affecting small droplets differently than large ones. The latter phenomenon leads to an effect which is commonly called droplet size segregation. It is the separation of small and large droplets.

The distribution of droplet sizes $f(\mathrm{d})$ at a given position and time is usually given in the form presented in Figure 2.1. In these type of representations the droplet diameter is used as measure of droplet sizes assuming the droplets to be spheres. All kinds of statistics can be applied to droplet distributions and various averages can be defined. The most relevant quantity in the design of combustion devices is the Sauter mean diameter (SMD). It is defined by

$$\mathrm{d}_{32} := \frac{\sum_i \mathrm{d}_i{}^3 n_i}{\sum_i \mathrm{d}_i{}^2 n_i} \ , \tag{2.6}$$

where d_i [m] is the diameter and n_i is the number of droplets in size-classe i (see Figure 2.1). The SMD is a ratio of quantities which are proportional to the average mass and surface of droplets at a given point. Large SMD values are observed in regions of dense

[4]Fundamental experiments on the fragmentation of ligaments were performed by Eggers and Villermaux [46, 176], whereas the collision of droplets was investigated experimentally by Qian and Law [130].

sprays where the influence of evaporation is small, and low values of SMD where broadly dispersed droplets are observed and evaporation has a strong influence.

The Rosin-Rammler (Weibull) distribution [100, 141]

$$f(\mathrm{d}; D_m, n) = \begin{cases} \dfrac{n}{D_m}\left(\dfrac{\mathrm{d}}{D_m}\right)^{n-1} \exp\left(-\dfrac{\mathrm{d}^n}{{D_m}^n}\right), & \mathrm{d} \geq 0\,, \\ 0\,, & \mathrm{d} < 0\,, \end{cases} \tag{2.7}$$

is often used to fit measured droplet distribution functions, where the fitting parameters D_m [m] and n [-] are the mean diameter and the measure of the spread of droplet diameters, respectively. The Rosin-Rammler distribution can also be used as presumed probability density function (PDF) in numerical methods where D_m and n are free parameters that have to be determined. Groll [71] fixes n and relates D_m to the SMD.

The collision, breakup, size segregation and evaporation of droplets can lead to considerable changes in the droplet size distribution. Therefore, the representation of a droplet size distribution by means of one mean value or a presumed PDF is not sufficient for the prediction of injection processes into turbulent gases.

2.2.4 Particle Trajectory Crossing

The standard example for particle trajectory crossing (PTC) is an impinging gas flow laden with droplets. One such configuration is the opposed jet flame setup depicted in Figure 2.2, which is seeded with oil droplets [14, 64]. In this configuration, the droplets are usually very small and they follow perfectly the gas flow. It is unlikely that these droplets cross the impingement plane. Increasing their size or using heavier solid particles, changes in the gas flow have less influence on the dispersed entities. Thus, they are able to continue directly through the impingement plane. If the cloud of droplets is dilute, i.e. it has a large droplet Knudsen number, droplets or particles from both sides can cross the impingement plane without risk of collision. At the crossing points the (ensemble-averaged) velocity distribution is locally bi- or multi-modal which is the main characteristic of particle trajectory crossing.

It is known from real [143] and numerical experiments [105] of dispersed particles in turbulent gas flows, that particles accumulate in regions of low fluctuating velocities. These areas behave like local and time-dependent impingement zones, which are prone to PTC. In polydisperse spray flows, PTC is even more likely because the size-dependent drag force on the droplets leads to broad velocity distributions [73]. In the configuration depicted in Figure 1.2, for example, large droplets 'overtake' smaller ones as they experience stronger decelerations.

Another example for PTC is the splashing of dilute sprays on inclined and heated walls [61]. Due to the formation of fuel vapour cushions between droplets and wall, droplets can rebound from the wall. If the spray is dilute enough, the rebounding droplets cross those who are approaching the wall [62] and again a bi-modal or multi-modal velocity distribution arises. Sprays cannot be considered as dilute for spray-wall interaction in car diesel engines [163]. Effects like fuel droplet deposition on the wall, formation of a film and collision of incident and rebounding droplets are also possible. Nevertheless, only when all incident droplets are deposited or collide with rebounding droplets, PTC is not present.

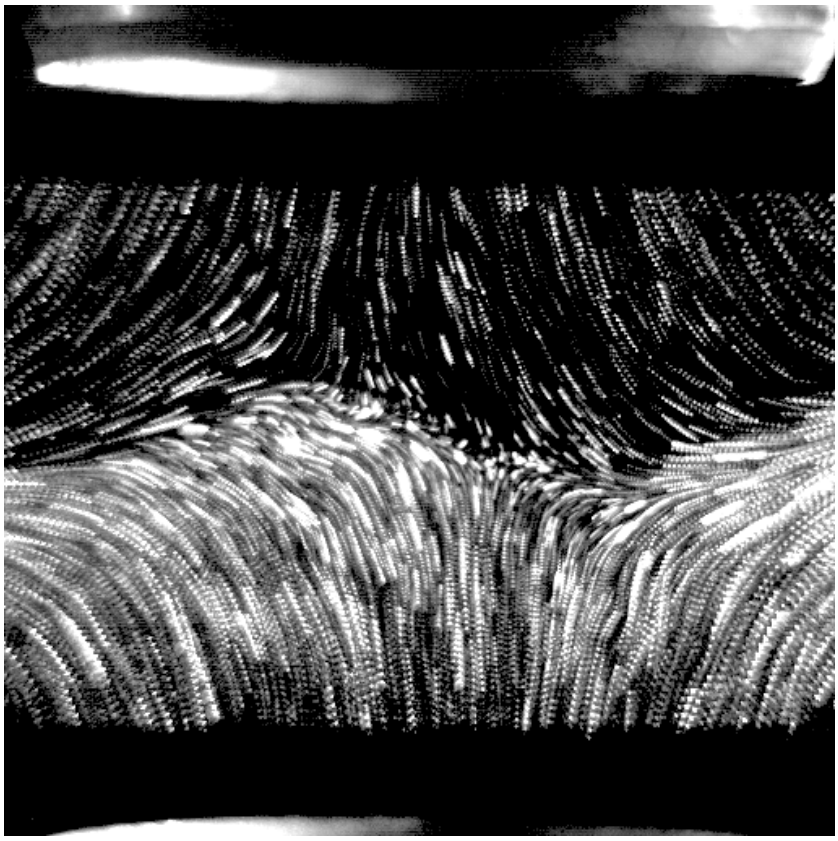

Figure 2.2: Oil droplets (PIV-seeding) in an opposed jet flame configuration [14, 64].

From a statistical point of view, it is concluded that in technical spray configurations, PTC, collision and breakup may be present simultaneously at the same location.

2.3 Principle Physical Approaches to Sprays

In multiphase flows, particularly in spray flows, different physical models are applied depending on the phenomena of interest. If the investigator intends to study the droplet deformation, temperature distribution, mass or heat losses while a droplet is evaporating, breaking or colliding, the detailed processes at the gas-droplet interface should be considered [110, 150]. In this case, the liquid behaviour and the surrounding gas flow have to be captured as accurate as possible using the continuum assumption. This 'microscopic' approach, which considers the entire complexity of the flow, allows the development and assessment of models for drag forces, evaporation, collision, heat transfer, etc. Unfortunately, due to the extraordinary computational requirements, it is feasible only for a few droplets within a relatively short time interval.

If a dense spray is studied the details of the droplet-gas and droplet-droplet interactions are not affordable, in particular when the length scales of the system are large, long time intervals are of interest and the gas flow is turbulent. The simplest physical model for this type of flows is a 'macroscopic' approach that is based on a mixture con-

tinuum assumption [80]. For this model strong physical assumptions are introduced such as the spray and the gas have the same mean velocity and temperature or the size of the droplets have no influence on the flow. This approach considers only mean (mixture) quantities, i.e. the mass of the droplet-gas mixture, the mass averaged (barycentric) velocity, the averaged temperature and the concentrations of droplets, fuel vapour and other gas components. The main advantage of this simple physical model is that only one set of multicomponent NS-like equations has to be solved. However, it is questionable whether this physical model is appropriate for the modelling of sprays in combustion systems. In these systems it cannot be assumed that the droplets have the same velocity as the gas. In addition, the evaporation process can hardly be modelled accurately because the droplet size is unknown.

In between these two extreme physical approaches various compromises are possible. In the case when the precise capturing of the droplet/gas interfaces is not intended the dispersed phase and the carrier phase are treated with separate physical models. In technical spray flows the gas is turbulent and therefore direct numerical simulations (DNS), large-eddy simulation (LES) and Reynolds averaged Navier-Stokes (RANS) simulations are applied. All these methods are based on the physical model of the NS equations (see Section 3.4). The droplets are usually assumed to be spherical point masses with the properties of mass (or droplet size), momentum (or velocity), enthalpy (or temperature), composition or other characteristic properties.

The coupling between the continuous and the dispersed phase can be done on three different levels. In one-way coupling the gas will affect the dispersed phase properties (mass, velocity, temperature, etc.) but the dispersed phase has no influence on the carrier flow. This model is appropriate for dilute spray flows where the overall liquid mass fraction is small and droplets do not concentrate in certain regions. A two-way coupling is preferred if the influence of the spray on the gas cannot be neglected and mass and momentum transfers between droplets and gas are important. If, in addition, the droplet-droplet interaction is accounted for, a four-way coupling is enforced. It also takes into account the breakup and collision of droplets. The modelling of sprays in combustion systems requires at least a two-way coupling because the fuel vapour/air mass fraction depends strongly on the mass transfer from the droplet to the gas phase. In this work, a one-way coupling is considered. This assumption is enforced not because it is a good approximation for spray flows in combustion systems, but it allows the analysis of the solution methods for the dispersed phase without being affected by inaccuracies of the coupling between carrier and dispersed phase.

Different physical models exist for the description of the dispersed phase flow. In discrete particle simulations (DPS) [105, 115, 174] each physical droplet is taken into account and the collision of droplets are explicitly modelled by checking for all collision events. This approach, which requires large computational resources, is applied in fundamental studies that aim at understanding droplet transport and droplet-droplet interactions in turbulent carrier phases. As each physical droplet is captured and the surrounding gas is commonly treated with DNS or LES, this approach can also be considered as 'microscopic'.

The less computational expensive and widely used EL and EE methods are based on a statistical approach which assumes the spray to be a cloud of spherical point droplets.

The ensemble average over this cloud allows the definition of 'mesoscopic' variables, such as droplet size, velocity, temperature or other characteristic droplet quantities at each position in the domain. The interaction between droplets and gas are also ensemble averaged. This approach allows the consideration of the standard spray models for drag force, gravity, evaporation, heat transfer, breakup, collision and coalescence (see Sections 2.4 and 2.5) in terms of the 'mesoscopic' variables [55]. In this work, the latter approach is pursued because it allows describing technical spray flows within sufficiently large time intervals.

2.4 Droplet-Gas Interaction

In this section, it is intended to describe the interaction between a spray and the gaseous phase it is suspended in. Before concluding on the global behaviour of this two phase system, the mass, momentum and energy interactions between *one* droplet and the gas are investigated, neglecting the presence of other droplets. The aerodynamic effects that originate from the relative motion between droplet and ambient gas are pressure gradients, viscous boundary layers, separated flows and wakes on the far side of the gas flow approaching the droplet. These gas flow effects and the internal liquid circulation, driven by surface-shear forces on the droplet, are fluid-dynamic features that heavily influence the motion of a droplet and the heat and mass transfer between droplet and gas. In general, the relative motion results in an increase of heat and mass transfer rates in the gas film surrounding a droplet [158].

In this work, the droplets are assumed to be point masses equipped with the properties of size, velocity and temperature. The drag force influencing the velocity of a point droplet is set equal to the surface integral of all pressures acting on a real droplet with the same surface and barycentric velocity. The same idea is followed for the evaporation and heat transfer model. They describe the change of size and temperature of the point droplet.

In the present work, the size of a droplet is characterised by the droplet surface, s [m^2]. As the droplets are assumed spherical, the surface of a droplet can be mapped to its diameter or volume without loss of generality. Using the surface, nonlinearities in the models for drag and evaporation can be avoided and the numerical methods for the solution of the balance equations derived in Chapters 4 and 5 simplify considerably. In this study, all physical models are written in terms of the droplet surface, s.

2.4.1 Forces on Droplets

The forces on bodies submerged in a gaseous environment is dealt with for quite some time (cf. [121, 164]) and rather sophisticated drag models exist (cf. [33]). In this work, a droplet is considered to be affected by a drag force, $\mathbf{F}_d$ [N] and the gravity force, $(m_d\, g\, \mathbf{e}_g)$, i.e.

$$\mathbf{F} = \mathbf{F}_d + m_d\, g\, \mathbf{e}_g \ , \tag{2.8}$$

where $\mathbf{F}$ [N] is the total force on a droplet, m_d [kg] is the droplet mass, $g = 9.81\,\mathrm{m\,s^{-2}}$ the acceleration of gravity, and $\mathbf{e}_g$ the unit normal vector pointing into the direction of gravity.

The dependencies of the drag force are confined to the droplet surface, the relative velocity between gas and droplet, $\mathbf{v}_{\mathrm{rel}} := \mathbf{U}_g - \mathbf{v}$ $[\mathrm{m\,s^{-1}}]$, the gas density, ρ_g, the dynamic viscosity of the gas, η_g $[\mathrm{kg\,(m\,s)^{-1}}]$ and the surface tension, σ_d $[\mathrm{N\,m^{-1}}]$. The unstationary behaviour of the droplet, buoyancy effects, compressibility of the gas, rotation effects, the fluid motion within the droplet or other more subtle forces are not considered. It can be shown that terms originating from these phenomena are negligible for large ratios of droplet to gas densities, droplets of small sizes (relative to a characteristic length scale of the gas) and low droplet Mach numbers

$$\mathrm{Ma}_d := \frac{|\mathbf{v}_{\mathrm{rel}}|}{c} < 0.03 \ , \tag{2.9}$$

where c $[\mathrm{m\,s^{-1}}]$ is the speed of sound in the gas. Based on the above dependencies the following functional relation for the drag force is postulated

$$\mathbf{F}_d = \tilde{\mathbf{F}}_d(s, \rho_g, \eta_g, \sigma_d, \mathbf{v}_{\mathrm{rel}}) \ . \tag{2.10}$$

Assuming the number of independent variables on the right-hand side of (2.10) to be complete, a dimensional analysis [11, 80] leads to the expression

$$\mathbf{F}_d = \rho_g s |\mathbf{v}_{\mathrm{rel}}| \tilde{F}_d(\mathrm{Re}_d, \mathrm{We}) \mathbf{v}_{\mathrm{rel}} \ , \tag{2.11}$$

with the definitions of the dimensionless numbers:

droplet Reynolds number
$$\mathrm{Re}_d := \frac{\rho_g \sqrt{s}\ v_{\mathrm{rel}}}{\sqrt{\pi}\,\eta_g} \ , \tag{2.12}$$

Weber number
$$\mathrm{We} := \frac{\rho_g |\mathbf{v}_{\mathrm{rel}}|^2 \sqrt{s}}{\sqrt{\pi}\,\sigma_d} \ . \tag{2.13}$$

If the dynamic effects of the droplet surface, which are dominated by the surface tension, are neglected, the dependence of $\tilde{F}_d$ [-] on the Weber number can be set aside. The droplet surface tension will be important for the modelling of breakup and collision (see Section 2.5).

It remains to find the functional dependence between $\tilde{F}_d$ and Re_d using either analytical, numerical or experimental methods to analyse the behaviour of a single droplet in a moving gas environment (cf. [149] or [169]). In the context of experiments relation (2.11) is commonly written as

$$\mathbf{F}_d = \frac{1}{8} C_d\, \rho_g\, s\, |\mathbf{v}_{\mathrm{rel}}|^2\, \frac{\mathbf{v}_{\mathrm{rel}}}{|\mathbf{v}_{\mathrm{rel}}|} \ , \tag{2.14}$$

with the coefficient of drag, C_d [-], depending on the droplet Reynolds number. Another common form of expression (2.14) is

$$\mathbf{F}_d = \frac{m_d}{\tau_d} \mathbf{v}_{\mathrm{rel}} \ , \tag{2.15}$$

where τ_d [s] is called droplet response time or droplet relaxation time in the gas flow. The droplet response time depends on Re_d, $|\mathbf{v}_{\mathrm{rel}}|$, the mass density of droplet liquid, ρ_ℓ

$[\mathrm{kg\,m^{-3}}]$, and the size of the droplet. The coefficient of drag and the response time are related by

$$\frac{1}{\tau_d} = \frac{3\sqrt{\pi}}{4} C_d \frac{\rho_g}{\rho_\ell} s^{-1/2} |\mathbf{v}_{\mathrm{rel}}|, \quad \text{with} \quad \rho_\ell = m_p \frac{s^{3/2}}{6\sqrt{\pi}} \,. \tag{2.16}$$

The dimensionless Stokes number, St, defined via the response time and a characteristic time scale of the gas, τ_g [s], i.e.

$$\mathrm{St} := \frac{\tau_d}{\tau_g} \,, \tag{2.17}$$

quantifies the ability of a droplet to follow the gas. It plays an important role in all acceleration and deceleration processes of droplets in a gas. In the case of an opposed jet flow (see Figure 2.2), the Stokes number determines whether the particles cross the impingement plane or not. For small Stokes numbers ($\mathrm{St} \ll 1$) the particles remain on their respective side of the opposed jet configuration and have nearly the same velocity as the gas. For larger Stokes numbers ($\mathrm{St} > 1$) changes in the gas motion have less affects on the droplets and PTC is more likely (see Section 2.2.4). For sprays suspended in a turbulent gas flow, the turbulence modulation in the gas and the droplet dispersion is also dominated by the Stokes number [145].

For small droplet Reynolds numbers ($\mathrm{Re}_d < 1$) the Stokes law [164] assumes the functions C_d and τ_d to have the simple form

$$C_{d,\mathrm{St}} = \frac{24}{\mathrm{Re}_d} \quad \text{and} \quad \tau_{d,\mathrm{St}} = \frac{\rho_\ell s}{18\pi\eta_g} \,. \tag{2.18}$$

For higher droplet Reynolds numbers Schiller and Naumann [148] proposed a correction which reads

$$C_{d,\mathrm{SN}} = \begin{cases} C_{d,\mathrm{St}} \left(1 + 0.15 \cdot \mathrm{Re}_d^{0.687}\right), & \mathrm{Re}_d < 10^3, \\ 0.44, & \mathrm{Re}_d \geq 10^3 \,. \end{cases} \tag{2.19}$$

For the sake of simplicity, in Section 4.5.1, the general drag force model (2.15) is specialised to the Stokes law.

2.4.2 Evaporation and Droplet Heating

In combustion systems, particularly in direct injection engines, the droplet evaporation can be critical because [163]

(i) it has a direct effect on the combustion rate,

(ii) it influences the emission formation.

Poor evaporation typically causes increased soot and unburned hydrocarbon emission. Fast evaporation (e.g. under flash boiling conditions) leads to extra NO_x emission because the rapid premixed combustion is associated with high temperatures [163].

Unfortunately, the evaporation process can be very complex under realistic combustion conditions. Factors that increase the complexity of evaporation models are

(i) the multicomponent character of carbon fuels [94, 180],

(ii) very high or sometimes supercritical pressures and temperatures in the combustion chamber ,

(iii) the interaction between droplets in the turbulent gas environment,

(iv) the interaction between flame and un-vaporised droplets [135].

In this work, the focus is not on the development of new evaporation models (for a recent overview see Laurent [94]). Instead, it is intended to check the new Euler method, which is presented in Chapters 4 to 6, whether it is in agreement with the robust standard models for the evaporation of single-component droplets.

Sirignano [158] identified six types of droplet-evaporation models. In order of increasing complexity, they are called

(i) constant droplet-temperature model (d^2-law), i.e.

$$\frac{ds}{dt} = \mathrm{K} = \text{const.} \,, \tag{2.20}$$

(ii) infinite liquid-conductivity model (uniform droplet temperature varying with time),

(iii) spherically symmetric transient droplet heating model (limited conductivity model),

(iv) effective-conductivity model,

(v) vortex model of droplet heating,

(vi) Navier-Stokes solution.

The main difference between these models is the treatment of the heating of the liquid phase because it is the rate controlling factor in the process of droplet evaporation [158].

In this work, the models (i) and (ii) are used where the constant K for model (i) is obtained from model (ii) by assuming the velocity and temperature difference between droplet and surrounding gas to be zero. In the following, the focus will be on the infinite liquid-conductivity model introduced by Abramzon and Sirignano [1].

The model of Abramzon and Sirignano [1] assumes a spherical droplet to be supended in a quasi-steady gas flow with negligible pressure drop. It allows variable physical properties of the droplet and variable Prandtl, Schmidt, and Lewis numbers (to be defined) in the boundary layer around the droplet. The gas phase calculation around a droplet is based on the one-dimensional film theory [149], which considers the change of thermal and diffusional film thicknesses due to Stefan flow. Abramzon and Sirignano [1] assumed a transient liquid heating inside the droplet using an 'effective' thermal conductivity of the liquid fuel. In this work, the position is taken that either the heat conductivity in the liquid is very fast or the droplets are very small compared to the characteristic length scales of the gas flow. This justifies the assumption of a time-varying but uniform temperature in the droplet and on its surface.

The evaporation and heat transfer model is based on the relations

$$\frac{ds}{dt} = \mathrm{K}(s, \mathbf{v}, \theta) \tag{2.21}$$

for the surface of a droplet and

$$\frac{d\theta}{dt} = \mathrm{R}(s, \mathbf{v}, \theta) \tag{2.22}$$

for the uniform temperature of a droplet, θ [K]. Assuming the droplets to be spherical, the size, velocity and temperature-dependent evaporation rate K [$\mathrm{m^2 s^{-1}}$] is related to the mass transfer $\dot{m}_d := dm_d/dt$ [$\mathrm{kg\,s^{-1}}$] via

$$\mathrm{K}(s, \mathbf{v}, \theta) = \frac{6\sqrt{\pi}}{\rho_\ell \, s^{1/2}} \, \dot{m}_d(s, \mathbf{v}, \theta) \ . \tag{2.23}$$

The rate of change of the temperature R [$\mathrm{K\,s^{-1}}$] is related to the gas/droplet heat conduction, $\dot{\mathrm{Q}}_{gl}$ [W], mass transfer and the latent heat, $L(\theta)$ [$\mathrm{J\,kg^{-1}}$], through

$$\mathrm{R}(s, \mathbf{v}, \theta) = \frac{\dot{\mathrm{Q}}_{gl}(s, \mathrm{v}, \theta) + \dot{m}_d(s) \, L(\theta)}{c_p(\theta) \, m_d(s)} \ , \tag{2.24}$$

where the specific heat capacity of the droplet, c_p [$\mathrm{J(kg\ K)^{-1}}$], depends on the droplet temperature.

Notice, that R and K are strongly coupled via the mass transfer and their dependence on the temperature. In the following paragraphs the mass and heat transfers, as derived by Abramzon and Sirignano [1], are outlined.[5]

The Mass Transfer.
Abramzon and Sirignano [1] assumed the mass transfer to have the form

$$\dot{m}_d(s, \mathbf{v}, \theta) = \sqrt{\pi} s^{1/2} \rho_g D_{va}(\tilde{\theta}) \mathrm{Sh}_{0,\mathrm{mod}}(\mathbf{v}, \tilde{\theta}) \ln(1 + \mathrm{B_m}(\tilde{\theta})) \ , \tag{2.25}$$

with the diffusivity of fuel vapour in air, D_{va} [$\mathrm{m^2 s^{-1}}$], the modified Sherwood number, $\mathrm{Sh}_{0,\mathrm{mod}}$ [–], the coefficient for mass transfer, B_m [–], and the mean temperature within the thermal film surrounding the droplet, $\tilde{\theta}$ [K].

The diffusivity depends strongly on the mean temperature and the pressure in the thermal film. Analytical expressions for binary gas systems at low pressures are available in Poling et al. [127]. The mean temperature in the thermal film is commonly approximated by a 1/3-law, i.e.

$$\tilde{\theta} = \theta + \frac{1}{3}(\theta_g - \theta) \ , \tag{2.26}$$

where θ_g [K] is the absolute gas temperature far away from the droplet. The modified Sherwood number is defined by

$$\mathrm{Sh}_{0,\mathrm{mod}} := 2 + \frac{\mathrm{Sh}_0 - 2}{F(\mathrm{B}_m)} \ , \tag{2.27}$$

where

$$\mathrm{Sh}_0 := 1 + (1 + \mathrm{Re}_d \mathrm{Sc})^{1/3} \cdot g(\mathrm{Re}_d), \quad g(\mathrm{Re}_d) := \begin{cases} 1 & \mathrm{Re}_d \leq 1, \\ \mathrm{Re}_d{}^{0.077} & \text{otherwise} \ , \end{cases} \tag{2.28}$$

[5] For more details the reader is referred to Groll [71] and Ochs [116].

is the Sherwood number, defined according to Clift et al. [28]. The function $F(\mathrm{B}_m)$ in (2.27) is a correlation of numerical results for the Falkner-Skan solution. Abramzon and Sirignano [1] proposed the following form

$$F(\mathrm{B}_m) = (1+\mathrm{B}_m)^{0.7}\frac{\ln(1+\mathrm{B}_m)}{\mathrm{B}_m} \quad \text{for} \quad 0 \le \mathrm{B}_m \le 20,\ 1 \le \mathrm{Pr},\ \mathrm{Sc} \le 3\ . \tag{2.29}$$

The Prandtl and Schmidt numbers are defined by

$$\mathrm{Pr} := \frac{\bar{c}_{pg}\bar{\eta}_g}{\bar{\lambda}_g}, \qquad \mathrm{Sc} := \frac{\bar{\eta}_g}{\bar{\rho}_g D_{va}}\ , \tag{2.30}$$

with the average specific heat capacity of the gas, $\bar{c}_{pg}$ $[\mathrm{J(kg\,K)^{-1}}]$, and the average thermal conductivity, $\bar{\lambda}_g$ $[\mathrm{W(mK)^{-1}}]$, in the gas mixture of the thermal film. The averaged dynamic viscosity and density in the definition of the Schmidt number are taken from the diffusional film.

The coefficient of mass transfer, B_m, (also called Spalding number of mass transfer) introduced in (2.25), is defined according to

$$\mathrm{B}_m(\theta) := \frac{Y_{\mathrm{sat}}(\theta) - Y_\infty}{1 - Y_{\mathrm{sat}}(\theta)}\ , \tag{2.31}$$

where Y_∞ is the minimum mass fraction of fuel vapour in the gas far away from the droplet and Y_{sat} is the saturation mass fraction. Knowing the droplet (surface) temperature and assuming the gas phase to be saturated in the vicinity of the droplet surface the saturation mass fraction can be evaluated using the Clausius-Clapeyron equation [71].

It should be noted that B_m is related to the droplet temperature via the saturation mass fraction. Therefore, the mass transfer $\dot{m}_d$ is nonlinearly coupled to the droplet temperature as well.

The Heat Transfer.
In the model proposed by Abramzon and Sirignano [1], the temperature of a droplet is influenced by the heat conduction from the hotter to the colder phase and the consumption of energy due to the phase change of droplets. Heat radiation and other more subtle influences, e.g. the Dufour effect, are neglected. The analysis of [1] leads to the model

$$c_p\, m_d\, \mathrm{R}(s,\mathbf{v},\theta) = \mathrm{Nu}\,\sqrt{\pi}\, s^{1/2}\bar{\lambda}_g(\theta_f - \theta) - \dot{m}_d\, L(\theta)\ , \tag{2.32}$$

where Nu is the dimensionless Nusselt number. The coefficient of heat transfer (also called Spalding number for heat transfer)

$$\mathrm{B}_h := \frac{\bar{c}_{pF}(\theta_g - \theta)}{(c_p\, m_d\, \mathrm{R})/\dot{m}_d + L(\theta)} \tag{2.33}$$

is defined in order to parameterise the influence of the Stefan flow on

$$c_p\, m_d\, \mathrm{R}(s,\mathbf{v},\theta) = \dot{m}_d\left(\frac{\bar{c}_{pF}(\theta_g - \theta)}{\mathrm{B}_h} - L(\theta)\right)\ , \tag{2.34}$$

with only one parameter. The quantity $\bar{c}_{pF}$ is the average vapour specific heat of the film with the average temperature $\tilde{\theta}$ (see (2.26)) in the thermal film. Relation (2.34) is the principle expression to determine $\mathrm{R}(s, \mathbf{v}, \theta)$. It requires the specification of B_h and $L(\theta)$.

Before doing so, the definition of B_h in (2.33) will further be discussed. It allows the derivation of

$$\dot{m}_d \overset{(2.32)}{=} \sqrt{\pi}\, s^{1/2} \frac{\bar{\lambda}_g}{\bar{c}_{pF}} \mathrm{Nu}\, \mathrm{B}_h \overset{(2.25)}{=} \sqrt{\pi} s^{1/2} \rho_g D_{va} \mathrm{Sh}_{0,\mathrm{mod}} \ln(1 + \mathrm{B_m}) \ , \tag{2.35}$$

which can be used to relate B_h and B_m. To this end, the modified Nusselt number

$$\mathrm{Nu}_{0,\mathrm{mod}} := \mathrm{Nu} \frac{\mathrm{B}_h}{\ln(1 + \mathrm{B}_h)} = 2 + \frac{\mathrm{Nu}_0 - 2}{F(\mathrm{B}_h)} \ , \tag{2.36}$$

is introduced, where F is the function defined in (2.29) (satisfying $0 \geq \mathrm{B}_h$) and Nu_0 is defined by (see $(2.30)_1$ and $(2.28)_2$)

$$\mathrm{Nu}_0 := 1 + (1 + \mathrm{Re}_d \mathrm{Pr})^{1/3} g(\mathrm{Re}_d) \ . \tag{2.37}$$

This new definition leads to

$$\frac{\bar{c}_{pg}}{\bar{c}_{pF}} \underbrace{\frac{\bar{\lambda}_g}{\rho_g \bar{c}_{pg} \mathrm{D}_{va}}}_{=\mathrm{Le}} \mathrm{Nu}_{0,\mathrm{mod}} \ln(1 + \mathrm{B}_h) = \mathrm{Sh}_{0,\mathrm{mod}} \ln(1 + \mathrm{B}_m) \ , \tag{2.38}$$

which can further be modified to yield

$$\mathrm{B}_h = (1 + \mathrm{B}_m)^{\phi_B} - 1, \qquad \phi_B := \frac{\ln(1 + \mathrm{B}_h)}{\ln(1 + \mathrm{B}_m)} = \left(\frac{\bar{c}_{pF}}{\bar{c}_{pg}} \right) \left(\frac{\mathrm{Sh}_{0,\mathrm{mod}}}{\mathrm{Nu}_{0,\mathrm{mod}}} \right) \frac{1}{\mathrm{Le}} \ , \tag{2.39}$$

a direct correlation between the coefficients of mass and heat transfer.

The latent heat of evaporation is obtained from the Clausius-Clapeyron equation [71]

$$L(\theta) = \frac{R_0}{M_v} \left(\frac{1}{\theta} - \frac{1}{\tilde{\theta}} \right)^{-1} \ln \left(\frac{p_{\mathrm{sat}}(\tilde{\theta})}{p_{\mathrm{sat}}(\theta)} \right) \tag{2.40}$$

using the ideal gas law and the assumption of large specific volume of the fuel vapour compared to the liquid. The quantities R_0 $[\mathrm{J\,(mol\,k)^{-1}}]$, M_v $[\mathrm{kg\,mol^{-1}}]$ and p_{sat} $[\mathrm{N\,m^{-1}}]$ are the universal gas constant, the molar mass of the fuel vapour and the saturation pressure, respectively. The saturation pressure can be obtained from the tables found in [173].

Algorithm to find the Heat and Mass Transfer.
The Nusselt and Sherwood numbers, Nu_0 and Sh_0, the coefficient for mass transfer, B_m, and the modified Sherwood number, $\mathrm{Sh}_{0,\mathrm{mod}}$, can be evaluated using relations (2.37), (2.28), (2.31) and (2.27), respectively. The coefficient for the heat transfer, B_h and the modified Nusselt number, $\mathrm{Nu}_{0,\mathrm{mod}}$, can only be evaluated if $\mathrm{R}(s, \mathbf{v}, \theta)$ is known or the Lewis number in (2.39) is set to one. Unfortunately, the change of temperature is not known in advance and it is not intended to specialise the model to one specific Lewis

number. Abramzon and Sirignano [1] introduced an algorithm that allows the iterative determination of B_h and $\mathrm{Nu}_{0,\mathrm{mod}}$ with the initial condition

$$\mathrm{Nu}_{0,\mathrm{mod}}^{(0)} = \mathrm{Nu}_0 \ . \tag{2.41}$$

With the following iterative scheme an approximation of the modified Nusselt number can be obtained

$$\phi_B^{(n)} = \frac{\bar{c}_{pg}}{c_p} \frac{\mathrm{Sh}_{0,\mathrm{mod}}}{\mathrm{Nu}_{n,\mathrm{mod}}^{(n-1)}} \mathrm{Le}^{-1} \ , \tag{2.42}$$

$$\mathrm{B}_h^{(n+1)} = (1+\mathrm{B}_m)^{\phi_B^{(n)}} - 1 \ , \tag{2.43}$$

$$\mathrm{Nu}_{0,\mathrm{mod}}^{(n+1)} = 2 + \frac{\mathrm{Nu}_0 - 2}{F(\mathrm{B}_h^{(n)})} \ . \tag{2.44}$$

This scheme is deduced from equations $(2.39)_{1,2}$ and (2.36). The iteration is continued until the condition

$$\left| \frac{\mathrm{B}_h^{(n+1)}}{\mathrm{B}_h^{(n)}} - 1 \right| < \varepsilon \ll 1 \tag{2.45}$$

is satisfied. Knowing B_h or $\mathrm{Nu}_{0,\mathrm{mod}}$ allows the determination of the rate of change of temperature R (2.34) and the heat conduction $\dot{\mathrm{Q}}_{gl}$ (2.24).

2.5 Droplet-Droplet Interaction

In this section, the focus is on the secondary breakup (Section 2.5.1) and collision (Section 2.5.2) of droplets. Although in Chapters 5 and 6 the physical models for these phenomena are not used, breakup and collision terms are retained in the theoretical treatment of Chapter 4. The primary breakup of the continuous liquid phase into ligaments and large droplets is also not addressed. It requires additional sub models that are not in agreement with the assumption of droplets being spherical point masses. For an overview of primary breakup models see [103, 163].

For high pressure injection systems (see Figure 1.2) the fragmentation of the continuous liquid core into droplets starts very close to the nozzle orifice. This is due to cavitation in the nozzle, liquid turbulence and high liquid to gas momentum ratio [93]

$$\mathrm{Mom}_d := \frac{\rho_\ell |\mathbf{v}|^2}{\rho_g |\mathbf{U}_g|^2} \tag{2.46}$$

at the entrance of the combustion chamber. Therefore, the assumption of droplets being spherical point masses is already valid close to the nozzle orifice but not directly at or in the nozzle.

The large droplets which form directly behind the nozzle are strongly effected by the surrounding gas flow. The aerodynamic forces lead to further disintegration into smaller droplets (secondary breakup) and to a strong deceleration (in car engines) or accelerations (in aeroplane engines). The deceleration increases the probability of collision of the droplets, whereas the acceleration results into a fast thinning and evaporation of the spray.

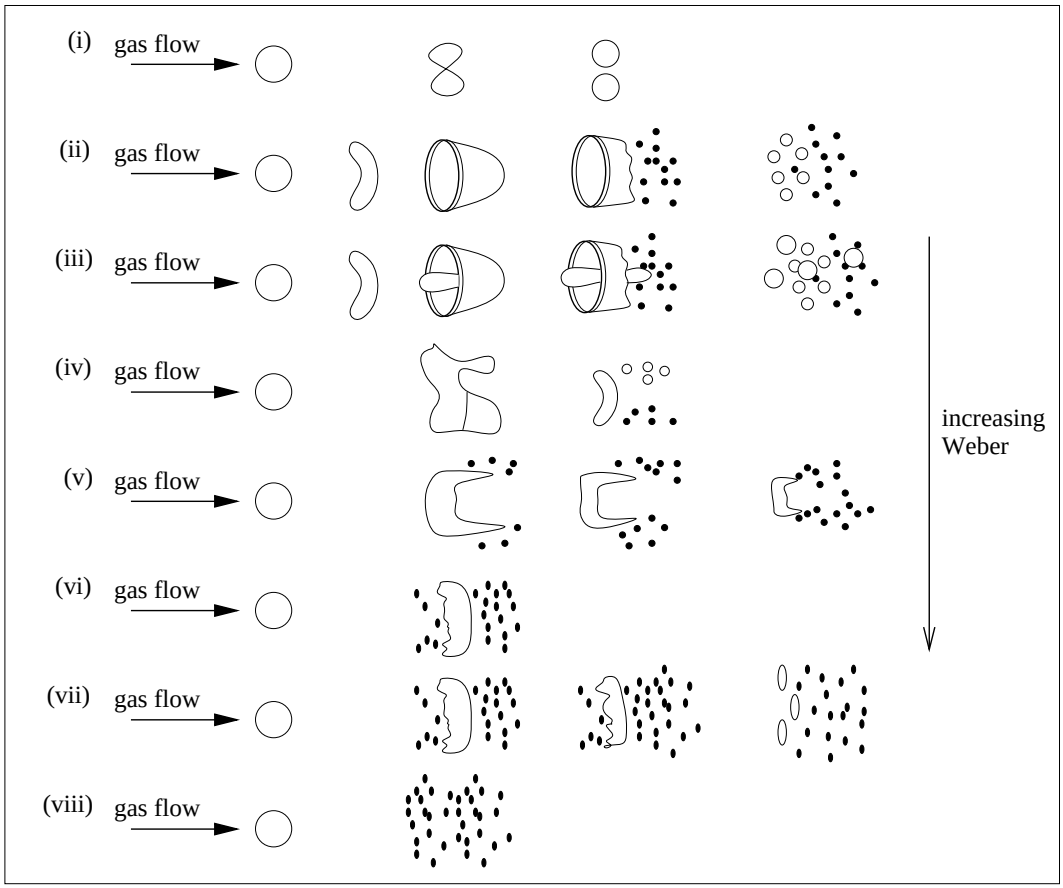

Figure 2.3: Secondary breakup regimes (after [125]).

2.5.1 Secondary Breakup of Droplets

The principle causes of secondary breakup of a droplet are the aerodynamic pressures employed on the droplet surface and the distortion of it. If these forces are large compared to the counteracting surface tension the droplet fractures into several pieces, called daughter droplets.

Critical Weber Number.
The relative velocity between droplet and gas, $\mathbf{v}_{\text{rel}}$, and the droplet surface tension, σ_d, dominate the fragmentation process. Consequently, the dimensionless Weber number, defined in (2.13), is the characteristic measure for the breakup behaviour of liquid droplets. It relates the dynamic pressure to the surface tension. If the Weber number is above the critical Weber number, $\text{We}_c = 12$, the deformation of the droplet is too large and it breaks. Depending on the Weber number of a droplet, several breakup regimes and mechanisms have been identified in experimental studies [125, 156]. They are called vibrational breakup ((i) in Figure 2.3), bag-breakup ((ii) and (iii) in Figure 2.3), sheet-stripping ((iv) to (vi) in Figure 2.3) and catastrophic breakup ((vii) and (viii) in Figure 2.3). In combustion systems all these mechanisms may be present simultaneously. Near the nozzle, where the relative velocity is high and the droplets are large, the catastrophic breakup is domi-

nating, whereas the small droplets in some distance from the nozzle experience vibrational breakup. As these mechanisms are based on different physical phenomena, the daughter droplet distributions are different for each mechanism (see Figure 2.3). Therefore, a single model for all breakup mechanisms is not sufficient. The famous Taylor-Analogy Breakup (TAB) model [10, 120], which is implemented in the KIVA II code, is a model for the vibrational breakup regime only and requires one additional variable. In the following paragraphs the model of Dufour [43] is presented which is based on a statistical point of view.

Frequency of Fragmentation.
Although the fragmentation of a droplet is a fast process, it does not happen instantaneously. The deformation of a droplet takes a certain amount of time before the droplet breaks. One important time scale of droplet fragmentation is the characteristic time for the Rayleigh-Taylor instabilities generated on the surface of droplets in the vibrational breakup regime. It can be expressed as [43]

$$\tau_{\mathrm{RT}} := \frac{s}{\sqrt{\pi}\,|\mathbf{U}_g - \mathbf{v}|}\sqrt{\frac{\rho_\ell}{\rho_g}}\ . \tag{2.47}$$

The experimental studies of Pilch and Erdman [125] use this time scale to define the time scale of fragmentation, τ_{fra} [s]. Their correlation reads [43] [6]

$$\frac{\tau_{\mathrm{fra}}}{\tau_{\mathrm{RT}}} = \begin{cases} 6(\mathrm{We}-12)^{-0.25} & \text{if} \quad 12 \le \mathrm{We} \le 18, \\ 2.45(\mathrm{We}-12)^{0.25} & \text{if} \quad 18 \le \mathrm{We} \le 45, \\ 14.1(\mathrm{We}-12)^{-0.25} & \text{if} \quad 45 \le \mathrm{We} \le 351, \\ 0.766(\mathrm{We}-12)^{0.25} & \text{if} \quad 351 \le \mathrm{We} \le 2670, \\ 5.5 & \text{if} \quad 2670 \le \mathrm{We}. \end{cases} \tag{2.48}$$

If it is assumed that the time of fragmentation is small compared to a characteristic time scale of the gas flow and the Weber number of a droplet is larger than the critical Weber number, the probability of fragmentation within the time Δt is

$$p_{\mathrm{frag}} = \min\left(\frac{\Delta t}{\tau_{\mathrm{frac}}}, 1\right)\ . \tag{2.49}$$

Therefore, the frequency of fragmentation, ν_{frag} [s^{-1}], is defined by

$$\nu_{\mathrm{frag}} := \begin{cases} 0 & \text{if} \quad \mathrm{We} \le \mathrm{We}_c, \\ \frac{\Delta t}{\tau_{\mathrm{frag}}} & \text{if} \quad \mathrm{We} > \mathrm{We}_c\ . \end{cases} \tag{2.50}$$

Size Distribution after Fragmentation.
The distributions of daughter droplets in secondary breakup are rarely studied experimentally because the fragmentation process is relatively fast and in technical applications

[6] Other correlations can be found in [79], [88] and [114].

the Weber number is high. Recent investigations of these processes and an overview on experimental studies is given by Villermaux [176].

One method to model the distribution of daughter droplets is the consideration of mean diameters. The SMD is commonly used. It is defined by

$$\mathrm{d}_{mn} = \left(\frac{\int_0^{+\infty} \mathrm{d}^m f(\mathrm{d}) d\mathrm{d}}{\int_0^{+\infty} \mathrm{d}^n f(\mathrm{d}) d\mathrm{d}} \right)^{\frac{1}{m-n}} = \frac{1}{\sqrt{\pi}} \left(\frac{\int_0^{+\infty} s^{m/2} f(s) ds}{\int_0^{+\infty} s^{n/2} f(s) ds} \right)^{\frac{1}{m-n}} , \tag{2.51}$$

with $m = 3$ and $n = 2$, which can be easily measured experimentally [178].

In various models, the daughter droplets are assumed to have the same size. Therefore, the SMD and the conservation of mass are sufficient to deduce the number of droplets resulting from the breakup of one droplet. This approach does not take into account the dispersion of droplet sizes, which is observed for most breakup mechanisms (see Figure 2.3). To resolve this problem Hsiang and Faeth [79], O'Rourke and Amsden [120] and Pilch and Erdman [125] have proposed presumed log-normal, normal and exponential forms of the daughter distribution adapting the parameters of these fixed functions in order to preserve the SMD and to conserve the mass. Unfortunately, these distributions lead to droplets of larger sizes than the original 'mother' droplets. Dufour [43] proposed a presumed daughter distribution of the form

$$g_s(s, \mathbf{v}^\diamond, s^\diamond) := \begin{cases} \dfrac{\alpha}{8\pi} \exp\left(-\dfrac{\gamma^2}{4\pi} s \right) & \text{if} \quad s < s^\diamond , \\ 0 & \text{if} \quad s > s^\diamond , \end{cases} \tag{2.52}$$

where $\mathbf{v}^\diamond$ and $s^\diamond$ are the velocity and surface of a droplet before fragmentation. The parameters α [m^{-2}], γ [m^{-1}] are determined using the conservation of mass

$$\begin{aligned} (s^\diamond)^{3/2} &= \int_0^{s^\diamond} s^{3/2} g_s(s, \mathbf{v}^\diamond, s^\diamond) ds = \frac{\alpha I(\gamma, s^\diamond)}{\gamma^5}, \\ I(\gamma, s^\diamond) &:= -\frac{\gamma \sqrt{s^\diamond}}{\sqrt{4\pi}} \exp\left(-\frac{\gamma^2}{4\pi} s^\diamond \right) \left(\frac{3}{4} - \frac{\gamma^2 s^\diamond}{8\pi} \right) + \frac{3\sqrt{\pi}}{8} \mathrm{erf}\left(\gamma \sqrt{\frac{s^\diamond}{4\pi}} \right) \end{aligned} \tag{2.53}$$

and the preservation of the SMD

$$\begin{aligned} \mathrm{d}_{32} &= \frac{\gamma^4 s^{\diamond 3/2}}{4\pi^{3/2} \alpha J(\gamma, s^\diamond)} , \\ J(\gamma, s^\diamond) &= \frac{1}{2} \left(1 - \exp\left(-\frac{\gamma^2 s^\diamond}{4\pi} \right) \left(1 + \frac{\gamma^2 s^\diamond}{4\pi} \right) \right) , \end{aligned} \tag{2.54}$$

where $\mathrm{erf}(x)$ is the classical error function defined by

$$\mathrm{erf}(x) = \frac{2}{\sqrt{\pi}} \int_0^x exp(-t^2) dt < 1 . \tag{2.55}$$

With some minor simplifications (cf. [43]) the parameters of the exponential function are obtained from

$$\gamma = \frac{3\sqrt{\pi}}{2\mathrm{d}_{32}}, \qquad \alpha = \frac{\gamma^5 s^{\diamond 3/2}}{(4\pi)^{3/2} I(\gamma, s^\diamond)} . \tag{2.56}$$

The SMD used in $(2.56)_1$ still has to be modelled. Wert [178] proposed the following correlation

$$\frac{\mathrm{d}_{32}\sqrt{4\pi}}{\sqrt{s^\diamond}} = \begin{cases} 0.32(\mathrm{We}^\diamond)^{-1/3}\left(\dfrac{4.1}{(\mathrm{We}^\diamond-12)^{1/4}}\right)^{2/3} & \text{if} \quad \mathrm{We}^\diamond \in]12,18], \\ 0.32(\mathrm{We}^\diamond)^{-1/3}\left(\dfrac{2.45\sqrt{\mathrm{We}^\diamond-12}-1.9}{(\mathrm{We}^\diamond-12)^{1/4}}\right)^{2/3} & \text{if} \quad \mathrm{We}^\diamond \in]18,45] \\ 0.32(\mathrm{We}^\diamond)^{-1/3}\left(\dfrac{12.2}{(\mathrm{We}^\diamond-12)^{1/4}}\right)^{2/3} & \text{if} \quad \mathrm{We}^\diamond \in]45,+\infty]. \end{cases} \tag{2.57}$$

where $\mathrm{We}^\diamond$ is the Weber number of droplets before fragmentation. This model for the SMD completes the model for the daughter distribution, which is defined for the whole range of possible Weber numbers.

Velocity of Fragments.
Concerning the velocity distribution of the daughter droplets not many correlations can be found in the literature. The most common correlation, which was proposed by Hsiang and Faeth [79], assumes that all daughter droplets with the same size have the same velocity. Their correlation reads

$$\mathbf{v}_{\mathrm{frag}} = \mathbf{U}_g + \frac{\mathbf{v}^\diamond - \mathbf{U}_g}{1+2.7\left(\sqrt{\frac{\rho_g}{\rho_\ell}}\sqrt{\frac{s^\diamond}{s}}\right)^{2/3}} \ . \tag{2.58}$$

This relation considers the fact that the relative velocity ratio of newly created droplets to original droplets is as small as the ratio of their sizes is large. This is in agreement with the fact that the momentum of the fragments is smaller than that of the original droplet.

Operator of Secondary Breakup.
The operator of secondary breakup, $\mathcal{Q}$, which models the fragmentation of droplets in the kinetic spray equation (see Chapter 3) is now introduced. To this end, a function $H(s,\mathbf{v},s^\diamond,\mathbf{v}^\diamond)$ is defined to represent the size and velocity distribution of the droplet fragments. For the sake of simplicity the distribution is decoupled into two parts that take into account the size and velocity distribution, respectively. The decoupling reads [43]

$$H(s,\mathbf{v},s^\diamond,\mathbf{v}^\diamond) = \frac{H(s,\mathbf{v},s^\diamond,\mathbf{v}^\diamond)}{\int_{\mathbf{v}} H(s,\mathbf{v},s^\diamond,\mathbf{v}^\diamond)d\mathbf{v}} \int_{\mathbf{v}} H(s,\mathbf{v},s^\diamond,\mathbf{v}^\diamond)d\mathbf{v} = g_{\mathbf{v}}(s,\mathbf{v},s^\diamond,\mathbf{v}^\diamond)g_s(s,s^\diamond,\mathbf{v}^\diamond) \ . \tag{2.59}$$

In this representation, the function g_s considers exclusively the size distribution of daughter droplets, whereas g_v represents the velocity distribution (conditional PDF) for each size. The size distribution proposed by Dufour [43] is modelled by the exponential relation (2.52) using the parameters defined in (2.56) and (2.57). Modelling function g_v with the model of Hsiang and Faeth [79], (2.58), the function reduces to

$$g_{\mathbf{v}}(s,\mathbf{v},s^\diamond,\mathbf{v}^\diamond) = \delta(\mathbf{v}-\mathbf{v}_{\mathrm{frag}}(s,s^\diamond,\mathbf{v}^\diamond)) \ . \tag{2.60}$$

It is assumed that the fragments of a droplet of size $s^\diamond$ and velocity $\mathbf{v}^\diamond$ have the same velocity provided that they are of same size.

The operator of the secondary breakup consists of two parts, i.e.

$$\mathcal{Q} = -\mathcal{Q}^- + \mathcal{Q}^+ \ . \tag{2.61}$$

The first term, $\mathcal{Q}^-$, quantifies the loss of droplets due to breakup and a second term $\mathcal{Q}^+$ reflects the gain of smaller daughter droplets. The loss of large droplets is based on the model of fragmentation frequency, (2.50), and the number distribution function $f(s, \mathbf{v})$.[7] It reads

$$\mathcal{Q}^-(s, \mathbf{v}) := -\nu_{\text{frag}}(s, \mathbf{v}) f(s, \mathbf{v}) \ . \tag{2.62}$$

To obtain the gain of daughter droplets of size s and velocity $\mathbf{v}$ (within the general volume $ds \times d\mathbf{v}$) it is sufficient to consider all the original droplets that disintegrate and that are larger than size s. The portion of droplets that have the appropriate size and velocity contribute to $\mathcal{Q}^+$. These considerations yield relation

$$\mathcal{Q}^+(s, \mathbf{v}) := \int_{s>s^\diamond} \int_{\mathbf{v}} \nu_{\text{frag}}(s^\diamond, \mathbf{v}^\diamond) f(s^\diamond, \mathbf{v}^\diamond) H(s, \mathbf{v}, s^\diamond, \mathbf{v}^\diamond) \mathbf{d}s^\diamond \mathbf{d}\mathbf{v}^\diamond \ , \tag{2.63}$$

where ν_{frag} and $H(s, \mathbf{v}, s^\diamond, \mathbf{v}^\diamond)$ are specified in (2.50) and (2.59), respectively.

2.5.2 Collision and Coalescence of Droplets

The collision of two solid particles leads to a unique result, i.e. the interchange of momentum. For droplets, on the other hand, the event of collision can lead to rebound, coalescence or other, more subtle effects. In any case, the collision of droplets results into changes of the droplet sizes and velocities. It is obvious that the collision of droplets is more likely if the liquid volume fraction in a spray system is high. To quantify the importance of collision, the average time between two collisions, $\bar{\tau}_c$ [s], is compared with the average droplet response time, $\bar{\tau}_d$ (see (2.15)). With these time scales the droplet Knudsen number, (2.5), can be redefined by

$$\text{Kn}_d = \frac{\bar{\tau}_c}{\bar{\tau}_d} \ . \tag{2.64}$$

It allows the following categorisation of sprays:

(i) If $\text{Kn}_d \gg 1$, the droplets have enough time to adapt to the gas phase before they collide. The spray system is denoted as *dilute*.

(ii) If $\text{Kn}_d \ll 1$, the motion of droplets is dominated by collisions and the spray system is regarded as *dense*.

(iii) If Kn_d is of the order of 1 the coupling between transport and collision of droplets are important for the correct prediction of the spray.

[7] The number distribution function is introduced rigorously in Chapter 3.

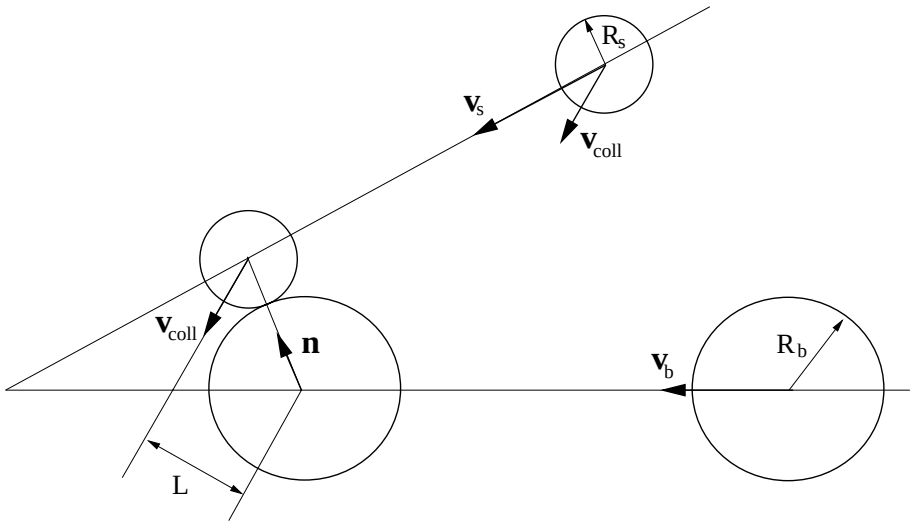

Figure 2.4: Sketch of two colliding droplets (after [163]).

In Chapters 4 to 6 the spray is assumed to be dilute and therefore only the transport, drag force and evaporation are considered. However, as a collision term is considered in the mathematical model (Chapter 3) the phenomenon of colliding droplets is briefly discussed here.

Collision and coalescence have been extensively studied. It is a subject of high interest in meteorology [8, 22, 92], soot formation [186] or crystallisation [30]. For sprays in combustion systems, collision models were proposed by Achim [2], Dufour [43], Estrade [47], Laurent et al. [97], O'Rourke [119] or Rueger et al. [144].

Regimes of Collision.
The collision of two droplets is determined by various parameters. The dimensionless impact parameter, b, the ratio of droplet radii, Δ, and the collision Weber number, $\mathrm{We}_{\mathrm{col}}$ play important roles in the categorisation and modelling of droplet collision. They are defined by

$$0 < b := \frac{L}{R_s + R_b} < 1, \quad 0 < \Delta := \frac{R_s}{R_b} < 1, \quad \mathrm{We}_{\mathrm{col}} := \frac{2\rho_\ell R_s v_{\mathrm{col}}^2}{\sigma_d} , \tag{2.65}$$

where the collision velocity is specified as

$$v_{\mathrm{col}} := |\mathbf{v}_s - \mathbf{v}_b| . \tag{2.66}$$

For the definition of L, R_s, R_b, $\mathbf{v}_s$ and $\mathbf{v}_b$ see Figure 2.4. The impact parameter characterises the degree of excentricity of the collision. The ratio of the droplet radii accounts for the dissymmetry of the colliding droplets concerning their mass. The collision Weber number quantifies the ratio of the surface energy that restores the spherical shape of the droplet and the kinetic energy that is leading to breakup. Experimental and numerical studies [2, 8, 47] show that the impact parameter and the collision Weber number can be used to define five regimes of collision. These are the regimes of (see Figure 2.5)

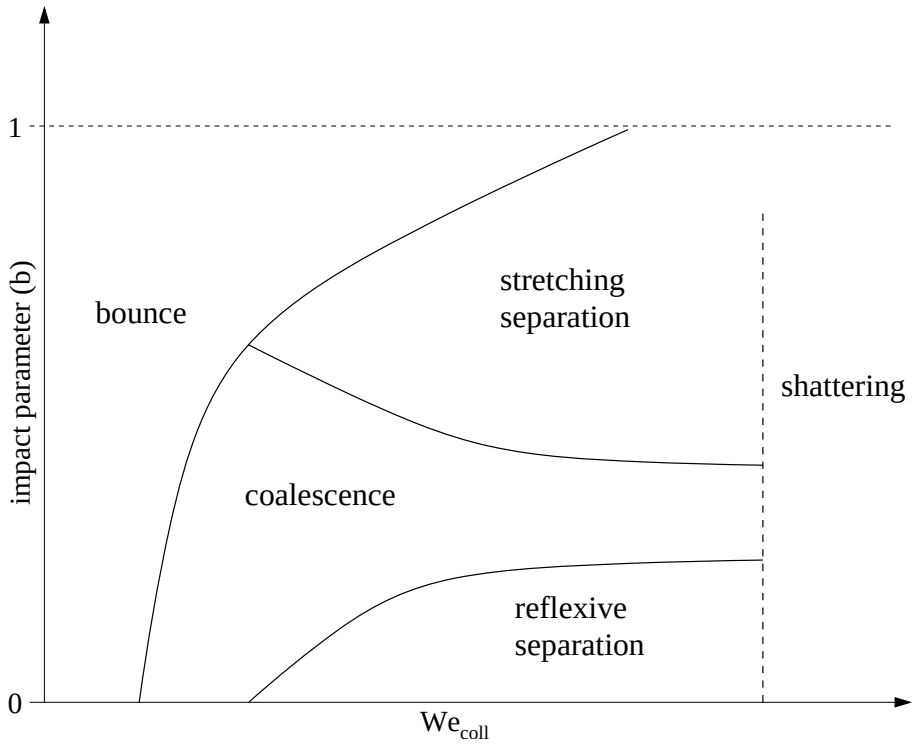

Figure 2.5: Impact parameter vs. collision Weber number; regimes of colliding droplets (after [163]).

(i) bouncing of droplets that have similar sizes,

(ii) definite coalescence,

(iii) temporal coalescence followed by separation through reflection,

(iv) temporal coalescence followed by separation through stretching,

(v) creation of satellite particles (shattering).

Each of these regimes requires a special collision model. It is common practice [43] to incorporate efficiencies for collision, coalescence and separation that reflect the probability of the respective collision. They are denoted as E_{coll}, E_{coal}, E_{ref} and E_{stre}, respectively and satisfy the conditions

$$0 < E_{coll} < 1, \quad E_{coal}, E_{ref}, E_{stre} \geq 0 \quad \text{and} \quad E_{coal} + E_{ref} + E_{stre} = 1 \ , \tag{2.67}$$

where the shattering regime is usually set asside and the mass of small satellites is neglected.

Operator of Coalescence.
Similar to the operator of secondary breakup, the operator of coalescence, $\Gamma(f)$, which depends on the number density function, f, is divided into two parts, i.e.

$$\Gamma(f) = -\Gamma^{-}(f) + \Gamma^{+}(f) \ . \tag{2.68}$$

The first term represents the droplets that collide and the second, the droplets that result from this collision. The rate at which droplets of size s and velocity $\mathbf{v}$ disappear due to collision is obtained from the consideration of all possible collision partners of size s° and velocity $\mathbf{v}^\circ$. The resulting term has the following structure[8]

$$\Gamma^-(f)(s,\mathbf{v}) = \int_{\mathbf{v}^\circ}\int_{s^\circ}\int_0^1 f(s,\mathbf{v})f(s^\circ,\mathbf{v}^\circ)\left\{E_{coll}(E_{coal}+E_{ref})\frac{(\sqrt{s}+\sqrt{s^\circ})^2}{2}b\right\}db\,ds^\circ\,d\mathbf{v}^\circ\ , \tag{2.69}$$

assuming the separation due to stretching to not affect the size and velocity of colliding droplets.

The term $\Gamma^+(f)$ consists of two parts, one for the separation due to reflection and one for the definite coalescence, i.e.

$$\Gamma^+(f) = \Gamma^+_{ref}(f) + \Gamma^+_{coal}(f)\ . \tag{2.70}$$

The first term quantifies the production of droplets having size s and velocity $\mathbf{v}$ and originating from the separation of droplets that originally had the size s° and velocity $\mathbf{v}^\circ$. The size of droplets can be assumed to remain the same before and after collision. However, the velocity of the produced droplets can change. It is modelled by the elastic collision law

$$\begin{aligned}\mathbf{v}'_s &= \mathbf{v}_s - \frac{2s_b^{3/2}}{s_b^{3/2}+s_s^{3/2}}\{(\mathbf{v}_s-\mathbf{v}_b)\cdot\mathbf{n}\}\mathbf{n}, \qquad s'_s = s_s\ ,\\ \mathbf{v}'_b &= \mathbf{v}_b + \frac{2s_s^{3/2}}{s_b^{3/2}+s_s^{3/2}}\{(\mathbf{v}_s-\mathbf{v}_b)\cdot\mathbf{n}\}\mathbf{n}, \qquad s'_b = s_b\ ,\end{aligned} \tag{2.71}$$

where the conservation of mass and momentum, and the unit normal vector between the centres of the droplets, $\mathbf{n}$, have been used. The operator for the reflecting droplets reads

$$\Gamma^+_{ref}(f)(s,\mathbf{v}) = \int_{\mathbf{v}^\circ}\int_{s^\circ}\int_0^1 f(s',\mathbf{v}')f(s^\circ,\mathbf{v}^\circ)\left\{E_{coll}E_{ref}\frac{(\sqrt{s'}+\sqrt{s^\circ})^2}{2}b\right\}db\,ds^\circ\,d\mathbf{v}^\circ\ . \tag{2.72}$$

In the case when two droplets definitely coalesce, the new droplet exhibits the following size and velocity

$$\begin{aligned}s &= (s_s^{3/2}+s_b^{3/2})^{2/3},\\ \mathbf{v} &= \frac{s_s^{3/2}}{s_s^{3/2}+s_b^{3/2}}\mathbf{v}_s + \frac{s_b^{3/2}}{s_s^{3/2}+s_b^{3/2}}\mathbf{v}_b\ .\end{aligned} \tag{2.73}$$

With these relations, the coalescence of a droplet with velocity $\mathbf{v}^*$ and size $s^* < s$, and a droplet of velocity $\mathbf{v}^\diamond$ and size $s^\diamond$ can be expressed as

$$\Gamma^+_{coal}(f)(s,\mathbf{v}) = \frac{1}{2}\int_{\mathbf{v}^\circ}\int_{s^\circ}\int_0^1 f(s^\diamond,\mathbf{v}^\diamond)f(s^*,\mathbf{v}^*)J\left\{E_{coll}E_{coal}\frac{(\sqrt{s^\diamond}+\sqrt{s^*})^2}{2}b\right\}db\,ds^*\,d\mathbf{v}^*\ , \tag{2.74}$$

[8] In the kinetic theory of gases the term, $dS = E_{coll}(E_{coal}+E_{ref})\frac{(\sqrt{s}+\sqrt{s^\circ})^2}{2}bdb$, is called the infinitesimal cross section of collision [172].

where the change of variables (see (2.73))

$$(s^\diamond, \mathbf{v}^\diamond) = \left((s^{3/2} - s^{*3/2})^{3/2}, \frac{s^{3/2}\mathbf{v} - s^{*3/2}\mathbf{v}^*}{s^{\diamond 3/2}} \right) \tag{2.75}$$

was performed and the Jacobian $J = \frac{s^5}{s^{\diamond 5}}$ was used. It should be noted, that the factor $1/2$ in (2.74) takes into account the fact that in the integration over s^* every collision is counted two times.

2.6 Droplet-Wall Interaction

When droplets hit a wall, break, evaporate, get absorbed, deposit, or rebound with a certain velocity and size, they are said to splash on that wall. In this section a new statistical model for splashing is derived that is able to account for elastic and non-elastic droplet-wall interactions, droplet-wall friction, breakup of droplets and mass deposition on the wall.

Lets consider a droplet that is rebound from a flat wall, facing towards $-\mathbf{e}_x$, with the velocities

$$U = -\alpha_x U', \quad V = \alpha_y V' \quad \text{and} \quad W = \alpha_z W' \quad [\mathrm{m\,s^{-1}}] \tag{2.76}$$

in the directions $-\mathbf{e}_x$, $\mathbf{e}_y$ and $\mathbf{e}_z$, with diameter

$$D = \beta_d D' \ [\mathrm{m}] \tag{2.77}$$

and mass

$$M = (1 - \gamma) M' \ [\mathrm{kg}] \ . \tag{2.78}$$

The symbols with a prime represent the respective quantities of the droplet before splashing and the parameters α_x, α_y, α_z, β_d and γ are related to the coefficient of restitution, friction between droplet and wall, partition of the droplet and loss of fluid mass on the wall, respectively. It is obvious from the interpretation of the parameters, that they are not constant. They should rather depend on the conditions on or in the vicinity of the wall. In the case of a dry wall, at least the wall temperature and the wall roughness are of relevance [138, 142]. The wall temperature is necessary to predict the sudden evaporation of droplets on the wall and the formation of the air cushions between droplets and wall [61, 62]. If a liquid film forms on the surface of a wall, which is usually changing in thickness, the splashing mechanism will be completely changed [140]. In this case the splashing parameters must also depend on the thickness of the film. One can also think of porous walls on which some part of the mass is absorbed or deposited during splashing [134]. For a recent review on splashing processes the reader is referred to Yarin [184]. It has to be remarked that splashing parameters describe the behaviour of the droplets close to the wall. The heavy interaction between incident and splashed droplets some distance away from the wall [89] can be captured independent of the splashing model by employing separate collision, coalescence and breakup models. In this work the parameters are assumed to be constant because the splashing test case is merely used to verify the method introduced in Chapters 4 and 5. However, more complex models can be incorporated.

Extending model (2.76)-(2.78) to a set of equally sized droplets of size d′ before and d after splashing yields

$$\begin{aligned} u = -\alpha_x u', \quad v = \alpha_y v', \qquad w = \alpha_z w' \ , \\ \mathrm{d} = \beta_d \mathrm{d}', \qquad m = (1-\gamma) m' \ , \end{aligned} \tag{2.79}$$

where all droplets in this set have the same properties u', v', w', d′, m' before and u, v, w, d, m after splashing. If these droplets are assumed to be spherical, their mass, m [kg], and their number, n [-], are related by

$$m = \frac{4}{3}\rho_\ell \pi \left(\frac{\mathrm{d}}{2}\right)^3 n \ . \tag{2.80}$$

Relation $(2.79)_{4,5}$ and (2.80) are used to obtain the splashing condition,

$$n = \frac{1-\gamma}{\beta_d^3} n' \ , \tag{2.81}$$

a relation between the number of droplets before and after splashing. Consequently, droplets of diameter d′ (or surface s'), mass m' and velocity $\mathbf{v}' = (u', v', w')^{\mathrm{T}}$ are splashed into $(1-\gamma)/\beta_d^3$ droplets of diameter $\beta_d \mathrm{d}'$ (or surface $\beta_d^2 s'$), mass m, and velocities $\mathbf{v} = (-\alpha_x u',\, \alpha_y v',\, \alpha_z w')^{\mathrm{T}}$.

Denoting the number of incident droplets of surface between s' and $s' + ds'$ and velocities between $\mathbf{v}$ and $\mathbf{v}' + d\mathbf{v}'$ by $f^+(\mathbf{v}', s')d\mathbf{v}'ds'$ and those that are reflected by $f^r(\mathbf{v}, s)d\mathbf{v}ds$, relation (2.81) can be transformed into the splashing condition

$$\begin{aligned} f^r(\mathbf{v}, s)d\mathbf{v}ds = \frac{1-\gamma}{\beta_d^3} f^+(\mathbf{v}', s')d\mathbf{v}'ds' \ , \\ u = -\alpha_x u', \quad v = \alpha_y v', \quad w = \alpha_z w', \quad s = \beta_d^2 s' \ . \end{aligned} \tag{2.82}$$

In the subsequent chapter the function f which is closely related to f^r and f^+ will be rigorously defined and denoted the number density function. For the introduction of the splashing condition the above motivation of f^r and f^+ is sufficient. Using $(2.82)_{2,3,4,5}$ in equation $(2.82)_1$ yields the final form of the splashing condition

$$f^r(u, v, w, s)d\mathbf{v}ds = -\frac{1-\gamma}{\alpha_x \alpha_y \alpha_z \beta_d^5} f^+(-\frac{u}{\alpha_x}, \frac{v}{\alpha_y}, \frac{w}{\alpha_z}, \frac{s}{\beta^2})d\mathbf{v}ds \ . \tag{2.83}$$

So far, it has not been possible to capture the phenomenon of splashing with Euler methods because they assume that, locally, only one droplet velocity is defined for a particular size and position. This assumption does not hold for splashing sprays since, near the wall, ensemble averaged velocity distributions may be bi- or multi-modal. In Chapters 4 to 6 a method will be presented that does not rely on the assumption of mono-modal velocity distributions and therefore allows the accurate description of splashing sprays.

Chapter 3

A Mathematical Model for Spray Flows

3.1 Introduction

A model that uses mathematical language to transform the essential aspects of a physical model into a form that can be used to describe the behaviour of a physical system is called a mathematical model. In this transformation pieces of information on the physical system are lost because additional assumptions are enforced *first*, to define benign mathematical variables and *second*, allow the derivation of solutions to the mathematical model. For solid, liquid or gaseous materials, the mathematical model usually consists of partial differential equations (PDE) that relate variables, like mass density, deformation, velocity, temperature, etc., to position and time. These PDEs, together with initial and boundary conditions, are said to be well-posed if a unique solution exists. This property cannot be proven for all models. For engineers and physicists, the solutions of the mathematical models are acceptable if certain realisability conditions are satisfied. They require, for example, that:

(i) the mass density and number of droplets are positive and finite,

(ii) the absolute temperature and entropy production [5] are always positive for given systems,

(iii) a system can only consume a limited amount of energy,

(iv) a body of finite size cannot shrink to one point.

There are other, more heuristic rules which allow an engineer to approve the solution of a mathematical model. Therefore, the existence and uniqueness of solutions to the proposed mathematical model are not addressed in this work. The results in Chapter 6 demonstrate that no spurious solutions are introduced by the mathematical model proposed in Chapter 4.

The mathematical models for single-phase fluids are generally based on the continuum assumption. It allows the postulation of balance laws that have the form [80][1]

$$\frac{\partial \psi}{\partial t} + \nabla_{\mathbf{x}} \cdot (\psi \mathbf{u}) = -\nabla_{\mathbf{x}} \cdot (\mathbf{\Phi}) + \Pi + \Gamma \ , \tag{3.1}$$

where $\psi(\mathbf{x}, t)$ is a general physical variable, $\mathbf{u}(\mathbf{x}, t)$ the velocity and $\mathbf{\Phi}(\mathbf{x}, t)$, $\Pi(\mathbf{x}, t)$ and $\Gamma(\mathbf{x}, t)$ the corresponding flux, production and supply terms. Similar equations can be postulated for each phase in a multi-phase flow assuming all phases to be present at each position (see Section 3.3.2). In the present study, models based on these postulates are called classical Euler-Euler methods.

However, for spray flows with high droplet Knudsen number the continuum assumption is not valid for the dispersed phase. Instead, a kinetic approach [16, 24, 26] is used that is based on an ensemble average over a cloud of droplets. The kinetic equation that follows from these considerations is a PDE for a distribution function. In the theory of rarefied gases the velocity distribution of gas molecules is considered. In the case of spray flows, the velocity, size, temperature, composition or other characteristic properties of the spray can be used.

In Section 3.2 the definition of a distribution function for spray flows, called number density function (NDF), is given and the kinetic spray equation that constitutes a PDE for the NDF is introduced. Section 3.3 is devoted to the different mathematical ways to solve the kinetic spray equation. The Lagrange, classical Euler and various moment methods are outlined briefly and their applicability to spray flows is discussed. In addition, reasons are given for why the sectional method (SM) of Dufour and Villedieu [44] and the quadrature-based third-order method of moments (QBMoM) of Fox [56] and Le Lostec et al. [99] are used in Chapters 4 to 6. Section 3.4 deals with the mathematical models for single-phase flows and the influence of droplets on the mathematical model of the gas phase.

3.2 The Kinetic Spray Equation

Sprays in combustion chambers exhibit a high degree of randomness because the number of droplets is very large, the gas flow is turbulent and many processes, such as breakup, collision, evaporation, chemical reactions, etc., are present simultaneously. The tools to describe these types of stochastic processes are taken from statistical mathematics. The concepts of kinetic equations, presented by Fox [55], Minier and Peirano [112], Pai [123], Pope [128] and Reeks [133], were found to be the right mathematical basis for dispersed multiphase systems. The models developed in subsequent Chapters are based on the kinetic spray equation, which constitutes a specialisation of the general kinetic concepts. The detailed definitions of the quantities involved and an exact mathematical derivation of the kinetic equations are treated in references [55], [123] or [133].

Following Fox [55], a less mathematical motivation of the kinetic concept for dispersed multiphase systems is given in Section 3.2.1. It is then specialised to spray flows in Section

[1] The operator $\nabla_{\mathbf{x}}$, called nabla operator, represents a vector of derivatives with respect to the components of position, i.e. $\nabla_{\mathbf{x}} = (\partial/\partial x_1, \partial/\partial x_2, \partial/\partial x_3)^{\mathrm{T}}$. Consequently, $\nabla_{\mathbf{x}}(\mathbf{a})$ and $\nabla_{\mathbf{x}} \cdot \mathbf{a}$ represent the gradient and divergence of vector $\mathbf{a}$, respectively.

3.2.2 and the resulting equation, called the kinetic spray equation, is disposed of its units in Section 3.2.3.

3.2.1 Fundamentals of Kinetic Equations

The properties of the dispersed phase are generally characterised by quantities called internal or external variables. External variables are the position and time of the dispersed phase and momentum (or velocity), enthalpy (or temperature), mass (or size for spherical droplets) and composition are denoted as internal variables.

The number density function (NDF) is used to describe the distribution of internal properties for a given control volume. In a system of dispersed entities, $\mathbf{x} = (x_1, x_2, x_3)$ is designated as the physical position of a control volume of size

$$d\mathbf{x} = dx_1 dx_2 dx_3 \ , \tag{3.2}$$

$\mathbf{u} = (u_1, u_2, u_3)^{\mathrm{T}}$ is the velocity vector and $\boldsymbol{\xi} = (\xi_1, \xi_2, \ldots, \xi_N)$ is the vector which consists of all internal variables except the velocity. The NDF, $f(\mathbf{x}, t; \mathbf{u}, \boldsymbol{\xi})$,[2] is defined by the expected number of entities in the physical volume $d\mathbf{x}$ and in the internal-variable space (phase space) volume $d\mathbf{u} \times d\boldsymbol{\xi}$:

$$f \, d\mathbf{x} d\mathbf{u} d\boldsymbol{\xi} \ . \tag{3.3}$$

The NDF is not a random quantity. Instead it can be considered as the ensemble average of an infinite number of realisations of the dispersed phase 'motion'. It can be shown to be a smooth and differential function with respect to time, position and internal-variable space [55]. The integration of f over all possible internal variables yields

$$n(\mathbf{x}, t) = \int_{\boldsymbol{\xi}} \int_{\mathbf{u}} f(\mathbf{x}, t; \mathbf{u}, \boldsymbol{\xi}) d\mathbf{u} d\boldsymbol{\xi} \ , \tag{3.4}$$

which is the total particle-number concentration at position $\mathbf{x}$ and time t. In reference [55] this motivation of the NDF is put on a sound mathematical footing by relating it to the multi-particle joint PDF. This quantity contains all information on the dispersed entities in the system. It is also possible to include the ambient gas flow into the statistical considerations. For a treatise on these issues the reader is referred to [55], [112] and [123].

The general kinetic equation is a PDE for the NDF. It can be derived from the general balance equation for the multi-particle joint PDF [55]. In the present study, the general kinetic equation

$$\frac{\partial f}{\partial t} + \nabla_{\mathbf{x}} \cdot (\mathbf{u} f) + \nabla_{\mathbf{u}} \cdot (\mathbf{A} f) + \nabla_{\boldsymbol{\xi}} \cdot \left(\dot{\boldsymbol{\xi}} f \right) = h(f) \tag{3.5}$$

is regarded as postulate. It accounts for the accumulation (first term), the convection in physical (second term) and in internal variable space (third and fourth term). These are

[2] From this point on, external and internal variables in the argument list of the NDF will be separated by a semicolon. The explicit dependence of the NDF on these variables is mentioned only when required for clarity.

continuous changes of the NDF. The term on the right-hand side represents discontinuous jumps in the internal variable space which is due to discrete events in the dispersed phase. In the next section a physical meaning will be given to these terms.

The convection in physical space, modelled by $\nabla_{\mathbf{x}} \cdot (\mathbf{u}f)$ in equation (3.5), requires different approaches depending upon the type of flow. In laminar, dispersed, multiphase flows, the gas velocity can be described by one definite value at one point and time. However, the dispersed phase in this laminar gas flow can exhibit velocity dispersion because *first*, the drag force is size-dependent and *second*, particle trajectory crossing, which leads to multi-modal velocity distributions, is possible. Another effect which can lead to velocity dispersion is the Brownian motion in the gas phase which acts on the dispersed entities. This effect must be accounted for, when the size of the entities is of the order of the mean free path in the gas. In this work, the Brownian motion is not considered.

For turbulent dispersed multiphase flows all flow quantities fluctuate in an unpredictable manner around their mean values. To obtain an equation for the mean fields of the flow, a Reynolds average [123, 128, 133] or LES filter [53, 84, 146] operation is usually applied to the kinetic equation (3.5). Following the approach adapted by Fox [55], a one-point joint PDF [51] of $\mathbf{u}$ and f, denoted as $p_{\mathbf{u},f}$, is used to define the Reynolds-averaged velocity

$$\langle \mathbf{u} \rangle := \int_f \int_{\mathbf{u}} \mathbf{u}^* p_{\mathbf{u},f}(\mathbf{u}^*, f^*) d\mathbf{u}^* df^* \ , \tag{3.6}$$

and the Reynolds-averaged NDF

$$\langle f \rangle := \int_f \int_{\mathbf{v}} f^* p_{\mathbf{u},f}(\mathbf{u}^*, f^*) d\mathbf{u}^* df^* \ . \tag{3.7}$$

The fluctuations around these fields are obtained from

$$\mathbf{u}' := \mathbf{u} - \langle \mathbf{u} \rangle \tag{3.8}$$

and

$$f' := f - \langle f \rangle \ . \tag{3.9}$$

The Reynolds-average of the general kinetic equation (3.5) reads

$$\frac{\partial \langle f \rangle}{\partial t} + \nabla_{\mathbf{x}} \cdot (\langle \mathbf{u} f \rangle) + \nabla_{\mathbf{u}} \cdot (\mathbf{A} \langle f \rangle) + \nabla_{\boldsymbol{\xi}} \cdot \left(\dot{\boldsymbol{\xi}} \langle f \rangle \right) = \langle h(f) \rangle \ . \tag{3.10}$$

For simplicity, $\mathbf{A}$ and $\dot{\boldsymbol{\xi}}$ are assumed to depend only on $\mathbf{u}$ and $\boldsymbol{\xi}$. This assumption allows the Reynolds average to commuted with the derivatives of time, space and internal variables. The definitions in (3.8) and (3.9) allow the decomposition of the higher-order term arising in the Reynolds-averaged kinetic equation, i.e.

$$\langle \mathbf{u} f \rangle = \langle \mathbf{u} \rangle \langle f \rangle + \langle \mathbf{u}' f' \rangle \ . \tag{3.11}$$

Applying a gradient-diffusion model to the turbulent flux, which reads

$$\langle \mathbf{u}' f' \rangle = -\mathrm{D}_t \nabla_x \langle f \rangle \ , \tag{3.12}$$

equation (3.10) is closed (except for the term on the right-hand side). The turbulent diffusivity, D_t, can be modelled by solving separate equations for the turbulent kinetic energy and the turbulent energy dissipation of the dispersed phase. With these considerations equation (3.10) reduces to

$$\frac{\partial\langle f\rangle}{\partial t} + \nabla_{\mathbf{x}}\cdot\left(\langle\mathbf{u}\rangle\langle f\rangle - \mathrm{D}_t\nabla_x\langle f\rangle\right) + \nabla_{\mathbf{u}}\cdot\left(\mathbf{A}\langle f\rangle\right) + \nabla_{\boldsymbol{\xi}}\cdot\left(\dot{\boldsymbol{\xi}}\langle f\rangle\right) = \langle h(f)\rangle \ . \tag{3.13}$$

The closure of the term $\langle h(f)\rangle$ is strongly dependent on the application. However, it is usually a quadratic function of f. This is confirmed by the models of breakup and collision presented in Chapter 2.

3.2.2 Specialisation to Sprays

The general kinetic equation (3.5) is now specialised to spray flows, where the internal variables are chosen to be the droplet velocity, $\mathbf{v}$, the surface of a spherical droplet, s, and the droplet temperature, θ. The temporal changes of these variables are set equal to the acceleration $\mathbf{F}/m_p$, evaporation, K, and heating, R, of a droplet, respectively. The models for these effects were introduced in Chapter 2. The term h which represents discontinuous effects between dispersed entities is specialised to the breakup, $\mathcal{Q}$, and collision, Γ, of droplets (see also Chapter 2). With these considerations, the kinetic equation for a spray flow can be written as

$$\frac{\partial f}{\partial t} + \nabla_{\mathbf{x}}\cdot(\mathbf{v}f) + \nabla_{\mathbf{v}}\cdot\left(\frac{\mathbf{F}(\mathbf{v},s)}{m_d(s)}f\right) + \frac{\partial}{\partial s}\left(\mathrm{K}(\mathbf{v},s,\theta)f\right) + \frac{\partial}{\partial\theta}\left(\mathrm{R}(\mathbf{v},s,\theta)f\right) = \mathcal{Q}(f)(\mathbf{v},s) + \Gamma(f)(\mathbf{v},s) \ . \tag{3.14}$$

It was coined the kinetic spray equation by Williams [179]. The dependencies of the NDF are

$$f = f(\mathbf{x},t;\mathbf{v},s,\theta) \ . \tag{3.15}$$

To lay open the relation of the droplet force to the gas velocity the general force model, introduced in (2.8) and (2.15), is substituted into equation (3.14), i.e.

$$\frac{\partial f}{\partial t} + \nabla_{\mathbf{x}}\cdot(\mathbf{v}f) + \nabla_{\mathbf{v}}\cdot\left\{\left(\frac{\mathbf{U}_g(\mathbf{x},t)-\mathbf{v}}{\tau_d(\mathbf{v},s)} + g\mathbf{e}_g\right)f\right\} + \frac{\partial}{\partial s}\left(\mathrm{K}(\mathbf{v},s,\theta)f\right) + \frac{\partial}{\partial\theta}\left(\mathrm{R}(\mathbf{v},s,\theta)f\right) = \mathcal{Q}(f)(\mathbf{v},s) + \Gamma(f)(\mathbf{v},s) \ . \tag{3.16}$$

The Reynolds-averaging of equation (3.16) does not lead to the form as given in equation (3.13) because the droplet force depends on the gas velocity and therefore, the Reynolds-average and the velocity derivatives do not commute. However, in this work, the position is taken that $\nabla_{\mathbf{x}}\cdot(\mathrm{D}_t\nabla_{\mathbf{x}}\langle f\rangle)$ in (3.13) represents those turbulent interactions between gas and droplets that were not taken into account by the drag force. In the case when a turbulent gas flow is solved by a DNS or analytical solutions of the gas flow are accounted for (assumed here), the instantaneous gas velocity at one position and time

is available. Hence, the gas velocity in the drag model contains all the information on the gas flow and the averaging or filtering is not necessary. If the turbulent gas flow is described by RANS or LES, only a filtered gas velocity is known at a position and time. Using this velocity for the drag force, the small-scale fluctuations of the gas are neglected. Indeed, the influence of small-scale gas fluctuations on droplets with large Stokes numbers can be neglected because of their large inertia. If the Stokes number of a droplet is of order one or smaller, it is shown by Février et al. [51] that the drag force model with the filtered gas velocity leads to poor predictions of the droplet velocities. This defect asks for a dispersion model, which describes the small-scale gas fluctuations on the droplets.

Février et al. [51] and Kaufmann et al. [84] outlined how an averaged PDF can be defined for the dispersed phase that allows the commutation of velocity derivatives and average operation. This approach leads to balance equations for averaged mass, momentum and other moments of this PDF which include unclosed turbulent fluxes. However, in this work the statistical approach of Fox [55] is followed that requires further investigations to be coupled with LES and RANS models of the gas flow.

3.2.3 Dimensionless Kinetic Spray Equation

The reasons to dispose the kinetic spray equation (3.16) and all the including quantities of their units are that:

(i) with dimensional analysis [11, 162] the number of governing parameters characterising a physical phenomenon can be reduced to a linear independent set of dimensionless[3] numbers,

(ii) the comparison and classification of configurations exhibiting, for example, different size and time scales but the same physical phenomena, are facilitated,

(iii) with the choice of a distinguished system within the International System of Units (SI) the quantities can also be normalised,

(iv) the dimensionless terms in a PDE can easily be compared.

The kinetic spray equation (3.16) is scaled with the dimensional constants X_{char} [m], V_{char} [$\mathrm{m\,s^{-1}}$], Θ_{char} [K] and S_{char} [$\mathrm{m^2}$], which represent characteristic length, velocity, temperature and surface scales of the gas and spray flow, respectively. The choice of these parameters cannot be determined rationally. It depends on the spray configuration that is in focus and on the objectives of the investigator. Here, X_{char} is identified with the size of the computational domain, V_{char} and Θ_{char} equal the velocity and temperature in the far field gas flow and S_{char} represents the size of the initially largest droplet. With these parameters the dimensionless variables

$$t = \tau_g t^* \,, \quad \mathbf{x} = X_{\text{char}} \mathbf{x}^* \,, \quad \mathbf{v} = V_{\text{char}} \mathbf{v}^* \,, \quad s = S_{\text{char}} s^* \,, \quad \theta = \Theta_{\text{char}} \theta^* \,, \tag{3.17}$$

[3] In this section, the dimension of a quantity refers to its characteristic scale and unit (in the International System of Units (SI)). It shall not be confused with the dimension of a vector space or the fractional dimension [71].

and the dimensionless function for the gas velocity

$$\mathbf{U}_g(\mathbf{x},t) = V_{\text{char}}\mathbf{U}_g^*(\mathbf{x}^*,t^*) \tag{3.18}$$

are defined, where $\tau_g = X_{\text{char}}/V_{\text{char}}$ [s] is the characteristic time scale for the gas flow. The dimensionless form of the NDF is derived from the assumption that the number of droplets in the infinitesimal volume $[\mathbf{x},\, \mathbf{x}+d\mathbf{x}]\times\, [\mathbf{v},\, \mathbf{v}+d\mathbf{v}]\times\, [s,\, s+ds]\times\, [\theta,\, \theta+d\theta]$ is the same as in the corresponding dimensionless volume $[\mathbf{x}^*,\, \mathbf{x}^*+d\mathbf{x}^*]\times\, [\mathbf{v}^*,\, \mathbf{v}^*+d\mathbf{v}^*]\times\, [s^*,\, s^*+ds^*]\times\, [\theta^*,\, \theta^*+d\theta^*]$. The dimensionless NDF, following from the change of variables in (3.17), is defined by

$$f^*(\mathbf{x}^*,t^*;\mathbf{v}^*,s^*,\theta^*) = f(\mathbf{x},t;\mathbf{v},s,\theta)X_{\text{char}}^3V_{\text{char}}^3S_{\text{char}}\Theta_{\text{char}}\ . \tag{3.19}$$

With these definitions at hand, the kinetic spray equation (3.16) is written as[4]

$$\begin{aligned}\frac{\partial}{\partial t^*}(f^*) + \nabla_{\mathbf{x}^*}\cdot(\mathbf{v}^*f^*) + \nabla_{\mathbf{v}^*}\cdot\left\{\left(\frac{\mathbf{U}_g^*-\mathbf{v}^*}{\tau_d/\tau_g} + \frac{g\tau_g}{V_{\text{char}}}\mathbf{e_g}\right)f^*\right\}\\ + \frac{\partial}{\partial s^*}\left(\frac{\tau_g\mathrm{K}}{S_{\text{char}}}f^*\right) + \frac{\partial}{\partial\theta^*}\left(\frac{\tau_g\mathrm{R}}{\Theta_{\text{char}}}f^*\right) = \tau_g\Gamma + \tau_g\mathcal{Q}\ ,\end{aligned} \tag{3.20}$$

which was already multiplied by $(\tau_g X_{\text{char}}^3V_{\text{char}}^3S_{\text{char}}\Theta_{\text{char}})$. From equation (3.20) the definitions of the dimensionless numbers are obtained as

$$\mathrm{St}(s^*,\mathbf{v}^*) := \frac{\tau_d(S_{\text{char}}s^*, V_{\text{char}}\mathbf{v}^*)}{\tau_g}\ , \tag{3.21}$$

$$\mathrm{Ev}(s^*,\mathbf{v}^*,\theta^*) := \frac{\tau_g}{-S_{\text{char}}/\mathrm{K}(S_{\text{char}}s^*, V_{\text{char}}\mathbf{v}^*, \Theta_{\text{char}}\theta^*)} =: \frac{\tau_g}{\tau_{ev}(s^*,\mathbf{v}^*,\theta^*)}\ , \tag{3.22}$$

$$\mathrm{He}(s^*,\mathbf{v}^*,\theta^*) := \frac{\tau_g}{\Theta_{\text{char}}/\mathrm{R}(S_{\text{char}}s^*, V_{\text{char}}\mathbf{v}^*, \Theta_{\text{char}}\theta^*)} =: \frac{\tau_g}{\tau_{he}(s^*,\mathbf{v}^*,\theta^*)}\ . \tag{3.23}$$

They are called Stokes number, evaporation number and heat transfer number, respectively. Analogous to the response time for the drag force, τ_d, evaporation and heat transfer time scales, τ_{ev} and τ_{he}, are introduced. The evaporation number and the corresponding time scale are defined positive if the droplets evaporate. A negative evaporation number and evaporation time scale refer to the condensation of vapour on the droplet surface. The sign of the heat transfer number, He, and the heat time scale, τ_{he}, is positive if heat is transferred to a droplet. The definitions are chosen such that τ_{ev} and τ_{he} are predominantly positive in combustion systems. The Froude number for a spray system is defined by

$$\mathrm{Fr} := \frac{V_{\text{char}}}{g\tau_g}\ . \tag{3.24}$$

The breakup and collision terms are written as

$$\mathcal{Q}^*(s^*,\mathbf{v}^*) := \tau_g\mathcal{Q}(S_{\text{char}}s^*, V_{\text{char}}\mathbf{v}^*), \quad \Gamma^*(s^*,\mathbf{v}^*) := \tau_g\Gamma(S_{\text{char}}s^*, V_{\text{char}}\mathbf{v}^*)\ . \tag{3.25}$$

[4]The arguments of the dependent quantities are suppressed.

Substituting all definitions in (3.17)-(3.19) and (3.21)-(3.25) into (3.20) yields

$$\frac{\partial}{\partial t}(f) + \nabla_{\mathbf{x}} \cdot (\mathbf{v}f) + \nabla_{\mathbf{v}} \cdot \left\{ \left(\frac{\mathbf{U}_g - \mathbf{v}}{\mathrm{St}} + \frac{1}{\mathrm{Fr}}\mathbf{e_g} \right) f \right\} - \frac{\partial}{\partial s}\left(\mathrm{Ev}f\right) + \frac{\partial}{\partial \theta}\left(\mathrm{He}f\right) = \Gamma(f) + \mathcal{Q}(f) \ . \quad (3.26)$$

In this equation and the remainder of this work the asterisks, $(\cdot)^*$, of the dimensionless variables and functions are suppressed for reasons of readability and simplicity. If dimensional quantities are introduced in the sequel, they will be marked explicitly.

The linear independent set of the four dimensionless numbers {St, Ev, He, Fr} and the dimensionless collision and breakup terms, $\Gamma(f)$ and $\mathcal{Q}(f)$, fully characterise a spray configuration in which the physical phenomena of transport, drag force, evaporation, droplet heating, gravity, collision and breakup of droplets are present. Note that the dimensionless numbers defined in (3.21)-(3.25) are constant for a spray configuration only if a special type of flow is considered or more restrictive assumptions are introduced to simplify the form of the physical models. Consequently they can be used to characterise different regions of a spray flow.

3.3 Approaches to Solve the Kinetic Spray Equation

Apart from its dependencies on $\mathbf{x}$ and t, the NDF in equation (3.26) has five degrees of freedom, i.e. the velocity components, v_i with $i \in [1, 2, 3]$, the surface variable, s and the temperature variable, θ. Assuming that the PDE (3.26) is supplemented by appropriate initial and boundary conditions and all physical models are explicitly specified, then there is no way to find an analytical expression for $f(\mathbf{x}, t; \mathbf{v}, s, \theta)$. This is only possible when very restrictive assumptions are enforced (see Appendix A). In addition, it is not possible to find an approximation of $f(\mathbf{x}, t; \mathbf{v}, s, \theta)$ with the numerical algorithms commonly used in CFD because those methods are based on the assumption that all quantities depend on position and time variables only. In this section an overview is given over the methods that are used to reduce PDE (3.26) to a system of PDE's which can be tackled with the known numerical methods. With these methods the NDF or moments of it can only be approximated.

3.3.1 The Lagrangian Particle Tracking Method

The Lagrangian particle tracking method[5] is used in EL methods to describe the dispersed droplet phase (for references see Section 1.3). This approach is based on the tracking of numerical entities, called parcels, that represent several droplets. The k^{th} parcel is characterised by its position $\mathbf{x}_k$, velocity $\mathbf{v}_k$, surface area s_k and temperature θ_k. Each parcel is assumed to undergo the physical processes of transport, evaporation, gravitational ac-

[5] In the literature this approach is also called Lagrangian Monte-Carlo approach [45] or Direct Simulation Monte-Carlo method (DSMC) [13].

celeration and drag force, which are captured by solving the equations

$$\frac{d\mathbf{x}_k}{dt} = \mathbf{u}_k, \qquad \frac{d\mathbf{u}_k}{dt} = \frac{\mathbf{U}_g(\mathbf{x}_k, t) - \mathbf{v}_k}{\mathrm{St}(s_k, \mathbf{v}_k)} + \frac{1}{\mathrm{Fr}}\mathbf{e}_g, \tag{3.27}$$

$$\frac{ds_k}{dt} = -\mathrm{Ev}(\mathbf{v}_k, s_k, \theta_k), \qquad \frac{d\theta_k}{dt} = \mathrm{R}(\mathbf{v}_k, s_k, \theta_k), \tag{3.28}$$

for each of the N_d parcels ($k = 1, \ldots, N_d$). The breakup and collision can either be considered by monitoring the collision between parcels [6] or by using a stochastic treatment of collision and breakup [144]. To model the influence of the dispersed phase on the gas phase, the respective quantities, i.e. the droplet forces, mass transfer, etc., are ensemble, time or volume averaged over a representative sample of parcels.

The Lagrangian particle tracking method can also be used to solve the kinetic spray equation (3.26). It is then called particle discretisation (PD) method. For this method the NDF is approximated by a sum of Dirac delta functions,

$$f_{\mathrm{PD}}(\mathbf{x}, t; \mathbf{v}, s, \theta) = \sum_k^{N_d} w_k(t)\delta(\mathbf{x} - \mathbf{x}_k(t))\delta(\mathbf{v} - \mathbf{v}_k(t))\delta(s - s_k(t))\delta(\theta - \theta_k(t)) \ , \tag{3.29}$$

where w_k is the weight of the k^{th} parcel. The substitution of the approximate NDF into the kinetic spray equation (3.26) yields – after some algebra – the evolution equations in (3.27) plus one equation for the weight. This reads

$$\frac{\mathrm{d}w_k}{\mathrm{d}t} = \left(\Gamma(f_{\mathrm{PD}}) + \mathcal{Q}(f_{\mathrm{PD}})\right)|_k \ . \tag{3.30}$$

Thus, the weight is only changing when collision, breakup or droplet-wall interaction is considered.

In this work, a PD method was provided by Nechtan Le Lostec and Philippe Villedieu (ONERA/DMAE, Toulouse), that is used in Chapter 6 to compare with the new Euler method introduced in Chapters 4 and 5. It is regarded as accurate 'reference' solution method because a large number of parcels and small sample volumes and sample times are used.

3.3.2 The Classical Eulerian Approach

The method that is denoted here as classical Eulerian approach or classical Euler method was first proposed by Truesdell [170] in 1957 and put on a sound mathematical footing by Bowen [20], Drew and Passman [42] and Passman et al. [124]. This method is based on the following suppositions[6]

(i) Each spatial point of the mixture is simultaneously occupied by material of all phases.

(ii) *'All properties of the mixture must be mathematical consequences of properties of the constituents'* [171].

[6] Truesdell [171] coined these assumptions 'metaphysical principals'.

(iii) *'So as to describe the motion of a constituent, we may in imagination isolate it from the rest of the mixture, provided we allow properly for the actions of the other components upon it'* [171].

(iv) *'The motion of the mixture is governed by the same equations as is a single body'* [171].

Obviously, this 'mixture continuum hypothesis' is physically not correct, but it is made whenever mathematical formulae are laid down to describe the physical processes that take place within a multiphase system, be it miscible or immiscible. However, the atomistic structure of matter makes this assumption always dubious at sufficiently small scales. In fact, the mixture continuum hypothesis should always be viewed as a certain homogenisation process [42].

Supposition (ii) can be restated as: *'The whole is no more than the sum of its parts'* [171] and the fourth can be expressed by the words: *'In its motion as a whole a body does not know whether it is a mixture or not'* [171]. The third supposition allows for the application of the balance laws (e.g. balance laws of mass, momentum, moment of momentum, energy and entropy) for every phase, but in contrast to the balance laws for single-material bodies, these equations are no longer conservative. This means that interaction (production) terms may be non-zero and then express the effect of all other phases upon one particular phase and vice versa. One can also think of the third supposition as cutting free a constituent and introducing the correct reaction quantities which counteract the cutting operation.

Based on this classical theory, models have been proposed for spray flows (cf. [71, 77]), that assume the gas and droplet phase to be two fluids that are described with two coupled sets of NS-like equations. In these two-fluid models stress tensors are introduced that rely on the definition of a pressure in the dispersed phase. Kaufmann [83] has shown that this pressure leads to an unstable behaviour of the well-known pressure correction procedure [50] because the resulting system is not necessarily hyperbolic. In addition, these Euler methods rely on the strong assumption that at one point only one velocity of each phase is possible. This assumption contradicts the PTC because bi- or multi-modal velocity distribution at crossing points cannot be described.

3.3.3 Eulerian Approaches based on Rarefied Gas Theory

To prevent the difficulties mentioned in Section 3.3.2 and to take into account turbulent effects, Février et al. [51] and Kaufmann et al. [84] used balance equations for higher-order velocity moments that are based on the conditional particle velocity PDF introduced by Reeks [133]. These type of Euler methods solve transport equations for the mean velocity $U_i^d := \int_{\mathbf{v}} v_i f_{\mathbf{v}} d\mathbf{v}$ and the central velocity moments

$$R_{ij} := \frac{1}{n}\int_{\mathbf{v}} v_i' v_j' f_{\mathbf{v}} d\mathbf{v}, \quad S_{ijk} := \frac{1}{n}\int_{\mathbf{v}} v_i' v_j' v_k' f_{\mathbf{v}} d\mathbf{v}, \quad Q_{ijkl} := \frac{1}{n}\int_{\mathbf{v}} v_i' v_j' v_k' v_l' f_{\mathbf{v}} d\mathbf{v}, \qquad (3.31)$$

where $\mathbf{v}' = (\mathbf{v} - \mathbf{U}^d)$ is the velocity fluctuation and n the number density of droplets. The different models are categorised as first, second or higher-order models, depending on the order of moments that are considered. In the frame of kinetic spray equation (3.26),

first-order models assume the NDF to have the form

$$f_{\text{first}}(\mathbf{x},t;\mathbf{v},s,\theta) = n(\mathbf{x},t)\delta(\mathbf{v}-\mathbf{U}^d(\mathbf{x},t))\delta(s-\bar{s}(\mathbf{x},t))\delta(\theta-\bar{\theta}(\mathbf{x},t)) \ , \tag{3.32}$$

where $\bar{s}$ and $\bar{\theta}$ are the average surface area and temperature of droplets at a position and time. The substitution of this approximate NDF into the kinetic spray equation (3.26), the multiplication with 1, $s^{3/2}$, $s^{3/2}\mathbf{v}$ and $s^{3/2}\theta$, respectively and the integration of the resulting equations in the complete internal-variable space yields

$$\begin{aligned}
&\frac{\partial n}{\partial t} + \nabla_{\mathbf{x}}\cdot(\mathbf{U}^d n) = -\psi_n(\mathbf{U}^d,\bar{s},\bar{\theta}) + C_n(\mathbf{U}^d,\bar{s}) \ , \\
&\frac{\partial m}{\partial t} + \nabla_{\mathbf{x}}\cdot(\mathbf{U}^d m) = -\psi_m(\mathbf{U}^d,\bar{s},\bar{\theta}) + C_m(\mathbf{U}^d,\bar{s}) \ , \\
&\frac{\partial m\mathbf{U}^d}{\partial t} + \nabla_{\mathbf{x}}\cdot(m\mathbf{U}^d\otimes\mathbf{U}^d) = -D(\mathbf{U}^d,\bar{s}) - \psi_{mv}(\mathbf{U}^d,\bar{s},\bar{\theta}) + C_{mv}(\mathbf{U}^d,\bar{s}) \ , \\
&\frac{\partial h}{\partial t} + \nabla_{\mathbf{x}}\cdot(\mathbf{U}^d h) = -H(\mathbf{U}^d,\bar{s},\bar{\theta}) - \psi_{mv}(\mathbf{U}^d,\bar{s},\bar{\theta}) + C_{mv}(\mathbf{U}^d,\bar{s}) \ .
\end{aligned} \tag{3.33}$$

In these equations, m represents the dimensionless mass density and h the dimensionless enthalpy of droplets. D, ψ, H and C are the source terms for droplet forces, evaporation, heating, collision and breakup for each averaged droplet field, respectively. Note that only one average velocity is defined at a position. Thus, similar to the classical Eulerian approach, all droplets at the same location have the same velocity which is equal to the mean of all the particles arriving at that location ('sticky-particle' model). On the other hand, the transport equations (3.33) do not include pressure terms (pressure-less gas dynamics), and an equation for the number of droplets does not have to be postulated, as is the case for the classical Euler method. This model will be used in Chapter 6 to compare with the new Eulerian approach derived in Chapters 4 and 5.

Second and higher-order models (in velocity space) rely on transport equations for n, $\mathbf{U}^d$, the second-order central moment $R_{ij}(\mathbf{x},t)$ and higher-order moments if desired. To close the collision terms in the moment equations the velocity distribution is assumed to be close to an equilibrium distribution corresponding to the local exponential (Maxwellian) distribution. The unknown higher-order moments appearing in the transport equations are closed by using a gradient-diffusion model. The second-order model of Simonin [157], for example, uses the closure

$$S_{ijk} = -K_{ip}\frac{\partial}{\partial x_p}R_{jk} - K_{jp}\frac{\partial}{\partial x_p}R_{ki} - K_{kp}\frac{\partial}{\partial x_p}R_{ij} \ , \tag{3.34}$$

where $K_{pq} = (3/\tau_d + 1/\tau_c)^{-1}R_{pq}$. This model can describe flows that deviate only slightly from the equilibrium velocity distribution. Therefore, bi- or multi-modal velocity distributions, which would be necessary to tackle PTC, cannot be captured with these kind of methods.

3.3.4 Moment Methods

In this work, the focus is on moment methods because they lead to numerical algorithms that are able to describe the unsteady behaviour of polydisperse sprays. Moment methods do not aim to solve for the NDF explicitly or approximations of it but only for some chosen moments. The moments of the NDF with respect to the surface, temperature and velocity variables are generally defined by

$$\mathrm{M}_{ijk}^{K,L,M}(\mathbf{x},t) := \int_{\mathbb{R}^3}\int_{\mathbb{R}_+}\int_{\mathbb{R}_+} s^K \theta^L v_i v_j v_k f(\mathbf{x},t;\mathbf{v},s,\theta) ds\, d\theta\, d\mathbf{v} \ , \tag{3.35}$$

where K, L and M are the orders of the moment with respect to the surface, temperature and velocity variable, respectively. M agrees also with the number of velocity indices. The moments are averaged quantities of the NDF but can also be interpreted as mean physical fields in the droplet cloud. The moments related to $[K,L,M] = [0,0,0]$ and $[K,L,M] = [3/2,0,0]$, for example, are proportional to the (average) number and (average) mass of droplets at one point in space and time (see Section 4.3.2). Moment methods are based on equations, called moment transport equations, that follow from the integration of the kinetic spray equation (3.26) with respect to the internal variables.[7] These integro-PDE are unclosed because *first*, the physical models arising in the integrated kinetic spray equation are non-linear functions of the internal variables and the integrals of these functions cannot be expressed in terms of any of the moments arising in the moment transport equations. *Second*, the transport equation of the highest order moment in velocity contains a moment that exceeds the order of the highest moment by one. This moment is unknown because no transport equation is formulated for it.[8] The various moment methods (for an overview see Grosch et al. [72], Marchisio et al. [108] or Ramkrishna [132]) differ in the way these unclosed integrals and the unknown velocity moment are approximated. In the remainder of this work, the focus is on quadrature and sectional methods because they are moment methods that allow the closure of the kinetic spray equation without limiting the generality of the physical spray models.

Quadrature methods are moment methods that, in case of the kinetic spray equation (3.26), are based on the following approximation of the NDF

$$\begin{aligned} f_{\mathrm{Qu}}(\mathbf{x},t;\mathbf{v},s,\theta) &= \sum_{\alpha=1}^{\beta} w_\alpha(\mathbf{x},t)\boldsymbol{\delta}\left[\mathbf{v}-\mathbf{U}_\alpha(\mathbf{x},t)\right]\delta\left(s-s_\alpha(\mathbf{x},t)\right)\delta\left(\theta-\theta_\alpha(\mathbf{x},t)\right) \ , \\ \boldsymbol{\delta}\left[\mathbf{v}-\mathbf{U}_\alpha\right] &:= \prod_{i=1}^{d}\delta\left(v_i-(U_i)_\alpha\right) \ . \end{aligned} \tag{3.36}$$

[7] For a detailed derivation of the moment transport equations see Section 4.2.

[8] If, by some means, the moment transport equations could be solved for a finite set of moments, the NDF could only be reconstructed, if at all, for some special forms of the NDF. For a Gaussian distribution, for example, the first three moments M^K, $(K = 0, 1, 2)$ would be sufficient. As outlined in Section 2.2.3 and shown in Chapter 6 the size distribution of sprays can change considerably when breakup, collision, drag forces or droplet-wall interaction are present. Therefore, the reconstruction of the NDF with analytical expressions like the Rosin-Rammler distribution (cf. [71, 100]) can be misleading. Instead, it is much more natural to interpret the numerical results and its comparison with experiments on the level of moments.

Here, β is the number of nodes, d the dimension of the velocity space, $w_\alpha(\mathbf{x},t)$ the weight of node α, which is required to be non-negative. $\mathbf{U}_\alpha$, s_α and θ_α are the internal variables at node α, also called abscissas. With this approximation every integral in the integrated kinetic spray equation and the unknown velocity moment are transformed into a summation of the weighted integrands evaluated at the nodes. This obviously closes the moment equations if the weights and abscissas are known. The variants of the quadrature method differ in the way the weights and abscissas are computed. However, all of them rely on relations of the form[9]

$$\mathrm{M}_{ijk}^{K,L,M} = \sum_{\alpha=1}^{\beta} w_\alpha s_\alpha^K \theta_\alpha^L U_{\alpha i} U_{\alpha j} U_{\alpha k} \ , \tag{3.37}$$

where all quantities in (3.37) depend on $\mathbf{x}$ and t only. In this sum relation the moment is generally known from a previous time step, an initial or boundary condition. The purpose of the quadrature algorithms is to find the weights and abscissas using equation (3.37) and the known moments. The number of moments must at least equal $(3+d)\beta$, which is the number of unknown weights and abscissas in (3.36). The choice of moments is not unique and depends on the quadrature method and the objectives of the investigator. Poor choices can lead to non-unique abscissas and negative weights, i.e. unphysical situations [57]. It should be noted, that closure (3.36) does not limit the choice of physical models, i.e. the non-linearities of the models for $\mathrm{Ev}(\mathbf{v},s,\theta)$, $\mathrm{He}(\mathbf{v},s,\theta)$, $\Gamma(f_{\mathrm{Qu}})$ or $\mathcal{Q}(f_{\mathrm{Qu}})$ (see Chapter 2) do not prevent the closure of the moment transport equations.

The *quadrature method of moments* (QMoM) was first formulated in 1997 by McGraw [109] for an aerosol system undergoing the physical processes of condensation, evaporation, coalescence and breakup. In its original version QMoM was applied to kinetic spray equations with one internal variable. McGraw [109] chose the droplet radius and transported the moments, M^k of order $k = 0,\ldots,2\beta-1$ ($\beta = 3, 4$ or 5). The main part of QMoM is the computation of the weights and abscissas from the 2β moments, i.e. the solution of the 2β nonlinear equations of form (3.37). This problem is poorly conditioned if it is solved directly. The product-difference (PD) algorithm (cf. [67, 129]) is used in every numerical time step to transform the 2β-dimensional equation system into a well conditioned eigenvalue problem which can then be solved accurately. The resulting weights and abscissas can then – in the next time step – be used to calculate the source and sink terms in the moment transport equations.

The idea of McGraw was extended independently by many authors (for an overview see [56, 72, 106]). However, the method is limited to one (mono-variate) or maximal two (bi-variate) internal variables (cf. [183]), which prevents its application to polydisperse, non-isothermal sprays that experience PTC. Although QMoM is not able to describe the full complexity of the kinetic spray equation (3.26), it is nevertheless an excellent tool to model, for example, the evaporation of multi-component droplets [94] or the aggregation and breakage of chemical agents in crystallisation processes [108].

[9] This relation justifies the name 'quadrature methods' because the numerical integration, called quadrature, relies on the approximation $\int f(x)dx = \sum_{\alpha=1}^{\beta} \varpi_\alpha f(x_\alpha)$. The quantities ϖ_α and x_α, which are called weights and abscissas, are determined by the Gauss quadrature, for example.

The *direct quadrature method of moments* (DQMoM), developed by Marchisio and Fox [53, 107], is a quadrature method that can, in principle, consider as many internal variables as is desired (cf. [54]). Instead of solving transport equations for the moments and applying the PD algorithm at every time step, DQMoM solves transport equations 'directly' for the weights and abscissas of every node α. Only the initial weights and abscissas have to be computed using the PD algorithm for one or some expensive nonlinear solver (cf. [57]) for multiple internal variables. In the context of sprays, the transport equations for weights and abscissas can easily be transformed into a form that is equivalent to the transport equation of the droplet volume fraction, size, enthalpy and droplet momentum of β droplet phases. The source and sink terms for the drag force, collision, coalescence and breakup of the latter transport equations are calculated from a linear equation system of size 2β, which requires the abscissas to be non-zero and distinct. This leads to substantial difficulties, in particular, when droplets disappear. In the case of evaporation, droplets that approach the size $s = 0$ have to be erased from the system. This implies that the transport equation for the zeroth-order moment $\mathrm{M}^{0,0,0}(\mathbf{x}, t)$, which represents the number of droplets, must include a sink term, representing the number of disappearing droplets.

To illustrate how DQMoM deals with the loss of droplets at $s = 0$, let us consider the simple situation where a homogeneous and isothermal spray in a box is evaporating and finally disappearing according to some chosen evaporation model $\mathrm{Ev}(s)$.[10] In this case, the kinetic spray equation (3.26) is expressed as

$$\frac{\partial}{\partial t}(f(t;s)) = \frac{\partial}{\partial s}\left(\mathrm{Ev}(s) f(t;s)\right) \ . \tag{3.38}$$

To obtain the moment transport equations, (3.38) is multiplied by s^K and the resulting equation is integrated over all possible droplet surfaces. These operations yield

$$\frac{\partial}{\partial t}(\mathrm{M}^K) = \int_{\mathbb{R}_+} s^K \frac{\partial}{\partial s}\left(\mathrm{Ev} f\right) ds \ , \tag{3.39}$$

which can be further transformed into

$$\frac{\partial}{\partial t}(\mathrm{M}^K(\mathbf{x}, t)) = \left[s^K \mathrm{Ev(s)} f(\mathbf{x}, t; s)\right]_{s=0}^{s=\infty} - K \int_{\mathbb{R}_+} s^{K-1} \mathrm{Ev(s)} f(\mathbf{x}, t; s) ds \ . \tag{3.40}$$

With the assumption, that the sizes of the droplets are not larger than some finite value, equation (3.40) turns into

$$\frac{\partial}{\partial t}(\mathrm{M}^K(\mathbf{x}, t)) = -\delta_{K0} \mathrm{Ev}(0) f(\mathbf{x}, t; 0) - K \int_{\mathbb{R}_+} s^{K-1} \mathrm{Ev(s)} f(\mathbf{x}, t; s) ds \ , \tag{3.41}$$

where the term δ_{K0} represents the Kronecker delta

$$\delta_{K0} = \begin{cases} 1 & \text{if } K = 0, \\ 0 & \text{otherwise} \ . \end{cases} \tag{3.42}$$

[10] This situation is purely theoretical. Evaporation always leads to heat exchange between gas- and liquid phase. The resulting temperature difference contradicts the assumption of isothermal conditions. However, for clarity reasons the temperature variable is abandoned in this gedankenexperiment.

As expected, the first term on the right-hand side of (3.41) is non-zero only for the transport equation of moment M^0. It should also be noted that the quantity $\mathrm{Ev}(0)f(\mathbf{x},t;0)$ is a pointwise quantity in surface space. Within the frame of DQMoM the information about the droplet distribution at point $s=0$ is not accessible because, as mentioned above, the abscissas are not allowed to approach zero. Consequently, the sink term $\mathrm{Ev}(0)f(\mathbf{x},t;0)$ in the transport equation of the zeroth-order moment is not closed using DQMoM. Extending the complexity of the spray to dynamic, non-isothermal and inhomogeneous conditions does not resolve this difficulty.

Fox et al. [59] regard the quantity $\psi(\mathbf{x},t) := \mathrm{Ev}(0)f(\mathbf{x},t;0)$ as additional unknown, besides the weights and abscissas, and introduce additional assumption, called ratio constraints, to solve for the source and sink terms of the weights and abscissas. For smooth initial distribution functions in size space they can show, by comparison to Lagrangian calculations, that the ratio constraints yield acceptable results for a stationary one-dimensional configuration. They also show that the unknown $\psi(\mathbf{x},t)$ can be set to zero, if the initial distribution function is composed of Dirac peaks only (see also Friedrich and Weigand [60]). However, Fox et al. [59] admit that for more complicated initial distribution functions the specification of the evaporation flux with DQMoM is problematic.

Besides the work of Fox et al. [59], Madsen [104] and Friedrich and Weigand [60] apply DQMoM to sprays in complex nozzle configurations. They regard the diameter of the droplets as internal variable and couple their mono-variate version of DQMoM to a commercial CFD solver. This software is used to transport the weights and abscissas in space and time. Friedrich and Weigand [60] consider evaporation but set the unknown $\psi(\mathbf{x},t)$ to zero, whereas Madsen [104] is not investigating evaporation.

The general concept of DQMoM allows the consideration of velocity distributions which are not mono-modal. However, Desjardins et al. [39, 38] and Fox [56] refrain from using DQMoM for describing PTC. They mention (without proving it explicitly) that the discontinuous change of the weights and abscissas at PTC-points can lead to difficulties.

The above defects of DQMoM shall not hide the fact, that it is most suitable for applications where coalescence, accumulation, coagulation, sintering and breakup processes of particles, droplets or other dispersed agents are present (for an overview see Grosch et al. [72]). In the field of turbulent combustion, for example, Zucca et al. [186] used DQMoM to describe the nucleation, growth, aggregation and oxidation of nano-particles (soot) in a turbulent non-premixed ethylene-air flame. Even for the treatment of the LES-filtered reactive scalar PDF transport equation DQMoM is applied [131]. In Chapter 2 evaporation and PTC were identified to be crucial in spray systems. As DQMoM can capture these effects only in a very crude manner (if at all) it is not further investigated in this work.

The *quadrature-based method of moments* (QBMoM) was developed recently by Desjardins et al. [38, 39] and later refined by Fox [56] and Le Lostec et al. [99]. It was formulated to treat PTC in monodispersed isothermal particle flows. Therefore, the internal variables in equation (3.26) are the velocity components only. In contrast to QMoM and DQMoM, the weights and abscissas, defined in (3.36), are obtained from the transported moments through algebraic expressions. The QBMoM algorithm uses *first*, the set of velocity moments $\{\mathrm{M}^0, \mathrm{M}_i^1, \mathrm{M}_{ii}^2, \mathrm{M}_{iii}^3\}$ in each direction, $\mathbf{e}_i$, $(i=1,\ldots,d)$, to compute

the uncoupled weights and abscissas of a two node approximation in each direction $\mathbf{e}_i$ [166]. *Second*, the nodes are coupled by enforcing the weights and abscissas to reproduce the second-order cross moments M^2_{ij} [56, 99].[11] With two nodes in each direction, $\mathbf{e}_i$, a bi-modal velocity distribution can be described. Conceptually, the method is not limited to two nodes. By using the PD algorithm to compute the weights and abscissas for each real space direction it was shown by Fox [58] that more than two nodes are possible. In this case, the crossing of droplets with multiple velocities can be captured. This, of course, comes at the expense of transporting more moments.

In this thesis, a variant of QBMoM is considered that combines the approaches of Fox [56] and Le Lostec et al. [99]. It controls the second-order cross moments, M^2_{ij}. In Chapter 4 the method of Fox [56] is explained in more detail (as it was implemented into the program code by the Author), whereas for the approach of Le Lostec et al. [99] the reader is referred to original paper.

The sectional method (SM) allows the description of polydisperse, non-isothermal sprays that undergo evaporation, collision and break-up but no PTC [34, 43]. It was originally suggested by Greenberg, Tambour and co-workers [68, 69], rigorously defined on a kinetic level by Laurent, Massot and Villedieu [96, 97] and extended to second-order in size space by Dufour and Villedieu [44] and Laurent [95]. In this work, the approach of Dufour and Villedieu [44] is pursued. The main ideas of this method are *first*, the discretisation of the surface space $[0,\,\infty)$ into N_s+1 fixed intervals $I_k = [s_k,\,s_{k+1})$ $(k = 1,\ldots,N_s)$, $I_{N_s+1} = [s_{N_s+1},\,\infty)$ (with $s_{N_s+1} = 1$), called sections. *Second*, the approximation of the NDF according to

$$f_{\mathrm{Sec}}(\mathbf{x},t;s,\mathbf{v}) = \sum_{k=1}^{N_s+1} \mathbb{1}_{s_k\le s<s_{k+1}} a_k(\mathbf{x},t)\delta\left(\mathbf{v}-\mathbf{U}_k(\mathbf{x},t)\right)\delta\left(\theta-\theta_k(\mathbf{x},t)\right) g_k(\mathbf{x},t;s)\ , \tag{3.43}$$

$$\mathbb{1}_{s_k\le s<s_{k+1}} = \begin{cases} 1 & \text{if} \quad s_k \le s < s_{k+1}\ , \\ 0 & \text{otherwise} \end{cases}$$

and *third* the transport of the moments $\mathrm{M}^{0,0,0}_k$, $\mathrm{M}^{3/2,0,0}_k$, $\mathrm{M}^{3/2,1,0}_k$ and $\mathrm{M}^{3/2,0,1}_{k,i}$ defined by [12]

$$\mathrm{M}^{K,L,M}_{k;lmn} := \int_{\mathbb{R}^3}\int_{\mathbb{R}_+}\int_{s_k}^{s_{k+1}} s^K\theta^L v_i v_j v_k f(\mathbf{x},t;\mathbf{v},s,\theta)ds\,d\theta\,d\mathbf{v} \tag{3.44}$$

in every section I_k [44]. The function $g_k(\mathbf{x},t;s)$ in approximation (3.43) represents a presumed shape of the surface distribution function in Section I_k. Dufour and Villedieu [44] assume the form

$$g_k(\mathbf{x},t;s) = \exp\left(-b_k s\right), \quad k = 1,\ldots,N_s+1 \quad \text{with} \quad b_{N_s+1} > 0\ . \tag{3.45}$$

They proved that this approximation leads to a finite-volume discretisation in surface space that is second-order accurate. In addition, it was shown that the resulting transport

[11] The approach of Desjardins et al. [38, 39] does not control the cross moments of second-order.

[12] The relation between the moments in (3.44) and (3.35) follows directly from the additivity of integrals, i.e. $\mathrm{M}^{K,L,M}_{lmn} = \sum_{k=1}^{N+1}\mathrm{M}^{K,L,M}_{k;lmn}$.

schemes guarantee stability and positivity criteria on the number, mass and velocity of droplets. Consequently, the mass and number of droplets which are proportional to $\mathrm{M}_k^{0,0,0}$ and $\mathrm{M}_k^{3/2,0,0}$ are always non-negative [43]. Dufour [43] and Laurent [95] discuss other higher-order SM's, i.e. higher-order polynomials of the surface variable s. They conclude that relation (3.45) delivers the most accurate results. Another argument that supports approximation (3.45) is the experiment of Laurent et al. [98]. There, the tail of the droplet distribution is shown to be exponentially decreasing as a function of the droplet surface. This justifies the assumption of $b_{N_s+1} > 0$.

The key task of the SM – similar to other moment methods – is the determination of parameters a_k, b_k, $U_{k;i}$ and θ_k in (3.43) from the moments $\mathrm{M}_k^{0,0,0}$, $\mathrm{M}_k^{3/2,0,0}$, $\mathrm{M}_{k;i}^{3/2,0,1}$ and $\mathrm{M}_k^{3/2,1,0}$ $(i = 1, \ldots, d)$. To this end, the following relations are used

$$\begin{aligned} \mathrm{M}_k^{0,0,0} &= a_k \int_{s_k}^{s_{k+1}} \exp(-b_k s) ds \;, & \mathrm{M}_k^{3/2,1,0} &= a_k \theta_k \int_{s_k}^{s_{k+1}} s^{3/2} \exp(-b_k s) ds \;, \\ \mathrm{M}_k^{3/2,0,0} &= a_k \int_{s_k}^{s_{k+1}} s^{3/2} \exp(-b_k s) ds \;, & \mathrm{M}_{k;i}^{3/2,0,1} &= a_k U_{k;i} \int_{s_k}^{s_{k+1}} s^{3/2} \exp(-b_k s) ds \;, \end{aligned} \tag{3.46}$$

for each section I_k, $k = 1, \ldots, N_s + 1$. However, the detailed derivation of the appropriate algorithm will be given in Chapter 4. Here, the main assumptions that are tacitly made when approximation (3.43) is enforced remain to be discussed. There are four principle assumptions [34]:

(i) For a given droplet size, at a given point $(\mathbf{x}, t)$ there are only one characteristic average velocity

$$\bar{\mathbf{v}}(\mathbf{x}, t; s) = \frac{\int_{\mathbb{R}^3} \int_{\mathbb{R}_+} \mathbf{v} f(\mathbf{x}, t; \mathbf{v}, s, \theta) \, d\theta \, d\mathbf{v}}{\int_{\mathbb{R}^3} \int_{\mathbb{R}_+} f(\mathbf{x}, t; \mathbf{v}, s, \theta) \, d\theta \, d\mathbf{v}} \tag{3.47}$$

and one characteristic average temperature

$$\bar{\theta}(\mathbf{x}, t; s) = \frac{\int_{\mathbb{R}^3} \int_{\mathbb{R}_+} \theta f(\mathbf{x}, t; \mathbf{v}, s, \theta) \, d\theta \, d\mathbf{v}}{\int_{\mathbb{R}^3} \int_{\mathbb{R}_+} f(\mathbf{x}, t; \mathbf{v}, s, \theta) \, d\theta \, d\mathbf{v}} \;. \tag{3.48}$$

(ii) The velocity and temperature dispersion around the average velocity $\bar{\mathbf{v}}(\mathbf{x}, t; s)$ and the average temperature $\bar{\theta}(\mathbf{x}, t; s)$ are zero in all directions, regardless of the point $(\mathbf{x}, t, s)$. This implies that all droplets in one section have the same velocity and the same temperature, i.e.

$$\bar{\mathbf{v}}(\mathbf{x}, t; s) = \bar{\mathbf{v}}_k(\mathbf{x}, t) \quad \text{and} \quad \bar{\theta}(\mathbf{x}, t; s) = \bar{\theta}_k(\mathbf{x}, t) \quad \text{for} \quad s_k \leq s < s_{k+1} \;. \tag{3.49}$$

(iii) The number density of droplets defined by

$$n(\mathbf{x}, t; s) := \int_{\mathbb{R}^3} \int_{\mathbb{R}_+} f(\mathbf{x}, t; \mathbf{v}, s, \theta) \, d\theta \, d\mathbf{v} \tag{3.50}$$

decreases exponentially with the surface variable going to infinity.

It follows from the first two assumptions that the SM cannot be applied to PTC. The last assumption is significant for sprays that coalesce because then droplets of size larger than $s = 1$ are generated.

3.3.5 Comparison of the Methods

The above discussion (Sections 3.3.2 to 3.3.4) has shown, that none of the Euler methods can solve the kinetic spray equation in its full complexity. The Lagrange method (Section 3.3.1), on the other hand, is able to consider all spray effects. However, the computational cost to solve for the trajectory of each parcel increases with the mass loading and the unsteadiness of the dispersed flow (see discussion in Chapter 1).

The postulates of the classical Euler method (Section 3.3.2) rely on the definition of a spurious pressure for the dispersed phase and the exclusion of velocity dispersion. These assumptions constrain the application to spray flows in which the droplet Knudsen number is very small and no PTC is present. Those Euler methods which are based on the ideas of the rarefied gas theory do not rely on the definition of a dispersed phase pressure. They allow the dispersion in velocity space and they were extended to turbulent flows [51, 84]. Nevertheless, the dispersion of the velocity is restricted to distributions which are close to kinetic equilibrium, i.e. it is difficult to describe spray systems that exhibit large droplet Knudsen numbers and PTC-effects with these kind of methods [99]. Consequently, the concentration of droplets at the rim of vortices tends to be overpredicted. Both Euler methods, mentioned above, have not been rigorously extended to polydisperse spray flows. In contrast, the quadrature methods, QMoM and DQMoM, were developed exclusively for polydisperse droplet, particle or bubble flows. Breakup, coalescence, drag forces, nucleation and growth of dispersed entities are phenomena that can be described accurately. Unfortunately, evaporation can only be considered if strong assumptions on the evaporation model and the droplet size distribution are introduced.

The QBMoM was exclusively developed to describe non-equilibrium velocity effects in dispersed flows. It allows the consideration of collision effects but assumes the particles to be isothermal, monodisperse and not changing in size. Evaporation and coalescence, which are important effects in technical spray flows, have not been accounted for within the frame of this method. The SM, on the other hand, addresses the polydisperse character of sprays. It can describe evaporation, breakup and coalescence effects. However, the dispersion in velocity space is not considered. The QBMoM and the SM are methods that apply to very special features of the spray flow. It is shown in Chapters 4 to 6 that their combination results in a robust method that can describe both, the polydisperse character of sprays and non-equilibrium velocity distributions.

3.4 Mathematical Models for Gas Flows

In this work, the focus is on the description of the dispersed phase. Obviously, the gas phase plays a major role in technical spray flows. A large variety of gas flow solvers are available that can, in principle, be incorporated. However, for the testing of the new method, developed in Chapters 4 to 6, analytical solutions are used to prevent the introduction of errors stemming from the gas flow solver or the coupling with it.

In this section the standard mathematical model for single-phase, multicomponent gas flows is introduced (Section 3.4.1) which is commonly used for describing the gas in combustion systems. In addition, the coupling between the gas and droplet phase is addressed (Section 3.4.2). For detailed treatises on the mathematical description of gas

flows the reader is referred to Giovangigli [66], Lamb [90] and Landau and Lifschitz [91].

3.4.1 Single-Phase, Multicomponent Gas Flows

The mathematical models for multicomponent single-phase gas flows are based on the balance laws for mass, momentum, energy and species concentration.[13] They are obtained from equation (3.1) by specialising the general physical variable to the mass density ρ_g [kg m^{-3}], specific momentum $\rho_g \mathbf{U}_g$ [kg s^{-1}m^{-2})], specific enthalpy h [J kg^{-1}] and the species concentration (mass fraction) Y_α [-] in the gas. With these specifications, the single-phase balance equations for a multicomponent gas mixture can be expressed as

$$\text{mass:} \quad \frac{\partial \rho_g}{\partial t} + \nabla_{\mathbf{x}} \cdot (\rho_g \mathbf{U}_g) = 0 \ , \tag{3.51}$$

$$\text{momentum:} \quad \frac{\partial \rho_g \mathbf{U}_g}{\partial t} + \nabla_{\mathbf{x}} \cdot (\rho_g \mathbf{U}_g \otimes \mathbf{U}_g) = \nabla_{\mathbf{x}} \cdot \mathbf{T} + \rho_g g \mathbf{e}_g \ , \tag{3.52}$$

$$\text{energy:} \quad \frac{\partial \rho_g h}{\partial t} + \nabla_{\mathbf{x}} \cdot (\rho_g h \mathbf{U}_g) = T_{ij} \frac{\partial U_{gi}}{\partial x_j} + \frac{\partial p}{\partial t} + \mathbf{U}_g \cdot \nabla_{\mathbf{x}} p - \nabla_{\mathbf{x}} \mathbf{q} + \rho_g \mathfrak{r} \ , \tag{3.53}$$

$$\text{concentration:} \quad \frac{\partial \rho_g Y_\alpha}{\partial t} + \nabla_{\mathbf{x}} \cdot (\rho_g Y_\alpha \mathbf{U}_g) = - \nabla_{\mathbf{x}} \cdot \mathbf{J}_\alpha + \Pi_\alpha \ , \quad \alpha = 1, \ldots, n \ . \tag{3.54}$$

In these equations $\mathbf{T}$ [N m^{-2}], $g\mathbf{e}_g$ [m s^{-2}], $T_{ij} \frac{\partial U_{gi}}{\partial x_j}$ [N m^{-2}s^{-1}], p [N m^{-2}], $\mathbf{q}$ [W m^{-2}], $\mathfrak{r}$ [W kg^{-1}], $\mathbf{J}_\alpha$ [kg m^{-2}s^{-1}] and Π_α [kg m^{-3}s^{-1}] represent the stress tensor, gravitational acceleration, viscous dissipation rate, pressure, heat flux vector, radiation, diffusion flux vector of component α in the gas mixture and a source/sink term for chemical reactions, respectively. From the definition of the concentration, $Y_\alpha := \rho_\alpha / \rho_g$, the sum relation $1 = \sum_\alpha Y_\alpha$ is obtained which reduces the number of concentration equations. The remaining $4 + n$ equations have to be supplemented by physical models, called material laws, and initial and boundary conditions to close the equation system. For general fluids, the stress tensor is split into an isotropic pressure part, p, and an extra stress tensor, $\mathbf{T}^{\mathrm{E}}$ [N m^{-2}], describing the friction in the fluid, i.e.[14]

$$\mathbf{T} = -p\mathbf{I} + \mathbf{T}^{\mathrm{E}} \ . \tag{3.55}$$

Assuming the fluid to be Newtonian, the extra stress tensor can be written as

$$\mathbf{T}^{\mathrm{E}} = \zeta_g \nabla_{\mathbf{x}} \cdot \mathbf{U}_g \, \mathbf{I} + 2\eta_g \mathbf{E} \ , \tag{3.56}$$

where ζ [kg (m s)$^{-1}$] is the volume viscosity and η_g [kg (m s)$^{-1}$] the dynamic viscosity of the gas. The tensor $\mathbf{E}$ [s^{-1}] is the deviatoric part of the rate of deformation tensor

$$\mathbf{D} := \frac{1}{2} \left(\nabla_{\mathbf{x}} \mathbf{U}_g + (\nabla_{\mathbf{x}} \mathbf{U}_g)^{\mathrm{T}} \right) , \ [\mathrm{s}^{-1}] \ . \tag{3.57}$$

[13] Other scalar equations are usually introduced to describe the progress of the chemical reaction in the flame [126].

[14] The balance equation for the moment of momentum, which is skipped in the above list of balance equations, leads to the symmetry of the stress tensor, i.e. $\mathbf{T} = \mathbf{T}^{\mathrm{T}}$.

With these definitions, the material law for the stress tensor is written as

$$\begin{aligned}\mathbf{T} &= -p\mathbf{I} + \zeta_g(\nabla_{\mathbf{x}} \cdot \mathbf{U}_g)\mathbf{I} + 2\eta_g\mathbf{E} \\ &= -p\mathbf{I} + \zeta_g(\nabla_{\mathbf{x}} \cdot \mathbf{U}_g)\mathbf{I} + 2\eta_g\left(\mathbf{D} - \frac{1}{3}(\nabla_{\mathbf{x}} \cdot \mathbf{U}_g)\mathbf{I}\right) .\end{aligned} \tag{3.58}$$

The substitution of equation (3.58) into the balance law (3.52) yields the transport equation for momentum used in the compressible Navier-Stokes equations. To investigate the order of magnitude of the various terms in the momentum equation, it is disposed of its dimensions. The typical dimensions are a characteristic velocity $[v]$, viscosity $[\eta]$, pressure $[p]$, gravity $[g]$ and density $[\rho]$. From these quantities the typical viscous-diffusion length $[x] := [\eta]\,([\rho][v])^{-1}$ and the corresponding time scale $[t] := [x]\,[v]^{-1}$ can be defined. The order of magnitude of the sound velocity c $[\mathrm{m\,s^{-1}}]$ is then $[c]^2 := [p]\,[\rho]^{-1}$. With these definitions the following dimensionless numbers can be defined:

$$\text{Reynolds number:} \qquad \mathrm{Re}_g := \frac{[\rho][x][v]}{[\eta]} , \tag{3.59}$$

$$\text{Mach number:} \qquad \mathrm{Ma}_g := \frac{[v]}{[c]} , \tag{3.60}$$

$$\text{Froude number:} \qquad \mathrm{Fr}_g := \frac{[v]^2}{[x][g]} . \tag{3.61}$$

Disposing every quantity ϕ, in (3.52) of its dimension and defining $\hat{\phi} = \phi/[\phi]$ – after some algebra – the following two variants of equation (3.52) are obtained

$$\mathrm{Ma}_g^2\left(\frac{\partial\hat{\rho}_g\hat{\mathbf{U}}_g}{\partial\hat{t}} + \nabla_{\hat{\mathbf{x}}} \cdot \left(\hat{\rho}_g\hat{\mathbf{U}}_g \otimes \hat{\mathbf{U}}_g\right) - \nabla_{\hat{\mathbf{x}}} \cdot \hat{\mathbf{T}}^{\mathrm{E}} - \hat{\rho}_g\frac{1}{\mathrm{Fr}_g}\mathbf{e}_g\right) = -\nabla_{\hat{\mathbf{x}}}\hat{p} , \tag{3.62}$$

$$\frac{\partial\hat{\mathbf{U}}_g}{\partial\hat{t}} + \nabla_{\hat{\mathbf{x}}}\left(\hat{\mathbf{U}}_g\right)\hat{\mathbf{U}}_g = -\nabla_{\hat{\mathbf{x}}}\hat{p} + \frac{1}{\mathrm{Re}_g}\nabla_{\hat{\mathbf{x}}} \cdot \hat{\mathbf{T}}^{\mathrm{E}} - \frac{1}{\mathrm{Fr}_g}\mathbf{e}_g . \tag{3.63}$$

The first of these equations is usually used to justify the assumption of isobaric flows, which is appropriate for low Mach numbers. In this case the splitting $p(t,\mathbf{x}) = p_0(t) + \tilde{p}(t,\mathbf{x})$ is allowed and the pressure p_0 drops out in all balance equations (not in the equation of state) if it is assumed to be independent of time.

The second equation helps to differentiate between laminar and turbulent flows. For small Reynolds numbers the friction tensor $\hat{\mathbf{T}}^{\mathrm{E}}$, is dominant and the convective term (second term on the left-hand side of (3.63)) is damped. If the Reynolds number is large the non-linearities in the convective term are not reduced by the friction and a chaotic behaviour is observed. In this case the flow is said to be turbulent, i.e. the motion of the flow is random in the sense that a large variety of length and time scales are necessary to characterise the flow. There are various sophisticated simulation models to capture turbulent flows. They are called direct numerical simulation (DNS), large-eddy simulation

(LES), and Reynolds-averaged Navier-Stokes (RANS) methods (for an overview on these methods see Pope [128]).

The other unknown fluxes in equations (3.53) and (3.54) are commonly approximated by gradient-diffusion models, which read (Fourier law of heat transfer)

$$\mathbf{q} = -\lambda_g \nabla_{\mathbf{x}} \theta_g \tag{3.64}$$

and (Fick's law of diffusion)

$$\mathbf{J}_\alpha = \rho_g D_\alpha \nabla_{\mathbf{x}} Y_\alpha \ , \tag{3.65}$$

where λ_g [W (mK)$^{-1}$] is the thermal conductivity and D_α [m^{2}s^{-1}] the diffusion coefficient of the component α in the gas. With these models more subtle influences on the heat and diffusion flux vectors (e.g. the Soret and Dufour effects) are neglected. For more sophisticated models see Giovangigli [66].

The equations are completed by equations of state for the enthalpy and the thermodynamic pressure. For ideal gases, the equation of state for the enthalpy reads

$$h = \sum_\alpha Y_\alpha h_\alpha, \quad \text{with} \quad h_\alpha(\theta_g) = h_{\alpha 0} + \int_{\theta_{g0}}^{\theta_g} c_{p\alpha}(\theta^\circ) d\theta^\circ \ , \tag{3.66}$$

where h_α [J kg^{-1}] is the enthalpy of component α, $h_{\alpha 0}$ [J kg^{-1}] and θ_{g0} [K] the referential enthalpy and temperature and $c_{p\alpha}$ [J (kg K)$^{-1}$] the specific heat capacity of component α. The heat capacity of the gas mixture is obtained from $c_p = \sum_\alpha Y_\alpha c_{p\alpha}$. The equation of state for a ideal gas reads

$$\rho_g = \frac{p\bar{M}}{R\theta_g} \ , \tag{3.67}$$

where the universal gas constant, $R = 8.314$ J (K mol)$^{-1}$, and the molar mass, $\bar{M}$ [kg mol^{-1}] of the gas mixture

$$\bar{M} = \frac{1}{\sum_\alpha Y_\alpha / M_\alpha} \tag{3.68}$$

have been used. M_α [kg mol^{-1}] is the molar mass of component α.

In technical gas flows, some or all of the following assumptions are made:

(i) Stokes assumption: $\zeta_g = 0$,

(ii) incompressible fluid: $\rho_g \neq f(p)$,

(iii) small Mach number approximation: $p = p_0 + \tilde{p} \ \Rightarrow \quad \rho_g = f(\theta_g, p_0, Y_1, \ldots, Y_n)$,

(iv) density-preserving fluid: $\rho = \text{const.} \Rightarrow \nabla_{\mathbf{x}} \cdot \mathbf{U}_g = 0$.

If the fluid is compressible, i.e. none of the assumptions (i)-(iv) is enforced, p is a thermodynamic pressure which is related to the mass density, concentration and temperature of the fluid via equation (3.67) or some other equation of state. If the fluid is assumed incompressible but the change of temperature and composition is large, the density can, in general, not be assumed constant. This is only the case when the fluid is assumed

density-preserving. In the latter case p is a quantity that has to be determined together with the other 'free' variables ρ_g, $\mathbf{U}_g$, h (or θ_g) and Y_α. The Stokes assumption and the small Mach number approximation is usually enforced in the description of combustion systems.

3.4.2 Influence of the Spray on the Gas Phase

The spray is influencing the gas phase in various ways. *First*, the relative motion between droplet and ambient gas and the finite size of a droplet lead to the formation of viscous boundary layers, separated flows and wakes that change the velocity field of the gas flow. *Second*, the evaporation of droplets results into a mass and heat transfer between droplets and gas. The *third* interaction is the heat conduction which, in a combustion chamber, leads to the cooling of the gas. For the accurate prediction of combustion processes the heat and mass transfer are important processes because they determine the behaviour of the chemical reaction in the flame.

To obtain the balance equations for the gas flow in the gas-droplet mixture, the suppositions in Section 3.3.2 are enforced. This allows the derivation of the equations for

$$\text{mass:} \qquad \frac{\partial \bar{\rho}_g}{\partial t} + \nabla_{\mathbf{x}} \cdot (\bar{\rho}_g \mathbf{U}_g) = \bar{\pi}_m \ , \tag{3.69}$$

$$\text{momentum:} \qquad \frac{\partial \bar{\rho}_g \mathbf{U}_g}{\partial t} + \nabla_{\mathbf{x}} \cdot (\bar{\rho}_g \mathbf{U}_g \otimes \mathbf{U}_g) = -\nabla_{\mathbf{x}}(\bar{p}) + \nabla_{\mathbf{x}} \cdot \bar{\mathbf{T}}^{\mathrm{E}} + \bar{\rho}_g g \mathbf{e}_g + \bar{\boldsymbol{\pi}}_v \ , \tag{3.70}$$

$$\text{energy:} \qquad \frac{\partial \bar{\rho}_g h_g}{\partial t} + \nabla_{\mathbf{x}} \cdot (\bar{\rho}_g h_g \mathbf{U}_g) = \bar{T}_{ij} \frac{\partial U_{gi}}{\partial x_j} + \frac{\partial \bar{p}}{\partial t} + \mathbf{U}_g \cdot \nabla_{\mathbf{x}} \bar{p} - \nabla_{\mathbf{x}} \bar{\mathbf{q}} + \bar{\rho}_g \mathfrak{r} + \bar{\boldsymbol{\pi}}_h \ , \tag{3.71}$$

$$\text{concentration:} \qquad \frac{\partial \bar{\rho}_g Y_\alpha}{\partial t} + \nabla_{\mathbf{x}} \cdot (\bar{\rho}_g Y_\alpha \mathbf{U}_g) = -\nabla_{\mathbf{x}} \cdot \bar{\mathbf{J}}_\alpha + \bar{\Pi}_\alpha + \bar{\boldsymbol{\pi}}_Y \delta_{\alpha,\mathrm{fuel}} \ , \tag{3.72}$$

where $\bar{\pi}_m$, $\bar{\boldsymbol{\pi}}_v$, $\bar{\boldsymbol{\pi}}_h$ and $\bar{\boldsymbol{\pi}}_Y \delta_{\alpha,\mathrm{fuel}}$ are partial interaction production rate densities for the mass, momentum, energy and concentration, respectively. They follow from the interaction with the droplet phase. The evaporation of droplets results only in the change of the fuel vapour concentration, explaining the Kronecker delta $\delta_{\alpha,\mathrm{fuel}}$ in (3.72). The bars in the representations for the production rates and in $\bar{\rho}_g$, $\bar{p}$, $\bar{\mathbf{T}}^{\mathrm{E}}$, $\bar{\mathbf{q}}$, $\bar{\mathbf{J}}_\alpha$ and $\bar{\Pi}_\alpha$ reflect the partial character of these quantities. They are not defined with respect to the volume of the gas phase but with respect to the volume of the entire mixture, including the volume of the dispersed phase. The partial and true densities of a general gas quantity, $\boldsymbol{\phi}$, are related by

$$\bar{\boldsymbol{\phi}} = \nu_g \boldsymbol{\phi} \ , \tag{3.73}$$

where ν_g is the volume fraction of the gas phase. The gas volume fraction is an additional field that requires an additional balance equation. In most combustion applications the gas volume fraction is set equal to one because some distance away from the nozzle the volume fraction of the droplets is assumed to be small ($< 1.0.e{-}4$). Using this assumption, equations (3.69) to (3.72) turn into equations (3.51) to (3.54) with additional production

terms for the mass, momentum, energy and concentration. Models for these terms depend on the method that is used for the dispersed phase. It should be noted that the coupling between droplet and gas phase is done on an Eulerian level. Consequently, the EL method requires an averaging procedure that delivers the production terms for equations (3.69) to (3.72). The concept of EE does not require this kind of averaging because the production terms in the balance equations for the gas are the negative production terms in the equations for the dispersed phase. Hence, the coupling of the two phases does not require any additional coupling procedure.

Chapter 4

A New Moment Method for Polydisperse Sprays

4.1 Introduction

The objective of this work is to derive, verify, validate and apply a new moment method. This method is based on the numerical solution of moment transport equations deduced from the kinetic spray equation (3.26). In Chapter 3 the latter equation was ascertained to be the right choice for modelling spray combustion. It was also observed that currently there is no Euler method available that can solve the kinetic spray equation (3.26) in its full complexity. A new moment method is presented here that combines the advantages of the quadrature-based method of moments (QBMoM) [39, 56, 58, 99] with those of the sectional method (SM) [41, 44, 63, 96, 97]. The resulting Eulerian moment method is able to describe the polydisperse nature of sprays (evaporation, drag, splashing) and the coexistence of two or more droplet velocities at one location. The new method, dubbed the quadrature-based sectional method (QBSM), agrees with the moment methods presented in Chapter 3 in that it is based on moment transport equations and that these equations have to be closed. Here, a new and more general approximate NDF is proposed that reduces to the approximations of Dufour and Villedieu [44] and Fox [56] or Le Lostec et al. [99] when special sets of parameters are chosen.

The starting point of the derivations is the dimensionless kinetic spray equation (see (3.26))

$$\frac{\partial}{\partial t}(f) + \nabla_{\mathbf{x}} \cdot (\mathbf{v}f) + \nabla_{\mathbf{v}} \cdot \left\{ \left(\frac{\mathbf{U}_g - \mathbf{v}}{\mathrm{St}} + \frac{1}{\mathrm{Fr}} \mathbf{e_g} \right) f \right\} - \frac{\partial}{\partial s} (\mathrm{Ev} f) + \frac{\partial}{\partial \theta} (\mathrm{He} f) = \Gamma + \mathcal{Q} \ , \tag{4.1}$$

in which the physical models for the drag force, evaporation, heat transfer, collision and breakup are assumed to be given. In other words, the functions $\mathrm{St}(\mathbf{v}, s)$, $\mathrm{Ev}(\mathbf{v}, s, \theta)$, $\mathrm{He}(\mathbf{v}, s, \theta)$, $\Gamma(\mathbf{v}, s)$ and $\mathcal{Q}(\mathbf{v}, s)$ are considered as known. On this level of complexity the NDF is a function of the independent variables $(\mathbf{x}, t, \mathbf{v}, s, \theta)$. Only in some highly

restrictive configurations (see Appendix A) can equation (4.1) be solved analytically. The main difficulties that prevent the analytical treatment of equation (4.1) are:

(i) the large number of independent variables,

(ii) the highly nonlinear physical models (see Chapter 2).

Numerical treatment of equation (4.1) is not straight forward either but allows negotiation of difficulties in (i) and (ii) given certain limiting transformations and assumptions on the NDF.

In Section 4.2, equation (4.1) is transformed into a system of moment transport equations in which the moments of the NDF depend on position and time only. The price for the reduction of independent variables is the loss of information on the physical processes contained in the kinetic spray equation. Nevertheless, it will be shown in Chapter 6 that the more moments of the NDF are transported and controlled, the more physical spray phenomena can be described. Unfortunately, the number of transported moments is limited by the available computer resources. The desired accuracy of the spray description and the complexity of the application determines the number of transported moments and, with them, the computational effort that needs to be spend. In this work the intention is not to solve for a large number of moments or even to reconstruct the NDF from the moments. It is instead assumed that knowledge of a limited amount of moments is sufficient to draw conclusions for engineering applications or to compare with other simulations or experiments. It was shown in Section 3.4.2 that the coupling between the gas and the liquid phase is accomplished on an Eulerian level, i.e. in a frame which couples selected lower-order moments of the NDF with gas phase quantities. In Section 4.3 the transport equations for a general moment are closed by approximating the NDF in a way that is special to sprays. An explicit set of transported moments is chosen. The formulae to determine the unknown parameters of the new approximate NDF from the chosen moments are the subject of Section 4.4. The calculation of these parameters is structured in sectional and quadrature parts. The algorithm for the sectional part is similar to that of Dufour and Villedieu [44]. The quadrature part (Section 4.4.2) of the QBSM is explained for one and two dimensions in real space. The approaches of Desjardins et al. [39], Fox [56, 58] and Le Lostec et al. [99] agree with one another in one dimension. In two dimensions they differ in the way the weights and abscissas are approximated. As the new method can be based on either of these methods, a combination of the approaches from Fox [56] and Le Lostec et al. [99] is employed. The approach of Fox [56] is illustrated in detail below. As the method from Le Lostec et al. [99] was provided by the authors of reference [99] it is not explained here. The reader is referred to the original paper. In Section 4.5 the general kinetic spray equation (3.26) and the corresponding moment transport equations are explictly specified, by choosing expressions for the physical spray models. Finally, the closed moment transport equations will be summarised.

4.2 Moment Transport Equations

The transformation of the kinetic spray equation into moment transport equations can be split into the commutative moment transformations with respect to the velocity, temperature and surface variables. In general, this transformation, called moment transform,

consists of two mathematical operations that are applied consecutively to a PDE. First, the PDE is multiplied by the desired powers of the independent variables and then, the emerging equations are integrated over restricted or unrestricted domains in which the variables are defined. The integration is an irreversible operation, but allows the reduction of the independent variables.[1]

4.2.1 Moment Transform in Velocity and Temperature Space

The general moment for the velocity and temperature variables is defined by

$$\mathrm{M}_{lmn}^{L,M}(\mathbf{x},t;s) := \int_{\mathbb{R}_+}\int_{\mathbb{R}^d} \theta^L v_l v_m v_n f(\mathbf{x},t;\mathbf{v},s,\theta)\, d\mathbf{v}d\theta \ , \tag{4.2}$$

where L and M represent the order of the moment for the temperature and velocity variables, respectively. In addition, M agrees with the number of velocity indices. The moment transform of the kinetic spray equation (4.1) for the temperature and velocity variable yields the following expression

$$\begin{aligned}
&\frac{\partial}{\partial t}(\mathrm{M}_{lmn}^{L,M}) + \frac{\partial}{\partial x_i}(\mathrm{M}_{lmni}^{L,M+1}) \\
&\quad + \int_{\mathbb{R}_+}\int_{\mathbb{R}^d} \theta^L v_l v_m v_n \frac{\partial}{\partial v_i}\left\{\left(\frac{\mathbf{U}_{gi}-v_i}{\mathrm{St}(\mathbf{v},\mathrm{s})} + \frac{1}{\mathrm{Fr}}\mathbf{e}_\mathbf{g}\cdot\mathbf{e}_i\right) f\right\} d\mathbf{v}d\theta \\
&\quad - \int_{\mathbb{R}_+}\int_{\mathbb{R}^d} \frac{\partial}{\partial s}\left(\mathrm{Ev}(\mathbf{v},s,\theta)\theta^L v_l v_m v_n f\right) d\mathbf{v}d\theta \\
&\quad + \int_{\mathbb{R}_+}\int_{\mathbb{R}^d} \theta^L \frac{\partial}{\partial \theta}\left(\mathrm{He}(\mathbf{v},s,\theta) v_l v_m v_n f\right) d\mathbf{v}d\theta = \int_{\mathbb{R}_+}\int_{\mathbb{R}^d} \theta^L v_l v_m v_n \left(\Gamma + \mathcal{Q}\right) d\mathbf{v}d\theta \ .
\end{aligned} \tag{4.3}$$

Notice that

(i) the system of moment transport equations following from (4.3) is unclosed because an expression for the moment $\mathrm{M}_{lmni}^{L,M+1}$ in the equation for the highest velocity moment is missing,

(ii) the integrals in equation (4.3) cannot be evaluated because of the nonlinearities in the physical models (see Chapter 2) and the generality of $f(\mathbf{x},t;\mathbf{v},s,\theta)$,

(iii) the nonlinearities in the physical models also prevent a formulation of the integrals as explicit functions of the transported moments,

(iv) if it were somehow possible to close the above system and evaluate the integrals one would still be confronted with balance equations that exhibit five degrees of freedom. This problem could not be treated with the numerical methods known for CFD. For these methods all fields have to be functions of position and time only.

[1] The moment transform can also be regarded as an averaging or filtering process of a PDE.

(v) In this work, the gas velocity, $\mathbf{U}_g(\mathbf{x},t)$, is assumed to be supplied by some analytical or numerical solution of the gas flow.

The last integral on the left-hand side of equation (4.3) is written as

$$\begin{aligned}&\int_{\mathbb{R}_+}\int_{\mathbb{R}^d}\theta^L\frac{\partial}{\partial\theta}\left(\mathrm{He}(\mathbf{v},s,\theta)v_lv_mv_nf\right)d\mathbf{v}d\theta\\&\quad=\int_{\mathbb{R}^d}\left[\theta^L\mathrm{He}(\mathbf{v},s,\theta)v_lv_mv_nf\right]_{\theta=0}^{+\infty}d\mathbf{v}-L\int_{\mathbb{R}_+}\int_{\mathbb{R}^d}\theta^{L-1}\mathrm{He}(\mathbf{v},s,\theta)v_lv_mv_nf\,d\mathbf{v}d\theta\ .\end{aligned}\tag{4.4}$$

Assuming that no droplet has temperatures $\theta=0$ and $\theta=+\infty$, the first integral on the right-hand side of (4.4) can be discarded and equation (4.3) turns into

$$\begin{aligned}&\frac{\partial}{\partial t}(\mathrm{M}^{L,M}_{lmn})+\frac{\partial}{\partial x_i}(\mathrm{M}^{L,M+1}_{lmni})\\&\quad+\int_{\mathbb{R}_+}\int_{\mathbb{R}^d}\theta^Lv_lv_mv_n\frac{\partial}{\partial v_i}\left\{\left(\frac{\mathbf{U}_{gi}-v_i}{\mathrm{St}(\mathbf{v},\mathrm{s})}+\frac{1}{\mathrm{Fr}}\mathbf{e_g}\cdot\mathbf{e}_i\right)f\right\}d\mathbf{v}d\theta\\&\quad-\int_{\mathbb{R}_+}\int_{\mathbb{R}^d}\frac{\partial}{\partial s}\left(\mathrm{Ev}(\mathbf{v},s,\theta)\theta^Lv_lv_mv_nf\right)d\mathbf{v}d\theta\\&\quad-L\int_{\mathbb{R}_+}\int_{\mathbb{R}^d}\theta^{L-1}\mathrm{He}(\mathbf{v},s,\theta)v_lv_mv_nf\,d\mathbf{v}d\theta=\int_{\mathbb{R}_+}\int_{\mathbb{R}^d}\theta^Lv_lv_mv_n\left(\Gamma+\mathcal{Q}\right)d\mathbf{v}d\theta\ .\end{aligned}\tag{4.5}$$

Similar arguments will be applied to the third and fourth term on the left-hand side of equation (4.5), but only later when the set of transported moments has been specified (Section 4.5).

4.2.2 Moment Transform in Size Space

To transform equation (4.5) into a form that exhibits the independent variables, position and time only, another moment transform for the surface variable, s, has to be performed. In contrast to the moment transforms in the previous section, a more subtle transform is chosen which maintains the information on the polydisperse character of the spray. To this end, and similar to Dufour and Villedieu [44], Laurent and Massot [96] and Laurent et al. [97], the surface space $[0,+\infty)$ is split into (N_s+1) fixed intervals, $I_k=[s_k,\,s_{k+1})$ $(k=1,\ldots,N_s)$ and $I_{N_s+1}=[s_{N_s+1},\,+\infty)$ with $s_{N_s+1}=1$, called sections. The infinite section I_{N_s+1} is necessary when droplets are created that exceed the size of the largest initial droplet (here $s=1$), due to coalescence. With this discretisation of the surface space, the moment transform can be performed for each section independently. In doing so, every section I_k $(k=1,\ldots,N_s+1)$ is equipped with moments of the form[2]

$$\mathrm{M}^{K,L,M}_{k;lmn}(\mathbf{x},t):=\int_{s_k}^{s_{k+1}}\int_{\mathbb{R}_+}\int_{\mathbb{R}^d}s^K\theta^Lv_lv_mv_nf(\mathbf{x},t;\mathbf{v},s,\theta)d\mathbf{v}\,d\theta\,ds\ ,\tag{4.6}$$

[2]The semicolon in the lower index of the moment (4.6) should not be confused with the short notation of derivatives which is commonly used in continuum mechanics (cf. [151]). Here, the semicolon separates subscript k of the section I_k from subscripts l,m,n of the velocity components v_l, v_m and v_n.

where K is the order of the moment for the surface variable and k is the section index. Notice that the overall number of moments is increased by a factor of $(N_s + 1)$ when introducing sections in surface space.[3]

Equation (4.5) is then multiplied by s^K and integrated from s_k to s_{k+1} for all sections I_k $(k = 1, \ldots, N_s + 1)$, which yields

$$\begin{aligned}
&\frac{\partial}{\partial t}(\mathrm{M}^{K,L,M}_{k;lmn}) + \frac{\partial}{\partial x_i}(\mathrm{M}^{K,L,M+1}_{k;lmni}) \\
&\quad + \int_{s_k}^{s_{k+1}} \int_{\mathbb{R}_+} \int_{\mathbb{R}^d} s^K \theta^L v_l v_m v_n \frac{\partial}{\partial v_i} \left\{ \left(\frac{\mathbf{U}_{gi} - v_i}{\mathrm{St}(\mathbf{v}, \mathrm{s})} + \frac{1}{\mathrm{Fr}} \mathbf{e_g} \cdot \mathbf{e}_i \right) f \right\} d\mathbf{v} d\theta ds \\
&\quad - \int_{s_k}^{s_{k+1}} \int_{\mathbb{R}_+} \int_{\mathbb{R}^d} s^K \frac{\partial}{\partial s} \left(\mathrm{Ev}(\mathbf{v}, s, \theta) \theta^L v_l v_m v_n f \right) d\mathbf{v} d\theta ds \\
&\quad - L \int_{s_k}^{s_{k+1}} \int_{\mathbb{R}_+} \int_{\mathbb{R}^d} s^K \theta^{L-1} \mathrm{He}(\mathbf{v}, s, \theta) v_l v_m v_n f d\mathbf{v} d\theta ds \\
&\qquad = \int_{s_k}^{s_{k+1}} \int_{\mathbb{R}_+} \int_{\mathbb{R}^d} s^K \theta^L v_l v_m v_n \left(\Gamma + \mathcal{Q} \right) d\mathbf{v} d\theta ds \; .
\end{aligned} \tag{4.7}$$

With equation (4.7) the kinetic spray equation (4.1) is now reduced to a form in which all functions and integrals depend on position and time only. Hence, (iv) in Section 4.2.2 has been resolved, but not (i) to (iii). They are the subject of the following section.

4.3 Moment Closure

So far, only a general moment $\mathrm{M}^{K,L,M}_{k;lmn}$ and the corresponding unclosed moment transport equation (4.7) have been considered. The specification of the moments is strongly linked to the approximation of the NDF and vice versa. Therefore, in this section, the approximate NDF is introduced together with the set of transported moments. These two choices close the moment transport equations and all algorithms that are necessary for the QBSM unfold (see Section 4.4 and Chapter 5).

[3] In Chapter 6 it is shown that a reasonable N_s is between 5 and 10.

4.3.1 Approximation of the Number Density Function

In the remainder of this work the NDF is approximated by

$$f(\mathbf{x},t;\mathbf{v},s,\theta) \approx \tilde{f}(\mathbf{x},t;\mathbf{v},s,\theta)$$

$$= \sum_{k=1}^{N_s+1} \mathbb{1}_{s_k\le s<s_{k+1}} \exp\left(-b_k(\mathbf{x},t)s\right) \delta\left(\theta-\Theta_k(\mathbf{x},t)\right) \sum_{\alpha=1}^{\beta} n_k^\alpha(\mathbf{x},t)\boldsymbol{\delta}[\mathbf{v}-\mathbf{U}_k^\alpha(\mathbf{x},t)], \quad (4.8)$$

with the requirement

$$b_{N_s+1}(\mathbf{x},t) \ge 0 \quad (4.9)$$

and the definition

$$\boldsymbol{\delta}[\mathbf{v}-\mathbf{U}_k^\alpha(\mathbf{x},t)] = \prod_{i=1}^{d} \delta\left(v_i - U_{k;i}^\alpha(\mathbf{x},t)\right). \quad (4.10)$$

In the above formulae $d \in [1,2,3]$ denotes the number of real space dimensions, whereas β is the number of quadrature nodes in velocity space. Here, each velocity space direction will be represented by two nodes, so $\beta = 2^d$.[4] Now, let

$$\mathcal{W}_k^\beta = [b_k, \Theta_k, (n_k^\alpha, \mathbf{U}_k^\alpha)], \qquad \text{with} \quad k=1,\dots,N_s+1 \quad \text{and} \quad \alpha=1,\dots,\beta \quad (4.11)$$

denoting the set of $(2+(1+d)\beta)(N_s+1)$ currently unknown parameters, where $(n_k^\alpha, \mathbf{U}_k^\alpha)$ are called the quadrature parameters of node α in section I_k, with weight n_k^α and velocity abscissa $\mathbf{U}_k^\alpha$. Θ_k represents the temperature abscissa in section I_k and b_k is the parameter that defines the shape of the exponential function in section I_k. These unknowns are related to the set of transported moments (see Section 4.3.2).

The method following from (4.8) is regarded as a generalisation of the SM introduced by Domelevo [41], Gelbard et al. [63], Laurent and Massot [96], Laurent et al. [97] – more precisely, its variant proposed by Dufour and Villedieu [44] – and the QBMoM recently introduced by Fox [56] and Le Lostec et al. [99]. In the case of $N_s = 0$, $\beta > 1$, disregarding surface and temperature variables and the identification of $n_1^\alpha(\mathbf{x},t)$ with $w^\alpha(\mathbf{x},t)$, the quadrature approximation (3.36) is recovered from approximation (4.8). Conversely, for the case of $N_s > 0$, $\beta = 1$ the approximate NDF turns into that proposed by Dufour and Villedieu [44] (see relation (3.43)).

The quadrature part of approximation (4.8) allows the description of locally bi-modal (or multi-modal) velocity distributions, i.e. with (4.8) the collision-less crossing of two (or more) droplet distributions of different velocity scale and direction but same droplet size can be captured. In Chapter 2 various situations were illustrated in which crossing of spray distributions, here called particle trajectory crossing (PTC), is relevant. In all of these situations the NDF cannot be described with an equilibrium (also called Maxwellian) distribution

$$f_{eq}^k(\mathbf{v}) = \frac{\mathrm{M}_k^{0,0,0}}{(2\pi\sigma_{eq}^k)^{d/2}} \exp\left(-\frac{|\mathbf{v}-\mathbf{U}_k^p|^2}{2\sigma_{eq}^k}\right), \quad (4.12)$$

[4] Fox [58] showed very recently that the nodes in each velocity space direction can be increased to values larger than two. In this case the distribution in velocity space can be captured more accurately, i.e. bi-modal and tri- or multi-modal velocity distribution functions can be described. Distributions of this kind are present when the droplet Knudsen number is near one and the droplets collide, coalesce or break [58].

with mean $\mathbf{U}_k^p$ and variance σ_{eq}^k, known from kinetic gas theory (cf. [24, 26, 172]). This type of velocity distribution function is observed in flows where the droplet Knudsen number is very small, i.e. collision of droplets is ubiquitous. In this work, however, the dilute spray is not dominated by collisions (Kn_d is large) so the rare events of collision do not shape the velocity distribution function according to f_{eq}^k. Hence, it would be misleading to approximate the velocity part of the NDF with the equilibrium distribution (4.12). From this point of view, approximation (4.8) is regarded as a non-equilibrium distribution function.

Another issue that is central to the simulation of spray combustion is the accurate description of the mass transfer from the liquid to the gaseous fuel. The chemical reaction in the flame is determined by the mass ratio between vapour fuel and oxidiser which is strongly related to the evaporation process of the dispersed droplets. In Chapter 3 it was demonstrated that the kinetic spray equation is a reasonable mathematical model for spray combustion. If, in addition, an accurate evaporation model is chosen, then the local mass of droplets must not be distorted by strong artificial assumptions in the moment transform and the closure of the moment transport equations. By introducing an exponential function in s (see (4.8)) for each section I_k, additional degrees of freedom, b_k ($k = 1, \ldots, N_s+1$), are available that allow the control of the droplet mass. The unknown parameter b_k will later be related to the moment ratio $\mathrm{M}_k^{3/2,0,0}/\mathrm{M}_k^{0,0,0}$, which is proportional to the ratio of mass and number of droplets in section I_k. The exponential function guarantees that the number and mass of droplets are always positive, irrespective of the sign of b_k.[5] Besides the convincing mathematical arguments for this choice, experiments [98] confirm the exponential shape in the tail of the droplet distribution.

Assuming the parameters in the approximate NDF (4.8) to be known, then the substitution of $\tilde{f}(\mathbf{x}, t; \mathbf{v}, s, \theta)$ into the integrals of the moment transport equation (4.7) and into the spatial flux $\mathrm{M}_{k;lmni}^{K,L,M+1}$ of that equation yields a relation that contains no unknown terms, i.e. equation (4.7) is closed. The exact expressions for the moment equations are given in Section 4.5.2.

4.3.2 Choice of Moments

For the selection of an appropriate set of moments, it is advantageous to relate some of the moments, $\mathrm{M}_{k;lmn}^{K,L,M}$ defined in (4.6), to real physical fields. The number density of droplets, $n(\mathbf{x}, t)$ [m^{-3}] in section I_k is, by definition of the NDF, proportional to the zeroth-order moment $\mathrm{M}_k^{0,0,0}$ [-]. The mass density of droplets, $M_k(\mathbf{x}, t)$ [$\mathrm{kg\,m}^{-3}$], is defined by the relation

$$M_k(\mathbf{x}, t) := M_{\mathrm{char}} \int_{s_k}^{s_{k+1}} \int_{\mathbb{R}_+} \int_{\mathbb{R}^d} s^{3/2} f(\mathbf{x}, t; \mathbf{v}, s, \theta) d\mathbf{v}\, d\theta\, ds = M_{\mathrm{char}} \mathrm{M}_k^{3/2,0,0}(\mathbf{x}, t) \ , \qquad (4.13)$$

where the moment $\mathrm{M}_k^{3/2,0,0}$ [-] represents the dimensionless volume of droplets in section I_k and M_{char} [$\mathrm{kg\,m}^{-3}$] is the mass density of droplets with surface S_{char} [m^2] in the gas

[5] This proposition follows from the non-negative character of the integrands $[s^K \exp(-b_k s) f(\cdots)]$, $(K = 3/2, 0)$ in the definition of the moments $\mathrm{M}_k^{0,0,0}$ and $\mathrm{M}_k^{3/2,0,0}$ in (4.6).

flow with characteristic length scale X_{char} [m], i.e.

$$M_{\text{char}} := \frac{\rho_\ell (S_{\text{char}})^{3/2}}{6\sqrt{\pi}(X_{\text{char}})^3} \ . \tag{4.14}$$

The mass density of the droplet liquid, ρ_ℓ, is assumed to be constant. The volume specific enthalpy H_k [J m^{-3}] in section I_k is defined by

$$\begin{aligned} H_k(\mathbf{x},t) :&= M_{\text{char}}\, c_p^d \int_{s_k}^{s_{k+1}} \int_{\mathbb{R}_+} \int_{\mathbb{R}^d} s^{3/2}\theta f(\mathbf{x},t;\mathbf{v},s,\theta) d\mathbf{v}\, d\theta\, ds + H_0 \\ &= M_{\text{char}}\, c_p^d \mathrm{M}_k^{3/2,1,0}(\mathbf{x},t) + H_0 \ , \end{aligned} \tag{4.15}$$

with the reference enthalpy H_0 [J m^{-3}] and the specific heat capacity of a droplet c_p^d [J kg^{-1}K^{-1}]. The enthalpy is defined as a volumetric quantity because $\mathrm{M}_k^{3/2,1,0}$ and not $\mathrm{M}_k^{0,1,0}$ is chosen below to be an element of the set of transported moments. In this definition the specific heat capacity is assumed to be independent of the droplet temperature, θ. Finally, the momentum, $\mathbf{Im}_k$ [kg m^{-2}s^{-1}], of the droplets in section I_k is introduced by

$$\begin{aligned} \mathbf{Im}_k(\mathbf{x},t) :&= M_{\text{char}} V_{\text{char}} \int_{s_k}^{s_{k+1}} \int_{\mathbb{R}_+} \int_{\mathbb{R}^d} s^{3/2}\mathbf{v} f(\mathbf{x},t;\mathbf{v},s,\theta) d\mathbf{v}\, d\theta\, ds \\ &= M_{\text{char}} V_{\text{char}} \mathbf{M}_k^{3/2,0,1}(\mathbf{x},t) \ . \end{aligned} \tag{4.16}$$

The above quantities of number, mass, enthalpy and momentum of droplets are mentioned for reasons of clarity. However, in the remainder of this work all equations, algorithms, results, etc. will be expressed in terms of dimensionless quantities.

In order to determine the $(2+(1+d)\beta)(N_s+1)$ parameters in the approximate NDF (4.8), at least $(2+(1+d)\beta)(N_s+1)$ moments have to be chosen from the infinite set of possible moments. This choice should prevent non-unique abscissas, negative weights [57] and should allow the unique determination of b_k. Obviously, the lower-order moments $\mathrm{M}_k^{0,0,0}$, $\mathrm{M}_k^{3/2,0,0}$, $\mathrm{M}_k^{3/2,1,0}$ and $\mathrm{M}_{k;i}^{3/2,0,1}$ must be elements of the set of chosen moments. Otherwise the number, mass, enthalpy and momentum in a section are not controlled (see equations (4.13) to (4.16)), i.e. it cannot be guaranteed that these moments agree with those moments of the exact NDF, within some assessable error. For the velocity dispersion, all velocity moments up to the third-order are considered as well. This ensures that all directions in velocity space are treated equally and that the different velocity directions are coupled. With these considerations in mind, the chosen set of independent moments is specified as

$$\begin{aligned} \mathcal{V}_k^d := &\left\{ \mathrm{M}_k^{0,0,0}, \mathrm{M}_k^{3/2,0,0}, \mathrm{M}_k^{3/2,1,0}, \mathrm{M}_{k;l}^{3/2,0,1}, \mathrm{M}_{k;lm}^{3/2,0,2}, \mathrm{M}_{k;lmn}^{3/2,0,3} \right\}, \\ &\text{with} \quad l,m,n = 1,\ldots,d \ , \quad l \le m \le n \quad \text{and} \quad k = 1,\ldots,N_s+1 \ , \end{aligned} \tag{4.17}$$

which are 6 independent moments for one real space dimension ($d = 1$), 12 moments for two dimensions ($d = 2$) and 22 moments for three dimensions ($d = 3$) in each of the $N_s + 1$ sections. In the case of one dimension and two nodes ($\beta = 2$), the number of moments is equal to the number of parameters. However, for two and three dimensions the number of parameters exceeds that of the moments if $\beta = 2^d$ is chosen. One way to resolve this discrepancy is the extension of the set of velocity moments to the fourth order. Fox [56, 57] showed that an optimal set of moments, including the fourth and fifth-order moments, can be found for the computation of the weights and velocity abscissas in $\mathcal{W}_k^\beta$ but, as mentioned in [56], this introduces the following additional issues: *First*, the weights and abscissas have to be found numerically by solving a nonlinear system of equations and *second*, the optimal set of moments also includes moments of order five. Fox [56] has implemented a nonlinear solver that is able to evaluate the weights and velocity abscissas in set $\mathcal{W}_k^\beta$ using an optimal set of moments. He reports that the nonlinear solver converged but not in all cases. The transport of these additional moments and the nonlinear solver increase the computational costs drastically. Having these considerations in mind, it is preferable, in the manner of Fox [56] and Le Lostec et al. [99], to reduce the number of independent quadrature parameters in (4.8) such that all moments in $\mathcal{V}_k^d$, except the third-order cross moments, are controlled. In Section 4.4.2 this issue will be discussed in more detail.[6]

The general assumptions that are tacitly made when considering approximation (4.8) and the set of moments (4.17) are:

(i) For a given droplet surface, at a given point $(\mathbf{x}, t)$ there is only one characteristic average temperature

$$\bar{\theta}(\mathbf{x}, t; s) := \frac{\int_{\mathbb{R}^3} \int_{\mathbb{R}_+} \theta f(\mathbf{x}, t; \mathbf{v}, s, \theta)\, d\theta\, d\mathbf{v}}{\int_{\mathbb{R}^3} \int_{\mathbb{R}_+} f(\mathbf{x}, t; \mathbf{v}, s, \theta)\, d\theta\, d\mathbf{v}} \ . \tag{4.18}$$

The temperature dispersion around the average temperature $\bar{\theta}(\mathbf{x}, t; s)$ is zero in all directions, regardless of the point $(\mathbf{x}, t, s)$. This implies that all droplets in one section have the same temperature, i.e.

$$\bar{\theta}(\mathbf{x}, t; s) = \Theta_k(\mathbf{x}, t) \quad \text{for } s_k \leq s < s_{k+1} \ . \tag{4.19}$$

(ii) For a given droplet surface, at a given point $(\mathbf{x}, t)$, all velocity moments up to the third-order, i.e. (see (4.2))

$$\begin{gathered} \mathrm{M}_{lmn}^{0,M}(\mathbf{x}, t; s) = \int_{\mathbb{R}_+} \int_{\mathbb{R}^d} v_l v_m v_n f(\mathbf{x}, t; \mathbf{v}, s, \theta)\, d\mathbf{v} d\theta \ , \\ \text{with} \quad l, m, n = 1, \ldots, d \ , \quad l \leq m \leq n \quad \text{and} \quad M = 1, 2, 3 \ , \end{gathered} \tag{4.20}$$

fully characterise the spray behaviour in velocity space.

[6] Desjardins et al. [39] reduce the set of quadrature parameters as well, but in addition to the third-order cross moments, the second-order cross moments are not controlled either.

(iii) The number density of droplets for a given droplet surface at a given point $(\mathbf{x}, t)$, defined as

$$n(\mathbf{x}, t; s) := \int_{\mathbb{R}^3} \int_{\mathbb{R}_+} f(\mathbf{x}, t; \mathbf{v}, s, \theta)\, d\theta\, d\mathbf{v} \ , \tag{4.21}$$

decreases exponentially with the surface variable going to infinity. This assumption is justified by the experiments of Laurent et al. [98] and permits the assumption $b_{N_s+1} > 0$ (see (4.9)).

4.4 Computation of the Exponential and Quadrature Parameters

The key component of the combined moment method is the algorithm that computes the unknown parameters in set $\mathcal{W}_k^\beta$ (4.11) from the set $\mathcal{V}_k^d$ (4.17) of known moments. To this end, the relation

$$\mathrm{M}_{k;lmn}^{K,L,M}(\mathbf{x}, t) = \Theta_k^L(\mathbf{x}, t) \sum_{\alpha=1}^{\beta} n_k^\alpha(\mathbf{x}, t) \left[(U_l)_k^\alpha (U_m)_k^\alpha (U_n)_k^\alpha\right](\mathbf{x}, t) \int_{s_k}^{s_{k+1}} s^K \exp\left(-b_k(\mathbf{x}, t) s\right) ds \tag{4.22}$$

is used, which follows from the substitution of the approximate NDF (4.8) into the definition of the general moment $\mathrm{M}_{k;lmn}^{K,L,M}$ (4.6). The right-hand side of relation (4.22) is, in general, nonlinear and therefore it is not obvious that the unknown parameters of $\tilde{f}$ in $\mathcal{W}_k^\beta$ can be uniquely determined from the moments in set $\mathcal{V}_k^d$ which are known from a previous time step, an initial or boundary condition.

In Section 4.3 the moments were chosen such that the parameter b_k can be calculated prior to the rest of the unknown parameters. The unique determination of b_k is the subject of Section 4.4.1. The weights and abscissas for the temperature and velocity variable are dealt with in Section 4.4.2.

4.4.1 The Exponential Parameters

As previously mentioned the evolution of the surface of droplets is captured by discretising the surface space $[0, +\infty)$ into $(N_s + 1)$ fixed sections, $I_k = [s_k, s_{k+1})$ $(k = 1, \ldots, N_s)$ and $I_{N_s+1} = [s_{N_s+1}, +\infty)$ with $s_{N_s+1} = 1$ and approximating the surface distribution of droplets by a piecewise exponential function of the form

$$\tilde{f}(\mathbf{x}, t; \mathbf{v}, \theta, s) = \sum_{k=1}^{N_s+1} \mathbb{1}_{s_k \le s < s_{k+1}} a_k(\mathbf{x}, t, \mathbf{v}, \theta) \exp(-b_k s), \qquad s_k \le s < s_{k+1} \ . \tag{4.23}$$

In its pure form (a_k is no function of $\mathbf{v}$ and θ) this approach was developed by Dufour and Villedieu [44]. The propositions and proofs that are outlined in this section are similar to those of Dufour [43]. The determination of b_k is based on the following proposition:

Proposition 1. *Let I_k be an interval (finite or not) in surface space $[0, +\infty)$ and $f(\mathbf{x}, t; \mathbf{v}, \theta, s)$ a positive function on this interval with moments $\mathrm{M}_k^{0,0,0}$ and $\mathrm{M}_k^{3/2,0,0}$ defined in*

(4.6). Then, in this interval there exists a unique value $b_k \in \mathbb{R}$ *such that the function* $\tilde{f}$*, as defined in (4.23), has the same moment ratio*

$$\begin{aligned} g_{I_k}(b_k) :&= \frac{\int_{I_k}\int_{\mathbb{R}_+}\int_{\mathbb{R}^d} s^{3/2}\tilde{f}\,d\mathbf{v}d\theta ds}{\int_{I_k}\int_{\mathbb{R}_+}\int_{\mathbb{R}^d}\tilde{f}\,d\mathbf{v}d\theta ds} \\ &= \frac{\int_{I_k}\int_{\mathbb{R}_+}\int_{\mathbb{R}^d} s^{3/2}\exp(-b_k s)d\mathbf{v}d\theta ds}{\int_{I_k}\int_{\mathbb{R}_+}\int_{\mathbb{R}^d}\exp(-b_k s)d\mathbf{v}d\theta ds} =: \frac{\tilde{\mathrm{M}}_k^{3/2,0,0}}{\tilde{\mathrm{M}}_k^{0,0,0}} \end{aligned} \tag{4.24}$$

as function f*. In the infinite interval the parameter* b_k *is strictly positive. Therefore, it is possible to define a bijective function,* Ψ_k*, such that*

$$b_k = \Psi_k\left(\frac{\mathrm{M}_k^{3/2,0,0}}{\mathrm{M}_k^{0,0,0}}\right). \tag{4.25}$$

For the proof of this proposition see Appendix B. In the proof the following properties are shown:

(i) The function $g_{I_k}(b_k)$ is strictly decreasing and invertible on the interval I_k.

(ii) It exhibits the limits

$$\lim_{b_k\to-\infty} g_{I_k}(b_k) = (s_{k+1})^{3/2} \quad \text{and} \quad \lim_{b_k\to+\infty} g_{I_k}(b_k) = (s_k)^{3/2}\ . \tag{4.26}$$

(iii) In the infinite section I_{N_s+1}, where b_{N_s+1} is strictly positive, the relation

$$\lim_{b_k\to 0^+} g_{I_k}(b_k) = (s_{N_s+1})^{3/2} \tag{4.27}$$

holds true.

The strictly monotonic decay of $g_{I_k}(b_k)$ allows the unique solution of

$$\begin{aligned} g_I(b_k) = \frac{1}{1-e^{-b_k\Delta s}}\Bigg(& s_k^{3/2} - s_{k+1}^{3/2}e^{-b_k\Delta s} + \frac{3}{2b_k}(\sqrt{s_k} - \sqrt{s_{k+1}}e^{-b_k\Delta s}) \\ &+ \frac{3e^{-b_k s_k}}{2b_k}\int_{\sqrt{s_k}}^{\sqrt{s_{k+1}}} e^{-b_k r^2}dr\Bigg) \overset{!}{=} \frac{\mathrm{M}_k^{3/2,0,0}}{\mathrm{M}_k^{0,0,0}}\ , \end{aligned} \tag{4.28}$$

where $\mathrm{M}_k^{3/2,0,0}$ and $\mathrm{M}_k^{0,0,0}$ are known from a previous time-step, an initial or boundary condition. Due to the non-linear character of this equation, b_k cannot be found analytically. In this work, the root finder `DFZERO` of the SLATEC Common Mathematical Library [52] is used, which is based on the combination of the bisection method with the secant rule.

The limits of g_{I_k} for infinitely large and infinitely small values of b_k allows an flexible limitation of b_k. This is necessary because for very large (or very small) values of b_k– g_{I_k} is close to $(s_k)^{3/2}$ (or $(s_{k+1})^{3/2}$) – the (complex) error function on the left-hand side of equation (4.28) is difficult to evaluate with double precision accuracy. This situation is

observed when the NDF is discontinuous in surface space or a very small mass is present in a section. To prevent a large numerical error and the crash of the algorithm, a minimal and a maximal threshold, b_{min} and b_{max}, is introduced which can be translated into thresholds for the function $g_{I_k}(b_k)$, i.e.

$$(s_k)^{3/2} + \varepsilon_k^{max} \overset{!}{\leq} g_{I_k}(b_k) \overset{!}{\leq} (s_{k+1})^{3/2} - \varepsilon_k^{min} \ , \tag{4.29}$$

with

$$\varepsilon_k^{max} = g_{I_k}(b_{max}) - (s_k)^{3/2} \qquad \text{and} \qquad \varepsilon_k^{min} = (s_{k+1})^{3/2} - g_{I_k}(b_{min}) \ . \tag{4.30}$$

In case g_{I_k} is not within the interval $[(s_k)^{3/2} + \varepsilon_k^{max}, (s_{k+1})^{3/2} - \varepsilon_k^{min}]$ but still within $[(s_k)^{3/2}, (s_{k+1})^{3/2}]$, b_k is set to the minimal or maximal value and the moment $\mathrm{M}_k^{3/2,0,0}$ in one section is artificially modified, such that

$$\mathrm{M}_k^{3/2,0,0} = g_{I_k}(b_{max})\mathrm{M}_k^{0,0,0} \qquad \text{or} \qquad \mathrm{M}_k^{3/2,0,0} = g_{I_k}(b_{min})\mathrm{M}_k^{0,0,0} \tag{4.31}$$

is satisfied. The computation of the thresholds ε_k^{min} and ε_k^{max} can be conducted in a preprocessing step.

It is observed that b_k is obtained from $\mathrm{M}_k^{3/2,0,0}$ and $\mathrm{M}_k^{0,0,0}$ independently of the other moments in the set $\mathcal{V}_k^d$. The weights, n_k^α, velocity abscissas $\mathbf{U}_k^\alpha$ and the temperature Θ_k do not arise in these equations. Therefore, b_k can be uniquely determined prior to the temperature abscissas and quadrature parameters.

4.4.2 The Quadrature Parameters

The determination of the weights and abscissas in each section I_k, $(k = 1, \ldots, N_s + 1)$ is now based on the set of moments

$$\begin{gathered} \mathcal{V}_d^+ = \left\{ \mathrm{M}_k^{3/2,0,0}, \mathrm{M}_k^{3/2,1,0}, \mathrm{M}_{k;l}^{3/2,0,1}, \mathrm{M}_{k;lm}^{3/2,0,2}, \mathrm{M}_{k;lmn}^{3/2,0,3} \right\}, \\ \text{with} \quad l,m,n = 1,\ldots,d \ , \qquad l \leq m \leq n \ , \end{gathered} \tag{4.32}$$

where, in comparison with $\mathcal{V}_k^d$ in (4.17), $\mathcal{V}_d^+$ has been reduced by the zeroth-order moment $\mathrm{M}_k^{0,0,0}$. The information contained in this moment was previously used and passed into the exponential parameter b_k.

The unknown weights and abscissas are computed from relation (4.22) using the moments in $\mathcal{V}_d^+$ and the now known parameter b_k. Taking into account the fact that $[\int_{s_k}^{s_{k+1}} s^K \exp(-b_k(\mathbf{x},t)s)\, ds]$ is always positive for $0 \leq s_k < s_{k+1}$ and $K \geq 0$, then the modified moment

$$\begin{aligned} \bar{\mathrm{M}}_{k;lmn}^{K,L,M}(\mathbf{x},t) :&= \frac{\mathrm{M}_{k;lmn}^{K,L,M}(\mathbf{x},t)}{\int_{s_k}^{s_{k+1}} s^K \exp(-b_k(\mathbf{x},t)s)\, ds} \\ &= \Theta_k^L(\mathbf{x},t) \sum_{\alpha=1}^{\beta} n_k^\alpha(\mathbf{x},t) \left[(U_l)_k^\alpha (U_m)_k^\alpha (U_n)_k^\alpha \right](\mathbf{x},t) \end{aligned} \tag{4.33}$$

is introduced. Notice that this moment does not include the parameter b_k; hence, for each section I_k $(k = 1, \ldots, N_s + 1)$ the quadrature parameters

$$\mathcal{W}_\beta^+ = [\Theta_k, (n_k^\alpha, \mathbf{U}_k^\alpha)], \quad \text{with} \quad \alpha = 1, \ldots, \beta, \quad k = 1, \ldots, N_s + 1 \tag{4.34}$$

can be computed from the set of known modified moments

$$\begin{aligned} \bar{\mathcal{V}}_d^+ &= \left\{ \bar{\mathrm{M}}_k^{3/2,0,0}, \bar{\mathrm{M}}_k^{3/2,1,0}, \bar{\mathrm{M}}_{k;l}^{3/2,0,1}, \bar{\mathrm{M}}_{k;lm}^{3/2,0,2}, \bar{\mathrm{M}}_{k;lmn}^{3/2,0,3} \right\}, \\ \text{with} \quad & l, m, n = 1, \ldots, d, \quad l \le m \le n, \quad k = 1, \ldots, N_s + 1 \ . \end{aligned} \tag{4.35}$$

In Section 4.3 it was assumed that in one section all droplets exhibit the same mean temperature and no dispersion around this mean is present. With this assumption the temperature abscissa is set equal to the mean temperature

$$\Theta_k = \frac{\bar{\mathrm{M}}_k^{3/2,1,0}}{\bar{\mathrm{M}}_k^{3/2,0,0}} \ . \tag{4.36}$$

The weights and velocity abscissas

$$\mathcal{W}_\beta^\dagger = [(n_k^\alpha, \mathbf{U}_k^\alpha)], \qquad \text{with} \quad \alpha = 1, \ldots, \beta \quad \text{and} \quad k = 1, \ldots, N_s + 1 \tag{4.37}$$

still need to be determined from the set of modified moments

$$\begin{aligned} \bar{\mathcal{V}}_d^\dagger &= \left\{ \bar{\mathrm{M}}_k^{3/2,0,0}, \bar{\mathrm{M}}_{k;l}^{3/2,0,1}, \bar{\mathrm{M}}_{k;lm}^{3/2,0,2}, \bar{\mathrm{M}}_{k;lmn}^{3/2,0,3} \right\}, \\ \text{with} \quad & l, m, n = 1, \ldots, d \ , \qquad l \le m \le n \quad \text{and} \quad k = 1, \ldots, N_s + 1 \ . \end{aligned} \tag{4.38}$$

Although the number of nodes in each real space direction is the same (here, it is two), the extension from one to two and three dimensions is not trivial. In the sequel, the procedures for one [39] and two [56] real space dimensions are explained. Fox [56] extended this procedure to *three dimensions in real space* and to higher velocity moments [58] but these extensions where not implemented and not studied in this work.

In *one dimension in real space*, the relations between the moments in $\bar{\mathcal{V}}_1^\dagger$ and the parameters in $\mathcal{W}_2^\dagger$ are determined by (see relation (4.33))

$$\begin{aligned} \bar{\mathrm{M}}_k^{3/2,0,0} &= n_k^1 + n_k^2, & \bar{\mathrm{M}}_k^{3/2,0,1} &= n_k^1 U_k^1 + n_k^2 U_k^2, \\ \bar{\mathrm{M}}_k^{3/2,0,2} &= n_k^1 (U_k^1)^2 + n_k^2 (U_k^2)^2, & \bar{\mathrm{M}}_k^{3/2,0,3} &= n_k^1 (U_k^1)^3 + n_k^2 (U_k^2)^3 \ . \end{aligned} \tag{4.39}$$

From these relations it is not obvious that the parameters subsumed in $\mathcal{W}_2^\dagger$ can be uniquely determined by the moments in $\bar{\mathcal{V}}_1^\dagger$ because the right-hand sides of (4.39) are nonlinear. The uniqueness and the explicit formulation of the mapping $\bar{\mathcal{V}}_1^\dagger \to \mathcal{W}_2^\dagger$ is the subject of the following proposition:

Proposition 2. *Let* $\bar{\mathcal{V}}_1^\dagger$ *be the set of moments defined as*

$$\bar{\mathcal{V}}_1^\dagger = \left[\bar{\mathrm{M}}_k^{3/2,0,0}, \bar{\mathrm{M}}_k^{3/2,0,1}, \bar{\mathrm{M}}_k^{3/2,0,2}, \bar{\mathrm{M}}_k^{3/2,0,3} \right] \tag{4.40}$$

such that

$$(i)\ \bar{\mathrm{M}}_k^{3/2,0,0} > 0, \qquad (ii)\ \bar{\mathrm{M}}_k^{3/2,0,0}\bar{\mathrm{M}}_k^{3/2,0,2} \geqslant \left(\bar{\mathrm{M}}_k^{3/2,0,1}\right)^2 \ . \tag{4.41}$$

Then, up to a permutation between superscripts 1 and 2, there exists only one set $\mathcal{W}_2^\dagger$ *of parameters that satisfies the relations in (4.39). This solution is given by*

$$\begin{aligned} n_k^1 &= (\tfrac{1}{2} + x_k)\bar{\mathrm{M}}_k^{3/2,0,0} \ , & n_k^2 &= (\tfrac{1}{2} - x_k)\bar{\mathrm{M}}_k^{3/2,0,0} \ , \\ U_k^1 &= U_k^p - \left(\frac{n_k^2}{n_k^1}\right)^{1/2}\sigma_k^p \ , & U_k^2 &= U_k^p + \left(\frac{n_k^1}{n_k^2}\right)^{1/2}\sigma_k^p \ , \end{aligned} \tag{4.42}$$

$$x_k = \frac{q_k^p/2}{((q_k^p)^2 + 4(\sigma_k^p)^6)^{1/2}} \ .$$

The quantities U_k^p, σ_k^p *and* q_k^p *are defined by*

$$\begin{aligned} U_k^p &= \frac{\bar{\mathrm{M}}_k^{3/2,0,1}}{\bar{\mathrm{M}}_k^{3/2,0,0}} \ , \qquad \sigma_k^p = \left(\frac{\bar{\mathrm{M}}_k^{3/2,0,0}\bar{\mathrm{M}}_k^{3/2,0,2} - \left(\bar{\mathrm{M}}_k^{3/2,0,1}\right)^2}{\left(\bar{\mathrm{M}}_k^{3/2,0,0}\right)^2}\right)^{1/2} \ , \\ q_k^p &= \frac{1}{\bar{\mathrm{M}}_k^{3/2,0,0}}\left(\bar{\mathrm{M}}_k^{3/2,0,3} - \bar{\mathrm{M}}_k^{3/2,0,0}(U_k^p)^3 - 3\bar{\mathrm{M}}_k^{3/2,0,0}(\sigma_k^p)^2 U_k^p\right) \ . \end{aligned} \tag{4.43}$$

Equations (4.42) and (4.43) constitute the mapping $\bar{\mathcal{V}}_1^\dagger \rightarrow \mathcal{W}_2^\dagger$.

The proof to this proposition can be found in Appendix C. Note that U_k^p can be interpreted as mean velocity of droplets in one section and $(\sigma_k^p)^2$ as the velocity variance of the NDF. Note also that Propositions 1 and 2 are the key components of the QBSM because they prove the relation between the moments and the parameters to be unique and they even give explicit formulations of the parameters in terms of the known moments. The procedures for higher real space dimension rely on the same propositions.

For *two dimension in real space* an exact relation between the 12 parameters of the four node quadrature in[7]

$$\mathcal{W}_4^\dagger = [(n^\alpha, \mathbf{U}^\alpha)] \, , \qquad \text{with} \quad \alpha = 1, \ldots, 4 \tag{4.44}$$

and the moments up to the third-order is not possible because the number of moments in

$$\bar{\mathcal{V}}_2^\dagger = \left[\bar{\mathrm{M}}^0, \bar{\mathrm{M}}_x^1, \bar{\mathrm{M}}_y^1, \bar{\mathrm{M}}_{xx}^2, \bar{\mathrm{M}}_{yy}^2, \bar{\mathrm{M}}_{xy}^2, \bar{\mathrm{M}}_{xxx}^3, \bar{\mathrm{M}}_{yyy}^3, \bar{\mathrm{M}}_{yxx}^3, \bar{\mathrm{M}}_{yyx}^3\right] \tag{4.45}$$

is less than those of the parameters in $\mathcal{W}_4^\dagger$. However, in the following the quadrature parameters in $\mathcal{W}_4^\dagger$ will be reduced to allow its determination from the set of moments $\bar{\mathcal{V}}_2^\dagger$. Originally, this third-order moment method was proposed by Desjardins et al. [39],

[7] In the rest of this section, the order of the moments for the surface and the temperature variables ($K = 3/2$, $L = 0$) as well as the index for the section k are suppressed for simplicity. The procedure, outlined here, is the same for each sections, I_k.

but it did not control the second- and third-order cross moments. The methods of Fox [56] and Le Lostec et al. [99] can control the second-order cross moment, extending the approach of Desjardins et al. [39] to two (and three [56]) dimensions. They use the original version of Desjardins et al. [39] for the computation of the quadrature nodes in each direction (see one-dimensional explanations above) and couple the unidirectional nodes such that the second-order cross moment is controlled. The approaches of Desjardins et al. [39] and Le Lostec et al. [99] are not built on the requirement that all weights have to be positive. They introduce artificial thresholds and approximations that prevent this unphysical situation. In contrast, Fox [56] developed a more general procedure that guarantees the realisability of the weights and abscissas. It can be easily extended to three real space dimensions and the number of nodes in each direction can be increased using the product difference algorithm [58]. The price one has to pay for the realisability and the increased number of nodes is the transport of more moments. In the case of a four-node quadrature in two real space dimensions, for example, Le Lostec et al. [99] transport eight moments in each section, whereas Fox [56] has to transport all moments up the third-order (10 moments). In this work, the more general approach of Fox [56] is followed. It is supplemented with the more robust method of Le Lostec et al. [99], where numerical instabilities arise.

The quadrature-based moment method of Fox [56] commences with definitions of the mean droplet velocity vector

$$\mathbf{U}^p := \begin{bmatrix} \bar{\mathrm{M}}^1_x/\bar{\mathrm{M}}^0 \\ \bar{\mathrm{M}}^1_y/\bar{\mathrm{M}}^0 \end{bmatrix} , \tag{4.46}$$

and the velocity covariance matrix

$$\begin{aligned} \boldsymbol{\sigma}_U &= [\bar{\sigma}_{ij}] \\ &:= \frac{1}{\mathrm{M}^0} \int_{s_k}^{s_{k+1}} s^{3/2} \int_{\mathbb{R}_+} \int_{\mathbb{R}^2} (\mathbf{v}-\mathbf{U}^p) \otimes (\mathbf{v}-\mathbf{U}^p) f(\mathbf{x},t;\mathbf{v},s,\theta) d\mathbf{v} ds d\theta \\ &= \begin{bmatrix} \bar{\mathrm{M}}^2_{xx}/\bar{\mathrm{M}}^0 - (U^p_x)^2 & \bar{\mathrm{M}}^2_{xy}/\bar{\mathrm{M}}^0 - U^p_x U^p_y \\ \bar{\mathrm{M}}^2_{yx}/\bar{\mathrm{M}}^0 - U^p_y U^p_x & \bar{\mathrm{M}}^2_{yy}/\bar{\mathrm{M}}^0 - (U^p_y)^2 \end{bmatrix} . \end{aligned} \tag{4.47}$$

The main idea of Fox [56] is then to replace the velocity variable $\mathbf{v}$ by a new variable,

$$\mathbf{X} = \begin{bmatrix} X_1 \\ X_2 \end{bmatrix} := \mathbf{A}^{-1}(\mathbf{v}-\mathbf{U}^p) , \tag{4.48}$$

with

$$\mathbf{v} = \mathbf{A}\mathbf{X} + \mathbf{U}^p . \tag{4.49}$$

The linear transformation matrix $\mathbf{A}$ is chosen such that the covariance matrix $\boldsymbol{\sigma}_X$ has no off-diagonal elements. Fox [56] uses the Cholesky decomposition of the covariance matrix $\boldsymbol{\sigma}_U$, i.e.

$$\boldsymbol{\sigma}_U = \mathbf{L}^{\mathrm{T}}\mathbf{L}, \qquad \text{with} \qquad \mathbf{L} = \begin{bmatrix} \bar{\sigma}^{1/2}_{xx} & \bar{\sigma}_{xy}/\bar{\sigma}^{1/2}_{xx} \\ 0 & \bar{\sigma}^{1/2}_{yy} \end{bmatrix} , \tag{4.50}$$

and identifies the linear transformation $\mathbf{A}$ with the lower triangular matrix $\mathbf{L}^{\mathrm{T}}$. The Cholesky decomposition can only be applied to symmetric and positive definite matrices. As $\boldsymbol{\sigma}_U$ can become singular ($\det(\boldsymbol{\sigma}_U) = 0$), e.g. for dispersed flows that have no velocity dispersion, the method of Le Lostec et al. [99] is used in these cases.

In the case $\boldsymbol{\sigma}_U$ is non-singular, the covariance matrix of the variable $\mathbf{X}$ reduces to [8]

$$\boldsymbol{\sigma}_X = \begin{bmatrix} 1 & 0 \\ 0 & 1 \end{bmatrix}. \tag{4.51}$$

The new variable $\mathbf{X}$ is rotated and normalised in the sense that its second-order cross moments are zero and its unidirectional second-order moments are one. Therefore, the computation of the quadrature parameters corresponding to the variable $\mathbf{X}$, i.e.

$$\mathcal{W}_4^\circ = \left[(n_\alpha^\circ, \mathbf{X}_\alpha)\right], \qquad \text{with} \quad \alpha = 1, \ldots, 4 \tag{4.52}$$

is facilitated because the moments of variable $\mathbf{X}$

$$\begin{gathered} \bar{\mathrm{m}}_{ijk}^M := \frac{1}{\mathrm{M}^0} \int_{s_k}^{s_{k+1}} s^{3/2} \int_{\mathbb{R}_+} \int_{\mathbb{R}^2} X_i X_j X_k f^\circ(\mathbf{x}, t; \mathbf{X}, s, \theta) d\mathbf{X} ds d\theta, \\ \text{with} \quad M \in (0, 1, 2, 3)\ , \end{gathered} \tag{4.53}$$

reduce to

$$\begin{aligned} &\bar{\mathrm{m}}^0 = 1, \quad \bar{\mathrm{m}}_i^1 = 0, \quad \bar{\mathrm{m}}_{ii}^2 = 1, \quad \bar{\mathrm{m}}_{12}^2 = 0, \\ &\bar{\mathrm{m}}_{ijk}^3 = h_{ijk}(\mathbf{A}, \mathbf{U}^p, \bar{\mathrm{M}}_{xxx}^3/\bar{\mathrm{M}}^0, \bar{\mathrm{M}}_{yyy}^3/\bar{\mathrm{M}}^0, \bar{\mathrm{M}}_{yxx}^3/\bar{\mathrm{M}}^0, \bar{\mathrm{M}}_{yyx}^3/\bar{\mathrm{M}}^0)\ . \end{aligned} \tag{4.54}$$

The function h_{ijk} depends, in general, on all velocity moments up to the third-order. The function h_{ijk} is derived and explained in detail in Appendix D. Although the structure of the new variable $\mathbf{X}$ is more convenient, the 10 elements of set

$$\mathcal{V}_2^\circ = \left(\bar{\mathrm{m}}^0, \bar{\mathrm{m}}_1^1, \bar{\mathrm{m}}_2^1, \bar{\mathrm{m}}_{11}^2, \bar{\mathrm{m}}_{12}^2, \bar{\mathrm{m}}_{22}^2, \bar{\mathrm{m}}_{111}^3, \bar{\mathrm{m}}_{222}^3, \bar{\mathrm{m}}_{112}^3, \bar{\mathrm{m}}_{122}^3\right) \tag{4.55}$$

are still not enough for the 12 quadrature parameters in $\mathcal{W}_4^\circ$. To circumvent this problem, the eight unidirectional quadrature parameters $(n_{(i)1}^\circ, X_{(i)1})$ and $(n_{(i)2}^\circ, X_{(i)2})$ for each direction $\mathbf{e}_i$, $(i = 1, 2)$ of the new variable $\mathbf{X}$ are introduced. These parameters are used to define the two-dimensional four-node NDF approximation

$$\begin{aligned} \tilde{f}^\circ(\mathbf{X}, s, \theta) =& \delta(\theta - \Theta_k) \exp(-b_k s) \\ &\left[n_1^\circ \delta(X_1 - X_{(1)1}) \delta(X_2 - X_{(2)1}) + n_2^\circ \delta(X_1 - X_{(1)1}) \delta(X_2 - X_{(2)2}) \right. \\ &\left. + n_3^\circ \delta(X_1 - X_{(1)2}) \delta(X_2 - X_{(2)1}) + n_4^\circ \delta(X_1 - X_{(1)2}) \delta(X_2 - X_{(2)2})\right]. \end{aligned} \tag{4.56}$$

[8] Using the definition of $\boldsymbol{\sigma}_U$ in (4.47) and multiplying the tensors $\mathbf{A}^{-1}$ from the left and $\mathbf{A}^{-\mathrm{T}}$ from the right, $\left[\mathbf{A}^{-1} \boldsymbol{\sigma}_U \mathbf{A}^{-\mathrm{T}}\right]$ turns into the unity matrix. With the identity

$$\mathbf{A}^{-1}(\mathbf{v} - \mathbf{U}^p) \otimes (\mathbf{v} - \mathbf{U}^p)\mathbf{A}^{-\mathrm{T}} = \left[\mathbf{A}^{-1}(\mathbf{v} - \mathbf{U}^p)\right] \otimes \left[\mathbf{A}^{-1}(\mathbf{v} - \mathbf{U}^p)\right]$$

the integral in definition (4.47) turns into $\boldsymbol{\sigma}_X$.

In the definition of the velocity abscissas, (X_1^α, X_2^α), $\alpha = 1, \ldots, 4$, the tensor-product of the unidirectional abscissas was used, i.e.

$$\begin{bmatrix} (X_1^1, X_2^1) & (X_1^2, X_2^2) \\ (X_1^3, X_2^3) & (X_1^4, X_2^4) \end{bmatrix} = \begin{bmatrix} X_{(1)1} \\ X_{(1)2} \end{bmatrix} \otimes \begin{bmatrix} X_{(2)1} \\ X_{(2)2} \end{bmatrix} . \tag{4.57}$$

With approximation (4.56) the unidirectional moments can be written as

$$\begin{aligned}
\bar{\mathrm{m}}^0 &= n_1^\circ + n_2^\circ + n_3^\circ + n_4^\circ, \\
\bar{\mathrm{m}}_1^1 &= (n_1^\circ + n_2^\circ) X_{(1)1} + (n_3^\circ + n_4^\circ) X_{(1)2}, \\
\bar{\mathrm{m}}_2^1 &= (n_1^\circ + n_3^\circ) X_{(2)1} + (n_2^\circ + n_4^\circ) X_{(2)2}, \\
\bar{\mathrm{m}}_{11}^2 &= (n_1^\circ + n_2^\circ) {X_{(1)1}}^2 + (n_3^\circ + n_4^\circ) {X_{(1)2}}^2, \\
\bar{\mathrm{m}}_{22}^2 &= (n_1^\circ + n_3^\circ) {X_{(2)1}}^2 + (n_2^\circ + n_4^\circ) {X_{(2)2}}^2, \\
\bar{\mathrm{m}}_{111}^3 &= (n_1^\circ + n_2^\circ) {X_{(1)1}}^3 + (n_3^\circ + n_4^\circ) {X_{(1)2}}^3, \\
\bar{\mathrm{m}}_{222}^3 &= (n_1^\circ + n_3^\circ) {X_{(2)1}}^3 + (n_2^\circ + n_4^\circ) {X_{(2)2}}^3 .
\end{aligned} \tag{4.58}$$

Introducing the unidirectional weights as

$$\begin{aligned}
n_{(1)1}^\circ &= n_1^\circ + n_2^\circ, \qquad & n_{(1)2}^\circ &= n_3^\circ + n_4^\circ, \\
n_{(2)1}^\circ &= n_1^\circ + n_3^\circ, \qquad & n_{(2)2}^\circ &= n_2^\circ + n_4^\circ,
\end{aligned} \tag{4.59}$$

the relations in (4.58) can be split in two one-dimensional parts

$$\begin{aligned}
\bar{\mathrm{m}}^0 &= n_{(1)1}^\circ + n_{(1)2}^\circ, & \bar{\mathrm{m}}^0 &= n_{(2)1}^\circ + n_{(2)2}^\circ, \\
\bar{\mathrm{m}}_1^1 &= n_{(1)1}^\circ X_{(1)1} + n_{(1)2}^\circ X_{(1)2}, & \bar{\mathrm{m}}_2^1 &= n_{(2)1}^\circ X_{(2)1} + n_{(2)2}^\circ X_{(2)2}, \\
\bar{\mathrm{m}}_{11}^2 &= n_{(1)1}^\circ {X_{(1)1}}^2 + n_{(1)2}^\circ {X_{(1)2}}^2, & \bar{\mathrm{m}}_{22}^2 &= n_{(2)1}^\circ {X_{(2)1}}^2 + n_{(2)2}^\circ {X_{(2)2}}^2, \\
\bar{\mathrm{m}}_{111}^3 &= n_{(1)1}^\circ {X_{(1)1}}^3 + n_{(1)2}^\circ {X_{(1)2}}^3, & \bar{\mathrm{m}}_{222}^3 &= n_{(2)1}^\circ {X_{(2)1}}^3 + n_{(2)2}^\circ {X_{(2)2}}^3.
\end{aligned} \tag{4.60}$$

Knowing the moments on the left-hand side of these two sets of equations, the two-node quadrature formulae in (4.42) and (4.43) are used to determine the unidirectional quadrature parameters $(n_{(i)1}^\circ, X_{(i)1})$ and $(n_{(i)2}^\circ, X_{(i)2})$ for each direction $\mathbf{e}_i$, $(i = 1, 2)$. With the identities in (4.54), the quadrature formulae (4.42) and (4.43) turn into

$$\begin{aligned}
n_{(i)1}^\circ &= \tfrac{1}{2} + \gamma_i, \qquad & X_{(i)1} &= -\left(\frac{1 - 2\gamma_i}{1 + 2\gamma_i}\right)^{1/2}, \\
n_{(i)2}^\circ &= \tfrac{1}{2} - \gamma_i, \qquad & X_{(i)2} &= \left(\frac{1 + 2\gamma_i}{1 - 2\gamma_i}\right)^{1/2},
\end{aligned} \tag{4.61}$$

with

$$\gamma_i = \frac{\bar{\mathrm{m}}_{iii}^3/2}{[(\bar{\mathrm{m}}_{iii}^3)^2 + 4]^{1/2}} . \tag{4.62}$$

Due to the fact that $-\frac{1}{2} < \gamma_i < \frac{1}{2}$ for all values of $\bar{\mathrm{m}}^3_{iii}$, the weights $n^\circ_{(i)1}$ and $n^\circ_{(i)1}$ will always be positive for all directions $\mathbf{e}_i$, $(i = 1, 2)$.

Notice that (4.59) is a linear equation system for the two-dimensional weights n°_α, $\alpha = 1, \ldots, 4$, but only with rank three. The linearly independent set of equations

$$n^\circ_{(1)1} - n^\circ_{(2)2} = n^\circ_1 - n^\circ_4, \quad n^\circ_{(1)2} = n^\circ_3 + n^\circ_4, \quad n^\circ_{(2)2} = n^\circ_2 + n^\circ_4, \tag{4.63}$$

which is easily derived from (4.59), requires an additional equation to determine all two-dimensional weights n°_α. The solution to this problem is the second-order cross moment $\bar{\mathrm{m}}^2_{12}$ which, in the frame of the variable $\mathbf{X}$, is identically zero. The substitution of the approximate NDF (4.56) into the definition of $\bar{\mathrm{m}}^2_{12}$ (4.53) yields

$$X_{(1)1}X_{(2)1}n^\circ_1 + X_{(1)1}X_{(2)2}n^\circ_2 + X_{(1)2}X_{(2)1}n^\circ_3 + X_{(1)2}X_{(2)1}n^\circ_4 = 0 \ , \tag{4.64}$$

which is obviously independent of the relations in (4.63). Recall that the abscissas $X_{(i)\alpha}$ are known; hence equations (4.63) together with (4.64) are a full-rank linear equation system for the weights n°_α. The solution of these equations is finally

$$\begin{aligned} n^\circ_1 &= n^\circ_{(1)1}n^\circ_{(2)1} = (\tfrac{1}{2} + \gamma_1)(\tfrac{1}{2} + \gamma_2), \quad n^\circ_2 = n^\circ_{(1)1}n^\circ_{(2)2} = (\tfrac{1}{2} + \gamma_1)(\tfrac{1}{2} - \gamma_2), \\ n^\circ_3 &= n^\circ_{(1)2}n^\circ_{(2)1} = (\tfrac{1}{2} - \gamma_1)(\tfrac{1}{2} + \gamma_2), \quad n^\circ_4 = n^\circ_{(1)2}n^\circ_{(2)2} = (\tfrac{1}{2} - \gamma_1)(\tfrac{1}{2} - \gamma_2). \end{aligned} \tag{4.65}$$

As the weights $n^\circ_{(i)\alpha}$ are non-negative, n°_β, $\beta = 1, \ldots, 4$, are non-negative as well. Taking into account the relations $(4.61)_{2,4}$, (4.62) and (4.65), the mapping from the set of eight moments

$$\mathcal{V}^\square_2 := \left(\bar{\mathrm{m}}^0, \bar{\mathrm{m}}^1_1, \bar{\mathrm{m}}^1_2, \bar{\mathrm{m}}^2_{11}, \bar{\mathrm{m}}^2_{12}, \bar{\mathrm{m}}^2_{22}, \bar{\mathrm{m}}^3_{111}, \bar{\mathrm{m}}^3_{222}\right) \tag{4.66}$$

to eight independent quadrature parameters of set

$$\mathcal{W}^\square_4 := \left[(n^\circ_1, X_{(1)1}, X_{(2)1}), (n^\circ_2, X_{(1)1}, X_{(2)2}), (n^\circ_3, X_{(1)2}, X_{(2)1}), (n^\circ_4, X_{(1)2}, X_{(2)2})\right] \tag{4.67}$$

is possible. Notice that the two third-order cross moments $\bar{\mathrm{m}}^3_{211}$ and $\bar{\mathrm{m}}^3_{221}$ are not included in set $\mathcal{V}^\square_2$. Clearly, the information on these moments is lost but the remaining third-order moments are linear combinations of all third-order moments in the frame of $\mathbf{v}$. However, because the third-order cross moments in the $\mathbf{X}$-frame are not controlled an error is introduced in this procedure.[9] The parameters in $\mathcal{W}^\square_4$ are easily transformed into those of set $\mathcal{W}^\dagger_4$ by using equations (4.49) and $n_\alpha = \bar{\mathrm{M}}^0 n^\circ_\alpha$, $(\alpha = 1, \ldots, 4)$. Notice that although $\mathcal{W}^\dagger_4$ has 12 elements, only eight of them are independent. However, using a relation similar to (4.22) the quadrature parameters in $\mathcal{W}^\dagger_4$ can easily be projected onto the set of moments $\mathcal{V}^\triangle_2$, a subset of $\mathcal{V}_2$. The different transformations introduced in this section are summarised as

$$\mathcal{V}^\dagger_2 \leftrightarrow \mathcal{V}^\circ_2 \rightarrow \mathcal{V}^\square_2 \leftrightarrow \mathcal{W}^\square_4 \leftrightarrow \mathcal{W}^\dagger_4 \leftrightarrow \mathcal{V}^\triangle_2 \subset \mathcal{V}^\dagger_2 \ . \tag{4.68}$$

The error that is introduced in the transformation $\mathcal{V}^\dagger_2 \rightarrow \mathcal{V}^\triangle_2$ can be assessed by comparing the elements of the two sets.

[9] The procedures of Desjardins et al. [39] and Le Lostec et al. [99] do not control the third-order cross moments in the frame of $\mathbf{v}$.

4.5 Reduction of the Spray Model

In this section, the physical models are explicitly specified and the general moment transport equations in (4.7) are elaborated for the set of chosen moments $\mathcal{V}_k^2$ (4.17). The transport equations are closed by considering the approximate NDF supplemented with the algorithms in Section 4.4.

4.5.1 Choice of Physical Spray Models

In Chapter 2 physical spray models were introduced that allow the specification of the terms $\mathrm{St}(\mathbf{v}, s)$, $\mathrm{Ev}(\mathbf{v}, s, \theta)$, $\mathrm{He}(\mathbf{v}, s, \theta)$, $\Gamma(\mathbf{v}, s)$ and $\mathcal{Q}(\mathbf{v}, s)$ in equation (4.1) or (4.7). In this work, the focus is not on the question of whether the accuracy of QSBM is good or bad in comparison with experiments. The investigations are instead concerned with the issue of whether the QBSM is able to describe drag force, evaporation and heat transfer in crossing spray configurations. Therefore, the most simple and intuitive physical models are chosen. More refined models for drag, evaporation and heat transfer and the behaviour of the method concerning turbulence models of the dispersed phase, collision and breakup were not tested in this work. However, models for these spray effects exist (see Chapter 2) and, as long as they are in the frame of the kinetic spray equation (3.26), there is no theoretical reason why the QBSM should fail to describe these effects.

In Chapter 3 the force $\mathbf{F}$ [$\mathrm{kg\,m\,s^{-2}}$] on a droplet of mass m_d [kg] was reduced to the dimensionless form

$$\frac{X_{\mathrm{char}}}{(V_{\mathrm{char}})^2}\left(\frac{\mathbf{F}}{m_d}\right) = \frac{\mathbf{U}_g - \mathbf{v}}{\mathrm{St}(\mathbf{v}, s)} + \frac{1}{\mathrm{Fr}}\mathbf{e}_g \ , \tag{4.69}$$

where buoyancy, unsteady and other more subtle forces have been neglected [33]. The drag force model is further reduced to the Stokes law, which rejects the dependency of St on the velocity variable $\mathbf{v}$ and therefore is limited to droplet Reynolds numbers satisfying $\mathrm{Re}_d \leq 1$. Using relation $(2.18)_2$, the Stokes number is written as

$$\mathrm{St}(s) = \frac{\rho_\ell V_{\mathrm{char}} S_{\mathrm{char}}}{18\pi\eta_g X_{\mathrm{char}}} s = \mathrm{St}(1)s \ . \tag{4.70}$$

Notice that $\mathrm{St}(s)$ is proportional to the variable s, where the factor $\mathrm{St}(1)$ is the Stokes number of droplets with surface S_{char}.

The evaporation law

$$\frac{\partial s}{\partial t} = -\mathrm{Ev}(\mathbf{v}, s, \theta) \tag{4.71}$$

is used for the evaporation of droplets, where $\mathrm{Ev}(\mathbf{v}, s, \theta)$ is derived from the mass transfer $\dot{m}_d = \partial m_d/\partial t$ [$\mathrm{kg\,s^{-1}}$] and the assumption of spherical droplets. With these considerations the evaporation number can be written as

$$\mathrm{Ev}(\mathbf{v}, s, \theta) = -\frac{6\sqrt{\pi} X_{\mathrm{char}}}{\rho_\ell V_{\mathrm{char}} (S_{\mathrm{char}})^{3/2}} \dot{m}_d(\mathbf{v}, s, \theta) s^{-1/2} \ . \tag{4.72}$$

If the mass transfer $\dot{m}_v$ [$\mathrm{kg\,s^{-1}}$] is modelled by

$$\dot{m}_d(\mathbf{v}, s, \theta) = \sqrt{\pi}(S_{\mathrm{char}})^{1/2} s^{1/2} \rho_\ell D_{va} \mathrm{Sh}_{0,\mathrm{mod}}(\mathbf{v}, \theta) \ln(1 + \mathrm{B}_m(\theta)) \ , \tag{4.73}$$

(which is chosen according the approach of Abramzon and Sirignano [1]) Ev can be assumed to be independent of s. In Section 2.4.2 the definitions of parameters in (4.73) are given. If the velocity and temperature differences between gas and droplets are assumed to be negligible and the vapour concentration and the temperature in the gas are assumed to be constant, the evaporation number is constant. In some of the computations conducted in Chapter 6 the latter assumptions are enforced to study the QBSM.

As discussed in Section 2.4.2, the change of the droplet temperature is due to two physical effects. *First*, the temperature difference between droplet and gas leads to a heat conduction, $\dot{\mathrm{Q}}_{gl}$ [W], crossing the droplet surface. Drawing on the model of [1] the heat flux can be modelled as (see (2.34))

$$\dot{\mathrm{Q}}_{gl}(\mathbf{v}, s, \theta) = \frac{\bar{c}_{pF}\dot{m}_d}{\mathrm{B}_h}(\theta_g - \theta)\Theta_{\mathrm{char}}. \tag{4.74}$$

Second, the phase change of droplets into vapour is a process that consumes heat. The measure for this heat sink is the specific latent heat $L(\theta_s)$ [$\mathrm{J\,kg^{-1}}$] which depends on the temperature at the droplet surface θ_s. For the infinite conductivity model enforced in this work the surface temperature can be identified with the droplet temperature ($\Theta_{\mathrm{char}}\theta$) [K]. Heat conduction and latent heat can be combined to obtain a representation for the temperature change (see (2.34))

$$\mathrm{He}(\mathbf{v}, s, \theta) = \frac{X_{\mathrm{char}}}{V_{\mathrm{char}}\Theta_{\mathrm{char}}}\frac{\dot{m}_d(s, \mathbf{v}, \theta)}{c_p^d\, m_d(s)}\left(\frac{\bar{c}_{pF}\Theta_{\mathrm{char}}}{\mathrm{B}_h}(\theta_g - \theta) + L(\theta_s)\right) . \tag{4.75}$$

As stated in Section 2.4.2, the heat transfer number, B_h, can be computed by an iterative procedure proposed by Abramzon and Sirignano [1]. The exact values of the specific heat capacities c_p^d [$\mathrm{J\,kg^{-1}K^{-1}}$] for the droplet and $\bar{c}_{pF}$ [$\mathrm{J\,kg^{-1}K^{-1}}$] for the gas (see equation (2.33)) in the thermal boundary layer are found in tables [173] or are obtained from correlations [127]. Here, the heat capacities are assumed to be unaffected by temperature changes.

The collision and breakup terms are set to zero in the remainder of this work. With this strong simplification, dense sprays with droplet Knudsen numbers of the order of one cannot be described. The consideration of secondary droplet breakup near an atomization nozzle is out of reach with these assumptions. The extension of the QBSM to collision and breakup has to be postponed to future research. Dufour [43] and Laurent et al. [97] have shown that the sectional method can capture these effects and Fox [56] and Le Lostec et al. [99] introduced collision into their third-order quadrature method. Therefore, the considerations of these effects should, in principle, be possible with the combined method, QBSM. By neglecting any interaction between the droplets, the droplet Knudsen number is considered to be infinite.

The disregard of collision effects facilitates the sectional part of QBSM as no droplet larger than $s = 1$ (which corresponds to the largest initial droplet S_{char} [$\mathrm{m^2}$]) is ever present. Consequently, the surface space can be reduced to $[0, 1]$ and the infinite section I_{N_s+1} is of no use. In the remainder of this work, only the first N_s sections $I_k = [s_k,\ s_{k+1})$ ($k = 1, \ldots, N_s$) are considered where $s_1 = 0$ and $s_{N_s+1} = 1$.

4.5.2 Collection of the closed Moment Transport Equations

The introduction of the physical spray models into the unclosed moment transport equations in (4.7) yields the following system of equations for each section I_k, $k = 1, \ldots, N_s$,

$$
\begin{aligned}
\frac{\mathrm{d}}{\mathrm{d}t}(\mathrm{M}_k^{0,0,0}) &= -E^{0,0,0}(k,k) + E^{0,0,0}(k,k+1) \ , \\
\frac{\mathrm{d}}{\mathrm{d}t}(\mathrm{M}_k^{3/2,0,0}) &= -\left(E^{3/2,0,0}(k,k) + \mathcal{E}^{3/2,0,0}(k)\right) + E^{3/2,0,0}(k,k+1) \ , \\
\frac{\mathrm{d}}{\mathrm{d}t}(\mathrm{M}_k^{3/2,1,0}) &= -\left(E^{3/2,1,0}(k,k) + \mathcal{E}^{3/2,1,0}(k)\right) + E^{3/2,1,0}(k,k+1) + \mathcal{R}_k \ , \\
\frac{\mathrm{d}}{\mathrm{d}t}(\mathrm{M}_{k;i}^{3/2,0,1}) &= -\left(E_i^{3/2,0,1}(k,k) + \mathcal{E}_i^{3/2,0,1}(k)\right) + E_i^{3/2,0,1}(k,k+1) \\
&\quad + \frac{1}{\mathrm{Fr}}\mathbf{e_g}\cdot\mathbf{e}_i\mathrm{M}_k^{3/2,0,0} + D_{k;i}^1 \ , \\
\frac{\mathrm{d}}{\mathrm{d}t}(\mathrm{M}_{k;ij}^{3/2,0,2}) &= -\left(E_{ij}^{3/2,0,2}(k,k) + \mathcal{E}_{ij}^{3/2,0,2}(k)\right) + E_{ij}^{3/2,0,2}(k,k+1) \\
&\quad + \frac{1}{\mathrm{Fr}}\left(\mathbf{e_g}\cdot\mathbf{e}_i\mathrm{M}_{k;j}^{3/2,0,1} + \mathbf{e_g}\cdot\mathbf{e}_j\mathrm{M}_{k;i}^{3/2,0,1}\right) + D_{k;ij}^2 \ , \\
\frac{\mathrm{d}}{\mathrm{d}t}(\mathrm{M}_{k;lmn}^{3/2,0,3}) &= -\left(E_{lmn}^{3/2,0,3}(k,k) + \mathcal{E}_{lmn}^{3/2,0,3}(k)\right) + E_{lmn}^{3/2,0,3}(k,k+1) \\
&\quad + \frac{1}{\mathrm{Fr}}\left(\mathbf{e_g}\cdot\mathbf{e}_l\mathrm{M}_{k;mn}^{3/2,0,2} + \mathbf{e_g}\cdot\mathbf{e}_m\mathrm{M}_{k;ln}^{3/2,0,2} + \mathbf{e_g}\cdot\mathbf{e}_n\mathrm{M}_{k;lm}^{3/2,0,2}\right) + D_{k;lmn}^3 \ ,
\end{aligned}
\tag{4.76}
$$

where the material time derivative $\mathrm{d}(\cdot)/\mathrm{d}t$ is defined as [70]

$$
\frac{\mathrm{d}}{\mathrm{d}t}(\mathrm{M}_{k;lnm}^{K,L,M}) = \frac{\partial}{\partial t}(\mathrm{M}_{k;lnm}^{K,L,M}) + \frac{\partial}{\partial x_i}(\mathrm{M}_{k;lnmi}^{K,L,M+1}) \ , \tag{4.77}
$$

and the heat source term in the equation for $\mathrm{M}_k^{3/2,1,0}$ is introduced as

$$
\mathcal{R}_k = \int_{s_k}^{s_{k+1}} \int_{\mathbb{R}_+} \int_{\mathbb{R}^d} s^{3/2}\mathrm{He}(\mathbf{v}, s, \theta) f d\mathbf{v} d\theta ds \ . \tag{4.78}
$$

The first terms on the right-hand sides of equations (4.76), defined as

$$
\begin{aligned}
E_{lmn}^{K,L,M}(k,r) &= \int_{\mathbb{R}_+} \int_{\mathbb{R}^d} {s_r}^K \mathrm{Ev}(\mathbf{v}, s_r, \theta) v_l v_m v_n f(\mathbf{x}, t; \mathbf{v}, s_r, \theta) \ , \\
\mathcal{E}_{lmn}^{K,L,M}(k) &= K \int_{s_k}^{s_{k+1}} \int_{\mathbb{R}_+} \int_{\mathbb{R}^d} s^{K-1}\mathrm{Ev}(\mathbf{v}, \theta, s) v_l v_m v_n \theta^L f d\mathbf{v} ds d\theta \ ,
\end{aligned}
\tag{4.79}
$$

are related to evaporation. $E_{lmn}^{K,L,M}(k,r)$ can be interpreted as flux of the respective moment over an interface of section I_k. The term $\mathcal{E}_{lmn}^{K,L,M}(k)$ is a sink term of the respective

moment which captures the transfer of mass, momentum, heat, etc. from the droplet to the gas phase. Notice that the equation for the zeroth-order moment does only include evaporation flux terms. Hence, no droplet is erased within a section but only at the right interface of section I_1, i.e. the evaporation flux $E^{0,0,0}(1,1)$ leads to a loss of droplets. This structure of equation $(4.76)_1$ agrees very well with the phenomenon of evaporation because droplets fade away only when they have reached zero surface. In the next chapter the evaporation fluxes and sink terms will be rewritten to yield a conservative, finite volume-like scheme in surface space.

In equations $(4.76)_{4,5,6}$ the drag force is represented by the terms

$$D^M_{k;lmn} = -\int_{s_k}^{s_{k+1}} \int_{\mathbb{R}_+} \int_{\mathbb{R}^d} s^{3/2} v_l v_m v_n \frac{\partial}{\partial v_i} \left\{ \left(\frac{U_{gi} - v_i}{\mathrm{St}(1)s} \right) f \right\} d\mathbf{v} d\theta ds, \quad M = 1,2,3\ . \tag{4.80}$$

In the first three equations of (4.76) the drag related terms do not arise, because

$$\begin{aligned} D^0_{k;lmn} &= \int_{s_k}^{s_{k+1}} \int_{\mathbb{R}_+} \int_{\mathbb{R}^d} s^K \theta^L \frac{\partial}{\partial v_i} \left\{ \left(\frac{U_{gi} - v_i}{\mathrm{St}(1)s} \right) f \right\} d\mathbf{v} d\theta ds \\ &= \sum_{i=1}^{d} \left[\int_{s_k}^{s_{k+1}} \int_{\mathbb{R}_+} s^K \theta^L \left(\frac{U_{gi} - v_i}{\mathrm{St}(1)s} \right) f ds \right]_{-\infty}^{+\infty} \end{aligned} \tag{4.81}$$

vanishes if f goes to zero faster than any polynomial of velocity components $|v_i|$ can grow to ∞. For real configurations this assumption is always satisfied because no droplet with infinite velocity can exist. Using the latter argument, the drag term in (4.80) can be rewritten as

$$\begin{aligned} D^1_{k;l} &= \int_{s_k}^{s_{k+1}} \frac{s^{1/2}}{\mathrm{St}(1)} \int_{\mathbb{R}_+} \int_{\mathbb{R}^d} (\mathbf{U}_{gl} - v_l)\, f d\mathbf{v} d\theta ds, \\ D^2_{k;lm} &= \int_{s_k}^{s_{k+1}} \frac{s^{1/2}}{\mathrm{St}(1)} \int_{\mathbb{R}_+} \int_{\mathbb{R}^d} v_j (U_{gi} - v_i)(\delta_{il}\delta_{jm} + \delta_{im}\delta_{jl}) f d\mathbf{v} d\theta ds, \\ D^3_{k;lmn} &= \int_{s_k}^{s_{k+1}} \frac{s^{1/2}}{\mathrm{St}(1)} \int_{\mathbb{R}_+} \int_{\mathbb{R}^d} v_s v_t (U_{gr} - v_r)(\delta_{rl}\delta_{sn}\delta_{tm} + \delta_{rm}\delta_{sl}\delta_{tn} + \delta_{rn}\delta_{sm}\delta_{tl}) f d\mathbf{v} d\theta ds. \end{aligned} \tag{4.82}$$

The approximate NDF (4.8) remains to be substituted into the moment transport equations in (4.76). The structure of (4.76) is not changed by this substitution, only the terms $\mathcal{R}_k$, $E^{K,L,M}_{lmn}(k,r)$, $\mathcal{E}^{K,L,M}_{lmn}(k)$, $D^M_{k;lmn}$ in (4.78), (4.79), (4.82) and the unknown moments $\mathrm{M}^{K,L,M+1}_{k;lnmi}$ in (4.77) will finally by expressed in terms of the known parameters in $\mathcal{W}^\beta_k$

(4.11). The closed expressions read

$$\mathcal{R}_k = \int_{s_k}^{s_{k+1}} s^{3/2} \exp(-b_k s) \sum_{\alpha=1}^{\beta} n_k^\alpha \mathrm{He}(\mathbf{U}_k^\alpha, s, \Theta_k) ds \ ,$$

$$E_{lmn}^{K,L,M}(k,r) = {s_r}^K \exp(-b_k s_r) \mathrm{Ev}(\mathbf{U}_k^\alpha, s_r, \Theta_k) (\mathbf{U}_k^\alpha)_l (\mathbf{U}_k^\alpha)_m (\mathbf{U}_k^\alpha)_n \ ,$$

$$\mathcal{E}_{lmn}^{K,L,M}(k) = K \sum_{\alpha=1}^{\beta} n_k^\alpha (\mathbf{U}_k^\alpha)_l (\mathbf{U}_k^\alpha)_m (\mathbf{U}_k^\alpha)_n {\Theta_k}^L \int_{s_k}^{s_{k+1}} s^{K-1} \exp(-b_k s) \mathrm{Ev}(\mathbf{U}_k^\alpha, \Theta_k, s) ds \ ,$$

$$D_{k;l}^1 = \int_{s_k}^{s_{k+1}} \frac{s^{1/2}}{\mathrm{St}(1)} \exp(-b_k s) ds \sum_{\alpha=1}^{\beta} n_k^\alpha \left[U_{gl} - (\mathbf{U}_k^\alpha)_l\right],$$

$$D_{k;lm}^2 = \int_{s_k}^{s_{k+1}} \frac{s^{1/2}}{\mathrm{St}(1)} \exp(-b_k s) ds \sum_{\alpha=1}^{\beta} n_k^\alpha (\mathbf{U}_k^\alpha)_j \left[U_{gi} - (\mathbf{U}_k^\alpha)_i\right] (\delta_{il}\delta_{jm} + \delta_{im}\delta_{jl}),$$

$$D_{k;lmn}^3 = \int_{s_k}^{s_{k+1}} \frac{s^{1/2}}{\mathrm{St}(1)} \exp(-b_k s) ds \times \sum_{\alpha=1}^{\beta} n_k^\alpha (\mathbf{U}_k^\alpha)_s (\mathbf{U}_k^\alpha)_t \left[U_{gr} - (\mathbf{U}_k^\alpha)_r\right] (\delta_{rl}\delta_{sn}\delta_{tm} + \delta_{rm}\delta_{sl}\delta_{tn} + \delta_{rn}\delta_{sm}\delta_{tl}),$$

$$\mathrm{M}_{k;lmni}^{K,L,M+1} = \int_{s_k}^{s_{k+1}} s^K \exp(-b_k s) ds \sum_{\alpha=1}^{\beta} n_k^\alpha (\mathbf{U}_k^\alpha)_l (\mathbf{U}_k^\alpha)_m (\mathbf{U}_k^\alpha)_n (\mathbf{U}_k^\alpha)_i \ . \tag{4.83}$$

The integrals in (4.83) are either known analytically or they are computed with appropriate quadrature rules.

It is observed that the system of moment transport equations (4.76) supplemented by the relations in (4.83) is a highly nonlinear system due to the complicated relation between the parameters of the approximate NDF and the chosen moments. It is the objective of the next chapter to find appropriate numerical methods for the approximation of solutions to these equations.

Chapter 5

Numerical Model

5.1 Introduction

Equations (4.76) and (4.83), supplemented by appropriate initial and boundary conditions (see Chapter 6), can be considered as a mathematical model for the motion of a dilute spray, with infinite droplet Knudsen number, experiencing drag, heating or cooling, and evaporation. All terms in these equations depend on position $\mathbf{x}$, and time t. They exhibit the structure of balance equations [70] with the following properties:

(i) For each section I_k a set of balance equations has to be solved.

(ii) The sets are coupled through evaporation, drag and heat transfer terms.[1]

(iii) Pressure and deviatoric stress terms are absent.

(iv) The convective terms are functions of the parameters in the set $\mathcal{W}_k^4$ (4.11).

These properties rule out the well-known pressure correction procedure [50] because a pressure cannot be defined within a droplet flow that is collision-less. In addition, a numerical procedure is required that is not based on the incompressibility assumption. Instead, the numerical schemes that are derived in this chapter must be able to *first*, capture sharp jumps of all moments at crossing points and *secondly*, describe vacuum zones and regions of strong mass concentration, for example, at the center and rim of vortices, respectively. Another challenge is the lack of physical diffusion. In general, any type of diffusion contributes to the stability of the numerical schemes that are used for the discretisation of convective fluxes.

The numerical methods must also ensure that the mass transfer from the droplet to the gas phase, which is the key quantity in spray combustion, is not artificially changed by numerical errors. This requires the use of conservative schemes in surface space which prevent the unphysical creation or disappearance of droplets and droplet mass. In this

[1] The interaction between the different sections via the drag and heat transfer terms is only present when the balance laws for the gas and the droplets are solved simultaneously and a two-way coupling is considered. In this case, a weak interaction between the sections is possible.

work, the above requirements are met by using a fractional-step method in time. This approach allows the independent treatment of convection, droplet forces, heat transfer and evaporation with numerical methods that are exclusively designed for the approximation of the respective physical effects.

In Section 5.2 the Strang splitting is outlined. It is an accuracy-preserving variant of the fractional-step method. It is applied to the reduced kinetic spray equation (5.1) to obtain the sub problems, dealing exclusively with convection, droplet forces, heat transfer and evaporation. The application of the moment transforms and the moment closure, introduced in Chapter 4, to these sub problems leads to three systems of moment equations. These systems could also be derived from the moment transport equations in (4.76) but the approach followed here allows the derivation of numerical methods for convection and evaporation that are based on the finite volume schemes.

The subsystem of convection, which is a pressureless gas dynamic system [18], is treated in Section 5.3 by using the first- and second-order kinetic approximations of Bouchut et al. [19]. This explicit approach can capture the strong concentration of droplets, called delta-shocks, and it does not require a gradient-diffusion model to close the spatial fluxes of moments. It is in agreement with the approximate NDF, i.e. the parameters in $\mathcal{W}_k^4$ (4.11) are used to compute the fluxes.

In Section 5.4 the influence of the forces on the droplets is considered. For Stokes drag and gravity, the equation system that advances the moments in time can be solved semi-analytically. Therefore, only a small numerical error is introduced in the fractional step for the droplet forces. The sub problem of heat transfer is regarded as a first-order nonlinear ODE. It is solved numerically by taking the moments $\mathrm{M}_k^{0,0,0}$, $\mathrm{M}_k^{3/2,0,0}$ and $\mathrm{M}_k^{3/2,1,0}$ from a previous fractional step. In this work, the sub problem of droplet forces and heat transfer are treated in the same fractional step.

The change of moments due to evaporation is treated separately with a conservative, finite volume-like scheme in surface space (see Section 5.5). The fluxes over the interfaces of the sections, i.e. the interaction terms between the different sets of balance laws and the mass transfer to the gas are obtained naturally from the finite volume discretisation. Hence, no additional assumptions need to be imposed on the system of equations due to the coupling between sections and the interaction between droplets and gas.

In Section 5.6, the splashing model which was introduced in Chapter 2 is adapted to QBSM. Although it is only a crude model used for the validation of QBSM, it can easily be extended to more complex situations, e.g. sudden evaporation on the wall, creation of a liquid film with varying thickness, roughness effects of the wall, etc.

Chapter 5 is concluded by a section on the overall algorithm of the QBSM. This algorithm is applied to various test-cases in Chapter 6.

5.2 Fractional Step Method

The system of equations (4.76) is a spray model which exhibits various time scales and requires different numerical methods for each physical effect. The application of a fractional step method (cf. [102]), also called the operator splitting method (cf. [37] and references therein), allows the partitioning of the equation system (4.76) into decoupled systems for convection, droplet forces, heat transfer and evaporation which can be solved

with numerical methods that are optimised for the respective physical effect. In each fractional step a different aspect of the general problem is treated. In the convection step, for example, the information on the flow is exchanged between the cells in real space and the evaporation step leads to a coupling between the sections. The combination of these specialised methods is organised such that it delivers the solution to the global problem without introducing additional errors.

In addition, the fractional step method allows the solution of two- and three- dimensional convection problems by splitting it into two or three one-dimensional convection problems and using a one-dimensional convection scheme for each piece (cf. [101]). Fractional-step methods also facilitate the decoupling of small from larger time scales, which is necessary to capture, for example, the drag force on droplets having small Stokes numbers. The splitting error that is introduced by this procedure will also be discussed. In the derivation pursued here, Strang's splitting method is first applied to the kinetic spray equation (5.1) (see Section 5.2.1) then, in Section 5.2.2, the moment transforms and closure relation from Chapter 4 are used to obtain the sub problems for the chosen moments. Performing a Strang splitting directly on the equation system (4.76), (4.83) yields the same sub problems but the derivation followed here allows the deduction of kinetic-based, finite volume schemes for convection and evaporation.

5.2.1 Strang Splitting of the Kinetic Spray Equation

With the assumptions imposed on the spray model in Section 4.5, the kinetic spray equation (4.1) reduces to

$$\begin{aligned} &\frac{\partial}{\partial t}(f) + \nabla_{\mathbf{x}} \cdot (\mathbf{v} f) + \nabla_{\mathbf{v}} \cdot \left\{ \left(\frac{\mathbf{U}_g - \mathbf{v}}{\mathrm{St}(1) s} + \frac{1}{\mathrm{Fr}} \mathbf{e}_{\mathbf{g}} \right) f \right\} - \mathrm{Ev} \frac{\partial}{\partial s}(f) + \frac{\partial}{\partial \theta}(\mathrm{He} f) = 0 \ , \\ &\text{with} \quad t > t_n, \quad \mathbf{x} \in \mathcal{L} \subset \mathbb{R}^d, \quad \mathbf{v} \in \mathbb{R}^d, \quad 0 < s \leq 1, \quad \theta \in \mathbb{R}_+ \ , \end{aligned} \tag{5.1}$$

where $\mathcal{L}$ denotes the computational domain in real space. The general initial and boundary conditions for this problem are expressed as

$$f(\mathbf{x}, t_n; \mathbf{v}, s, \theta) = f_n(\mathbf{x}; \mathbf{v}, s, \theta) \qquad \text{in} \quad \mathcal{L} \times \mathbb{R}^d \times (0, 1] \times \mathbb{R}_+ \ , \tag{5.2}$$

$$f(\mathbf{x}, t; \mathbf{v}, s, \theta) = f_B(\mathbf{x}, t; \mathbf{v}, s, \theta) \qquad \text{in} \quad \partial\mathcal{L} \times [t_n, t] \times \mathbb{R}^d \times (0, 1] \times \mathbb{R}_+ \ , \tag{5.3}$$

$$\left. \frac{\partial f(\mathbf{x}, t; \mathbf{v}, s, \theta)}{\partial s} \right|_{s=0} = 0 \qquad \text{in} \quad \mathcal{L} \times [t_n, t] \times \mathbb{R}^d \times \mathbb{R}_+, \tag{5.4}$$

where $\partial\mathcal{L}$ is the boundary of the computational domain $\mathcal{L}$. The fractional step method is applied to the reduced kinetic spray equation in (5.1) by splitting the equation into three

sub problems that can be treated independently. These problems are

$$\text{convection:} \quad \frac{\partial}{\partial t}(f) + \nabla_{\mathbf{x}} \cdot (\mathbf{v}f) = 0, \qquad \text{in } \mathcal{L} \times [t_n, t], \tag{5.5}$$

$$f(\mathbf{x}, t_n) = f_{nc}(\mathbf{x}) \qquad \text{in } \mathcal{L}, \tag{5.6}$$

$$f(\mathbf{x}, t) = f_B(\mathbf{x}, t) \qquad \text{in } \partial\mathcal{L} \times [t_n, t], \tag{5.7}$$

$$\text{droplet forces, heat transfer:} \quad \frac{\partial}{\partial t}(f) + \nabla_{\mathbf{v}} \cdot \left\{ \left(\frac{\mathbf{U}_g - \mathbf{v}}{\mathrm{St}(1)s} + \frac{1}{\mathrm{Fr}}\mathbf{e_g} \right) f \right\} + \frac{\partial}{\partial \theta} \left(\mathrm{He}(\mathbf{v}, s, \theta) f \right) = 0$$

$$\text{in } [t_n, t] \times \mathbb{R}^d \times \mathbb{R}_+, \tag{5.8}$$

$$f(t_n; \mathbf{v}, \theta) = f_{nf}(\mathbf{v}, \theta) \qquad \text{in } \mathbb{R}^d \times \mathbb{R}_+, \tag{5.9}$$

$$\text{evaporation:} \quad \frac{\partial}{\partial t}(f) - \mathrm{Ev}(\mathbf{v}, \theta) \frac{\partial}{\partial s}(f) = 0 \qquad \text{in } [t_n, t] \times [0, 1], \tag{5.10}$$

$$f(t_n; s) = f_{ne}(s) \qquad \text{in } [0, 1], \tag{5.11}$$

$$\left. \frac{\partial f(\mathbf{x}, t; \mathbf{v}, s, \theta)}{\partial s} \right|_{s=0} = 0 \qquad \text{in } [t_n, t]. \tag{5.12}$$

In the convection sub problem the velocity, surface and temperature variables are fixed. In the evaporation step the position, velocity and temperature are not varying and, for the sub problem in which droplet forces and heat transfer are acting, the position and surface variables are unchanged.

The idea of the fractional step method is to alternate the solution of the problems (5.5)-(5.12) in such a way that at least the accuracy of the numerical scheme with the lowest order is preserved. Indeed, the Strang splitting in time [165], which is applied in this work, guarantees this property. It simply requires that in one fractional step only those physical effects are considered that have similar time scales [37]. Satisfying this requirement, the second-order accuracy of the overall method is achieved by using second-order schemes in all variables for each sub problem.

The procedure of Strang demands the following solution sequence for each time step $\Delta t = t_{n+1} - t_n$:

- **(i)** $\Delta t/2$ convection,
- **(ii)** $\Delta t/2$ droplet forces and heat transfer,
- **(iii)** Δt evaporation,
- **(iv)** $\Delta t/2$ droplet forces and heat transfer,
- **(v)** $\Delta t/2$ convection.

For each of the above steps the solution of the previous one is used as the 'initial condition' but for the first fractional step the solution of the previous time-step or the initial condition

of the overall problem is taken into account. Note that the sequence of fractional steps may be changed, but Descombes and Massot [37] recommend putting the sub problem with the smallest time scale at the beginning and end of the Strang procedure. It may seem that using a Strang splitting advances the solution by $3\Delta t$. However, in each fractional step only parts of the kinetic spray equation (5.1) are considered and each sub problem is advanced by Δt only.

5.2.2 Strang Splitting of the Moment Transport Equations

The system of moment transport equations defined in (4.76) and (4.83) is now split into three subsystems which are solved in the Strang sequence (see Section 5.2.1). To this end, the moment transforms and moment closure, as introduced in Chapter 4, are applied to each sub problem in (5.5)-(5.12) independently.

For each section I_k, $(k = 1, \ldots, N_s)$, the convection problem defined in (5.5)-(5.7) is transformed into

$$
\begin{aligned}
&\frac{\partial}{\partial t}(\mathrm{M}_k^{0,0,0}) + \frac{\partial}{\partial x_i}(\mathrm{M}_{k;i}^{0,0,1}) = 0 \ , && \frac{\partial}{\partial t}(\mathrm{M}_k^{3/2,0,0}) + \frac{\partial}{\partial x_i}(\mathrm{M}_{k;i}^{3/2,0,1}) = 0 \ , \\
&\frac{\partial}{\partial t}(\mathrm{M}_k^{3/2,1,0}) + \frac{\partial}{\partial x_i}(\mathrm{M}_{k;i}^{3/2,1,1}) = 0 \ , && \frac{\partial}{\partial t}(\mathrm{M}_{k;l}^{3/2,0,1}) + \frac{\partial}{\partial x_i}(\mathrm{M}_{k;li}^{3/2,0,2}) = 0 \ , \\
&\frac{\partial}{\partial t}(\mathrm{M}_{k;lm}^{3/2,0,2}) + \frac{\partial}{\partial x_i}(\mathrm{M}_{k;lmi}^{3/2,0,3}) = 0 \ , && \frac{\partial}{\partial t}(\mathrm{M}_{k;lmn}^{3/2,0,3}) + \frac{\partial}{\partial x_i}(\mathrm{M}_{k;lmni}^{3/2,0,4}) = 0 \ ,
\end{aligned}
\tag{5.13}
$$

with appropriate initial and boundary condition (see Chapter 6). This system of equations is considered as closed because the moment $\mathrm{M}_{k;lmni}^{3/2,0,4}$ in $(5.13)_6$ can be written in terms of the parameters $\mathcal{W}_k^4$ (4.11) using relation $(4.83)_7$. In Section 5.3 this system will again be untangled to obtain a first- and second-order convection scheme that uses the set of parameters $\mathcal{W}_k^4$ for the spatial fluxes in each equation of (5.13).

The sub problem (5.8), (5.9) for the droplet forces and heat transfer leads to the moment equations

$$
\begin{aligned}
&\frac{\partial}{\partial t}(\mathrm{M}_k^{0,0,0}) = 0 \ , && \frac{\partial}{\partial t}(\mathrm{M}_k^{3/2,0,0}) = 0 \ , \\
&\frac{\partial}{\partial t}(\mathrm{M}_k^{3/2,1,0}) = \mathcal{R}_k \ , && \frac{\partial}{\partial t}(\mathrm{M}_{k;l}^{3/2,0,1}) = \frac{1}{\mathrm{Fr}}\mathbf{e_g}\cdot\mathbf{e}_l\mathrm{M}_k^{3/2,0,0} + D_{k;l}^1 \ , \\
&\frac{\partial}{\partial t}(\mathrm{M}_{k;lm}^{3/2,0,2}) = +\frac{1}{\mathrm{Fr}}\left(\mathbf{e_g}\cdot\mathbf{e}_l\mathrm{M}_{k;m}^{3/2,0,1} + \mathbf{e_g}\cdot\mathbf{e}_m\mathrm{M}_{k;l}^{3/2,0,1}\right) + D_{k;lm}^2 \ , \\
&\frac{\partial}{\partial t}(\mathrm{M}_{k;lmn}^{3/2,0,3}) = +\frac{1}{\mathrm{Fr}}\left(\mathbf{e_g}\cdot\mathbf{e}_l\mathrm{M}_{k;mn}^{3/2,0,2} + \mathbf{e_g}\cdot\mathbf{e}_m\mathrm{M}_{k;ln}^{3/2,0,2} + \mathbf{e_g}\cdot\mathbf{e}_n\mathrm{M}_{k;lm}^{3/2,0,2}\right) + D_{k;lmn}^3 \ ,
\end{aligned}
\tag{5.14}
$$

with the heat transfer and drag terms defined in $(4.83)_1$ and $(4.83)_{4,5,6}$. Note that in subsystem (5.14), the number and mass of droplets, i.e. $\mathrm{M}_k^{0,0,0}$ and $\mathrm{M}_k^{3/2,0,0}$, remain constant. Consequently, the exponential parameter b_k computed from the ratio $\mathrm{M}_k^{3/2,0,0}/\mathrm{M}_k^{0,0,0}$ remains unchanged as well. Note also that during this sub problem neither a coupling

between the sections nor an interaction between the cells in real space is necessary. Instead it is regarded as coupling between the velocity abscissas. It is further observed that equation $(5.14)_3$ can be solved independently from the other equations in (5.14), allowing a numerical procedure which is optimised for the heat transfer (see Section 5.4).

Applying the moment transform and moment closure to the evaporation problem (5.10)-(5.12) yields the system

$$
\begin{aligned}
\frac{\partial}{\partial t}(\mathrm{M}_k^{0,0,0}) &= -E^{0,0,0}(k,k) + E^{0,0,0}(k,k+1)\ , \\
\frac{\partial}{\partial t}(\mathrm{M}_k^{3/2,0,0}) &= -\left(E^{3/2,0,0}(k,k) + \mathcal{E}^{3/2,0,0}(k)\right) + E^{3/2,0,0}(k,k+1)\ , \\
\frac{\partial}{\partial t}(\mathrm{M}_k^{3/2,1,0}) &= -\left(E^{3/2,1,0}(k,k) + \mathcal{E}^{3/2,1,0}(k)\right) + E^{3/2,1,0}(k,k+1)\ , \\
\frac{\partial}{\partial t}(\mathrm{M}_{k;i}^{3/2,0,1}) &= -\left(E_i^{3/2,0,1}(k,k) + \mathcal{E}_i^{3/2,0,1}(k)\right) + E_i^{3/2,0,1}(k,k+1)\ , \\
\frac{\partial}{\partial t}(\mathrm{M}_{k;ij}^{3/2,0,2}) &= -\left(E_{ij}^{3/2,0,2}(k,k) + \mathcal{E}_{ij}^{3/2,0,2}(k)\right) + E_{ij}^{3/2,0,2}(k,k+1)\ , \\
\frac{\partial}{\partial t}(\mathrm{M}_{k;lmn}^{3/2,0,3}) &= -\left(E_{lmn}^{3/2,0,3}(k,k) + \mathcal{E}_{lmn}^{3/2,0,3}(k)\right) + E_{lmn}^{3/2,0,3}(k,k+1)\ ,
\end{aligned}
\tag{5.15}
$$

which also follows from (4.76) by setting the terms of convection, droplet forces and heat transfer to zero. The terms $E_{lmn}^{K,L,M}(k,r)$ and $\mathcal{E}_{lmn}^{K,L,M}(k)$ are defined in $(4.83)_{2,3}$. The above equations couple the sets of moment transport equations of neighbouring sections through the flux term $E_{lmn}^{K,L,M}(k,r)$. $\mathcal{E}_{lmn}^{K,L,M}(k)$ can be considered as an interaction term with the gas phase. The system of equations in (5.15) is closed and can, in principle, be solved but it is not guaranteed that the number and mass of droplets will be conserved. In Section 5.5 the analytical solution of (5.10)-(5.12) will be used to derive a conservative finite volume-like scheme in surface space.

This section is concluded by addressing the advantages of applying the Strang splitting to the moment transport equations in (4.76) and (4.83). First of all, splitting into subsystems allows the application of standardised numerical schemes and even analytical techniques (see Section 5.4) without reducing the order of accuracy. Secondly, in the case when time scales of the different spray effects are known in advance, the efficiency and accuracy of the global scheme can be increased by performing a splitting which subsumes those physical effects that have comparable time scales [37]. Another issue, that is special to QBSM, is the possibility of computing the parameters in $\mathcal{W}_k^4$ (4.11) after every fractional step. The multiple alignment between moments in $\mathcal{V}_k^2$ (4.17) and parameters in $\mathcal{W}_k^4$ within one time step has a stabilising effect on the overall scheme.

5.3 Discretisation of the Convective Part

In this section the starting point is the two-dimensional system (5.13) which is written as

$$\frac{\partial \mathbf{W}^{(k)}}{\partial t} + \frac{\partial \mathbf{H}_x^{(k)}}{\partial x} + \frac{\partial \mathbf{H}_y^{(k)}}{\partial y} = 0 \ , \tag{5.16}$$

with

$$\mathbf{W}^{(k)} := \Big(\mathrm{M}_k^{0,0,0}, \mathrm{M}_k^{3/2,0,0}, \mathrm{M}_k^{3/2,1,0}, \mathrm{M}_{k;x}^{3/2,0,1}, \mathrm{M}_{k;y}^{3/2,0,1}, \mathrm{M}_{k;xx}^{3/2,0,2}, \mathrm{M}_{k;yy}^{3/2,0,2}, \mathrm{M}_{k;xy}^{3/2,0,2}, \mathrm{M}_{k;xxx}^{3/2,0,3}, \mathrm{M}_{k;yyy}^{3/2,0,3}, \mathrm{M}_{k;xyy}^{3/2,0,3}, \mathrm{M}_{k;xxy}^{3/2,0,3} \Big)^{\mathrm{T}} \ . \tag{5.17}$$

The flux terms in (5.16) are defined as

$$\begin{aligned} \mathbf{H}_x^{(k)} &:= \int_{\mathbb{R}^2} \int_{\mathbb{R}_+} \int_{s_k}^{s_{k+1}} v_x \mathbf{k}(v_x, v_y, s, \theta) \exp(-b_k s) \delta(\theta - \Theta_k) \sum_{\alpha=1}^{4} n_k^\alpha \boldsymbol{\delta}[\mathbf{v} - \mathbf{U}_k^\alpha] ds d\theta d\mathbf{v} \\ &= \int_{\mathbb{R}^2} v_x \mathrm{I}_{3/2}^{(k)} \mathbf{K}^{(k)}(v_x, v_y) \sum_{\alpha=1}^{4} n_k^\alpha \delta(v_x - (\mathbf{U}_k^\alpha)_x) \delta(v_y - (\mathbf{U}_k^\alpha)_y) dv_x dv_y \ , \end{aligned} \tag{5.18}$$

$$\begin{aligned} \mathbf{H}_y^{(k)} &:= \int_{\mathbb{R}^2} \int_{\mathbb{R}_+} \int_{s_k}^{s_{k+1}} v_y \mathbf{k}(v_x, v_y, s, \theta) \exp(-b_k s) \delta(\theta - \Theta_k) \sum_{\alpha=1}^{4} n_k^\alpha \boldsymbol{\delta}[\mathbf{v} - \mathbf{U}_k^\alpha] ds d\theta d\mathbf{v} \\ &= \int_{\mathbb{R}^2} v_y \mathrm{I}_{3/2}^{(k)} \mathbf{K}^{(k)}(v_x, v_y) \sum_{\alpha=1}^{4} n_k^\alpha \delta(v_x - (\mathbf{U}_k^\alpha)_x) \delta(v_y - (\mathbf{U}_k^\alpha)_y) dv_x dv_y \ , \end{aligned} \tag{5.19}$$

with

$$\mathbf{k}(v_x, v_y, s, \theta) := \big(1, s^{3/2}, \theta s^{3/2}, v_x s^{3/2}, v_y s^{3/2}, {v_x}^2 s^{3/2}, {v_y}^2 s^{3/2}, v_x v_y s^{3/2}, v_x^3 s^{3/2}, {v_y}^3 s^{3/2}, v_y {v_x}^2 s^{3/2}, v_x {v_y}^2 s^{3/2} \big)^{\mathrm{T}} \tag{5.20}$$

and

$$\mathrm{I}_{3/2}^{(k)} \mathbf{K}^{(k)}(v_x, v_y) := \mathrm{I}_{3/2}^{(k)} \left(\mathrm{I}_0^{(k)} / \mathrm{I}_{3/2}^{(k)}, 1, \Theta_k, v_x, v_y, {v_x}^2, {v_y}^2, v_x v_y, v_x^3, {v_y}^3, v_y {v_x}^2, v_x {v_y}^2 \right)^{\mathrm{T}} . \tag{5.21}$$

The integrals in (5.21) are defined as

$$\mathrm{I}_K^{(k)} = \int_{s_k}^{s_{k+1}} s^K \exp(-b_k s) ds \ . \tag{5.22}$$

The numerical solution of equation system (5.16) is not obvious because after defining the quantities $m_k := \mathrm{M}_k^{3/2,0,0}$ and $m_k \bar{v}_i^k := \mathrm{M}_{k;i}^{3/2,0,1}$, it follows from the second, fourth and fifth equation of (5.16), i.e.

$$\begin{aligned} &\frac{\partial}{\partial t}(m_k) + \frac{\partial}{\partial x_i}(m_k \bar{v}_i^k) = 0 \ , \\ &\frac{\partial}{\partial t}(m_k \bar{v}_i^k) + \frac{\partial}{\partial x_j}(m_k \bar{v}_i^k \bar{v}_j^k) = -\varepsilon \frac{\partial p}{\partial x_i} \ , \qquad \varepsilon \to 0, \end{aligned} \tag{5.23}$$

that the system of moment equations in (5.16) is related to a 'pressureless gas dynamic system' (cf. [18, 19, 27]). This type of system is considered as weakly hyperbolic because with $\varepsilon = 0$ equations (5.23) cannot be considered as (strongly) hyperbolic. Pressureless gas dynamic systems are known for the appearance of strong mass concentrations or vacuum states.[2] Nevertheless, these type of systems are extensively studied and established numerical schemes do exist [19]. In this work such a scheme is extended to equation system (5.16).

Before doing so, the Strang splitting will be applied to the convection as well. To this end, the two-dimensional convection problem (5.16) will be split into the one-dimensional convection parts (dimensional splitting [102]):

$$\text{convection in } x\text{-direction:} \qquad \frac{\partial \mathbf{W}^{(k)}}{\partial t} + \frac{\partial \mathbf{H}_x^{(k)}}{\partial x} = 0 \ , \tag{5.24}$$

$$\text{convection in } y\text{-direction:} \qquad \frac{\partial \mathbf{W}^{(k)}}{\partial t} + \frac{\partial \mathbf{H}_y^{(k)}}{\partial y} = 0 \ . \tag{5.25}$$

With these fractional steps the new Strang sequence reads

(i) $\Delta t/2$ convection in x-direction,

(ii) $\Delta t/2$ convection in y-direction,

(iii) $\Delta t/2$ droplet forces and heat transfer,

(iv) Δt evaporation, etc.

Note that the dimensional splitting is not the only possible way to treat the convection system (5.16). Dufour and Villedieu [44] developed a second-order scheme for two- and three-dimensional convection without using a splitting method or imposing any restriction on the type of grid.

5.3.1 Kinetic Schemes of Bouchut, Jin and Li

Numerical schemes for the one-dimensional convection systems (5.24) or (5.25) can either be derived with the method of Roe [139] (see also [43]) or the kinetic approximation of

[2] If $(5.23)_1$ is multiplied by $\bar{v}_i^k$ and the resulting equation is subtracted from the one-dimensional version of $(5.23)_2$, the well-known Burgers equation is obtained. This equation has no solution after finite time if the initial value $\bar{v}_n^k(x)$ is decreasing.

Bouchut [18]. In this work, the approach of Bouchut [18] is followed for the first- and second-order finite volume discretisation of convection problems (5.24) and (5.25).

The kinetic sub problem of convection in x-direction defined in (5.5) and (5.6) is written as[3]

$$\frac{\partial}{\partial t}(f) + v_x \frac{\partial}{\partial x}(f) = 0 \qquad \text{in } [t_n, t] \times \mathcal{L}_x \ , \tag{5.26}$$

$$f_{ncx}(x) = a(x, t_n) \sum_{\alpha=1}^{4} n^{\alpha}(x, t_n) \delta(v_x - U_x^{\alpha}(x, t_n)) \qquad \text{in } \mathcal{L}_x \ , \tag{5.27}$$

where the initial condition is equal to the approximate NDF introduced in (4.8). Assuming that the time-interval $[t_n, t]$ is small enough and the position of interest is sufficiently far away from the boundary, the boundary condition in (5.7) does not have an effect on the solution of the linear hyperbolic problem (5.26)-(5.27), which is

$$f(x, t) = f_{ncx}(x - (t - t_n)v_x) \ . \tag{5.28}$$

If the boundary conditions at $x = x_{\text{left}}$ and $x = x_{\text{right}}$, which may be of Dirichlet-, Neumann- or Robin-type are considered, the solution (5.28) has to be modified. However, for simplicity's sake, no boundary conditions are considered.

Thanks to the relation between $\mathcal{W}^4$ and $\mathcal{V}^2$, outlined in Section 4.4, (5.28) is an exact solution of (5.26)-(5.27) but in general f will not be of the form (4.8) when $t > t_n$. However, this exact solution allows the derivation of an entropy inequality, which ensures that the number and mass of droplets is always positive (realisability). It also guarantees the maximum principle on the averaged velocity. The proof is not given here; the interested reader is referred to Bouchut [18].

To obtain the final convection scheme, the equidistant discretisation $x_i \in \mathcal{L}_x$, $(i = 1, \ldots, N_x)$ is introduced with $x_1 = x_{\text{left}}$, $x_{N_x} = x_{\text{right}}$ and $\Delta x_i = x_i - x_{i+1}$. Integration of the moment equations (5.13) in the cell $]x_{i-1/2}, x_{i+1/2}[$ and the time-interval $]t_n, t_{n+1}[$ yields

$$\begin{aligned} &\frac{1}{\Delta x_i} \int_{x_{i-1/2}}^{x_{i+1/2}} \mathrm{M}_{lmn}^{K,L,M}(x, t_{n+1}) dx - \frac{1}{\Delta x_i} \int_{x_{i-1/2}}^{x_{i+1/2}} \mathrm{M}_{lmn}^{K,L,M}(x, t_n) dx \\ &\qquad + \frac{\Delta t}{\Delta x_i} \left(\phi_{lmn}^{K,L,M}(x_{i+1/2}, t_{n+1}) - \phi_{lmn}^{K,L,M}(x_{i-1/2}, t_{n+1}) \right) = 0 \ , \end{aligned} \tag{5.29}$$

with the flux term

$$\begin{aligned} &\phi_{lmn}^{K,L,M}(x, t) = \\ &\qquad \frac{1}{(t - t_n)} \int_{]t_n, t[} \int_{\mathbb{R}^2} \int_{\mathbb{R}_+} \int_{s_k}^{s_{k+1}} s^K \theta^L v_x v_l v_m v_n f_{ncx}(x - (t - t_n)v_x) ds \, d\theta \, dv_x \, dv_y \, dt \ . \end{aligned} \tag{5.30}$$

[3] In the remainder of this section the index k for section I_k is suppressed. The convection schemes are the same for all sections.

In this flux term the exact solution (5.28) was considered. It is advantageous to partition the velocity integral in (5.30) into two parts that consider the positive and the negative fluxes over an interface separately, i.e.

$$\phi_{lmn}^{K,L,M}(x,t_{n+1}) = \frac{1}{\Delta t}\left(\int_{t_n}^{t_{n+1}} \int_{\mathbb{R}} \int_{\mathbb{R}_+} \int_{\mathbb{R}_+} \int_{s_k}^{s_{k+1}} s^K \theta^L v_x v_l v_m v_n f_{ncx}(x-(t-t_n)v_x) ds\, d\theta\, dv_x\, dv_y\, dt \right.$$
$$\left. + \int_{t_n}^{t_{n+1}} \int_{\mathbb{R}} \int_{\mathbb{R}_-} \int_{\mathbb{R}_+} \int_{s_k}^{s_{k+1}} s^K \theta^L v_x v_l v_m v_n f_{ncx}(x-(t-t_n)v_x) ds\, d\theta\, dv_x\, dv_y\, dt \right). \quad (5.31)$$

Let

$$\mathrm{M}_{lmn}^{K,L,M}|_i^n = \frac{1}{\Delta x_i} \int_{x_{i-1/2}}^{x_{i+1/2}} \mathrm{M}_{lmn}^{K,L,M}(x,t_n) dx \quad (5.32)$$

be the space-averaged moment in one cell. Then (5.29) can be written in the conservative, finite volume form

$$\mathrm{M}_{lmn}^{K,L,M}|_i^{n+1} - \mathrm{M}_{lmn}^{K,L,M}|_i^n + \frac{\Delta t}{\Delta x_i}\left(\phi_{lmn}^{K,L,M}(x_{i+1/2},t_{n+1}) - \phi_{lmn}^{K,L,M}(x_{i-1/2},t_{n+1}) \right) = 0\ . \quad (5.33)$$

5.3.2 First-Order Finite Volume Scheme

To get a first-order upwind scheme, it is assumed that the chosen moments $\mathrm{M}_{k;lmn}^{K,L,M}$ are piecewise constant and the CFL condition

$$\Delta t |v_x| \leq \Delta x_i, \quad \text{for all} \quad i \quad (5.34)$$

is satisfied. With these assumptions, the substitution of the initial condition (5.27) and a change in variables, the fluxes in x-direction for the chosen moments in cell (i,j) can be

written in the vectorial form (see notation in (5.17) and (5.21))

$$\begin{aligned}\mathbf{W}|_{ij}^{n+1} - \mathbf{W}|_{ij}^{n} = -\frac{1}{\Delta x_i}\Big[&+ \int_{\mathbb{R}^2} \tfrac{1}{2}(v_x + |v_x|)\mathrm{I}_{3/2}\mathbf{K}(v_x, v_y) \sum_{\alpha=1}^{4} n^{\alpha}\boldsymbol{\delta}[\mathbf{v} - \mathbf{U}^{\alpha}]dv_x dv_y\Big|_{ij} \\ &+ \int_{\mathbb{R}^2} \tfrac{1}{2}(v_x - |v_x|)\mathrm{I}_{3/2}\mathbf{K}(v_x, v_y) \sum_{\alpha=1}^{4} n^{\alpha}\boldsymbol{\delta}[\mathbf{v} - \mathbf{U}^{\alpha}]dv_x dv_y\Big|_{i+1j} \\ &- \int_{\mathbb{R}^2} \tfrac{1}{2}(v_x + |v_y|)\mathrm{I}_{3/2}\mathbf{K}(v_x, v_y) \sum_{\alpha=1}^{4} n^{\alpha}\boldsymbol{\delta}[\mathbf{v} - \mathbf{U}^{\alpha}]dv_x dv_y\Big|_{i-1j} \\ &- \int_{\mathbb{R}^2} \tfrac{1}{2}(v_x - |v_x|)\mathrm{I}_{3/2}\mathbf{K}(v_x, v_y) \sum_{\alpha=1}^{4} n^{\alpha}\boldsymbol{\delta}[\mathbf{v} - \mathbf{U}^{\alpha}]dv_x dv_y\Big|_{ij}\Big] \ .\end{aligned} \tag{5.35}$$

The first two integrals in (5.35) represent the flux over the eastern interface (EI) of a cell in two-dimensional real space. Evaluating these integrals yields

$$\begin{aligned}\mathbf{G}_{EI}\big|_{ij} &= + \sum_{\alpha=1}^{4} n^{\alpha}\max(U_x^{\alpha}, 0)\mathrm{I}_{3/2}\mathbf{K}(U_x^{\alpha}, U_y^{\alpha})\big|_{ij} \\ &\quad + \sum_{\alpha=1}^{4} n^{\alpha}\min(U_x^{\alpha}, 0)\mathrm{I}_{3/2}\mathbf{K}(U_x^{\alpha}, U_y^{\alpha})\big|_{i+1j} \\ &= \mathbf{G}_{EI}^{+u}\big|_{ij} + \mathbf{G}_{WI}^{-u}\big|_{i+1j} \ .\end{aligned} \tag{5.36}$$

For the flux through the western interface (WI) of the same cell the following expression is obtained from integral three and four of equation (5.35)

$$\begin{aligned}\mathbf{G}_{WI}\big|_{ij} &= + \sum_{\alpha=1}^{4} n^{\alpha}\min(U_x^{\alpha}, 0)\mathrm{I}_{3/2}\mathbf{K}(U_x^{\alpha}, U_{\alpha y})\big|_{ij} \\ &\quad + \sum_{\alpha=1}^{4} n^{\alpha}\max(U_x^{\alpha}, 0)\mathrm{I}_{3/2}\mathbf{K}(U_x^{\alpha}, U_y^{\alpha})\big|_{i-1j} \\ &= \mathbf{G}_{WI}^{-u}\big|_{ij} + \mathbf{G}_{EI}^{+u}\big|_{i-1j} \ .\end{aligned} \tag{5.37}$$

From these expressions we obtain the first-order scheme

$$\mathbf{W}|_{ij}^{n+1} - \mathbf{W}|_{ij}^{n} + \frac{\Delta t}{\Delta x_i}\Big[\mathbf{G}_{EI}\big|_{ij} - \mathbf{G}_{WI}\big|_{ij}\Big] = \mathbf{0} \ , \tag{5.38}$$

which can also be written as

$$\mathbf{W}|_{ij}^{n+1} = \mathbf{W}|_{ij}^{n} - \frac{\Delta t}{\Delta x_i}\Big[\mathbf{G}_{EI}^{+u}\big|_{ij} + \mathbf{G}_{WI}^{-u}\big|_{i+1j} - \mathbf{G}_{WI}^{-u}\big|_{ij} - \mathbf{G}_{EI}^{+u}\big|_{i-1j}\Big] \ . \tag{5.39}$$

An expression similar to (5.38) or (5.39) can be found for convection in y-direction. It reads

$$\begin{aligned}\mathbf{W}|_{ij}^{n+1} - \mathbf{W}|_{ij}^{n} &= -\frac{\Delta t}{\Delta y_j}\left[\mathbf{J}_{NI}\big|_{ij} - \mathbf{J}_{SI}\big|_{ij}\right] \\ &= -\frac{\Delta t}{\Delta y_j}\left[\mathbf{J}_{NI}^{+v}\big|_{ij} + \mathbf{J}_{SI}^{-v}\big|_{ij+1} - \mathbf{J}_{SI}^{-v}\big|_{ij} - \mathbf{J}_{NI}^{+v}\big|_{ij-1}\right] ,\end{aligned} \tag{5.40}$$

with

$$\begin{aligned}\mathbf{J}_{NI}\big|_{ij} &= +\sum_{\alpha=1}^{4} n^{\alpha}\max(U_y^{\alpha},0)\mathrm{I}_{3/2}\mathbf{K}(U_x^{\alpha},U_y^{\alpha})\big|_{ij} \\ &\quad + \sum_{\alpha=1}^{4} n^{\alpha}\min(U_y^{\alpha},0)\mathrm{I}_{3/2}\mathbf{K}(U_x^{\alpha},U_y^{\alpha})\big|_{ij+1} \\ &= \mathbf{J}_{NI}^{+v}\big|_{ij} + \mathbf{J}_{SI}^{-v}\big|_{ij+1}\end{aligned} \tag{5.41}$$

and

$$\begin{aligned}\mathbf{J}_{SI}\big|_{ij} &= +\sum_{\alpha=1}^{4} n^{\alpha}\min(U_y^{\alpha},0)\mathrm{I}_{3/2}\mathbf{K}(U_x^{\alpha},U_{\alpha y})\big|_{ij} \\ &\quad + \sum_{\alpha=1}^{4} n^{\alpha}\max(U_y^{\alpha},0)\mathrm{I}_{3/2}\mathbf{K}(U_x^{\alpha},U_y^{\alpha})\big|_{ij-1} \\ &= \mathbf{J}_{WI}^{-u}\big|_{ij} + \mathbf{J}_{EI}^{+u}\big|_{i-1j} .\end{aligned} \tag{5.42}$$

It is concluded that the convection of the chosen moments can be described with the first-order finite volume schemes (5.39) in x-direction and (5.40) in y-direction. Notice that the flux terms can be evaluated with the parameters $\mathcal{W}^4$ from a previous time step, previous fractional step or the initial condition of the global problem. This resolves issue (iv) in Section 5.1.

5.3.3 Second-Order Finite Volume Scheme

The starting point of the derivation for the second-order finite volume scheme is the representation for the fluxes (5.30) of the chosen moments. In vectorial form these fluxes read

$$\begin{aligned}\boldsymbol{\phi}(x_{i+1/2},t_{n+1}) = \frac{1}{\Delta t}\int_{t_n}^{t_{n+1}}\int_{\mathbb{R}^2}\int_{\mathbb{R}_+}\int_{s_k}^{s_{k+1}} v_x\mathbf{k}(v_x,v_y,s,\theta) \\ \times\exp(-b_k(x_{i+1/2}-(t-t_n)v_x)s)\delta(\theta-\Theta_k(x_{i+1/2}-(t-t_n)v_x)) \\ \times\sum_{\alpha=1}^{4} n^{\alpha}(x_{i+1/2}-(t-t_n)v_x)\boldsymbol{\delta}[\mathbf{v}-\mathbf{U}^{\alpha}(x_{i+1/2}-(t-t_n)v_x)]dsd\theta dv_x dv_y dt .\end{aligned} \tag{5.43}$$

It is transformed into

$$\boldsymbol{\phi}(x_{i+1/2},t_{n+1}) = \frac{1}{\Delta t}\sum_{\alpha=1}^{4}\int_{t_n}^{t_{n+1}}\int_{\mathbb{R}^2} v_x \mathbf{K}(v_x,v_y) m^\alpha(x_{i+1/2}-(t-t_n)v_x)$$
$$\times\, \boldsymbol{\delta}[\mathbf{v}-\mathbf{U}^\alpha(x_{i+1/2}-(t-t_n)v_x)]dv_x dv_y dt \quad (5.44)$$

by evaluating the surface and temperature integrals and using the definition

$$m^\alpha(x) := I_{3/2}(x) n^\alpha(x)\ . \quad (5.45)$$

The change of variables $x = x_{i+1/2}-(t-t_n)v_x$ yields

$$\begin{aligned}\boldsymbol{\phi}(x_{i+1/2},t_{n+1}) &= \frac{1}{\Delta t}\sum_{\alpha=1}^{4}\int_{\mathbb{R}^2}\int_{x_{i+1/2}-v_x\Delta t}^{x_{i+1/2}} \mathbf{K}(v_x,v_y)m^\alpha(x)\boldsymbol{\delta}[\mathbf{v}-\mathbf{U}^\alpha(x)]dx dv_x dv_y \\ &=: \boldsymbol{\phi}^-(x_{i+1/2},t_{n+1}) + \boldsymbol{\phi}^+(x_{i+1/2},t_{n+1})\ ,\end{aligned} \quad (5.46)$$

with

$$\boldsymbol{\phi}^-(x_{i+1/2},t_{n+1}) =$$
$$-\frac{1}{\Delta t}\sum_{\alpha=1}^{4}\int_{\mathbb{R}}\int_{\mathbb{R}_-}\int_{x_{i+1/2}}^{x_{i+1/2}-v_x\Delta t} \mathbf{K}(v_x,v_y)m^\alpha(x)\boldsymbol{\delta}[\mathbf{v}-\mathbf{U}^\alpha(x)]dx dv_x dv_y \quad (5.47)$$

and

$$\boldsymbol{\phi}^+(x_{i+1/2},t_{n+1}) =$$
$$\frac{1}{\Delta t}\sum_{\alpha=1}^{4}\int_{\mathbb{R}}\int_{\mathbb{R}_+}\int_{x_{i+1/2}-v_x\Delta t}^{x_{i+1/2}} \mathbf{K}(v_x,v_y)m^\alpha(x)\boldsymbol{\delta}[\mathbf{v}-\mathbf{U}^\alpha(x)]dx dv_x dv_y\ . \quad (5.48)$$

The latter two integrals can be written as

$$\boldsymbol{\phi}^-(x_{i+1/2},t_{n+1}) = -\frac{1}{\Delta t}\sum_{\alpha=1}^{4}\int_{x_{i+1/2}}^{x_{i+3/2}} \mathbf{K}(U_x^\alpha(x),U_y^\alpha)m^\alpha(x)\mathbb{1}_{x>x_{i+1/2}-U_x^\alpha(x)\Delta t}dx\ , \quad (5.49)$$

$$\boldsymbol{\phi}^+(x_{i+1/2},t_{n+1}) = \frac{1}{\Delta t}\sum_{\alpha=1}^{4}\int_{x_{i-1/2}}^{x_{i+1/2}} \mathbf{K}(U_x^\alpha(x),U_y^\alpha)m^\alpha(x)\mathbb{1}_{x>x_{i+1/2}-U_x^\alpha(x)\Delta t}dx\ . \quad (5.50)$$

If $(\mathrm{I}_0/\mathrm{I}_{3/2})(x)$ in $\mathbf{K}$, $m^\alpha(x)$ and $U_x^\alpha(x)$ are reconstructed by constant functions the above first-order scheme is recovered. For a second-order approximation these terms are assumed to be linear in x. They read

$$\mu(x) := (\mathrm{I}_0/\mathrm{I}_{3/2})(x) = \bar{\mu}_i + D\mu_i(x - x_{i+1/2}), \tag{5.51}$$

$$m^\alpha(x) = m_i^\alpha + Dm_i^\alpha(x - x_{i+1/2}), \tag{5.52}$$

$$U_x^\alpha(x) = \bar{U}_x^\alpha|_i + DU_x^\alpha|_i(x - x_{i+1/2}). \tag{5.53}$$

The substitution of these relations into the fluxes (5.49) and (5.50) yields

$$\boldsymbol{\phi}^-(x_{i+1/2}, t_{n+1}) = -\frac{1}{\Delta t}\sum_{\alpha=1}^{4}\int_{x_{i+1/2}}^{x_{i+1/2}^{\alpha R}} \mathbf{K}(U_x^\alpha(x), U_y^\alpha) m^\alpha(x) dx, \tag{5.54}$$

$$\boldsymbol{\phi}^+(x_{i+1/2}, t_{n+1}) = \frac{1}{\Delta t}\sum_{\alpha=1}^{4}\int_{x_{i+1/2}^{\alpha L}}^{x_{i+1/2}} \mathbf{K}(U_x^\alpha(x), U_y^\alpha) m^\alpha(x) dx\ , \tag{5.55}$$

with the definitions

$$x_{i+1/2}^{\alpha R} := x_{i+1/2} - \Delta t \frac{\min(U_{i+1/2}^{\alpha R}, 0)}{1 + \Delta t DU_x^\alpha|_{i+1}}\ , \tag{5.56}$$

$$U_{i+1/2}^{\alpha R} := \bar{U}_x^\alpha|_{i+1} + (x_{i+1} - x_{i+3/2}) DU_x^\alpha|_{i+1}\ , \tag{5.57}$$

$$x_{i+1/2}^{\alpha L} := x_{i+1/2} - \Delta t \frac{\max(U_{i+1/2}^{\alpha L}, 0)}{1 + \Delta t DU_x^\alpha|_{i+1}}\ , \tag{5.58}$$

$$U_{i+1/2}^{\alpha L} := \bar{U}_x^\alpha|_i + (x_i - x_{i+1/2}) DU_x^\alpha|_{i+1}\ . \tag{5.59}$$

With these definitions, the fluxes $\boldsymbol{\phi}^-(x_{i+1/2}, t_{n+1})$ and $\boldsymbol{\phi}^+(x_{i+1/2}, t_{n+1})$ are obtained by evaluating integrals (5.54) and (5.55). The mean quantities $\bar{\mu}_i^\alpha$, $\bar{U}_x^\alpha|_i$ and the gradients $D\mu_i$, Dm_i^α and $DU_x^\alpha|_i$ remain to be defined. To satisfy the conservation of momentum and number of droplets the mean quantities are chosen according to

$$\bar{\mu}_i = \mu_i - \sum_{\alpha=1}^{4} \frac{D\mu_i Dm_i^\alpha}{12 m_i^\alpha} {\Delta x_i}^2, \tag{5.60}$$

$$\bar{U}_x^\alpha|_i = U_x^\alpha|_i - \frac{Dm_i^\alpha DU_x^\alpha|_i}{12 m_i^\alpha} {\Delta x_i}^2. \tag{5.61}$$

To satisfy the maximum principle on the velocities the slope-limiter

$$DU_x^\alpha|_i = \tfrac{1}{2}\left(\mathrm{sgn}(U_x^\alpha|_{i+1} - U_x^\alpha|_i) + \mathrm{sgn}(U_x^\alpha|_i - U_x^\alpha|_{i-1})\right) \times \min\left\{\frac{\mathrm{abs}(U_x^\alpha|_{i+1} - U_x^\alpha|_i)}{(1 - \Delta x_i Dm_i^\alpha/(6m_i))\Delta x_i}, \frac{\mathrm{abs}(U_x^\alpha|_i - U_x^\alpha|_{i-1})}{(1 - \Delta x_i Dm_i^\alpha/(6m_i))\Delta x_i}, \frac{1}{\Delta t}\right\} \tag{5.62}$$

is used. The same structure is used for the slope-limiter of $D\mu_i$. For the gradient Dm_i^α the `minmod`-limiter is used which satisfies the property of total variation diminishing solutions (cf. [102]).

Bouchut [18] showed that the type of scheme defined in (5.33) and (5.54)-(5.62) is of second-order accuracy in space and time if the CFL condition

$$\begin{gathered}\Delta t \max_{i,j,k} |\mathbf{U}_k^\alpha| \leq \min_{i,j}(\Delta x_i, \Delta y_j), \\ i = 1, \ldots, N_x, \quad j = 1, \ldots, N_y, \quad k = 1, \ldots, N_s\end{gathered} \tag{5.63}$$

is satisfied. The second-order accuracy in time stems from the very special property of the pressureless gas dynamics system [18].

5.4 Numerics for Droplet Forces and Heat Transfer

The objective of this section is the solution of moment equations (see (5.14))

$$\begin{aligned}
&\frac{\partial}{\partial t}(\mathrm{M}_k^{0,0,0}) = 0 \ , && \frac{\partial}{\partial t}(\mathrm{M}_k^{3/2,0,0}) = 0 \ , \\
&\frac{\partial}{\partial t}(\mathrm{M}_k^{3/2,1,0}) = \mathcal{R}_k \ , && \frac{\partial}{\partial t}(\mathrm{M}_{k;l}^{3/2,0,1}) = \frac{1}{\mathrm{Fr}}\mathbf{e_g}\cdot\mathbf{e}_l\mathrm{M}_k^{3/2,0,0} + D_{k;l}^1 \ , \\
&\frac{\partial}{\partial t}(\mathrm{M}_{k;lm}^{3/2,0,2}) = +\frac{1}{\mathrm{Fr}}\left(\mathbf{e_g}\cdot\mathbf{e}_l\mathrm{M}_{k;m}^{3/2,0,1} + \mathbf{e_g}\cdot\mathbf{e}_m\mathrm{M}_{k;l}^{3/2,0,1}\right) + D_{k;lm}^2 \ , \\
&\frac{\partial}{\partial t}(\mathrm{M}_{k;lmn}^{3/2,0,3}) = +\frac{1}{\mathrm{Fr}}\left(\mathbf{e_g}\cdot\mathbf{e}_l\mathrm{M}_{k;mn}^{3/2,0,2} + \mathbf{e_g}\cdot\mathbf{e}_m\mathrm{M}_{k;ln}^{3/2,0,2} + \mathbf{e_g}\cdot\mathbf{e}_n\mathrm{M}_{k;lm}^{3/2,0,2}\right) + D_{k;lmn}^3 \ ,
\end{aligned} \tag{5.64}$$

with the definitions of the heat transfer and drag force terms (see also $(4.83)_1$ and $(4.83)_{4,5,6}$)

$$\begin{aligned}
\mathcal{R}_k &= \int_{s_k}^{s_{k+1}} s^{3/2}\exp(-b_k s)\sum_{\alpha=1}^{4} n_k^\alpha \mathrm{He}(\mathbf{U}_k^\alpha, s, \Theta_k)ds \ , \\
D_{k;l}^1 &= \int_{s_k}^{s_{k+1}} \frac{s^{1/2}}{\mathrm{St}(1)}\exp(-b_k s)ds \sum_{\alpha=1}^{4} n_k^\alpha \left[U_{gl} - (\mathbf{U}_k^\alpha)_l\right] \ , \\
D_{k;lm}^2 &= \int_{s_k}^{s_{k+1}} \frac{s^{1/2}}{\mathrm{St}(1)}\exp(-b_k s)ds \sum_{\alpha=1}^{4} n_k^\alpha (\mathbf{U}_k^\alpha)_j \left[U_{gi} - (\mathbf{U}_k^\alpha)_i\right](\delta_{il}\delta_{jm} + \delta_{im}\delta_{jl}) \ , \\
D_{k;lmn}^3 &= \int_{s_k}^{s_{k+1}} \frac{s^{1/2}}{\mathrm{St}(1)}\exp(-b_k s)ds \\
&\qquad \times \sum_{\alpha=1}^{4} n_k^\alpha (\mathbf{U}_k^\alpha)_s (\mathbf{U}_k^\alpha)_t \left[U_{gr} - (\mathbf{U}_k^\alpha)_r\right](\delta_{rl}\delta_{sn}\delta_{tm} + \delta_{rm}\delta_{sl}\delta_{tn} + \delta_{rn}\delta_{sm}\delta_{tl}) \ .
\end{aligned} \tag{5.65}$$

Notice that $\mathrm{M}_k^{0,0,0}$ and $\mathrm{M}_k^{3/2,0,0}$ remain constant in this fractional step. Therefore, the exponential parameters b_k $(k = 1, \ldots, N_s)$ are not directly influenced by the droplet forces or heat transfer. Notice also that equation $(5.64)_3$ can be computed independently of the other equations in (5.64), i.e. the heat transfer and the droplet forces are uncoupled. Therefore, in the following two sections the two physical phenomena are treated separately with different numerical methods.

5.4.1 Droplet Forces

The drag force model of Stokes allows a semi-analytical solution of equations $(5.64)_{4,5,6}$, $(5.65)_{2,3,4}$. Thanks to the structure of the approximate NDF the equations $(5.65)_{2,3,4}$ can be transformed into[4]

$$
\begin{aligned}
D^1_{k;l} &= \int_{s_k}^{s_{k+1}} \frac{s^{1/2}}{\mathrm{St}(1)} \exp(-b_k s) ds \left(\bar{\mathrm{M}}^0_k U_{gl} - \bar{\mathrm{M}}^1_{k;l} \right) \ , \\
D^2_{k;lm} &= \int_{s_k}^{s_{k+1}} \frac{s^{1/2}}{\mathrm{St}(1)} \exp(-b_k s) ds \left(\bar{\mathrm{M}}^1_{k;j} U_{gi} - \bar{\mathrm{M}}^2_{k;ij} \right) \left(\delta_{il}\delta_{jm} + \delta_{im}\delta_{jl} \right) \ , \\
D^3_{k;lmn} &= \int_{s_k}^{s_{k+1}} \frac{s^{1/2}}{\mathrm{St}(1)} \exp(-b_k s) ds \left(\bar{\mathrm{M}}^2_{k;st} U_{gr} - \bar{\mathrm{M}}^3_{k;str} \right) \left(\delta_{rl}\delta_{sn}\delta_{tm} + \delta_{rm}\delta_{sl}\delta_{tn} + \delta_{rn}\delta_{sm}\delta_{tl} \right) \ ,
\end{aligned}
\tag{5.66}
$$

where the modified moments, $\bar{\mathrm{M}}^M_{k;lmn}$, are defined as (see also (4.33))

$$
\bar{\mathrm{M}}^M_{k;lmn} = \frac{\mathrm{M}^M_{k;lmn}}{\int_{s_k}^{s_{k+1}} s^{3/2} \exp(-b_k s) ds} \ . \tag{5.67}
$$

The time derivatives on the left-hand sides of (5.64) can be transformed into

$$
\frac{\partial}{\partial t}(\mathrm{M}^M_{k;lmn}) = \int_{s_k}^{s_{k+1}} s^{3/2} \exp(-b_k s) ds \frac{\partial \bar{\mathrm{M}}^M_{k;lmn}}{\partial t} \tag{5.68}
$$

because the exponential parameter b_k remains constant in this fractional step. With these modifications, the equations $(5.64)_{4,5,6}$ and (5.66) turn into

$$
\begin{aligned}
\frac{\partial}{\partial t}(\bar{\mathrm{M}}^1_{k;l}) &= \frac{1}{\mathrm{Fr}} \mathbf{e_g} \cdot \mathbf{e}_l \bar{\mathrm{M}}^0_k + \bar{D}^1_{k;l} \ , \\
\frac{\partial}{\partial t}(\bar{\mathrm{M}}^2_{k;lm}) &= \frac{1}{\mathrm{Fr}} \left(\mathbf{e_g} \cdot \mathbf{e}_l \bar{\mathrm{M}}^1_{k;m} + \mathbf{e_g} \cdot \mathbf{e}_m \bar{\mathrm{M}}^1_{k;l} \right) + \bar{D}^2_{k;lm} \ , \\
\frac{\partial}{\partial t}(\bar{\mathrm{M}}^3_{k;lmn}) &= \frac{1}{\mathrm{Fr}} \left(\mathbf{e_g} \cdot \mathbf{e}_l \bar{\mathrm{M}}^2_{k;mn} + \mathbf{e_g} \cdot \mathbf{e}_m \bar{\mathrm{M}}^2_{k;ln} + \mathbf{e_g} \cdot \mathbf{e}_n \bar{\mathrm{M}}^2_{k;lm} \right) + \bar{D}^3_{k;lmn} \ ,
\end{aligned}
\tag{5.69}
$$

[4] For this subsection the moment $\mathrm{M}^{3/2,0,M}_{k;lmn}$ is written as $\mathrm{M}^M_{k;lmn}$.

with

$$\bar{D}^1_{k;l} = \frac{1}{\bar{\mathrm{St}}_k}\left(\bar{\mathrm{M}}^0_k U_{gl} - \bar{\mathrm{M}}^1_{k;l}\right) \ ,$$

$$\bar{D}^2_{k;lm} = \frac{1}{\bar{\mathrm{St}}_k}\left(\bar{\mathrm{M}}^1_{k;j} U_{gi} - \bar{\mathrm{M}}^2_{k;ij}\right)\left(\delta_{il}\delta_{jm} + \delta_{im}\delta_{jl}\right) \ , \tag{5.70}$$

$$\bar{D}^3_{k;lmn} = \frac{1}{\bar{\mathrm{St}}_k}\left(\bar{\mathrm{M}}^2_{k;st} U_{gr} - \bar{\mathrm{M}}^3_{k;str}\right)\left(\delta_{rl}\delta_{sn}\delta_{tm} + \delta_{rm}\delta_{sl}\delta_{tn} + \delta_{rn}\delta_{sm}\delta_{tl}\right) \ ,$$

where

$$\frac{1}{\bar{\mathrm{St}}_k} := \frac{1}{\mathrm{St}(1)} \frac{\int_{s_k}^{s_{k+1}} s^{1/2}\exp(-b_k s)ds}{\int_{s_k}^{s_{k+1}} s^{3/2}\exp(-b_k s)ds} \tag{5.71}$$

is denoted as the modified Stokes number of section I_k. Equations (5.69) supplemented by (5.70) and (5.71) constitute a system of equations for the modified moments. It can be solved exactly using cumbersome analytical solution techniques. The minor assumptions, that will be enforced in the sequel, facilitates the solution considerably.

Equation $(5.69)_1$ can be solved analytically because $\bar{\mathrm{M}}^0_k$ is not changing in this fractional step. The solution in the time-interval $[t_n, t]$ reads

$$\bar{\mathrm{M}}^1_{k;l}(t) = \bar{\mathrm{M}}^1_{k;l}(t_n)\exp\left(-\frac{t-t_n}{\bar{\mathrm{St}}}\right) + \bar{\mathrm{M}}^0_k\big(U_{gl} + \frac{\bar{\mathrm{St}}}{\mathrm{Fr}}\mathbf{e}_g\cdot\mathbf{e}_l\big)\left[1-\exp\left(-\frac{t-t_n}{\bar{\mathrm{St}}}\right)\right]. \tag{5.72}$$

The analytical solution of equation $(5.69)_{2,3}$ is not easily accessible because the nonlinear functions $\bar{\mathrm{M}}^1_{k;l}(t)$ and $\bar{\mathrm{M}}^2_{k;lm}(t)$ arise. For these equations a numerical approach could be followed that assumes the right-hand sides of $(5.69)_{2,3}$ to be evaluated at time t_n.

However, in this work, it is preferred to solve for the velocities $(\mathbf{U}^\alpha_k)_l := U^\alpha_{k;l}$ directly using only the first equation in (5.69). To this end, the moments $\bar{\mathrm{M}}^1_{k;l}$ and $\bar{\mathrm{M}}^0_k$ are written in terms of the parameters $\mathcal{W}^4$, i.e.

$$\sum_{\alpha=1}^{4} n^\alpha_k(t)U^\alpha_{k;l}(t) = \sum_{\alpha=1}^{4} n^\alpha_k(t_n)U^\alpha_{k;l}(t_n)\exp\left(-\frac{t-t_n}{\bar{\mathrm{St}}}\right)$$
$$+\sum_{\alpha=1}^{4} n^\alpha_k(t_n)\big(U_{gl} + \mathbf{e}_g\cdot\mathbf{e}_l\frac{\bar{\mathrm{St}}}{\mathrm{Fr}}\big)\left[1-\exp\left(-\frac{t-t_n}{\bar{\mathrm{St}}}\right)\right]. \tag{5.73}$$

By assuming the weights n^α_k to be constant, equation (5.73) can be split into $d\times\beta$ $(d=2)$ equations for the velocity abscissas, i.e.

$$U^\alpha_{k;l}(t) = U^\alpha_{k;l}(t_n)\exp\left(-\frac{t-t_n}{\bar{\mathrm{St}}}\right) + \big(U_{gl} + \mathbf{e}_g\cdot\mathbf{e}_l\frac{\bar{\mathrm{St}}}{\mathrm{Fr}}\big)\left[1-\exp\left(-\frac{t-t_n}{\bar{\mathrm{St}}}\right)\right]. \tag{5.74}$$

The assumption of constant weights in the fractional step of droplet forces is weak. This follows from study of the exact solution of equation system (5.69) (not shown here).[5]

[5] An alternative to the semi-analytical approach outlined above is the numerical treatment of all equations in (5.69). In this approach the right-hand sides of (5.69) and (5.70) could be evaluated at a previous fractional step and the resulting integration could be performed by an ODE-solver. Unfortunately, equation system (5.69) can be very stiff for small Stokes numbers, which introduces difficulties to the accurate computation of the changes due to drag and gravity forces [97]. However, the numerical approach allows the use of more complex drag models (see Section 2.4.1).

5.4.2 Heat Transfer

The solution of equation $(5.64)_3$ is not accessible to an analytical or semi-analytical approach because He in $(5.65)_1$ is, in general, a non-linear function of Θ_k. Therefore, a numerical method has to be applied that assumes the right-hand side of $(5.64)_3$ to be known from a previous fractional step. The emerging ODE is solved using the ODE-solver `DLSODA` of the mathematically library ODEPACK [78]. `DLSODA` switches automatically between non-stiff and stiff solvers. The twelfth-order implicit Adams method was used for the non-stiff case and the fifth-order backward differentiation formulas (BDF) for the stiff case. The high order of accuracy is the standard for these routines. It can easily be reduced to accelerate the calculations. To prevent large numerical errors from the time-integration, the high-order methods are used.

5.5 Discretisation of the Evaporation Part

The derivation of the numerical scheme for the evaporation commences with the analytical solution of the linear hyperbolic PDE (see (5.10)-(5.12))

$$\frac{\partial}{\partial t}(f) - \mathrm{Ev}(\mathbf{v},\theta)\frac{\partial}{\partial s}(f) = 0 \qquad \text{in } [t_n,t]\times[0,1], \tag{5.75}$$

$$f(t_n;s) = f_{ne}(s) \qquad \text{in } [0,1], \tag{5.76}$$

$$\left.\frac{\partial f(\mathbf{x},t;\mathbf{v},s,\theta)}{\partial s}\right|_{s=0} = 0 \qquad \text{in } [t_n,t]. \tag{5.77}$$

The variables $\mathbf{v}$ and θ are fixed in the fractional step of evaporation and therefore the solution reads $f(t;s) = f_{ne}(s+\mathrm{Ev}(\mathbf{v},\theta)(t-t_n))$ for all $(t_n;0) \leq (t;s)$. This solution is used to derive a finite volume-like scheme for the moment equations in (5.15). The derivation of the scheme is similar to the kinetic approach pursued in Section 5.3.

The starting point of these derivations is the substitution of the above solution of equation (5.75)- (5.77) into the definition of a general moment at time $t_{n+1} = t_n + \Delta t$ (see (4.6))

$$\mathrm{M}^{K,L,M}_{k;lmn}(\mathbf{x},t_{n+1}) = \int_{\mathbb{R}_+}\int_{\mathbb{R}^2}\int_{s_k}^{s_{k+1}} s^K\theta^L v_l v_m v_n f_{ne}(s+\mathrm{Ev}(\mathbf{v},\theta)\Delta t;\mathbf{x},\mathbf{v},\theta)ds\,d\mathbf{v}\,d\theta\ . \tag{5.78}$$

After the change of variables $u = s + \mathrm{Ev}(\mathbf{v},\theta)\Delta t$ and a rearrangement, the integral in

(5.78) is transformed into[6]

$$\mathrm{M}_{k;lmn}^{K,L,M}(\mathbf{x},t_{n+1}) = \underbrace{\int_{\mathbb{R}_+}\int_{\mathbb{R}^2}\int_{s_k+\mathrm{Ev}\Delta t}^{s_{k+1}+\mathrm{Ev}\Delta t} u^K\theta^L v_l v_m v_n f_{ne}(u;\mathbf{x},\mathbf{v},\theta)du\,d\mathbf{v}\,d\theta}_{\text{(I)}}$$

$$+\underbrace{\int_{\mathbb{R}_+}\int_{\mathbb{R}^2}\int_{s_k+\mathrm{Ev}\Delta t}^{s_{k+1}+\mathrm{Ev}\Delta t}\left((u-\mathrm{Ev}\Delta t)^K-u^K\right)\theta^L v_l v_m v_n f_{ne}(u;\mathbf{x},\mathbf{v},\theta)du\,d\mathbf{v}\,d\theta}_{\text{(II)}}\ . \quad (5.79)$$

Integral (I) can be written as

$$\text{(I)} = \mathrm{M}_{k;lmn}^{K,L,M}(\mathbf{x},t_n) + \int_{\mathbb{R}_+}\int_{\mathbb{R}^2}\int_{s_{k+1}}^{s_{k+1}+\mathrm{Ev}\Delta t} u^K\theta^L v_i v_j v_k f_{ne}(u;\mathbf{x},\mathbf{v},\theta)du\,d\mathbf{v}\,d\theta$$

$$-\int_{\mathbb{R}_+}\int_{\mathbb{R}^2}\int_{s_k}^{s_k+\mathrm{Ev}\Delta t} u^K\theta^L v_i v_j v_k f_{ne}(u;\mathbf{x},\mathbf{v},\theta)du\,d\mathbf{v}\,d\theta, \quad (5.80)$$

where the integrals in (5.80) are regarded as flux terms through the interfaces of section I_k. Consequently, integral (II) represents the sink or source term for evaporation. To facilitate the evaluation of integral (II), it is decomposed into

$$\text{(II)} = \int_{\mathbb{R}_+}\int_{\mathbb{R}^2}\int_{s_k+\mathrm{Ev}\Delta t}^{s_{k+1}}\left((u-\mathrm{Ev}\Delta t)^K-u^K\right)\theta^L v_i v_j v_k f_{ne}(u;\mathbf{x},\mathbf{v},\theta)du\,d\mathbf{v}\,d\theta$$

$$+\int_{\mathbb{R}_+}\int_{\mathbb{R}^2}\int_{s_{k+1}}^{s_{k+1}+\mathrm{Ev}\Delta t}\left((u-\mathrm{Ev}\Delta t)^K-u^K\right)\theta^L v_i v_j v_k f_{ne}(u;\mathbf{x},\mathbf{v},\theta)du\,d\mathbf{v}\,d\theta\ . \quad (5.81)$$

As Ev is dependent on $\mathbf{v}$ and θ, the desired interchange of the integrals in (5.80) and (5.81) is not feasible. To circumvented this difficulty the above integrals are written as

$$\text{(I)} = \mathrm{M}_{k;lmn}^{K,L,M}(\mathbf{x},t_n) + \int_{s_{k+1}}^{s_{k+2}} u^K\int_{\mathbb{R}_+}\int_{\mathbb{R}^d}\theta^L v_i v_j v_k f_{ne}(u;\mathbf{x},\mathbf{v},\theta)\mathbb{1}_{u\le s_{k+1}+\mathrm{Ev}\Delta t}d\mathbf{v}\,d\theta\,du$$

$$-\int_{s_k}^{s_{k+1}} u^K\int_{\mathbb{R}_+}\int_{\mathbb{R}^d}\theta^L v_i v_j v_k f_{ne}(u;\mathbf{x},\mathbf{v},\theta)\mathbb{1}_{u\le s_k+\mathrm{Ev}\Delta t}d\mathbf{v}\,d\theta\,du \quad (5.82)$$

[6]For simplicity the dependencies of Ev are suppressed in the sequel.

and

$$(\mathrm{II}) = \int_{s_k}^{s_{k+1}} \int_{\mathbb{R}_+} \int_{\mathbb{R}^d} \left((u - \mathrm{Ev}\Delta t)^K - u^K\right) \theta^L v_i v_j v_k f_{ne}(u; \mathbf{x}, \mathbf{v}, \theta) \mathbb{1}_{u \geq s_k + \mathrm{Ev}\Delta t} d\mathbf{v}\, d\theta\, du$$

$$+ \int_{s_{k+1}}^{s_{k+2}} \int_{\mathbb{R}_+} \int_{\mathbb{R}^d} \left((u - \mathrm{Ev}\Delta t)^K - u^K\right) \theta^L v_i v_j v_k f_{ne}(u; \mathbf{x}, \mathbf{v}, \theta) \mathbb{1}_{u \leq s_{k+1} + \mathrm{Ev}\Delta t} d\mathbf{v}\, d\theta\, du\ . \quad (5.83)$$

Next, the initial distribution f_{ne} is set equal to the approximate NDF at time t_n. This allows the evaluation of the velocity and temperature integrals in (5.82) and (5.83). The resulting fluxes from section I_{k+1} to I_k are defined as (cf. $(4.79)_1$)

$$E^{K,L,M}_{lmn}(k, k+1) := \frac{\Delta s_k}{\Delta t} \Theta^L_k \sum_{\alpha=1}^{4} n^\alpha_{k+1}(t_n) U^\alpha_{k+1;l}(t_n) U^\alpha_{k+1;m}(t_n) U^\alpha_{k+1;n}(t_n)$$

$$\times \int_{s_{k+1}}^{s_{k+1} + \mathrm{Ev}(\Theta_{k+1}, \mathbf{U}^\alpha_{k+1})\Delta t} u^K \exp(-b_{k+1}(t_n) u) du\ , \quad (5.84)$$

where $\Delta s_k := s_{k+1} - s_k$. The sink terms are specified as (cf. $(4.79)_2$)

$$\mathcal{E}1^{K,L,M}_{k;lmn}(t_n) := \Theta^L_k \sum_{\alpha=1}^{4} n^\alpha_k(t_n) U^\alpha_{k;l}(t_n) U^\alpha_{k;m}(t_n) U^\alpha_{k;n}(t_n)$$

$$\times \int_{s_k + \mathrm{Ev}(\Theta_k, \mathbf{U}^\alpha_k)\Delta t}^{s_{k+1}} \left((u - \mathrm{Ev}\Delta t)^K - u^K\right) \exp(-b_k(t_n) u) du \quad (5.85)$$

and

$$\mathcal{E}2^{K,L,M}_{k;lmn}(t_n) := \Theta^L_k \sum_{\alpha=1}^{4} n^\alpha_{k+1}(t_n) U^\alpha_{k+1;l}(t_n) U^\alpha_{k+1;m}(t_n) U^\alpha_{k+1;n}(t_n)$$

$$\times \int_{s_{k+1}}^{s_{k+1} + \mathrm{Ev}(\Theta_{k+1}, \mathbf{U}^\alpha_{k+1})\Delta t} \left((u - \mathrm{Ev}\Delta t)^K - u^K\right) \exp(-b_{k+1}(t_n) u) du\ . \quad (5.86)$$

With the above considerations equation (5.79) can be written as

$$\mathrm{M}^{K,L,M}_{k;lmn}(\mathbf{x}, t_{n+1}) = \mathrm{M}^{K,L,M}_{k;lmn}(\mathbf{x}, t_n) - \frac{\Delta t}{\Delta s_k} \left[E^{K,L,M}_{lmn}(k-1, k) - E^{K,L,M}_{lmn}(k, k+1)\right]$$

$$+ \mathcal{E}1^{K,L,M}_{k;lmn}(t_n) + \mathcal{E}2^{K,L,M}_{k;lmn}(t_n)\ . \quad (5.87)$$

In the case when $K = 0$ and $M = 0$ no sink terms arise, which is very physical because evaporation does not lead to the reduction of droplets in $s \in]0, 1]$. Only at $s = 0$ are the droplets taken from the system. Note that Δt has to satisfy the restriction

$$\mathrm{Ev}\Delta t < (s_{k+1} - s_k), \tag{5.88}$$

otherwise the integrals in this section are not defined clearly, i.e. certain sections will not be considered.

Dufour [43] showed that an evaporation scheme, similar to (5.87), is second-order accurate in surface space.

5.6 Numerics for the Splashing Condition

In this section the splashing condition (2.83) is translated into a relation between the moments before splashing $\mathrm{M}_{k;klm}^{(K,L,M)+}$ and those after splashing $\mathrm{M}_{k;klm}^{(K,L,M)r}$. The substitution of relation (2.83) into the definition of $\mathrm{M}_{k;klm}^{(K,L,M)r}$ yields

$$\begin{aligned}\mathrm{M}_{k;klm}^{(K,L,M)r} &:= \int_{s_k}^{s_{k+1}} \int_{\mathbb{R}_+} \int_{\mathbb{R}^2} s^K \theta^L v_l v_m v_n f^r(\mathbf{x}, t; \mathbf{v}, s, \theta) d\mathbf{v} d\theta ds \\ &= \frac{\gamma - 1}{\alpha_x \alpha_y \beta_d^5} \int_{s_k}^{s_{k+1}} \int_{\mathbb{R}_+} \int_{\mathbb{R}^2} s^K \theta^L v_l v_m v_n f^+(-\frac{v_x}{\alpha_x}, \frac{v_y}{\alpha_y}, \frac{s}{\beta^2}, \theta) d\mathbf{v} d\theta ds \ . \end{aligned} \tag{5.89}$$

The right-hand side of (5.89) has to be related to the moments and parameters of the approximate NDF before splashing. To this end, the following substitutions are made

$$t = \frac{s}{\beta_d^2} \ , \quad u = -\frac{v_x}{\alpha_x} \ , \quad v = \frac{v_y}{\alpha_y} \ . \tag{5.90}$$

This change of variables yields

$$\begin{aligned}\mathrm{M}_{k;klm}^{(K,L,M)r} = (1 - \gamma)(-\alpha_x)^P (\alpha_y)^Q (\beta_d)^{2K-3} \\ \times \int_{\frac{s_k}{\beta_d^2}}^{\frac{s_{k+1}}{\beta_d^2}} \int_{\mathbb{R}_+} \int_{\mathbb{R}^2} t^K \theta^L u^P v^Q f^+(u, v, t, \theta) du dv d\theta dt \ , \end{aligned} \tag{5.91}$$

where P and Q are the order of moment $\mathrm{M}_{k;klm}^{(K,L,M)r}$ for the velocities v_x and v_y, respectively. The sum of P and Q must give M. The integral on the right-hand side of (5.91) is known from the moments and parameters of the incident droplets. Note that the boundaries of this integral do not necessarily agree with the boundaries of the sections. Therefore, an explicit evaluation of the integral in (5.91) is required using the parameters of the incident droplets.

The algorithm for the splashing boundary condition on a wall that is orientated, for example, towards $\mathbf{e_x}$ must permit the following properties:

(i) The moments of the incident droplets, $\mathrm{M}_{k;klm}^{(K,L,M)+}$, must be erased and the moments of the splashed droplets, $\mathrm{M}_{k;klm}^{(K,L,M)r}$, must be created at the wall according relation (5.91).

(ii) In the case when droplet velocity $\mathbf{v}$ on the wall is changed, an accumulation or thinning of the droplet distribution in real space is present.

To guarantee these properties, a layer of ghost cells is introduced 'behind' the wall of splashing. The boundary condition on the left interface of the first layer of cells in the computational domain (the actual position of the wall) is a zero-gradient boundary condition for the moments of incident droplets. Hence, only the moments of incident droplets reach the ghost cells. In these cells the moments of the splashed droplets, $\mathrm{M}_{k;klm}^{(K,L,M)r}$, are computed using relation (5.91). The moments of incident droplets are erased using the zero-gradient boundary condition on the left interface of each ghost cell. The accumulation or thinning of droplets is modelled by introducing a new moment field that 'lives' in the ghost cells only. The influx to this field are the moments of splashed droplets with the convection velocity of the incident droplets. The efflux from the field is calculated with the new moment field but with convection velocities of the splashed droplets. The efflux from the intermediate moment field is equal to the flux through the left interface of the first layer of cells in the computational domain. For the calculation of the fluxes into and out of the intermediate field, the parameters in $\mathcal{W}_k^4$ (4.11) ($k = 1, \ldots, N_s$) are computed from the respective moments. The introduction of the intermediate moment field allows the description of accumulation and thinning of droplets on the wall. The splashing boundary condition must be applied in every fractional step of convection.

If more complex models are used for the splashing parameters (see Section 2.5), the above algorithm remains valid but relation (5.91) has to be modified. In the case when the wall of splashing is facing a direction other than $\mathbf{e}_x$, the algorithm needs to be adapted but relation (5.91) remains unchanged.

5.7 The Global Algorithm

The global algorithm of the QBSM which is used in Chapter 6 is given in this section. It is coupled to the gas phase only through the gas velocity (one-way coupling). All schemes in the Strang splitting can be chosen to be of second-order accuracy in all variables, so it is possible to obtain an overall algorithm that is of second order as well. The sequence of operations proposed here may not be the only one possible but, as will be observed in Chapter 6, it gives convincing results compared with Lagrangian calculations. The global algorithm reads:

BEGIN

---

1. Initialisation of

physical and numerical constants,

boundary conditions and

initial NDF.

2. Calculation of

initial moments ($\mathcal{V}_k^2$) and

parameters ($\mathcal{W}_k^4$) for each section I_k, $(k = 1, \ldots, N_s)$.

3. Time-loop:

Calculation of the time-step

Strang splitting:

$\Delta t/2$	Convection in x-direction, Part I
$\Delta t/2$	Convection in y-direction, Part I
$\Delta t/2$	Droplet forces and heat transfer, Part I
Δt	Evaporation
$\Delta t/2$	Droplet forces and heat transfer, Part II
$\Delta t/2$	Convection in y-direction, Part II
$\Delta t/2$	Convection in x-direction, Part II

Storage of Data

4. Postprocessing

END

The parameters $\mathcal{W}_k^4$ (4.11) are computed from the moments in set $\mathcal{V}_k^2$ (4.17) for each section I_k after every fractional step of the Strang splitting (see formulae in Chapter 4). This algorithm can easily be extended to three dimensions in real space and to collision and breakup. Note that the fractional steps for convection, droplet forces and heat transfer can be solved for each section I_k independently. Hence, for these physical phenomena the computation for one section I_k can be conducted on processors that do not need to 'communicate' with the processors of other sections. The fractional step of evaporation (as well as collision and breakup) couples the sections but can be solved for each cell independently. These considerations demonstrate that, besides the domain decomposition in real space [137], a domain decomposition in surface space is conceivable and the computational time can be further reduced using adapted parallelisation strategies. In Chapter 6 the above algorithm is verified, validated and applied to various spray configurations.

Chapter 6

Verification, Validation and Application

6.1 Introduction

In this chapter the verification of QBSM is outlined and validation tests are reported. The method is also applied to a polydisperse spray affected by a Taylor-Green vortex gas flow [168]. This test case is used to demonstrate the ability of QBSM to describe unstationary turbulent spray flows. Unfortunately, the coupling between QBSM and a gas solver was not conducted. Therefore, tests in more complex configurations cannot be presented. The tests outlined here rely on analytical solutions of gas flows.

In this chapter the QBSM, or parts of it, are compared with semi-analytical solutions, Lagrangian calculations and experimental measurements in various one- and two-dimensional configurations. In these tests the behaviour of QBSM given different physical and numerical parameters is studied. To this end, the discretisation in real and surface space as well as the maximum Stokes number, the evaporation number and the splashing parameters are varied. For the monodisperse test configurations, the results of QBSM are also compared with those of the first-order Euler method outlined in Section 3.3.3.

In Section 6.2 the one-dimensional tests of the sectional part of QBSM are outlined and compared with, *first*, the semi-analytical solution derived in Appendix A, and *second*, with the spray experiment of Wong and Chang [182]. These configurations include the physical effects of drag force, gravity and evaporation. For the comparison with the experiment of Wong and Chang [182] the uniform temperature model of Abramzon and Sirignano [1] was considered. With these verification and validation tests and other results from the literature [44, 97], the area of validity for the sectional part of QBSM can be specified (see Section 6.2.3). The verification of the quadrature-based part of QBSM [56, 99] is reported in Section 6.3 where it is compared with Lagrangian calculations and with the first-order Euler method. The two-dimensional verification tests are the crossing of perpendicular moving spray jets with and without drag force and the instationary acceleration of a monodisperse spray in a Taylor-Green vortex. Further validation tests of the method can be found in Fox [56] and Le Lostec et al. [99]. The quadrature-based part of the QBSM is not tested in a one-dimensional setting because the number of quadrature parameters in $\mathcal{W}_k^2$ (4.11) and moments in $\mathcal{V}_k^1$ (4.17) is the same ($k = 1, \ldots, N_s$). Therefore,

the method is controlling all velocity moments up to the third-order and no additional errors are introduced by the transfer between moments and quadrature parameters.

To assess the ability of the full QBSM in a one-dimensional setting, it is applied to three simplified spray problems that change the spray distribution in surface space through splashing, evaporation and the Stokes drag force (see Section 6.4). All three test cases are organised in such a way that crossing of two spray distributions is included. Solutions to the same test cases were also computed using a Lagrange method.[1] They are regarded as accurate reference solutions.

In two dimensions the QBSM was applied to validation tests in which *first*, two perpendicular moving spray jets are crossing and *second*, a spray jet is splashed on a wall (see Section 6.5). For the crossing jets, the Stokes drag force and the d^2-evaporation law were considered. For the splashing test case, the splashing model (2.83) was taken into account. Again, the results are compared with reference Lagrangian computations. The two test cases can be extended to more complex models, i.e. the uniform temperature model for evaporation [1] can be applied and the splashing parameters in (2.83) can be assumed to be velocity-, size- and temperature-dependent (see Chapter 2).

In Section 6.6 the QBSM is applied to a two-dimensional configuration in which an evaporating polydisperse spray is influenced through drag force by a Taylor-Green vortex gas flow [168]. The solution of the QBSM is compared with Lagrangian results. This Taylor-Green test case can be considered as a first validation in a turbulent setting because unsteady and size-dependent acceleration droplets and crossing of sprays at local impingement planes are present. These are crucial effects in unstationary turbulent spray flows.

The results are presented in terms of the total zeroth-order moment, $M^{0,0,0}$ and the zeroth-order moment in a section, $M_k^{0,0,0}$ $(k = 1, \ldots, N_s)$. Here, these quantities are called number density and number density distribution of droplets, respectively. Other moments could also be presented but for the sake of readability they are only mentioned when it is necessary.

6.2 Verification and Validation of the Sectional Part

The sectional part of QBSM[2] (in this section it is simply called sectional method (SM)) relies on the sectional method of Dufour and Villedieu [44] but implementation in the program code was performed by the author. In a verification step, calculations with the SM are compared with a semi-analytical solution of a stationary and one-dimensional spray problem that takes into account evaporation, Stokes drag and gravity (see Appendix A). The objective is to analyse the global error of the sectional method and to study its dependence on the number of sections. In a validation step, the method is compared qualitatively with the experiment of Wong and Chang [182] in order to assess the ability of the method to deal with the uniform temperature model [1] for evaporation and heat transfer.

[1] The program code to the Lagrange method was mainly written by Nechtan Le Lostec and Philippe Villedieu (ONERA/DMAE Toulouse). It relies on the particle discretisation method explained in Section 3.3.1.

[2] Parts of the results presented here were published in Schneider et al. [152].

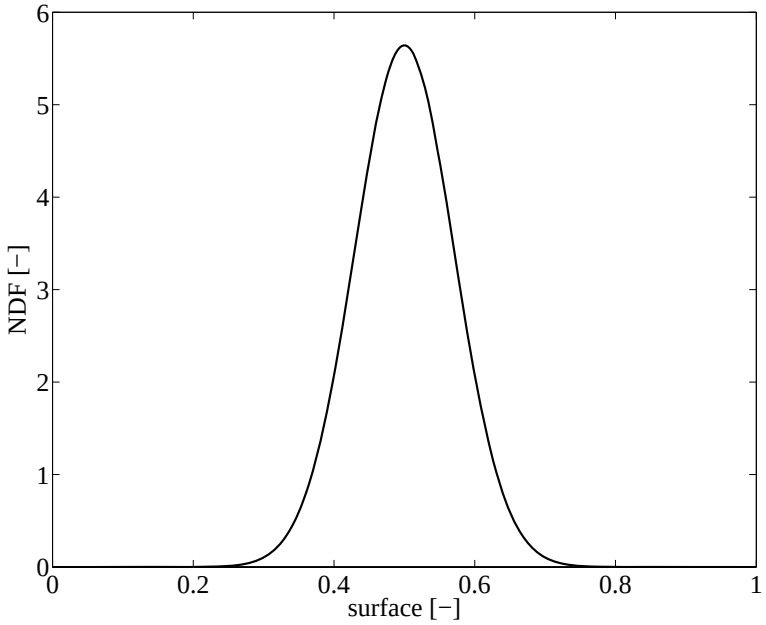

Figure 6.1: Prescribed number distribution function vs. surface variable; truncated Gaussian distribution (6.5) with mean $\mu = 0.5$, standard deviation $\sigma = 0.1/\sqrt{2}$, truncation value $s_c = 0.9$.

6.2.1 Comparison to a Semi-Analytical Solution

In this section the numerical error of the sectional method is studied by comparing it with the semi-analytical solution of a reduced kinetic spray equation which is derived in Appendix A. There, the equation

$$\frac{\partial}{\partial x}(vf(x;v,s)) + \frac{\partial}{\partial v}\left[\left(\frac{U_g - v}{\mathrm{St}(s)} + \frac{1}{\mathrm{Fr}}\right) f(x;v,s)\right] - \mathrm{Ev}\frac{\partial}{\partial s}(f(x;v,s)) = 0 \tag{6.1}$$

is solved for the dimensionless Sauter mean diameter (SMD)

$$\mathrm{d}_{32}(x) = \frac{\int_{\mathbb{R}_+}\int_{\mathbb{R}} s^{3/2} f(x;v,s)dvds}{\int_{\mathbb{R}_+}\int_{\mathbb{R}} s f(x;v,s)dvds}\ , \tag{6.2}$$

the dimensionless total mass of droplets

$$m(x) = \int_{\mathbb{R}_+}\int_{\mathbb{R}} s^{3/2} f(x;v,s)dvds \tag{6.3}$$

and the dimensionless total number of droplets

$$n(x) = \int_{\mathbb{R}_+}\int_{\mathbb{R}} f(x;v,s)dvds\ . \tag{6.4}$$

The stationary kinetic spray equation in (6.1) is one-dimensional in real and velocity space, the evaporation number is assumed to be constant ($\mathrm{Ev} = 0.94$) and the Stokes drag law

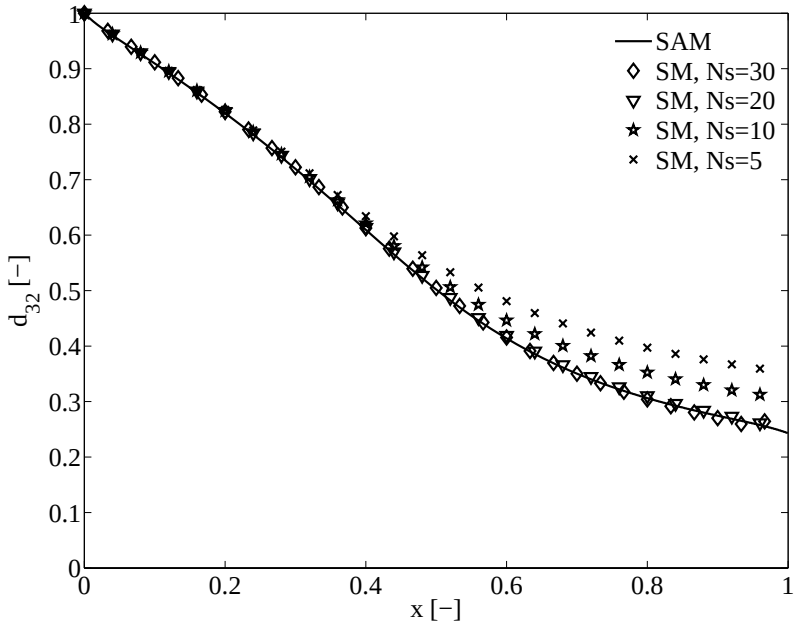

Figure 6.2: Sauter mean diameter (normalised by initial value) vs. position using a semi-analytical method (SAM) and the sectional method (SM); $N_x = 150$.

($\mathrm{St}_{\mathrm{char}} = 0.03$) is applied. This equation is complemented by the inflow condition

$$f(0;v,s) =: f_0(v,s) = \begin{cases} \frac{\exp\left(-0.5\frac{(s-\mu)^2}{\sigma^2}\right) - \exp\left(-0.5\frac{(s_c-\mu)^2}{\sigma^2}\right)}{M_0} & \text{in} \quad s_c \le s \le 1-s_c \ , \\ 0 \qquad \text{otherwise,} \end{cases} \tag{6.5}$$

which is a truncated Gaussian distribution with mean $\mu = 0.5$, standard deviation $\sigma = 0.1/\sqrt{2}$, truncation value $s_c = 0.9$ and normalisation factor which guarantees that $1 = \int\int f_0 ds dv$ (see Figure 6.1). With boundary condition (6.5) it is assumed that at the inflow (but only there) all droplets have the same velocity.

In Figure 6.2, the semi-analytical solution is plotted versus the numerical solution for four different numbers of sections $N_s = \{5, 10, 20, 30\}$ and 150 cells. Using only five sections, it is observed that the numerical error accumulates with the distance from the inlet and is largest at the outlet. With increasing number of sections the analytical solution is very well represented and only tiny numerical errors remain for the case $N_s = 20$ or $N_s = 30$. Although very simple models for evaporation and drag were used, the observations indicate that the numerical error decreases with increasing numbers of sections, a necessary condition to apply the sectional method to more complex spray problems. In Figure 6.3 the semi-analytical and numerical results for total mass and total number of droplets are depicted where in the numerical calculations 5 and 10 sections and 150 cells were used. The results for more sections than 10 show no observable difference between semi-analytical and numerical calculations and are not shown here. From this comparison it can be concluded that no mass or droplets are artificially taken from or added to the

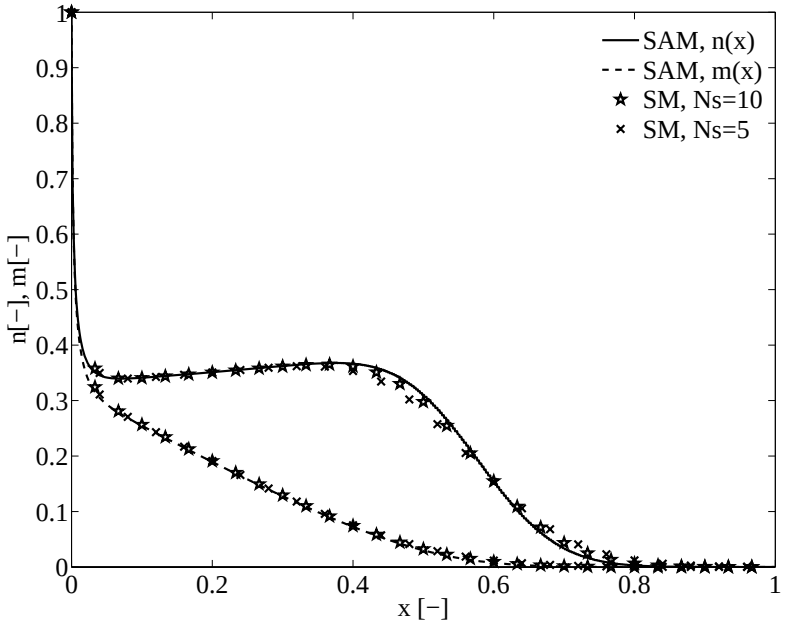

Figure 6.3: Total mass and number of droplets (normalised by initial value) vs. position using a semi-analytical method (SAM) and the sectional method (SM); $N_x = 150$.

system. Comparing the results in Figure 6.2 with those of Figure 6.3 it is observed that in the region where the solutions for d_{32} are deviating from the semi-analytical solution only a small amount of mass remains. Consequently, the errors in d_{32} have no strong impact on the overall dispersed phase calculation.

6.2.2 Comparison to the Experiment of Wong and Chang

To assess the use of the uniform temperature model [1] in the frame of the sectional method it is compared with the axis-symmetric evaporation experiment of Wong and Chang [182]. They considered an evaporating Tetralin ($C_{10}H_{10}$) spray that exhibits acceleration, heating and evaporation in a slowly moving N_2 gas stream which moves through a cylindrical tube. This tube is facing in the direction of gravity. The measurements are conducted with the phase Doppler particle analyzer (PDPA) at the end of the tube. The length of the tube is varied from 2 to 65 cm. The tube has a diameter of 2 cm and is insulated in order to simulate an adiabatic evaporation environment and to avoid fuel condensation on the tube wall. It is preheated to 75° C. At the entrance of the tube the polydisperse spray has a mean velocity of approx. 0.9 $\mathrm{m\,s^{-1}}$, a mean temperature of approx. 308.0 K and an SMD of approx. 30.0 μm. The distribution of droplet sizes ranges from 7.0 to 60.0 μm. The measured initial size distribution is depicted in Figure 6.4. The gas that surrounds the droplets has initially a velocity of approx. 1.0 $\mathrm{m\,s^{-1}}$, a mean temperature of approx. 348.0 K and an approximated mass fraction of Tetralin vapour, $Y_{Tg} = 5.0e{-}04$. This experiment was conducted under atmospheric pressure conditions. All measurements

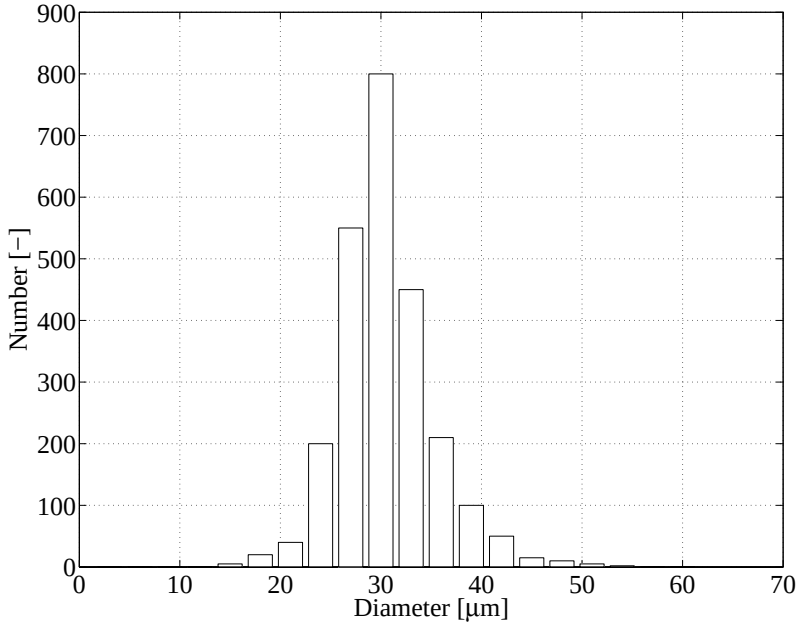

Figure 6.4: Number vs. diameter of droplets in a polydisperse spray; from experiment of Wong and Chang [182].

were made on the axis of symmetry, whereas the radial variation of the characteristic quantities, i.e. droplet size and velocity, were assessed and shown to not vary strongly in the middle of the tube.

In this work, the experiment of Wong and Chang [182] is modelled with the one-dimensional sectional method by using the following assumptions:

(i) The uniform temperature model of Abramzon and Sirignano [1] is considered for the evaporation.

(ii) A one-way coupling between gas and droplets is taken into account.

(iii) The properties of the surrounding gas, i.e. the velocity, temperature and the vapour mass fraction, are constant along the longitudinal axis.

(iv) The initial number density function depicted in Figure 6.4 is approximated by the distribution in (6.5) with mean $\mu = 0.5$, standard deviation $\sigma = 0.1/\sqrt{2}$ and truncation value $s_c = 0.9$ (see Figure 6.1).

(v) The characteristic values are $X_{\text{char}} = 65.0$ cm, $V_{\text{char}} = 1.0\ \text{m}\,\text{s}^{-1}$, $\Theta_{\text{char}} = 348.0$ K and $S_{\text{char}} = 60.0\ \mu$m. The resulting dimensionless numbers at the inflow are $\text{St}_{\max} = 0.07$ and $\text{Ev}_{\max} = 0.04$ using the mass density of Tetralin $\rho_{\text{C}_{10}\text{H}_{10}} = 0.969\ \text{g}\,\text{cm}^{-3}$ and the dynamic viscosity of of the gas-Tetralin mixture $\eta_{Tg} = 1.85e{-}04\ \text{g}\,(\text{cm}\ \text{s})^{-1}$.

These rather strong assumptions reduce the simulation effort significantly but at the same time they introduce strong errors into the physical model. This is particularly the case

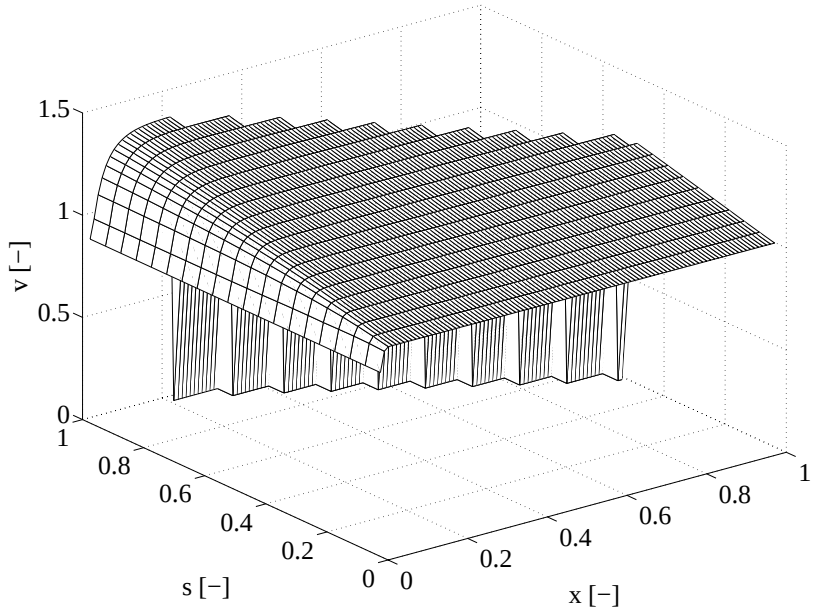

Figure 6.5: Droplet velocity vs. surface and position; sectional method for $N_s = 20$ and $N_x = 100$.

when a spray configuration is considered where saturation of the gas with Tetralin vapour is reached in the tube and the evaporation number reduces to zero.

For the discretisation of the surface space 20 sections are used. The computational domain is discretised by 150 cells and the second-order finite volume scheme is used for the convection. This large number of sections and cells is used to avoid numerical errors.

The results for the droplet velocity and temperature and for the evaporation number are depicted in Figures 6.5 - 6.7. The acceleration of droplets at the entrance, observed in Figure 6.5, is due to drag and gravity forces that are directed towards the end of the tube. Due to gravity, the droplets reach a velocity which is larger then that of the gas. The initial acceleration of large droplets is smaller than that of small ones, but the larger droplets reach higher velocities. This effect is due to the interaction between drag and gravity forces which point in opposite directions if $v > U_g$. The evaporation of droplets leads to a loss of large droplets in favour of smaller ones. If no large droplets are left the fields are set to zero.

The size-dependent increase of temperature, observed in Figure 6.6, is due to the heat transfer between gas and droplets. The consumption of heat due to the evaporation of droplets is not observed in the results as the droplet temperature remains equal to the constant gas temperature after the initial heat transfer ($x > 0.2$). For this configuration one can conclude that the time scale for the heat conduction is smaller than that of the evaporation process (see Figures 6.6 and 6.8).

In Figure 6.7 the evaporation number is plotted versus the position and surface space. It is confirmed that the evaporation depends directly on the velocity and the temperature variable and only indirectly on the size of droplets. The gravity force which results in

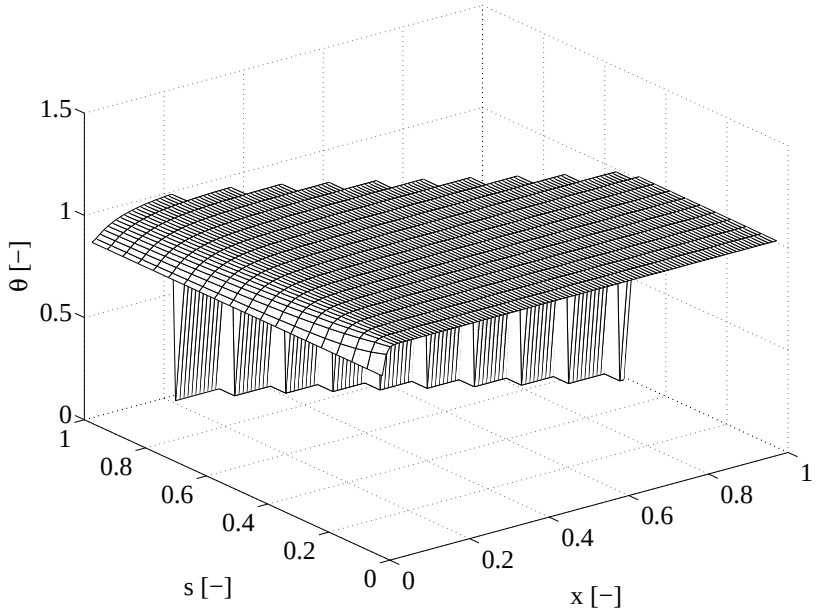

Figure 6.6: Droplet temperature vs. surface and position; sectional method for $N_s = 20$ and $N_x = 100$.

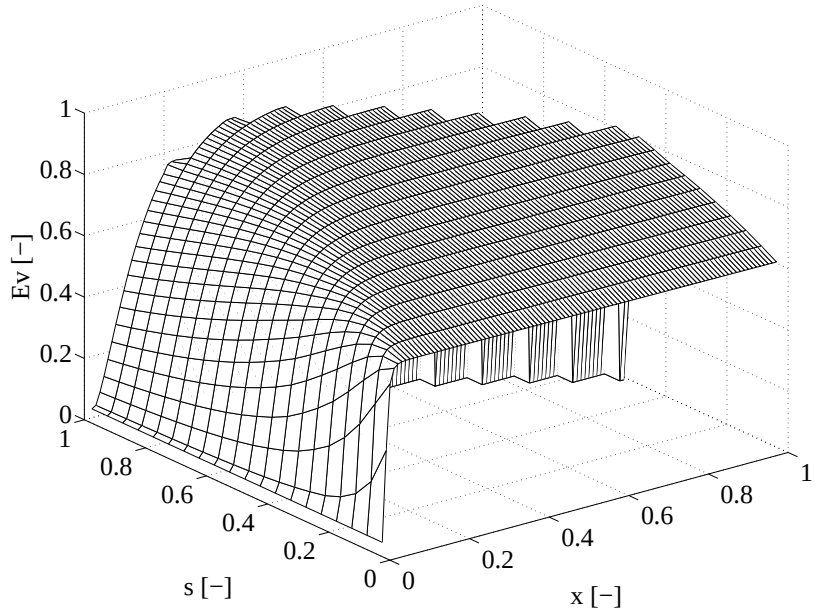

Figure 6.7: Evaporation number vs. surface and position; sectional method for $N_s = 20$ and $N_x = 100$.

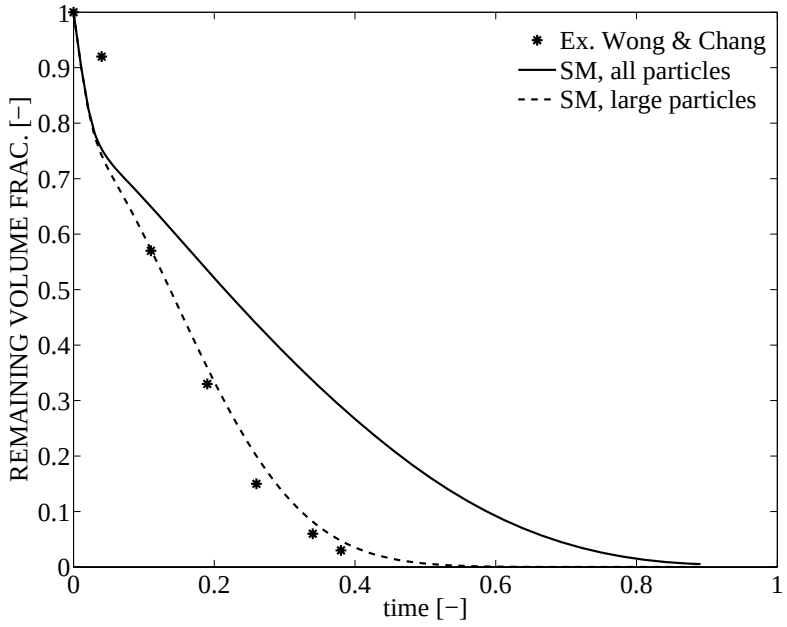

Figure 6.8: Remaining volume fraction (normalised by initial values) vs. time a droplet remains in the tube; measurements from Wong and Chang [182] and sectional method (SM) with all droplets (solid line) and droplets of size d > 20 μm (dashed line), $N_s = 20$ and $N_x = 100$.

larger velocities of larger droplets also results in higher evaporation rates for the droplets of large sizes. Without the gravity force, the evaporation number would be the same for all droplet sizes but only when they have reached the temperature of the gas. The steep initial increase of the evaporation number is due to the rising temperature of droplets. This reflects the fact that a liquid is usually more volatile if it has a higher temperature.

In Figure 6.8 the remaining volume fraction of droplets at the middle axis is plotted versus the average time a droplet remains in the tube (this quantity is proportional to the position). In the case when all droplets are considered in the computation (solid line), the remaining volume fraction of the measured and the computed results differ drastically. There may be several reasons for this deviation. *First*, the strong assumptions that were made for the physical model. *Second*, the weakness of the PDPA to capture all droplets, particularly small ones or *third*, the large Reynolds number ($\approx 1.0e5$) of the N_2-Tetralin gas mixture. The latter issue does not allow the assumption of a laminar flow and therefore it is possible that particularly small Tetralin droplets reach the wall and stick there.

Omitting all droplets with size $d < 20\mu$m in the computations (dashed line) a much better agreement between measurements and sectional method is obtained. It is not intended to draw any strong conclusion from these results. This would only hide the fact that assumptions (i)-(iv) should be softened to achieve acceptable predictions of realistic spray flows. The modified numerical result (dashed line) only indicates that small droplets may not be considered in the measurements.

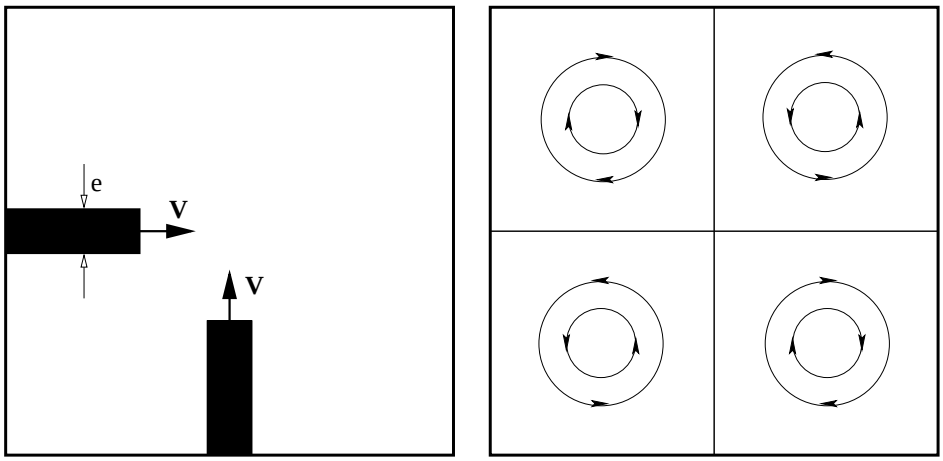

Figure 6.9: Schematic sketch of the two test cases: crossing of perpendicular spray jets (left); Taylor-Green gas flow (right) (after [99]).

6.2.3 Discussion of Results

The first conclusion that can be drawn is that the sectional method can describe the effects of drag and gravity forces, evaporation and heat transfer of a polydisperse spray without introducing large numerical errors, e.g. at singular points like $s = 0$ or at the interfaces between sections. The schemes for the evaporation are shown to be conservative in the sense that no droplets or droplet mass is artificially erased or added by rounding errors (see Figure 6.3). Comparing the SMD obtained from a semi-analytical solution with the sectional method for different numbers of sections it is observed that as long as the droplet mass at a point is above some threshold, the SMD is nicely represented by 5 to 10 sections. Consequently, the results in Section 6.2.1 show that the numerical error of the sectional method can be controlled in surface (evaporation) and velocity space (drag and gravity forces).

The conclusions from the study of the uniform temperature model are limited because, *first*, strong assumptions (see issues (i)-(iv) at the beginning of this section) were made for the simulation model which are only justified in very dilute flows. *Second*, the PDPA measurements of Wong and Chang [182] must be disputed as it seems that some portion of small droplets are not captured. Nevertheless, it can be concluded from the comparison to the experiment of Wong and Chang [182] that the sectional method is suitable for evaporating flows with realistic physical parameters and the uniform temperature model gives reasonable results for the fields of droplet velocity, temperature and evaporation number (see Figures 6.5 to 6.7).

6.3 Verification of the Quadrature-Based Part

The 2 two-dimensional configurations considered for the verification of the quadrature-based part of the QBSM (in this section it is simply called QBMoM) are depicted schematically in Figure 6.9. The crossing of two perpendicular moving spray jets (Section 6.3.1) is tested for monodisperse sprays that are *first*, freely transported and *second*, affected

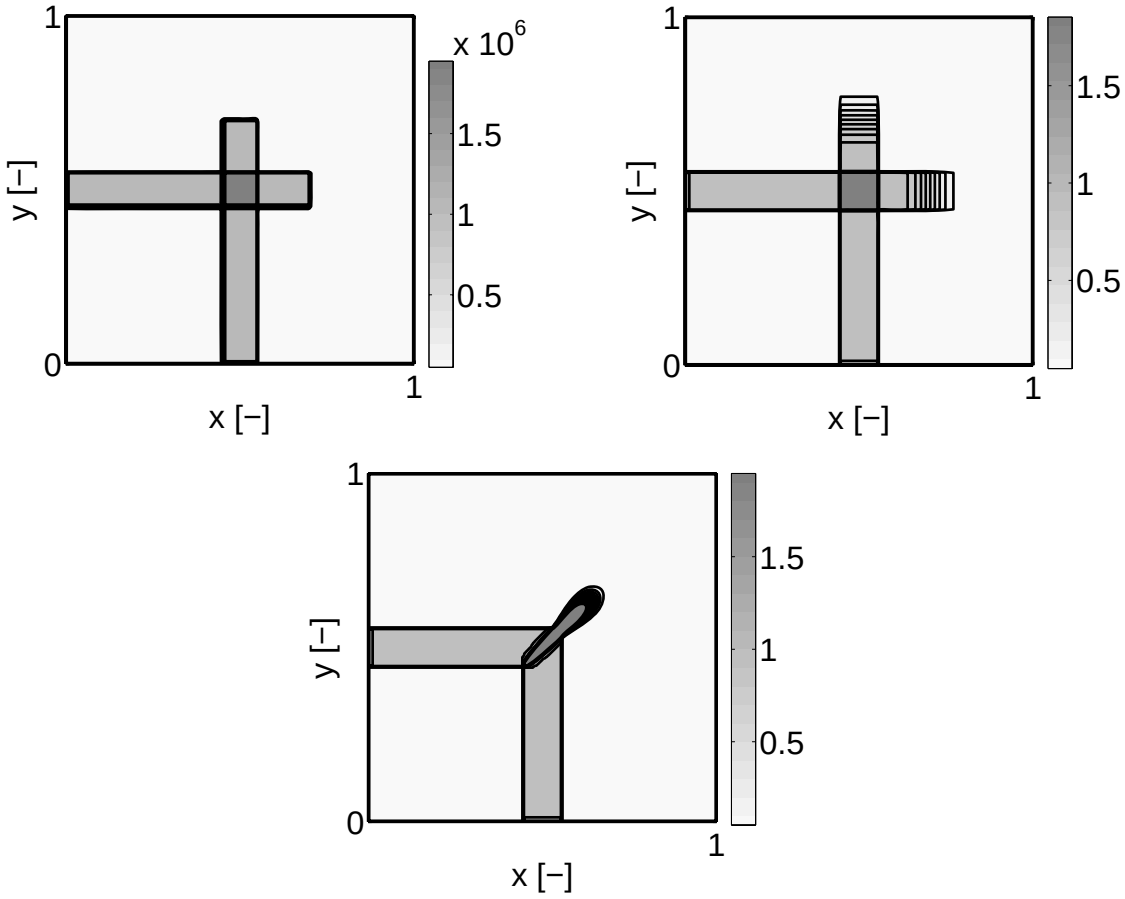

Figure 6.10: Number density of droplets ($M^{0,0,0}$) at t=0.7 without drag force; Lagrange method (top left); QBMoM (top right); first-order Euler method (bottom).

by Stokes drag force resulting from the velocity difference between droplets and gas. The gas is at rest.

In the Taylor-Green configuration (Section 6.3.2), an initially homogeneous distributed monodisperse spray is accelerated by four counter-rotating gas vortices, where periodic boundary conditions are applied.

6.3.1 Crossing of Monodisperse Spray Jets

In a two-dimensional domain of size 1×1, two monodisperse sprays of width $e = 0.1$ and initial velocity $\mathbf{v}_0 = 1$ enter the domain continuously from the bottom and the left (see Figure 6.9_1). The two sprays are expected to cross in the middle of the domain, irrespective of a drag force that may or may not act on them. The reason for this behaviour is the assumption of collisionless droplet clouds (infinite droplet Knudsen number). The top and right walls have zero-gradient boundary conditions, i.e. the spray jets are disappearing at these walls. A first-order convection scheme is used for QBMoM.

In the case where no drag force is acting on the droplets, QBMoM and Lagrangian results for $M^{0,0,0}$ are identical in the region where the jets cross (see Figures $6.10_{1,2}$). The

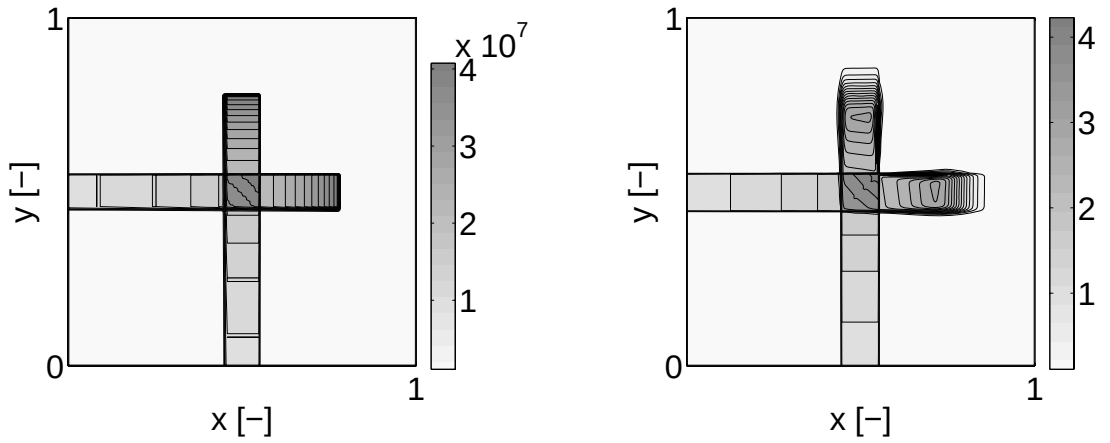

Figure 6.11: Number density of droplets ($M^{0,0,0}$) at t=1.5 with Stokes drag force (St = 1.0); Lagrange method (left); QBMoM (right).

only difference between these results is the numerical diffusion at the head of the spray jets which is observed in the QBMoM solution. Notice that in the crossing region the number density of droplets is the sum of the number densities of the incident spray jets. This behaviour cannot be predicted with the first-order Euler method which was presented in Section 3.3.3 (see Figure 6.10_3). For the latter method, all droplets that reach a crossing point change their velocity to the mean velocity at that point ('sticky-particle' model).

If a drag force is added, the spray jets adapt to the gas flow. As the gas flow is assumed to be at rest, the droplet clouds decelerate until they come to a standstill. The Stokes number is chosen to be St = 1.0. Again, the results for the Lagrange method and the QBMoM are qualitatively and quantitatively very similar (see Figure 6.11). Only at the boundaries and at the diagonal of the crossing region some minor defects are introduced. The results of the first-order Euler method are not depicted because, as has been shown already (see Figure 6.10_3), it is not able to capture the crossing behaviour of spray jets having infinite droplet Knudsen numbers.

6.3.2 A Monodisperse Spray in a Taylor-Green Vortex Gas Flow

The vortex configuration of Taylor & Green [168] consists of four (or more) eddies of the same size but different rotating directions (see Figure 6.9_2). In each of the square cells the gas velocity components are defined by

$$U_{gx} = \sin(\pi x)\cos(\pi y)\ , \qquad U_{gy} = -\sin(\pi y)\cos(\pi x)\ . \tag{6.6}$$

Periodic boundary conditions are prescribed at the boundaries of the computational domain. The velocity field of the gas flow is depicted in Figure 6.12_4.

Initially, the dispersed phase is distributed homogeneously in the whole computational domain. The drag force that is acting on the dispersed phase leads to an ejection of particles from the centres of the vortices. If the Stokes number is above the critical value St = $\pi/8$ [34], particles leave the vortex cells and PTC is observed. In the configuration

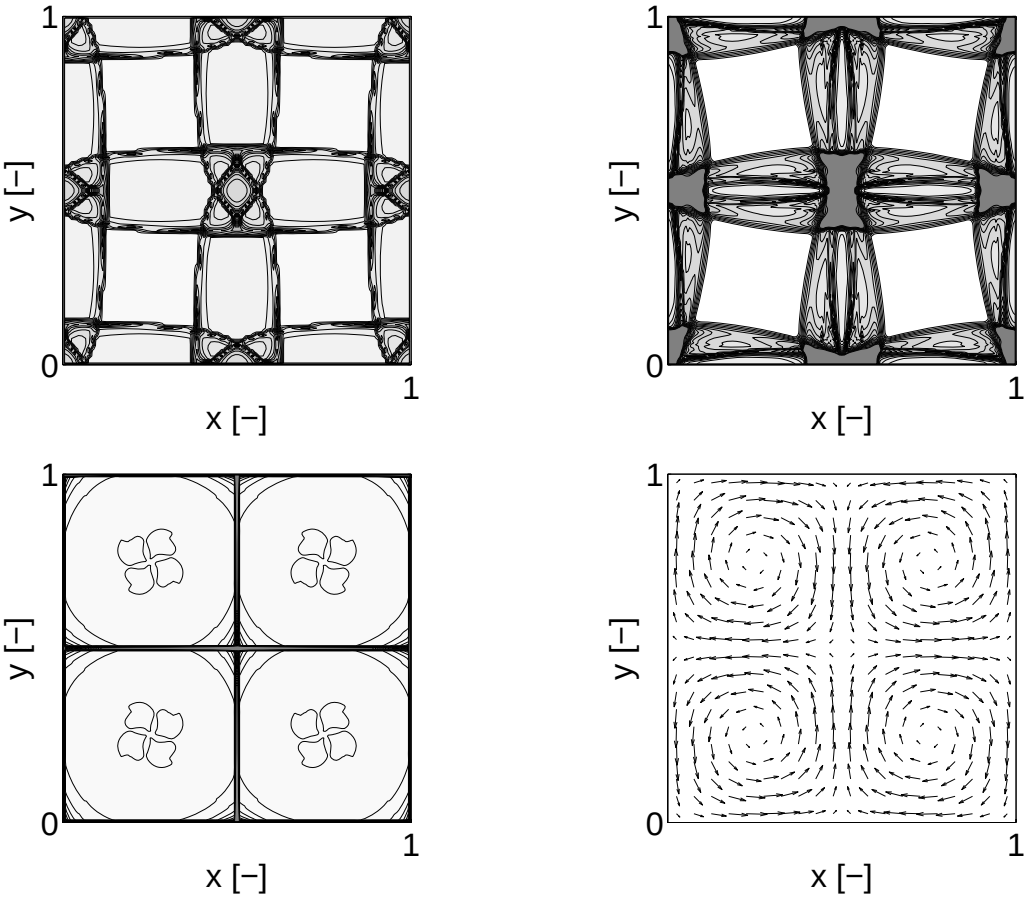

Figure 6.12: Number density of droplets ($M^{0,0,0}$) at t=1.2 in a Taylor-Green vortex configuration with drag force (St = 1.0); Lagrange method (top left); QBMoM (top right); first-order Euler method (bottom left); velocity field of the gas flow (bottom right).

tested here, the Stokes number is set equal to St = 1.0 and again a first-order convection scheme is used for QBMoM.

Although this configuration is very regular, it allows the mimicking of turbulent two-phase particle flows. Just like in turbulent flows [84], vacuum zones and regions of strong mass concentrations form at the centre and rim of the vortices, respectively. The PTC, which is expected at the boundaries of vortex cells, is also a main feature in turbulent two-phase flows.

In Figure $6.12_{1,2,3}$ the qualitative results for the Lagrange method, QBMoM and the first-order Euler method are shown. All methods conserve the mass of particles in the system (not shown here). As the Lagrangian calculation is conducted with a large number of droplets ($4.0e6$) and averaging cells ($N_x \times N_y = 100 \times 100$), it can be regarded as reference solution. The flow of the particles has the following features:

(i) initially unsteady behaviour of all structures (not shown here),

(ii) strong concentration at the rim of a vortex,

(iii) vacuum zones in the centre of a vortex,

(iv) particle transfer between vortex cells,

(v) multi-modal velocity distributions on various points in the domain.

Although the structures observed in the Lagrangian calculations, are not exactly reproduced by the QBMoM the issues in (ii) to (iv) are clearly demonstrated in Figure 6.12_2. The deviations between Lagrange method and QBMoM result mainly from the multi-modal (and not solely bi-modal) velocity distributions which are observed, for example, in the centre, corners and midpoints of edges (quad-modal points). However, the bi-modal PTCs at the boundaries between two vortex cells are well captured.

The first-order Euler method is not able to predict the ejection of particles from one vortex cell (see Figure 6.12_3). The reason is that bi-modal – not to mention multi-modal – velocity distributions cannot be described with this method.

6.3.3 Discussion of Results

QBMoM is shown to capture the crossing of perpendicular moving spray jets that may or may not be affected by a Stokes drag force. The first-order Euler method, on the other hand, fails to describe bi-modal velocity distributions in the region of crossing jets. With Stokes drag force, small interactions between the crossing jets is also observed using QBMoM. It is assumed that these interactions result from numerical diffusion. It smoothes the sharp jump in the higher velocity moments and the defective moments, particularly the cross moments, result into small deflexions of the jets. This numerical defect may be reduced by using higher-order convection schemes or finer real space discretisations.

The calculations in the Taylor-Green configuration (Section 6.3.2) demonstrate that QBMoM is far more accurate for unsteady gas-particle flows than the first-order Euler method. The main reason is that QBMoM captures bi-modal velocity distributions, whereas the 'sticky-particle' model assumes velocity distributions to be mono-modal (see Section 3.3.3). The velocity distributions are usually multi-modal in turbulent gas-particle

flows. In this case even the QBMoM is not able to capture all structures obtained with the Lagrange method. Therefore, the mass concentrations at the rims of vortices are stronger with QBMoM than they are for the reference Lagrange method. The extension to more than two quadrature nodes would further improve the accuracy of the QBMoM [58]. This, of course, would come at the expense of transporting more moments.

The computations outlined in this section deal only with monodisperse particle clouds where every particle has the same Stokes number. For polydisperse sprays, the Stokes number changes with the size of droplets, which leads to size-dependent accelerations or decelerations of droplets in the gas flow. This issue will be addressed in the following sections.

6.4 The New Moment Method in One Dimension

The QBSM is tested in three one-dimensional spray configurations that change the spray distribution in surface space, *first*, through evaporation (Section 6.4.1), *second*, through Stokes drag force (Section 6.4.2), and *third*, through splashing[3] (Section 6.4.3).[4] All test cases were organised in such a way that crossing of two spray distributions was included. The surrounding gas is at rest. Solutions to the same test cases were also computed using a Lagrange method (see Section 3.3.1). They are regarded as accurate reference solutions. The models for evaporation (d^2-law), splashing (see Sections 2.6 and 5.6) and drag (Stokes drag force) were incorporated into the Lagrangian code without any cut back.

The QBSM is studied by changing the numbers of sections, cells, the dimensionless numbers Ev and St, and the splashing parameters α, β_d and γ. The test cases for evaporation and splashing are considered to be stationary, whereas the drag test case is unstationary because the stopping of small droplets leads to their continuous accumulation.

6.4.1 Crossing Polydisperse Sprays with Evaporation

It was shown in Section 6.2 and also confirmed by Dufour and Villedieu [44], Laurent and Massot [96], Laurent et al. [97] that the sectional method can capture evaporation very accurately with general evaporation models. However, for a configuration where two or more evaporating spray distributions are crossing each other, the sectional method as well as all other first-order Euler methods fail to predict even qualitatively the correct solution of the kinetic spray equation.

Here, the QBSM is tested in a one-dimensional configuration in which two truncated Gaussian number density functions ($\mu = 0.5$, $\sigma = 0.2/\sqrt{2}$, $s_c = 1.0$ in equation (6.5)) with different initial velocities ($v_{\text{left}} = 1$, $v_{\text{right}} = -2/3$) at $x = 0$ and $x = 1$ are moving towards each other. The two initial spray distributions evaporate according to the d^2-law (Ev = 0.52), i.e. they are shifted towards $s = 0$ (see (5.75)-(5.77)). In this model, the droplet drag force as well as heating of droplets arising in (5.1) are assumed to be absent.

[3] This is most likely the first time splashing of a polydisperse spray has been captured by an Eulerian procedure. Desjardins et al. [39] were able to describe splashing for a monodisperse spray.

[4] These one-dimensional results are published in [153, 154].

With these assumptions the spray equation (5.1) reduces to

$$\begin{aligned} &\frac{\partial}{\partial t}(f(t;v,s)) + \frac{\partial}{\partial x}(vf(t;v,s)) - \mathrm{Ev}\frac{\partial}{\partial s}(f(t;v,s)) = 0 \ , \\ &\text{with} \quad t > t_n, \quad x \in [0,1], \quad v \in \mathbb{R}, \quad 0 < s \leq 1 \ , \end{aligned} \tag{6.7}$$

with the boundary conditions introduced in (5.76) and (5.77).

In Figure 6.13 the number density distribution of droplets in surface space, $\mathrm{M}_k^{0,0,0}$, is shown for steady calculations of QBSM with $N_s = \{5, 10, 20\}$ sections and $N_x = \{50, 100, 200\}$ cells at positions $x = 0.5$, $x = 0.7$ and $x = 0.9$. In addition, the inlet distribution (dashed lines) and the reference Lagrangian solutions (solid lines) are depicted.

In the plot for $x = 0.5$ and $x = 0.7$ (upper and middle graphs in Figure 6.13) the two spray jets have evaporated and overlap, i.e. the distributions are shifted towards $s = 0$ and the droplet number of the two distributions sum up to nearly twice of the inlet distribution. This behaviour indicates that the distributions are crossing each other. If the method could not predict the crossing behaviour, a strong mass concentration, called delta shock, would have formed at the point where the distributions first cross ($x = 0.6$). This shock would have moved according to the relation between the momenta of droplets in each section. All droplets that arrive at the delta shock would have concentrated there and, as the velocity of the left distribution is larger, no droplet coming from the right of the computational domain could have reached $x = 0.5$. Indeed, the lower plot in Figure 6.13 confirms the proposition that the two jets cross each other. The left peak represents the droplets coming from the left of the computational domain, whereas the right peak originates from the right and has evaporated only slightly. As droplets coming from the left are existing at position $x = 0.9$, they must have crossed the spray distribution coming from the right.

Calculations with 5 sections are very crude but can still capture the evaporation and crossing effect of the spray. Using a larger number of sections improves the results considerably but still, as shown in the lower plot of Figure 6.13, there is a discrepancy between the Lagrangian and QBSM calculations. This defect of QBSM may originate from small numerical interactions between the two distributions crossing each other. More elaborated analysis have shown that the introduction of only one exponential parameter b_k in the approximate NDF in (4.8) may be responsible for these artificial interactions. The introduction of exponential parameters for each quadrature node could presumably resolve this defect, but this would require a much more sophisticated algorithm for the determination of the exponential parameters and the transport of more moments.

The parameter study of the discretisation in real space gives the expected results. With smaller cell sizes the differences between QBSM and Lagrangian calculations reduce. By changing the values for Ev the sensitivity of the numerical method was tested. The number densities of droplets at positions $x = 0.5$, $x = 0.7$ and $x = 0.9$ are depicted in Figure 6.14. Beside the fact that the number densities are moving faster (slower) towards $s = 0$ when Ev is increased (decreased), the stability and accuracy of QBSM is not reduced. These results indicate that the QBSM does not restrict the choice of Ev.

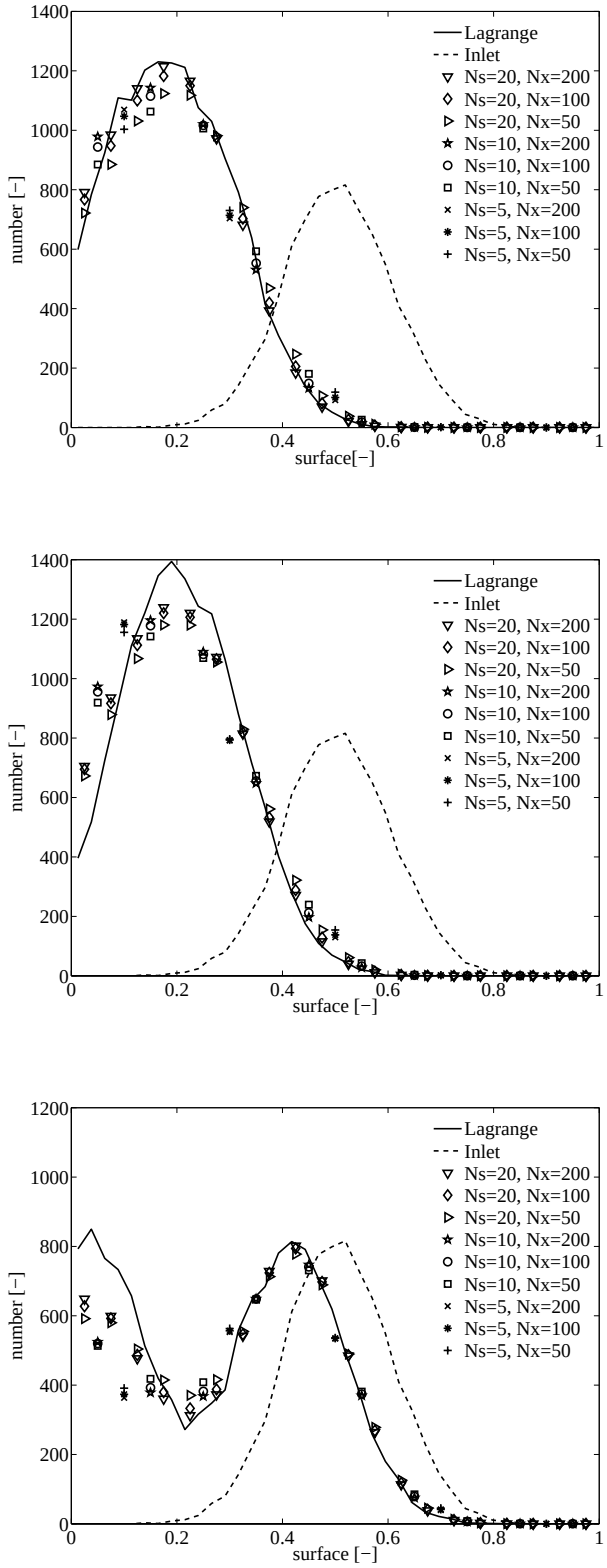

Figure 6.13: Number density of droplets ($M_k^{0,0,0}$) at $x = 0.5$ (upper), $x = 0.7$ (middle) and $x = 0.9$ (lower); evaporation and crossing of spray jets with Ev = 0.52; parameter study of the number of sections and cells.

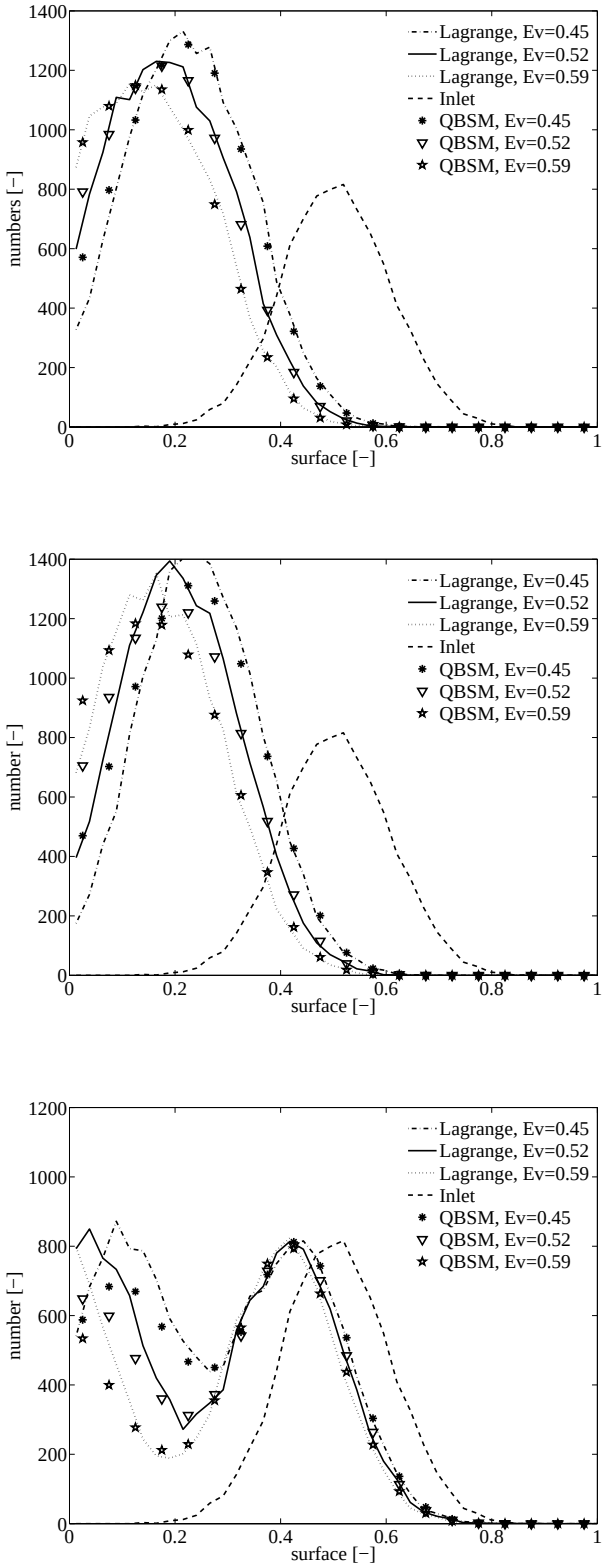

Figure 6.14: Number density of droplets ($M_k^{0,0,0}$) at $x = 0.5$ (upper), $x = 0.7$ (middle) and $x = 0.9$ (lower); evaporation and crossing of spray jets; various evaporation numbers; $N_s = 20$ and $N_x = 200$.

6.4.2 Crossing Polydisperse Sprays with Drag force

It was shown in Section 6.2 and in [44, 96, 97] that the sectional method can accurately predict the behaviour of spray droplets which are affected by drag and gravity forces. In a polydisperse spray which is accelerated or decelerated by the surrounding gas, the forces on the droplets, and consequently their velocities, are correlated, among other things[5], with the droplet sizes. For the SM, droplets collected in one section exhibit the same velocities. Therefore, it is expected that the more sections come into play for the discretisation of the size space, the more accurate the correlation between velocity and size variables is predicted. It is shown in this test case that the combination of the SM with the QBMoM does not change the ability of the combined method to capture the phenomenon of drag affecting a spray.

In this test configuration the truncated Gaussian number density functions ($\mu = 0.5$, $\sigma = 0.2/\sqrt{2}$, $s_c = 1.0$ in equation (6.5)) are moving towards each other, starting at the ends of the computational domain, $x \in [0, 1]$. During the crossing process they are affected by a Stokes drag force which results from the velocity difference between the spray and a non-moving gas. This drag test case can never reach a steady state because those droplets that are stopped by the gas before leaving the computational domain accumulate at a particular position until the computation stops. Smaller droplets decelerate faster and stop closer to where they came from. This phenomenon is commonly called the size segregation of droplets.

In Figure 6.15 the QBSM results of the drag test case (St = 2.43) at time $t = 5$ are depicted and compared with calculations using the reference Lagrange method. The number of sections and cells are varied according to $N_s = \{5, 10, 20\}$ and $N_x = \{50, 100, 200\}$ and the upper, middle and lower plots refer to the results at positions $x = 0.5$, $x = 0.7$ and $x = 0.9$. For all results shown in Figure 6.15, the number densities of droplets are much higher than the initial distribution. The reason for this behaviour is, *first*, the deceleration of droplets which leads to an accumulation and *second*, the overlap of the crossing distributions.

Note also that all number density distributions in Figure 6.15 exhibit an asymmetry which is due to the drag force. Small droplets on the left sides of the graphs experience a strong deceleration and stop before they leave the computational domain. The steep gradient, observed in all graphs, marks the border between stopped (left side of the steep gradient) and moving droplets (right of the steep gradient). In the plot for $x = 0.9$, on the left side of the steep gradient there are droplets which have not stopped and which agree very well with the number density distribution at the inlet. Those droplets belong to the distribution coming from the right.

The parameter study of QBSM for the number of sections and cells shows the expected results. Increasing the discretisation in size and real space decreases the difference between the Lagrangian and QBSM predictions. In the plot for $x = 0.9$ the improvement due to the increase from 50 to 200 cells is very pronounced. This behaviour can be explained by the fact that the increase of maximum number density between $x = 0.5$ and $x = 0.7$ is much smaller than between $x = 0.7$ and $x = 0.9$. This strong gradient

[5] In general, the acceleration and deceleration of a droplet is determined by its size, mass density, shape and dynamic behaviour. In the Stokes drag force model (2.18) only differences in size and mass density are considered.

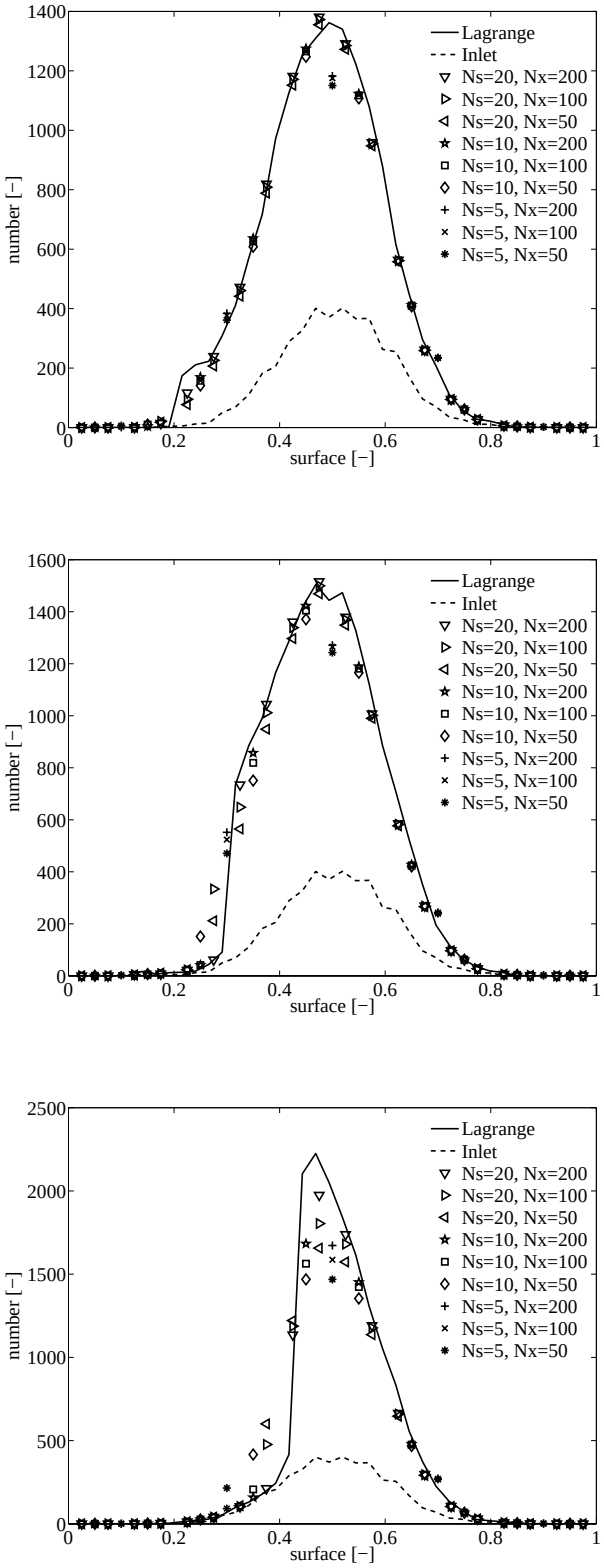

Figure 6.15: Number density of droplets ($M_k^{0,0,0}$) at $x = 0.5$ (upper), $x = 0.7$ (middle) and $x = 0.9$ (lower), $t = 5$; crossing sprays affected by Stokes drag with St = 2.43; various numbers of sections and cells.

of the number density in real space requires a finer x-discretisation in order to obtain a more accurate solution. For the variation of the number of sections there is only a small difference between solutions using 10 and 20 sections. With 5 sections, the behaviour of the drag effect can be captured only qualitatively.

The Stokes number of the largest droplets, $\mathrm{St}_{\mathrm{char}}$, is varied according to $\mathrm{St}_{\mathrm{char}} = \{1.22, 2.43, 3.64\}$ to test the sensitivity of the method. In Figure 6.16 the QBSM solutions with 20 sections and 200 cells are compared with the Lagrangian results at positions $x = 0.5$, $x = 0.7$ and $x = 0.9$. For the smallest $\mathrm{St}_{\mathrm{char}}$ the concentration of droplets is very pronounced for both the distributions moving to the left (left peak in Figure 6.16_2) and the distribution moving to the right (right peak in Figure 6.16_2). In the upper and middle plot of Figure 6.16 the gradients in size and real space are the steepest for the smallest Stokes number. In the plot for $x = 0.9$ the droplets coming from the left of the computational domain are not present. This behaviour is due to the strong deceleration and stopping of the droplets before reaching $x = 0.9$. In Figure 6.16_2 the QBSM results can predict the left peak very well but the right peak is not captured correctly. Small numerical errors in the computation quadrature parameters may be the reason for this behaviour. With larger Stokes numbers the gradients are less steep, the deceleration due to the drag force is smaller and the numerical error of QBSM is only minor.

6.4.3 Splashing of a Polydisperse Spray Jet on a Wall

In Section 2.6 the physical model for the splashing of droplets on a wall were introduced and translated to QBSM in Section 5.6. Here the results are reported for the one-dimensional and stationary splashing case, where droplets are continuously flowing into the computational domain $x \in [0, 1]$ from the left. The spray is transported through it without being affected by the gas. On the right end of the domain the spray is splashed according to the splashing condition (2.82) and the droplets that rebound cross the incident droplets. When the spray jet reaches the left inlet it is erased by using a zero gradient boundary condition. This test case is stationary and the only changes in the number density distribution in surface space take place at the right boundary. Therefore, the number density distributions are the same everywhere in the computational domain and the discretisation in real space is of secondary interest.

Figure 6.17 depicts the steady state solution of the number density distribution of droplets obtained for $N_s = \{5, 10, 20\}$ sections. They are compared with the Lagrangian calculations for the parameter set $(\alpha, \beta_d, \gamma) = (0.9, 0.7, 0.1)$. The number of cells is not varied because the spray is freely transported in the computational domain. Only at the boundary is the spray distribution changed. The high peak on the left side represents the splashed spray and is moving away from the wall (see averaged velocity distribution in Figure 6.18), whereas the smaller peak on the right, agreeing with the inlet distribution (dashed line), is moving towards the wall. For this test case the Lagrangian and QBSM solutions for 10 and 20 sections are very close to each other. Reduction in the number of sections to 5 results in some discrepancies, but the qualitative behaviour of the moment method persists.

The sensitivity of the method was also studied for the change of the splashing parameters. In Figures 6.18 to 6.20 the number density distributions are plotted versus the droplet surface at position $x = 0.9$ for the sets of parameters $(\alpha, \beta_d, \gamma) = \{(0.5, 0.7, 0.1),$

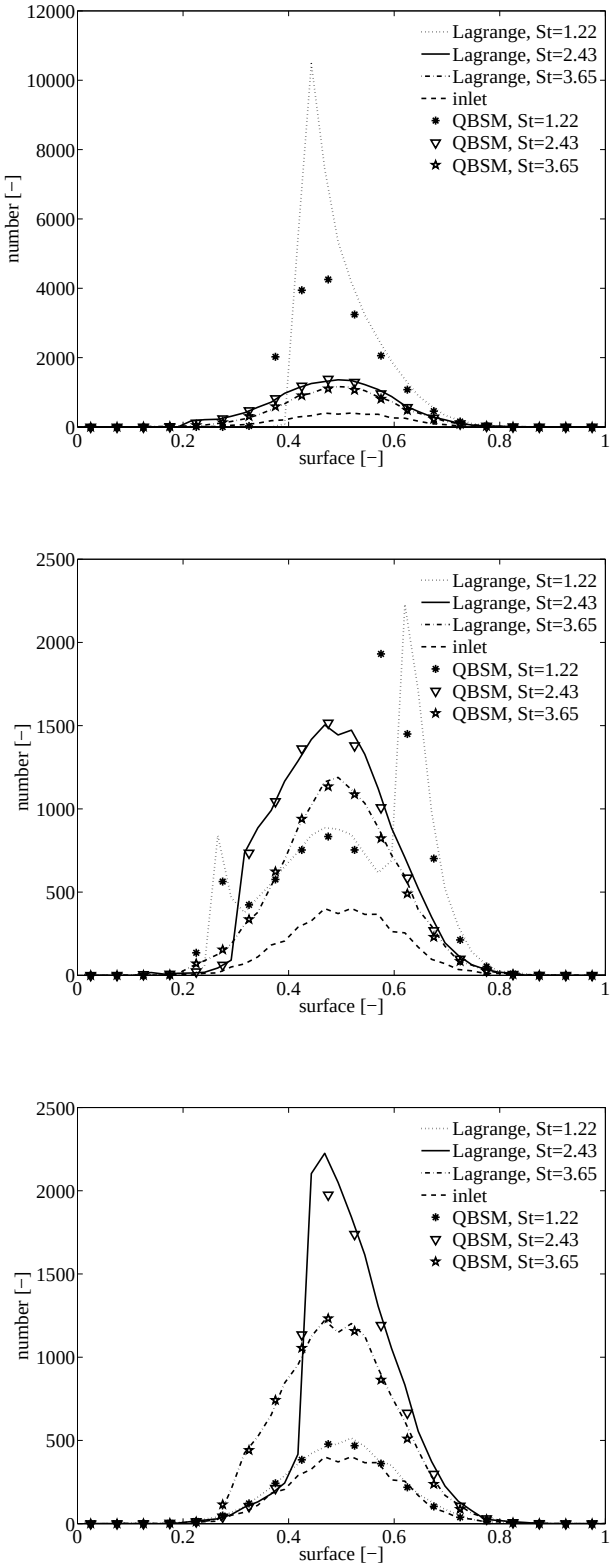

Figure 6.16: Number density of droplets ($M_k^{0,0,0}$) at $x = 0.5$ (upper), $x = 0.7$ (middle) and $x = 0.9$ (lower), $t = 5$; crossing sprays affected by Stokes drag; various Stokes numbers; $N_s = 20$ and $N_x = 200$.

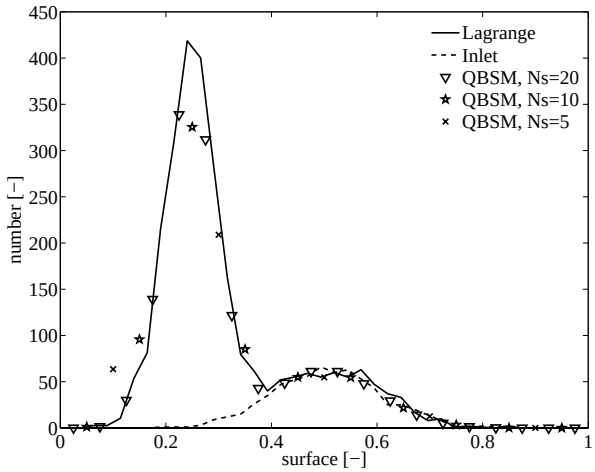

Figure 6.17: Number density of droplets ($M_k^{0,0,0}$) at $x = 0.9$; splashing at a wall with parameters $\alpha = 0.9$, $\beta_d = 0.7$ and $\gamma = 0.1$; parameter study of the number of sections.

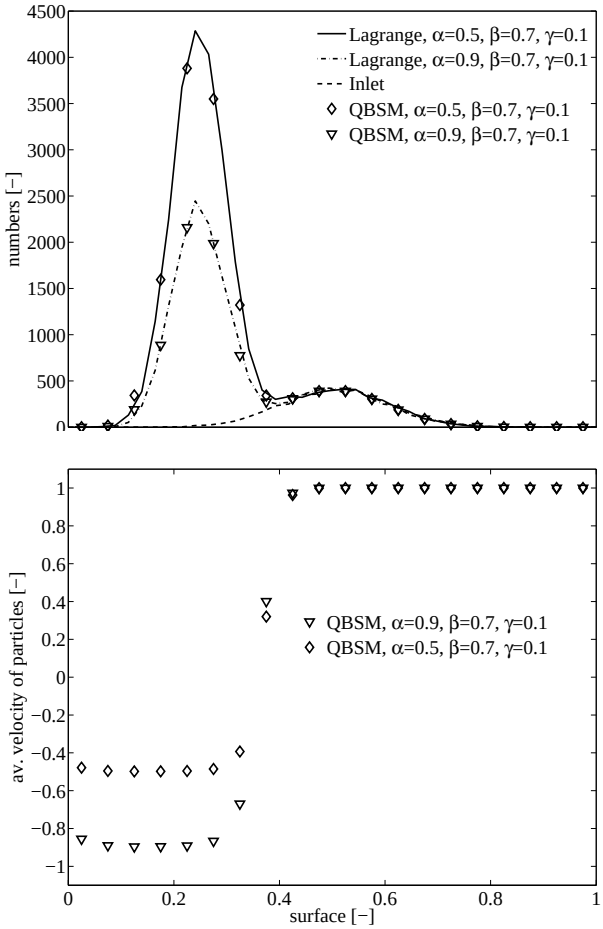

Figure 6.18: Number density of droplets (upper), distribution of averaged droplet velocities (lower) at $x = 0.9$; splashing parameters: $(\alpha, \beta_d, \gamma) = \{(0.5, 0.7, 0.1), (0.9, 0.7, 0.1)\}$; $N_s = 20$ and $N_x = 100$.

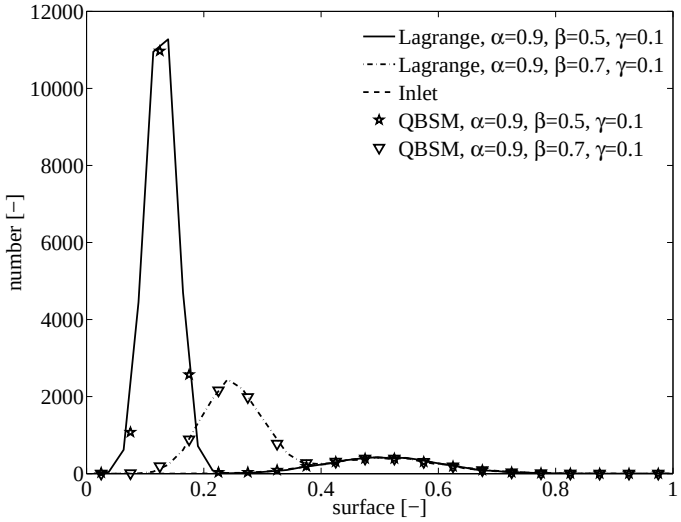

Figure 6.19: Number density of droplets ($M_k^{0,0,0}$) at $x = 0.9$; splashing at a wall with parameters (α, β_d, γ) = (0.9, 0.5, 0.1) and $(\alpha, \beta, \gamma) = (0.9, 0.7, 0.1)$; $N_s = 20$ and $N_x = 100$.

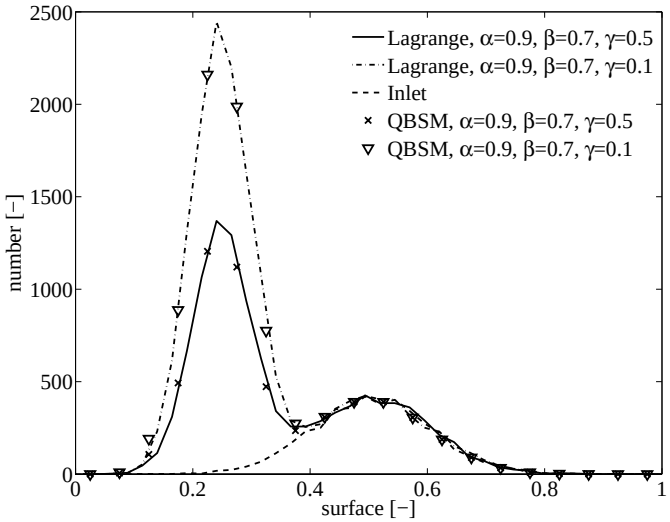

Figure 6.20: Number density of droplets ($M_k^{0,0,0}$) at $x = 0.9$; splashing at a wall with parameters $(\alpha, \beta_d, \gamma) = (0.9, 0.7, 0.5)$ and $(\alpha, \beta_d, \gamma) = (0.9, 0.7, 0.1)$; $N_s = 20$ and $N_x = 100$.

$(0.9, 0.5, 0.1)$, $(0.9, 0.7, 0.5)\}$. Each result is compared with a Lagrangian solution and with the result shown in Figure 6.17. In the lower plot of Figure 6.18 the distribution of averaged droplet velocities, $\mathrm{M}_k^{3/2,0,1}$ / $\mathrm{M}_k^{3/2,0,0}$, is also shown.

Figure 6.18 illustrates what happens when droplets are reflected inelastically on a wall. The reduction of the absolute velocity value (lower part of Figure 6.18) on the wall leads to an increase in the number density of splashed droplets (upper part of Figure 6.18), an obvious consequence of the mass conservation. The comparison between Lagrangian and QBSM calculations shows good agreement for this deceleration effect and also the average velocities agree with those expected from the model in the splashing condition (2.82).

The breakage of the droplets is determined by the parameter β_d. Smaller values of this quantity result in more but smaller daughter droplets after splashing. This behaviour is shown in Figure 6.19 for the Lagrangian and the QBSM calculations.

The model in (2.82) also included a parameter γ that allows the consideration of mass deposition on the wall or sudden liquid evaporation due to a hot wall. For large values of γ a large number of droplets is taken from the system. In Figure 6.20 Lagrangian and QBSM calculations are compared for two different values of γ. The QBSM results recover the reference Lagrangian solutions nicely.

6.4.4 Discussion of Results

For the evaporation test case in Section 6.4.1, the discretisation of the size space with a small number of sections leads to qualitative correct results but unfortunately some discrepancies between QBSM and Lagrangian calculations remain. This defect does not originate from the sectional part of QBSM because it was tested and found to be appropriate for non-crossing spray flows. The source of error may be some small interactions between the two distributions which could result from the consideration of only one instead of β (number of quadrature nodes) exponential parameters β_k for a section (4.8). Using an exponential parameter for each quadrature node would further increase the number of moments that have to be transported. To keep the computational costs limited parameters beyond those in (4.11) were not introduced.

The drag test case reveals a convincing agreement of QBSM with the Lagrangian reference calculations (Section 6.4.2). Minor problems arise when the maximum Stokes number decreases and the gradients between moving and non-moving droplets get steeper. In this case the system of moment transport equations gets stiff, numerical errors cannot be prevented. Nevertheless, the qualitative behaviour of QBSM for small Stokes numbers is correct.

In the test cases for splashing (Section 6.4.3), close agreement between QBSM and Lagrangian calculations is observed. The choice of splashing parameters is not limited by QBSM. It was explained in Section 2.6 how this simple model can be extended to more realistic splashing configurations by introducing dependencies of the splashing parameters on the droplet velocity, size and temperatures before splashing and on the properties in the vicinity of the wall. The splashing test case outlined above is used here, not to compare with experimental results but to assess the behaviour of QBSM when the number density function is changing in size and velocity space and a crossing of droplets is present.

The one-dimensional test cases outlined in this section have shown that QBSM is capable of describing evaporation, drag forces and splashing in configurations where PTC is present. These test cases also indicate that 5 to 10 sections are sufficient to capture the qualitative behaviour of the phenomena in surface space. As the configuration is limited to one real space dimension, the convection of the number density distribution is not assessed in more detail. This issue will be the subject of the following sections.

6.5 The New Moment Method in Two Dimensions

This section extends the above one-dimensional test cases (Section 6.4) to two dimensions in real space. The crossing of perpendicular moving spray jets, which was already considered for the verification of the QBMoM (Section 6.3), is used for two perpendicular moving polydisperse spray jets that experience drag or evaporation. The Stokes drag model and d^2-evaporation law are applied. In addition to the crossing jets, QBSM is tested in a splashing configuration, which is the extension of the configuration outlined in Section 6.4.3. In two dimensions the splashing can also have an impact on the droplet velocity component that is parallel to the wall.

It was shown in Sections 6.2 and 6.4 that QBSM delivers satisfying results with 10 sections in surface space. Here, the behaviour of QBSM is not tested further with respect to the number of sections. It is fixed to $N_s = 10$. In addition, the inlet distribution in surface space is taken to be the truncated Gaussian density function (6.5) with mean $\mu = 0.5$, standard deviation $\sigma = 0.1/\sqrt{2}$ and truncation value $s_c = 1.0$ (see Figure 6.1). The transport in real space is treated with the first-order convection scheme introduced in Section 5.3.2.

The same test cases were also computed with the reference Lagrangian method and compared with the QBSM calculations. The results of the two methods, depicted in Figures 6.21 to 6.23, differ by a large scaling factor. As the injection number density of droplets is normalised to one in the QBSM and to a power of 10 in the Lagrange calculations, the grey scales in the plots are of the same order of magnitude. This representation is kept to demonstrate that the Lagrange calculations were performed with a large number of parcels.

6.5.1 Crossing of Polydisperse Spray Jets

The configuration depicted in Figure 6.9_1 with $e = 0.1$ and injection droplet velocity $\mathbf{v}_0 = 1.0$ is used to test the behaviour of QBSM when two *polydisperse* spray jets cross each other. Besides the test in which the spray is affected by a drag force, QBSM is also studied in a configuration in which the spray evaporates.

The drag force is modelled by the Stokes law (see equation (2.18)), where the Stokes number ranges from zero to St = 2.0 for the largest droplet. Drag forces the spray flow to adapt to the motion of the gas. As the gas is assumed to be at rest, the droplets decelerate, accumulate and stop. Droplets with small Stokes numbers experience a faster deceleration than those with large Stokes numbers. The drag force is also acting in the crossing region. Therefore, accumulation and stopping of droplets is also present there. In

Figure 6.21 the number density of droplets ($M^{0,0,0}$) for the reference Lagrange calculation (left column) and QBSM (right column) are shown for different times $t = \{0.4, 1.0, 2.0\}$. The last row represents the structure of the calculations which remains for all times larger than $t = 2.0$. However, it is not the steady state solution because all droplets that are supplied to the system remain inside it.

The Lagrangian results (Figures $6.21_{1,3,5}$) demonstrate clearly that the droplets accumulate and that most of the droplets stop approx. at $(x, y) = (0.5, 0.65)$ and $(x, y) = (0.65, 0.5)$, respectively. These are the droplets which are approx. of size $s = 0.5$. Smaller droplets stop before these points (not shown here) and the largest droplets can reach the end of the domain (see Figure 6.21_5). This phenomenon is commonly called size segregation of droplets. It reflects the size dependence of the drag force and is strongly linked to the initial size distribution. When all droplets have the same size (see Figure 6.11), they stop at one point. Here, the droplets are initially distributed according to a truncated Gaussian distribution and therefore the stopping positions are distributed in the computational domain.

The solution of the QBSM is qualitatively very similar to the reference solution. It should be pointed out that

- before crossing the Lagrangian and QBSM solutions agree with each other (see Figures 6.21_1 and 6.21_2),
- the stopping positions of droplets having sizes around $s = 0.5$ are well reproduced by QBSM,
- the behaviour of droplets with large Stokes number is well predicted,
- no collision between the spray jets occurs.

However, some differences between Lagrange and QBSM results are observed. These are

- inconsistencies at the diagonal of the crossing region,
- small interactions of the jets at the points where the spray jets first cross,
- small influences of the crossing region on the spray jets downstream the crossing region.

The small 'bumps' at the diagonal of the crossing region result from the switch from the QBMoM of Fox [56] to that of Le Lostec et al. [99]. They are already observed in Figure 6.11. The reason for this switch is that the determinate of the covariance tensor $\boldsymbol{\sigma}_U$ (4.47) is zero at this diagonal. This behaviour can only be prevented when the situation $\det(\boldsymbol{\sigma}_U) = 0$ is also treated with the method of Fox [56] (for detailed explanations see Section 4.4.2). This task has to be postponed to future research.

It is assumed that the small interactions between spray jets at the first crossing points result from numerical diffusion. It smoothes the sharp jump in the higher-order moments and the defective moments, particularly the cross moments, result into a small deflexion of the jets. This numerical defect may be reduced by using higher-order convection schemes or finer real space discretisations. The small influences of the spray jet upstream the crossing region are assumed to also originate from the numerical smoothen of the jumps in the velocity moments.

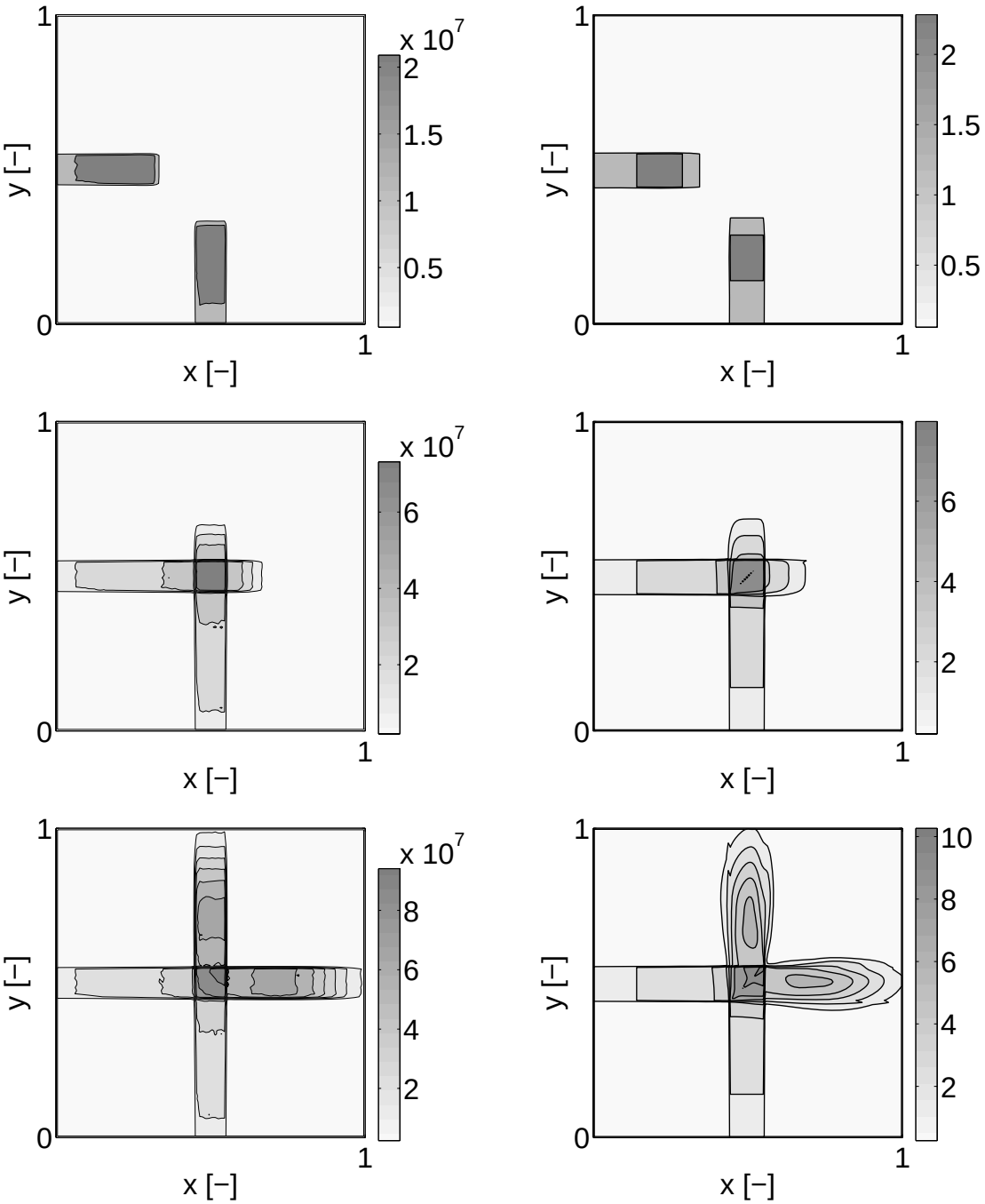

Figure 6.21: Number density of droplets ($M^{0,0,0}$) at $t = 0.4$ (top), $t = 1.0$ (middle) and $t = 2.0$ (bottom) with drag force ($St_{max} = 2.0$); Lagrange method (left column); QBSM (right column), $N_x = 150$, $N_y = 150$, $N_s = 10$.

It should be pointed out that QBSM calculations with only one section cannot predict the distribution of stopping positions because all droplets are assumed to have only one (average) Stokes number. For two sections, two distinct stopping positions are observed, etc. Consequently, the accurate prediction of segregation effects requires a fine discretisation of the droplet size distribution. From the results in Figures $6.21_{2,4,6}$ it is observed that 10 sections are sufficient to discretise a truncated Gaussian distribution.

The evaporation of droplets is modelled by a d^2-evaporation law that assumes the evaporation number to be constant for all droplet sizes, i.e. Ev = 0.8. As no drag force is acting on the droplets, they keep their initial velocities. In Figure 6.22 the number density

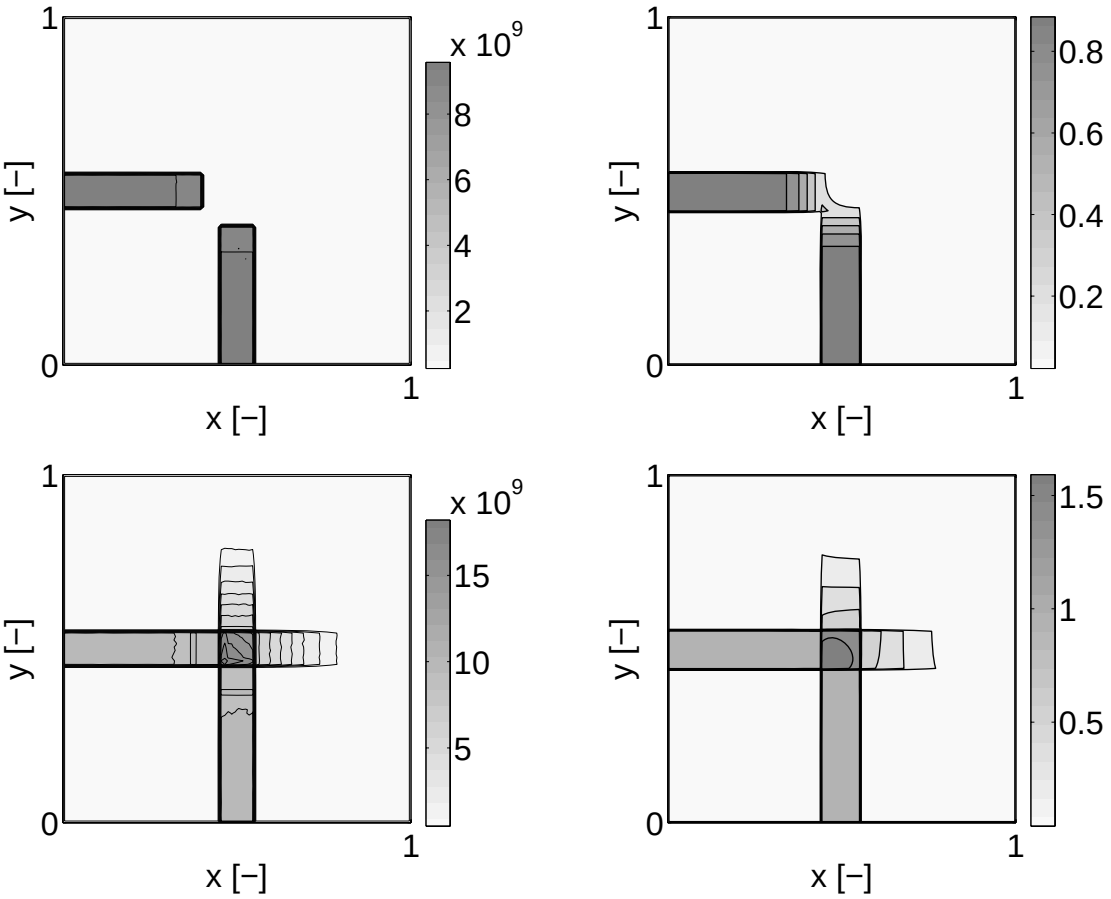

Figure 6.22: Number density of droplets ($M^{0,0,0}$) at $t = 0.4$ (top), $t = 1.0$ (bottom) with evaporation (Ev = 0.8); Lagrange method (left column); QBSM (right column), $N_x = 150$, $N_y = 150$, $N_s = 10$.

of droplets ($M^{0,0,0}$) for the reference Lagrange calculation (left column) and QBSM (right column) are shown for different times $t = \{0.4, 1.0\}$. The results for time $t = 1.0$ are the steady state solutions because droplets that enter the domain are also erased from it.

In Figures $6.22_{1,3}$ the Lagrangian results are depicted. It is observed that in the first 0.4 time units only a small number of droplets are completely evaporated. However, the number density of droplets reduces considerably when the large number of droplets with sizes around $s = 0.5$ start to disappear. Again, some sort of 'size segregation' effect is

observed which depends on the size distribution of droplets injected into the system. The segregation follows from the fact that large droplets take longer time to evaporate than smaller ones. Therefore their residence time in the computation domain is longer and they are convected deeper into the computation domain.

The results of the QBSM (see Figures $6.22_{2,4}$) recover the Lagrangian predictions very well. The only defects of these calculations are small interactions at the crossing lines between the jets and a slightly shorter penetration distance of the large droplets. This behaviour was already observed in the one-dimensional calculations (see Figure 6.13). In Section 6.4.1 this issue was discussed in more detail. There, it is concluded that the interaction between the jets and the reduction of the penetration distance can be prevented by using either more sections or introducing an exponential parameter b_k for each quadrature node. This, of course, would come at the expense of transporting more moments.

6.5.2 Splashing of a Polydisperse Spray Jet on a Wall

The splashing condition for QBSM, developed in Sections 2.6 and 5.6, is tested in a two-dimensional configuration. A spray jet is entering the domain and moves towards the wall with an impact angle of 45°. It is not affected by drag or evaporation. At the wall the droplets break, reduce their velocity and deposit on the wall according the parameters $(\alpha_x, \alpha_y, \beta_d, \gamma) = (0.9, 0.9, 0.7, 0.1)$. In comparison with the one-dimensional test case outlined in Section 6.4.3 an additional splashing parameters, α_y, is introduced that is able to model the friction between droplets and wall. Here, the velocity parameters are set equal in order that impact angle and reflection angle are the same. In Figure 6.23 the number densities ($M^{0,0,0}$), resulting from the Lagrangian (left) and QBSM (right)

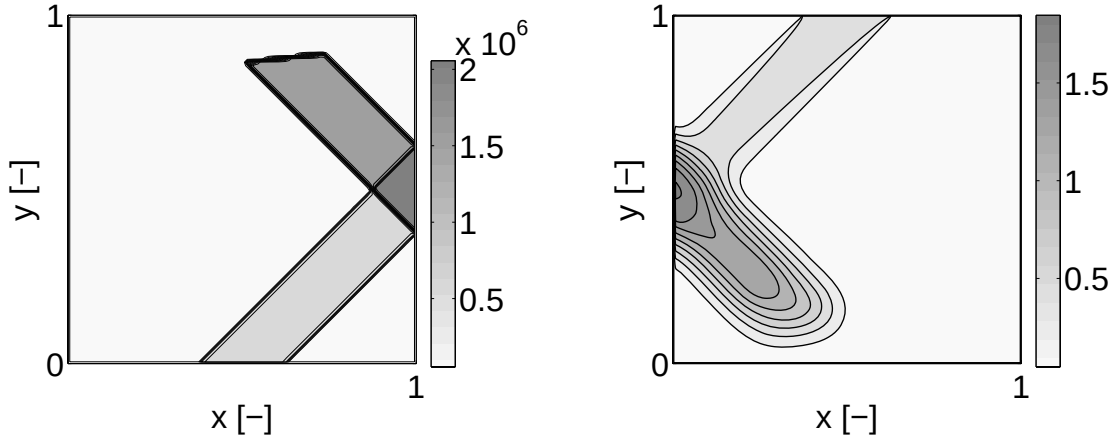

Figure 6.23: Number density of droplets ($M^{0,0,0}$) at $t = 1.3$; splashing on a wall with parameters $\alpha_x = 0.9$, $\alpha_y = 0.9$, $\beta_d = 0.7$, $\gamma = 0.1$; Lagrange method (left); QBSM (right), result rotated by 180°, $N_x = 200$, $N_y = 200$, $N_s = 10$.

calculations at $t = 1.3$ are depicted. The number density distribution in size space obtained from the two methods are compared in Figure 6.24 where three representative positions are chosen. Figure 6.24_1 depicts the number density distribution at a position

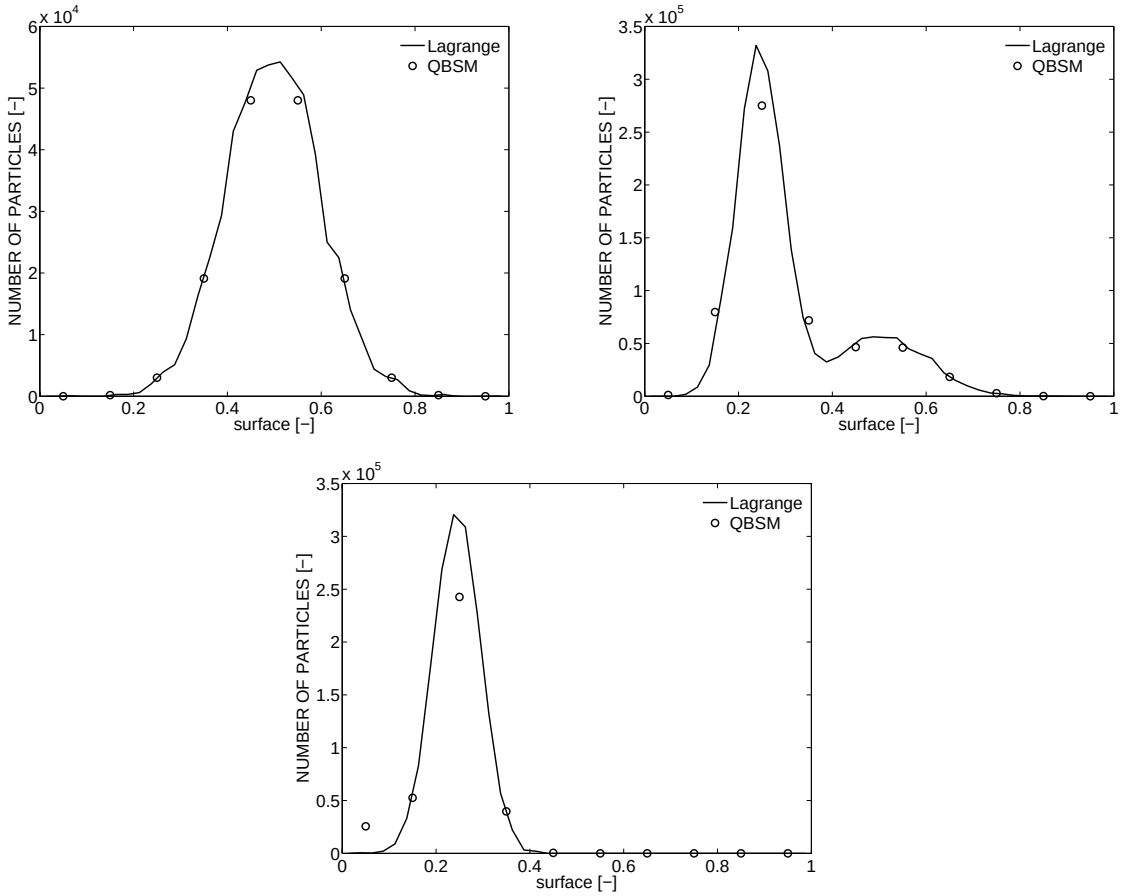

Figure 6.24: Number density of droplets ($M_k^{0,0,0}$) in the incident jet (top left), crossing region (top right) and after splashing (bottom); parameters: $\alpha_x = 0.9$, $\alpha_y = 0.9$, $\beta_d = 0.7$, $\gamma = 0.1$; Lagrange method (solid line); QBSM (circles), $N_x = 200$, $N_y = 200$, $N_s = 10$.

in the incident spray jet, Figure 6.24_2 are the distributions taken from the crossing region and Figure 6.24_3 is obtained from the spray jet leaving the wall. To compare the results from QBSM with those from the Lagrangian calculations, the QBSM results in a section are multiplied by the overall number density of Lagrange droplets at the postion in the incident jet. The same number is also used to scale the QBSM results in the crossing region and the splashed jet.

The Lagrangian results (Figure 6.23_1) demonstrate that the impact angle and the reflection angle are indeed the same and the splashing with the chosen set of parameters leads to an overall increase of droplets. The counteracting phenomena are the deposition of droplets on the wall, which leads to an reduction of droplets, and the fragmentation and accumulation of droplets which results into an increase of droplets. A triangular region forms at the wall, in which incident and splashed droplets cross their trajectories. It should be noted that no size segregation effect is observed although a polydisperse spray is considered. This would only be the case, when the splashing parameters depend on the size of the incident droplets.

The number density of droplets resulting from QBSM (Figure 6.23_2) show that the impact angle and reflection angle are the same, a crossing region is forming at the wall and the overall number density in the jet of splashed droplets is larger than the density in the incident jet. In addition, the head of the splashed jet has reached approximately the same position as that in the Lagrange calculations. However, a large numerical diffusion is observed which seems to be stronger than in the other test cases. This is not true. The other test cases were merely organised in such a way that droplets are only moving in one coordinate direction. If the jet has velocity components in both coordinate directions the numerical diffusion of both directions is present.

Figure 6.24 proves that the number densities of the incident and splashed jets are indeed crossing each other in the near wall region. The left and right peak in Figure 6.24_2 agree in size and scale with the distributions depicted in Figures 6.24_3 and 6.24_1, respectively. However, the sharp peak of the splashed droplets is underpredicted by QBSM. It is assumed that this effect results from the large numerical diffusion observed in Figure 6.23_2. The number density distribution shown in Figure 6.24_2 agrees very well with those in Figure 6.17 (see Section 6.4). Therefore, the conclusion from the parameter study in the one-dimensional test cases do also apply to two-dimensional splashing. The splashing parameter α_y is not varied here as it is shown that impact and reflection angle agree with each other. This indicates that the change of the droplet velocity components in wall-direction are captured accurately.

6.5.3 Discussion of Results

The results in Section 6.5 demonstrate that the QBSM developed in Chapters 4 and 5 can be extended to two dimensions in real space, taking into account the effects of drag force, evaporation, splashing and collisionless crossing of polydisperse sprays.

The results for the crossing of perpendicular moving spray jets (see Section 6.5.1) demonstrate that QBSM can capture bi-modal velocity distributions while drag forces or evaporation are acting on the droplets. The size segregation, which is due to the polydisperse character of the spray, is well predicted by QBSM. However, small jet interactions at the boundaries of the crossing region are observed. The origin of these defects is assumed

to be the numerical smoothen of the jumps in higher-order velocity moments. There are other inconsistencies, arising in the drag test case. They follow from the inability of the QBMoM of Fox [56] to describe situations where $\det(\boldsymbol{\sigma}_U) = 0$. The more robust QBMoM of Le Lostec et al. [99] supports this situation, however it introduces other small errors. As the methods of Fox [56] and Le Lostec et al. [99] were introduced only recently, it is expected that other, more robust numerical procedures will be available in future, building on these methods.

The splashing test case, which is a boundary condition for the transported moments, can only be described with methods that take into account the polydisperse character of sprays and that consider (at least) bi-modal velocity distributions close to the wall. Therefore, the QBSM is particularly suitable for describing splashing jets (see Section 6.5.2). Of course, in real splashing cases the incident and splashed droplets interact heavily in the crossing region and the splashing parameters depend on the droplets reaching the wall. However, it was explained in Sections 2.6 and 5.6 how this simple model can be extended to more realistic situations.

The main problem in two-dimensional configurations is the numerical diffusion in real space. It can lead to large errors (see Figure 6.23_2) that distort the physical content of the solution. It is desirable to implement and test the second-order scheme developed in Section 5.3.3. The other action to prevent numerical diffusion could be the increase of cells in the computational domain. This, of course, would come at the expense of higher computational costs.

6.6 Polydisperse Spray Jets in a Taylor-Green Vortex

Sprays in combustion systems are usually carried by *turbulent* gas flows. Therefore, it is necessary to extend the rather theoretical test cases in the previous sections to configurations in which the gas flow in inhomogeneous. In this section two polydisperse spray jets are injected into a counter-clockwise rotating Traylor-Green vortex gas flow (see Section 6.3.2 and Figure 6.12_4). In the first configuration only a drag force is acting from the gas on the droplets (St = 2.0). In a second configuration the spray exhibits drag forces (St = 2.0) and evaporation (Ev = 0.4). Similar to the test cases in Section 6.5.1 the two spray jets are crossing each other but before doing so they are deflected by the Taylor-Green vortex. Again, the first-order convection scheme (see Section 5.3.2) is used, the inlet distribution in surface space is taken to be the truncated Gaussian density function (6.5) with mean $\mu = 0.5$, standard deviation $\sigma = 0.1/\sqrt{2}$ and truncation value $s_c = 1.0$ (see Figure 6.1) and the number of sections is $N_s = 10$.

6.6.1 Results for a Polydisperse Spray

In Figure 6.25 results of the QBSM (right) and Lagrangian (left) calculations are depicted for the times $t = 0.6$ (top), $t = 1.1$ (middle) and $t = 2.0$ (bottom), where beyond $t = 1.9$ the solution is not changing anymore. After injection the spray jets are first decelerated by the gas flow. At the same time they are deflected from the centre of the vortex and size segregation of droplets is observed. As the gas has a stronger influence on small droplets they tend to follow the vortex much faster. The diffusion-like widening in the

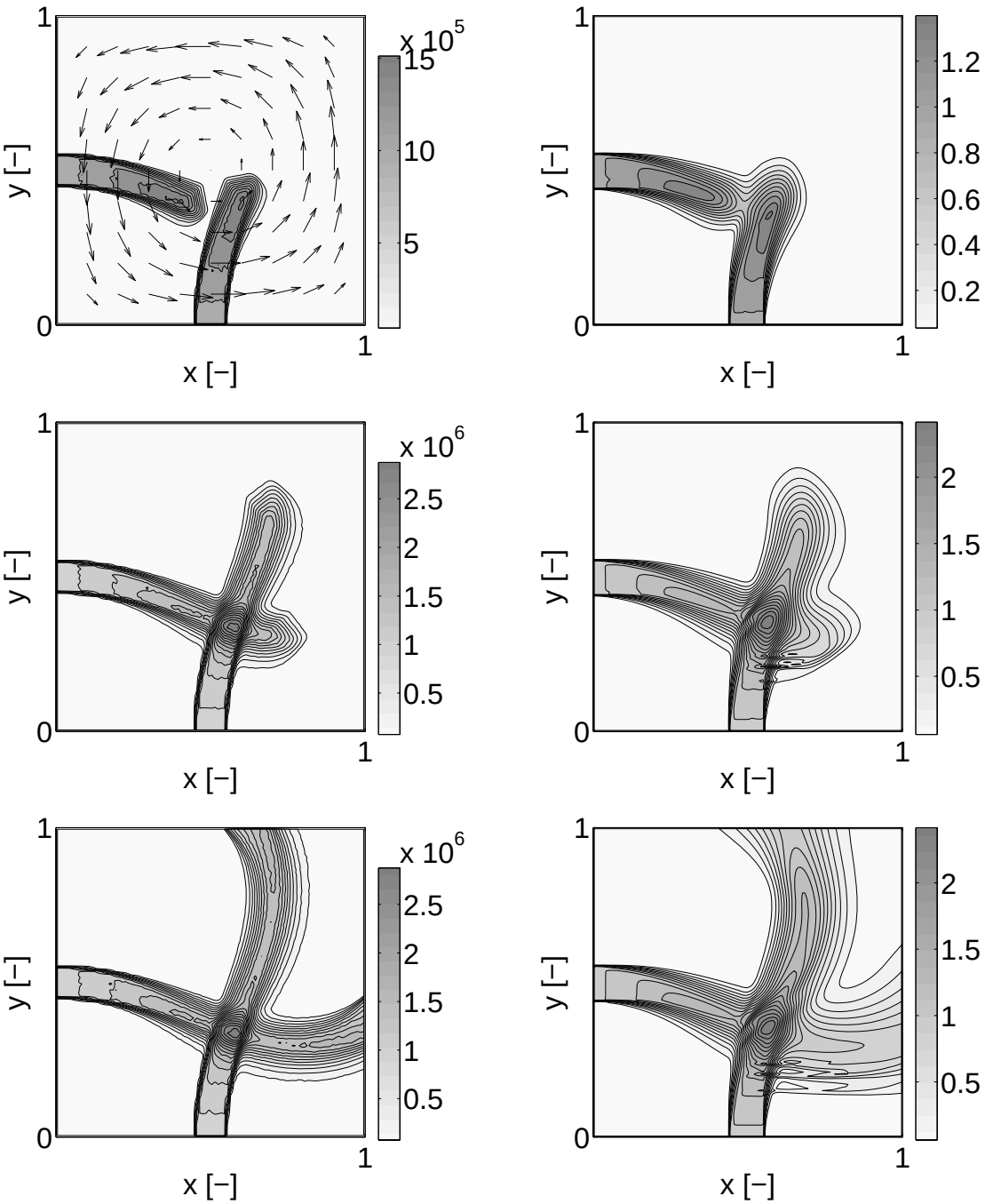

Figure 6.25: Number density of droplets ($M^{0,0,0}$) at $t = 0.6$ (top), $t = 1.1$ (middle) and $t = 2.0$ (bottom); polydisperse droplets accelerated in Taylor-Green vortex ($St_{max} = 2.0$); Lagrange method (left column); QBSM (right column), $N_x = 150$, $N_y = 150$, $N_s = 10$.

Lagrangian calculations (see Figures $6.25_{1,3,5}$) is exclusively due to the size segregation effect. The shape of the widening is determined by the initial distribution, which in this case is a truncated Gaussian distribution. In the crossing region the spray jet, coming from the left, has already separated into fibres with large droplets (upper part of the jet) and fibres with small droplets (lower part of the jet). In the results for the QBSM (see Figures $6.25_{2,4,6}$) it is observed that, despite the numerical diffusion, the size segregation of droplets and the deflection by the gas flow is well represented. However, in the fibres for the small droplets interactions between the two jets are observed in the crossing region.

These results demonstrate again that the crossing of droplets with relatively large Stokes numbers can be well predicted by QBSM, whereas droplets with small Stokes numbers lead to numerical difficulties. The investigation of this defect has to be postponed to future research.

6.6.2 Results for an Evaporating Polydisperse Spray

In Figure 6.26 the results for QBSM (right) and the Lagrange method (left) are presented for the case where evaporation is active (Ev = 0.4). It is observed that in contrast to the results in Figure 6.25, no droplet is leaving the computational domain through the boundaries but all of them evaporate within the domain. The steady state is reached after 1.7 time units. The comparison with the results in Section 6.6.1 demonstrates that the evaporating droplets tend to follow the gas flow much better than the non-evaporating droplets. This is obviously due to the reduction of the Stokes number which is proportional to the surface of a droplet (for the Stokes law). The behaviour of the spray jets before crossing is very similar to the non-evaporating test case.

The results of the QBSM in Figures $6.26_{2,4,6}$ reveal that the method can accurately describe evaporation effects. The unsteady behaviour of the spray jets, penetration distance into the domain and reduction of the Stokes number is well described. The only discrepancies, which were already observed in Section 6.6.1, are the numerical diffusion and the interaction of small droplets in the crossing region.

6.6.3 Discussion of Results

The test cases discussed in this section demonstrate that QBSM can deal with sprays suspended in inhomogeneous gas flows and still allow the simultaneous consideration of drag forces, evaporation and PTC. It is a first step in the extension to more applied configurations in which the gas flow is turbulent. The Taylor-Green configuration allows a rigorous assessment of the size segregation in polydisperse sprays, the unsteady behaviour of sprays, the evaporation-convection interaction and the crossing of sprays. QBSM is shown to reproduce qualitatively and quantitatively the behaviour of all these effects. The only drawbacks observed in these tests are the numerical diffusion and the interaction of small droplets in the crossing region. As mentioned above, the numerical diffusion can be reduced by using higher-order convection schemes or finer real space discretisations of the computational domain. There are various possible sources for the interaction of the small droplets. *First*, the assumption of constant weights in the semi-analytical solution of the drag force sub problem may lead to errors in the higher-order moments if the droplets have small Stokes numbers. *Second*, the mapping of moments into the frame of

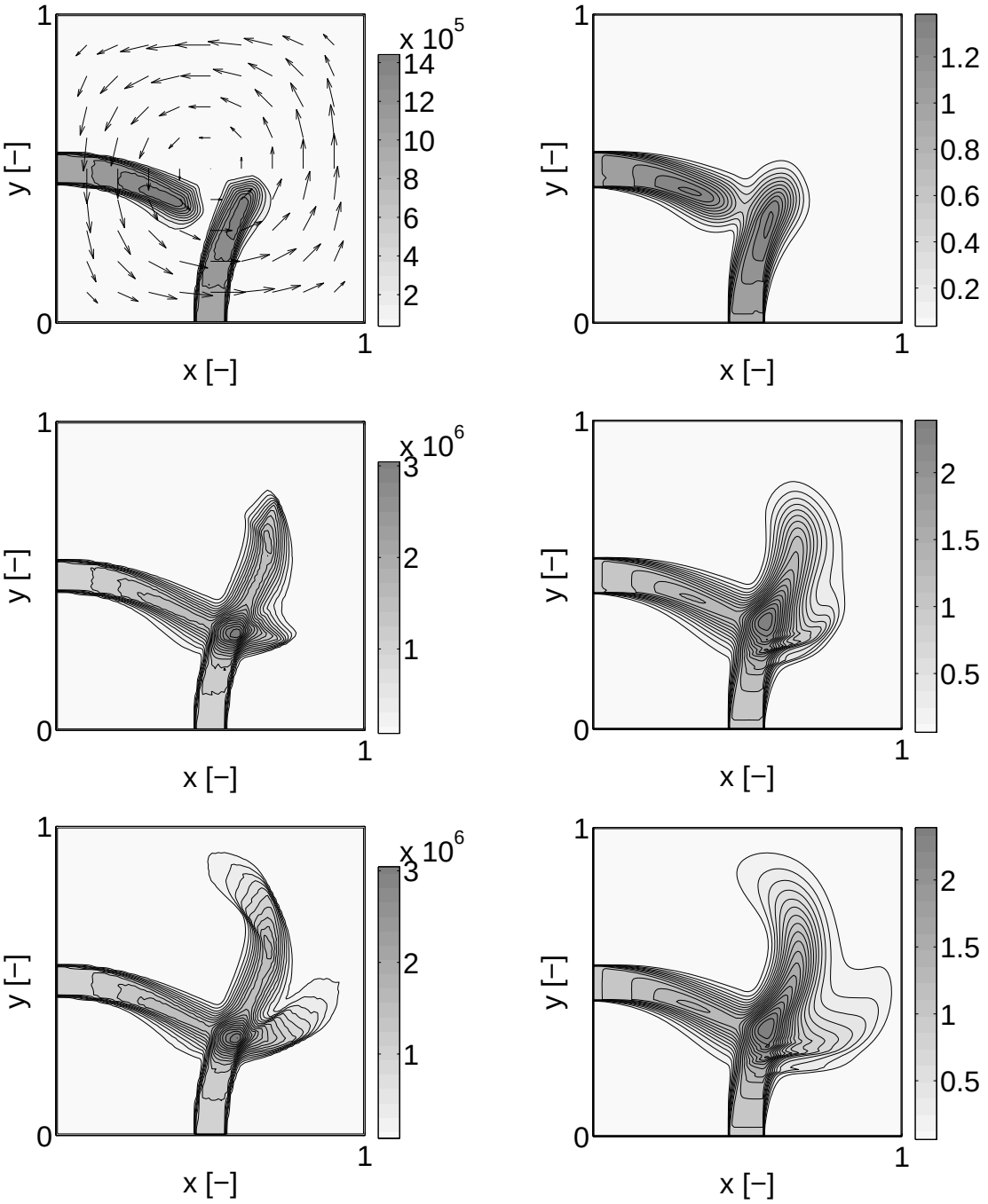

Figure 6.26: Number density of droplets ($M^{0,0,0}$) at $t = 0.6$ (top), $t = 1.1$ (middle) and $t = 2.0$ (bottom); polydisperse droplets accelerated in Taylor-Green vortex ($St_{max} = 2.0$) with evaporation ($Ev = 0.4$); Lagrange method (left column); QBSM (right column), $N_x = 150$, $N_y = 150$, $N_s = 10$.

X (see Section 4.4.2) may be poorly conditioned if the droplets are small or *third*, the number of exponential parameters b_k in the approximate NDF (see Section 4.3) may not be sufficient. The study of these issues has to be postponed to future research as changes to the algorithms would be considerable. In realistic turbulent spray flows the crossing of droplets with small Stokes numbers is less pronounced because their ability to follow the gas flow is good. As the gas flow does not undergo crossing, it is less likely that droplets of small Stokes numbers exhibit multi-modal velocity distributions. Therefore, the error that is introduced by QBSM for small droplets will not amplify in realistic spray flow configurations.

Chapter 7

Conclusions

In this work a new Euler method, called the quadrature-based sectional method (QBSM), was developed, implemented and tested. It allows the description of the main spray effects in the fuel injection of combustion systems. The focus was on the polydispersity of fuel droplet clouds and the particle trajectory crossing (PTC). They are crucial issues in the application of Euler methods to spray flows in combustion systems. The derivation of the mathematical model of the QBSM included the following issues:

(i) Choice of Eulerian approach:

The alternatives to the sectional method (SM) of Dufour and Villedieu [44] (the quadrature method of moments (QMoM) [109], the direct QMoM (DQMoM) [107] and the SM of Laurent et al. [97]) were theoretically assessed and found to be either not suitable or less accurate for describing of evaporating droplet clouds. QMoM and DQMoM encounter a singularity when surface abscissas reach zero values. This defect introduces considerable mathematical complications; its treatment is only feasible with strong assumptions on the evaporation model and the shape of the number density function (NDF) in size space [59]. The SM of Laurent et al. [97] is not built on the conservation of the number of droplets and therefore a larger numerical error is expected in the computation of the mass transfer between fuel droplets and gas [43]. All four methods allow the consideration of droplet breakup and coalescence and, in principle, they can be combined with the quadrature-based method of moments (QBMoM) of Fox [56] and Le Lostec et al. [99]. The SM of Dufour and Villedieu [44], which was used in this work, guarantees the non-negativity of the number and mass of droplets (realisability) and is second order accurate in surface space.

(ii) Closure of the moment equations derived from the kinetic spray equation:

The moment transform of the kinetic spray equation with respect to the velocity, surface and temperature variables yields an unclosed system of moment equations for each section in surface space. The unknown terms in these equations are closed by assuming the NDF, which is a joint size-velocity-temperature distribution function, to have a form that allows the consideration of evaporation, drag force, heating, breakup, collision, PTC and splashing on a wall. This approximate NDF goes together with the choice of moments that have to be transported. Here, moments are

chosen that are proportional to the mean number, mass, momentum and enthalpy of droplets in a section. For the consideration of PTC all velocity moments up to the third order are considered. The method that follows from these choices reduces to the SM of Dufour and Villedieu [44] and the QBMoM of Fox et al. [59] or Le Lostec et al. [99], respectively, if special sets of parameters are chosen. It is shown that this mathematical model does not restrict the use of standard physical models for drag, evaporation and splashing, as long as they are in accordance with the kinetic spray equation. In the new mathematical model the surface, mean number and mass of droplets are controlled which is crucial for describing evaporation processes in combustion systems.

(iii) The mapping from the transported moments to the parameters of the approximate NDF:

The uniqueness of the mapping between the transported moments and the parameters of the approximate NDF is shown and an explicit algorithm is proposed. It combines the specialised algorithms of the SM [44] and the QBMoM [59, 99].

The mathematical model results in highly coupled equations that include source terms for evaporation, droplet forces and heat transfer. Neither pressures nor deviatoric stresses arise. Therefore, standard numerical models cannot be used only numerical schemes that are based on the kinetic origin of the moment transport equations. The following methods and schemes were applied:

(i) The fractional step method to tackle the multi-physics character of the problem:

The system of moment transport equations includes processes of very different time scales. Heat transfer and drag force, for example, are generally much faster then evaporation processes. Therefore, the Strang splitting [165] is applied which allows the independent numerical treatment of different spray effects without reducing the accuracy of the numerical model.

(ii) The numerical treatment of sub problems for convection, evaporation, drag forces and heat transfer:

For convection, the kinetic approximation of Bouchut [18], which was developed for pressure-less gas equations, is extended to the chosen set of transported moments. It is not based on a gradient-diffusion model but considers the parameters of the approximate NDF which are known in terms of the transported moments. First- and second-order finite volume schemes are proposed. Similar to the convection, a conservative finite volume-like scheme for evaporation is proposed in surface space. The interaction terms between neighbouring sections and the mass transfer between droplets and gas follow naturally from this scheme. Limitations on the physical model or assumptions on the NDF do not have to be introduced. The sub problems for the droplet forces and heat transfer are captured by a semi-analytical solution and the stiff ODE-solver DLSODA [78], respectively.

(iii) The algorithm of QBSM:

A two-dimensional version of a QBSM-algorithm is proposed that can be extended to three real space dimensions. Its structure is dominated by the Strang splitting.

The alignment between transported moments and the parameters of the approximate NDF after every fractional step has a stabilising effect on the numerical method. Although not demonstrated in this work, it is argued that, besides the domain decomposition in real space [137], a domain decomposition in surface space is conceivable.

The implementation of the algorithms proposed in the mathematical and numerical model was performed. Due to the structural difference to existing open-source CFD codes, the algorithms were written into a new separate program. Sophisticated numerical methods for the root finding and solution of ODEs were taken from the mathematical libraries SLATEC [52] and ODEPACK [78]. The implemented modules which constitute the QBSM method are:

(i) the Strang splitting procedure [165],

(ii) the SM of Dufour and Villedieu [44],

(iii) the QBMoM of Fox [56],

(iv) the coupling of the SM [44] and the QBMoM [56, 99],

(v) the first- and second-order schemes for convection and evaporation,

(vi) the uniform temperature model of Abramzon and Sirignano [1] for evaporation and heat transfer,

(vii) the numerical treatment of droplet forces and heat transfer using a semi-analytical solution and the ODE-solver DLSODA [78], respectively.

The modules are embedded into a FORTRAN 95 framework. For pre- and post processing MATLAB and GNUPLOT were used. The QBMoM variant of Le Lostec et al. [99] and the Lagrange solvers were, for the most part, developed and implemented by Nechtan Le Lostec and Philippe Villedieu (ONERA/DMAE, Toulouse).

The verification and validation procedure included comparison with a semi-analytical solution, the experiment of Wong and Chang [182] and Lagrangian calculations. The test cases were organised such that the complexity increases. The following conclusions were drawn from these tests:

(i) Verification and Validation of the SM and the QBMoM:

By comparing the results of the implemented SM [44] to a semi-analytical solution of a one-dimensional, stationary evaporation-drag-gravity problem (see Appendix A) the method is shown as very accurate for numbers of sections above 10. It is further observed that the evolution of the total droplet mass, which is a principle quantity for the spray evaporation in combustion systems, can be reproduced by 5 sections committing only a small numerical error. Comparison of the computational results with the measurements of Wong and Chang [182] concludes that the SM works stably for realistic physical parameters and the uniform temperature model returns reasonable results.

The comparison of results from the QBMoM with those of the reference Lagrange method in a crossing configuration of two spray jets reveals a good quantitative agreement. In the unsteady Taylor-Green configuration, quad-modal velocity points are present which cannot be described with QBMoM. Nevertheless, the mass transfer between the vortex cells can be captured. The first-order Euler method, which in these tests is equivalent to the classical Euler method, is not able to predict the crossing of sprays because it assumes the velocity distribution to be mono-modal. For the Taylor-Green configuration, this flaw of the first-order Euler method results in a concentration of all droplets at the boundaries of the vortex cells. This behaviour is not correct because the spray in the Taylor-Green configuration is assumed to be collisionless.

(ii) Verification and Validation of QBSM in one real space dimension:

QBSM was tested in three one-dimensional test cases that included the effects of convection, evaporation, drag force, splashing and PTC. All these spray effects were captured by QBSM. For sufficiently large numbers of sections and cells the quantitative comparisons with the reference Lagrangian calculations are convincing for evaporation, splashing and PTC. For the effect of the drag force, large Stokes numbers are required to yield good results. For small Stokes numbers, the gradients in real and surface space are very steep and a fine discretisation in real and surface space is necessary to capture the drag effect also quantitatively.

(iii) Verification and Validation of QBSM in two real space dimensions:

QBSM was tested in three two-dimensional configurations where evaporation, drag force and splashing affect two crossing spray jets. The crossing of two spray jets that are affected by Stokes drag force can be reproduced qualitatively. The minor interactions in the crossing region are most likely due to numerical diffusion at the crossing points. In the case where evaporation is affecting the crossing sprays, the results from QBSM and the reference Lagrange method are in good agreement. In the splashing test case QBSM is shown to capture the fragmentation of droplets, loss of droplet mass on the wall, inelastic rebound of droplets and the frictional behaviour of droplets on the wall. The comparison with the Lagrange method demonstrates that higher-order convection schemes have to be used in QBSM to avoid the numerical diffusion in real space.

These tests demonstrate that the concepts derived in the mathematical and numerical models are indeed appropriate, i.e. the crossing of droplet trajectories and the polydisperse character of sprays can simultaneously be captured.

The application of QBSM to the unsteady motion of evaporating droplet clouds has been tested in a Taylor-Green vortex gas flow [168]. This configuration can be considered as a preliminary study to more advanced validation tests, for example, in homogenous turbulence and more technical turbulent spray configurations [160, 161]. The following critical issues of Euler methods in turbulent spray flows are studied in this Taylor-Green configuration:

(i) Size segregation of droplets due to drag forces and evaporation:

The most obvious characteristic of polydispersity in spray flows is the segregation of droplets according to their size which can be very pronounced in turbulent spray flows. This effect cannot be described with methods that assume all droplets to have the same mean velocity. QBSM, on the other hand, is shown to accurately reproduce the size segregation of droplets using only 10 sections.

(ii) Accumulation and thinning effects of the droplet density:

In unsteady turbulent spray flows accumulation and thinning of droplets due to drag forces and evaporation are dominant processes (see Figure 1.2). They have a strong influence on the formation of the fuel/oxidiser gas mixture. It is shown that QBSM can capture these effects in an inhomogeneous gas environment.

(iii) Particle trajectory crossing at local impingement planes:

It is shown that QBSM is able to predict the crossing of spray jets, while inhomogeneous drag forces and evaporation is acting on the droplets. The comparison with highly-resolved Lagrangian computations reveals a convincing agreement.

In all two-dimensional configurations a considerable numerical diffusion in real space is observed. It can be reduced by describing the convection with second-order finite volume schemes or by using a finer space discretisation.

Despite the minor numerical defects observed in this work, QBSM was clearly demonstrated to capture the polydisperse nature of sprays as well as the coexistence of two droplet velocities at one location and size. If extended to more complex configurations, this method can become a good alternative to existing CFD models in describing unsteady, polydisperse sprays.

Chapter 8

Future work

The work presented here is the starting point for the development of a more precise and robust Euler-Euler method that, some day, may compete with the Euler-Lagrange method. There are various tasks to be tackled before the QBSM is ready for the simulation of technical spray flows. The next steps in this development should be:

(i) implementation of the second-order convection scheme proposed in Section 5.3.3,

(ii) introduction of breakup and collision models to describe spray flows with smaller droplet Knudsen numbers (dense spray flows) near the nozzle,

(iii) extension to three dimensions in real space,

(iv) one- and two-way coupling with a gas solver,

(v) extension to tri- and quad-modal velocity distributions,

(vi) refinement of physical models.

With these extensions, the QBSM would be ready to describe dense spray systems in simple spray configurations with low gas Reynolds numbers. It would also be appropriate for turbulent flows in which a gas solver is used that resolves all length and time scales of the gas motion. To describe unsteady polydisperse sprays in a turbulent gas environment within complex configurations, the following adjustments need to be performed:

(vii) The program code must be rewritten to run on massively parallelised computers.

(viii) A turbulence model must be introduced for the dispersed phase.

(ix) The method must support unstructured grids.

Every one of these steps requires extensive verification and validation to make sure that no flaw is introduced and realistic flow configurations can be described. The Lagrange method, which has been refined for decades now, is most suitable for comparison purposes. It already includes all the above features and very accurate solutions are obtained when large numbers of parcels and highly resolved grids are used. The comparison of the QBSM with the Lagrange method also allows assessment of the computational performance. Validation of QBSM with the help of complex spray experiments [160, 161] is achievable when issues (i) to (ix) have been addressed and satisfying solutions have been found.

Appendix A

Semi-Analytical Solution to the Kinetic Spray Equation

The objective of this appendix is the derivation and semi-analytical solution to a reduced problem of the type (3.26). It is used in Chapter 6 to verify the moment method proposed in Chapters 4 and 5. The following treatment partly follows Dufour [43].

A.1 Reduced Kinetic Spray Equation

The model (3.26) does not allow any analytical treatment, unless the physical models are specified and the number of variables is truncated in such a way that an analytical solution is accessible. In the first step, the number of variables of f is reduced by considering a one-dimensional, stationary and isothermal spray configuration, i.e. t and θ are dropped from the argument list of f and the position and velocity vectors turn into the scalar variables x and v, respectively. It is then assumed that the discontinuous interactions between the droplets are not significant, the Stokes drag force model is justified and the droplets evaporate according to the law that allows Ev to be a constant. The introduction of these assumptions into equation (3.26) yields

$$\frac{\partial}{\partial x}(v f(x;v,s)) + \frac{\partial}{\partial v}\left[\left(\frac{U_g - v}{\mathrm{St}(s)} + \frac{1}{\mathrm{Fr}}\right) f(x;v,s)\right] - \mathrm{Ev}\frac{\partial}{\partial s}(f(x;v,s)) = 0 \ . \tag{A.1}$$

The Stokes number $\mathrm{St}(s)$ is written as (see equation (2.18))

$$\mathrm{St}(s) = s\,\mathrm{St}_{\mathrm{char}} \quad \text{with} \quad \mathrm{St}_{\mathrm{char}} := \mathrm{St}(S_{\mathrm{char}}) = \frac{1}{\tau_s}\frac{\rho_\ell S_{\mathrm{char}}}{18\pi\eta_g} \ , \tag{A.2}$$

to lay open the linear dependency of $\mathrm{St}(s)$ on the surface variable s. It is not expected that the crude evaporation model used here is appropriate for values of s close to zero. Therefore, the region $s < \varepsilon_s$, with $0 < \varepsilon_s \ll 1$ is removed from the domain of definition. This procedure also prevents any singular behaviour of the final boundary value problem (BVP) (see (A.3)-(A.5)) at $s = 0$. With these considerations, (A.1) reduces to

$$\begin{aligned} &\frac{\partial}{\partial x}(v f(x;v,s)) + \frac{\partial}{\partial v}\left[\left(\frac{U_g - v}{s\,\mathrm{St}_{\mathrm{char}}} + \frac{1}{\mathrm{Fr}}\right) f(x;v,s)\right] - \mathrm{Ev}\frac{\partial}{\partial s}(f(x;v,s)) = 0 \ , \\ &\qquad \text{in} \quad x \in (0,\,1], \quad v \in \mathbb{R} \quad \text{and} \quad s \in [\varepsilon_s,\,+\infty) \ , \end{aligned} \tag{A.3}$$

supplemented by the boundary conditions

$$f(0; v, s) = f_0(v, s) \qquad \text{in} \quad v \in \mathbb{R} \quad \text{and} \quad s \in [\varepsilon_s, +\infty) \ . \tag{A.4}$$

$$\left.\frac{\partial f(x; v, s)}{\partial s}\right|_{s=0} = \varepsilon_s \qquad \text{in} \quad x \in (0, 1] \quad \text{and} \quad v \in \mathbb{R} \tag{A.5}$$

A.2 The Method of Characteristics

In order to apply the method of characteristics [81] to the BVP (A.3)-(A.5), it is written in the quasilinear form[1]

$$sv\frac{\partial f}{\partial x} + \left(\frac{U_g - v}{\mathrm{St_{char}}} + \frac{s}{\mathrm{Fr}}\right)\frac{\partial f}{\partial v} - s\mathrm{Ev}\frac{\partial f}{\partial s} = \frac{1}{\mathrm{St_{char}}} f \ , \tag{A.6}$$

where equation (A.6) has been multiplied by s. It is observed that all functions in front of the derivatives of f are of class C^1 which justifies the application of the characteristic method and guarantees that the solution $f(x, v, s)$ is unique.

The method of characteristics commences with the parameterisation of x, s, v and f in terms of a scalar quantity t, which allows formulation of the coupled system of differential equations

$$\begin{aligned}
\frac{\mathrm{d}x}{\mathrm{d}t} &= v(t)s(t) \ , & x(t=0) &= x_0 = 0 \ , \\
\frac{\mathrm{d}v}{\mathrm{d}t} &= \frac{U_g - v(t)}{\mathrm{St_{char}}} + \frac{s(t)}{\mathrm{Fr}} \ , & v(t=0) &= v_0 \ , \\
\frac{\mathrm{d}s}{\mathrm{d}t} &= -s(t)\mathrm{Ev} \ , & s(t=0) &= s_0 \ , \\
\frac{\mathrm{d}f}{\mathrm{d}t} &= \frac{1}{\mathrm{St_{char}}} f(t) \ , & f(t=0) &= f_0(v_0, s_0) \ .
\end{aligned} \tag{A.7}$$

This system defines the characteristic curve $t \mapsto (x(t), v(t), s(t), f(t)) = \chi(t) \subset \mathbb{R}^4$ that includes the point $(x_0, v_0, s_0, f_0(v_0, s_0))$. To solve equation system (A.7), equation $(\mathrm{A.7})_2$ is divided by $(\mathrm{A.7})_3$ and equations $(\mathrm{A.7})_3$ and $(\mathrm{A.7})_2$ by $(\mathrm{A.7})_1$. This gives the relations

$$\begin{aligned}
\frac{\mathrm{d}v}{\mathrm{d}s} &= -\beta\,\frac{U_g - v(s)}{s} - \frac{1}{\mathrm{Fr\,Ev}} \ , \\
\frac{\mathrm{d}s}{\mathrm{d}x} &= -\frac{\mathrm{Ev}}{v} \ , \\
\frac{\mathrm{d}v}{\mathrm{d}x} &= \frac{U_g - v(x)}{s(x)v(x)\mathrm{St_{char}}} + \frac{1}{v(x)\mathrm{Fr}} \ ,
\end{aligned} \tag{A.8}$$

which are solved together with the 'initial conditions' $v(s = s_0) = v_0$ and $s(x = 0) = s_0$. The fixed parameter β is defined as

$$\beta := \frac{1}{\mathrm{Ev\,St_{char}}} = \frac{\tau_{ev}}{\tau_d} \ . \tag{A.9}$$

[1] The boundary conditions and the domain of defintion is suppressed for simplicity.

The first order ODE $(A.8)_1$ can easily be solved using standard solution methods (homogeneous plus particular solution). The velocity v, as a function of the variable s, reads

$$v(s, v_0, s_0) = U_g - (U_g - v_0)\left(\frac{s}{s_0}\right)^{\beta} + \frac{s}{\mathrm{Ev\,Fr}}\,\frac{1-\left(\frac{s}{s_0}\right)^{\beta}}{(\beta-1)} \qquad \text{for} \quad \beta \in (0,\,+\infty)\setminus\{1\} \tag{A.10}$$

and

$$v(s, v_0, s_0) = U_g - (U_g - v_0)\frac{s}{s_0} - \frac{s}{\mathrm{Ev\,Fr}}\,\ln\left(\frac{s}{s_0}\right) \qquad \text{for} \quad \beta = \frac{\tau_{ev}}{\tau_d} = 1\,. \tag{A.11}$$

In the remainder of Appendix A the much simpler but very special case of $\beta = 1$ is set aside. With result (A.10), the solution of ODE $(A.8)_2$ is obtained by a separation of variables. Using the definitions

$$d_1 = v_0 - U_g - \frac{s_0}{\mathrm{Ev\,Fr}(\beta-1)} \quad \text{and} \quad d_2 = \frac{1}{\mathrm{Ev\,Fr}(\beta-1)}\,, \tag{A.12}$$

the variable s follows from the solution of the algebraic equation

$$s^{(\beta+1)} + \frac{d_2}{2}\frac{s_0^{\beta}(\beta+1)}{d_1}\,s^2 + U_g\frac{s_0^{\beta}(\beta+1)}{d_1}\,s - \frac{s_0^{\beta}(\beta+1)}{d_1}\left(U_g s_0 + \frac{d_1}{s_0^{\beta}(\beta+1)}s_0^{(\beta+1)} + \frac{d_2}{2}s_0^2\right) = -\mathrm{Ev}\frac{s_0^{\beta}(\beta+1)}{d_1}x\,. \tag{A.13}$$

Choosing β to be some special integer number, an analytical solution to (A.13) can be derived 'by hand' or by using computer algebra systems. As β can take any value within $(0,\,+\infty)\setminus\{1\}$ the solution of (A.13) has to be approximated using, for example, the root finding algorithm `fzero` of MATLAB.

The differential equation $(A.7)_4$ remains to be solved. In terms of the parameter t, it is an easy task to find the solution

$$\breve{f}(t) = f_0 \exp\left(\frac{t}{\mathrm{St_{char}}}\right) \tag{A.14}$$

but here the objective is to find the NDF as a function of x, v and s. Having this in mind, the solution of $(A.7)_3$,

$$t(s, s_0) = -\frac{1}{\mathrm{Ev}}\ln\left(\frac{s}{s_0}\right) \tag{A.15}$$

is substituted into (A.14) to obtain

$$\breve{f}(s, v_0, s_0) = f_0(v_0, s_0)\left(\frac{s}{s_0}\right)^{-\beta}. \tag{A.16}$$

One may think that (A.16) is the solution of BVP (A.3)-(A.5) but, as x and v do not appear explicitly in (A.16), it can only be an intermediate result. The situation is even worse because the relations between s and x, and s and v are highly complex. Therefore, an explicit expression for $f(x; v, s)$ is not achievable.

A.3 Semi-Analytical Solution to the Moments of the NDF

As mentioned above, the purpose of this semi-analytical derivation is the comparison with the numerical calculations in Chapter 6. There, the moment method does not solve for the NDF explicitly, but for moments of the type

$$n^{KM}(x, v_1, v_2, s_1, s_2) := \int_{s_1}^{s_2} \int_{v_1}^{v_2} s^K v^M f(x; v, s) dv ds \ . \tag{A.17}$$

Therefore, it is sufficient to find the solutions for certain moments of the reduced NDF. As will be demonstrated in the following, a semi-analytical form of $n^{KM}(x, s_1, s_2, v_1, v_2)$ can indeed be found. To this end, the variables in the integral of (A.17) are changed according to

$$s = \mathrm{F}_{x1}(v_0, s_0) \quad \text{and} \quad v = \mathrm{F}_{x2}(v_0, s_0), \quad \text{with} \quad x_0 = 0 \ , \tag{A.18}$$

and the new domain of integration in (A.17) is

$$\mathcal{D} = \mathrm{F}_x^{-1} \left([s_1, s_2] \times [v_1, v_2] \right) = \left([s_{01}, s_{02}] \times [v_{01}, v_{02}] \right) \ . \tag{A.19}$$

With these modifications, the integral in (A.17) turns into

$$n^{KM}(x, s_1, s_2, v_1, v_2) = \int_{\mathcal{D}} \mathrm{F}_{x1}^K(s_0, v_0) \mathrm{F}_{x2}^M(s_0, v_0) f_0(s_0, v_0) \mathrm{J}(x, s_0, v_0) ds_0 dv_0 \ , \tag{A.20}$$

where J is the Jacobian of the mapping $\mathbf{F}_x = \{\mathrm{F}_{x1}, \mathrm{F}_{x2}\}$. It can be evaluated via the relation

$$\frac{\mathrm{dJ}(x, s_0, v_0)}{\mathrm{d}x} = \mathrm{J}(x, s_0, v_0) \nabla_{s,v} \cdot \left(\frac{\mathrm{dF}_{x1}}{\mathrm{d}x}, \ \frac{\mathrm{dF}_{x2}}{\mathrm{d}x} \right)^{\mathrm{T}} \ . \tag{A.21}$$

This equation is a specialisation of a general result from tensor algebra (cf. Chadwick [25]). By using $(\mathrm{A.8})_{2,3}$ and applying the chain rule of differentiation, equation (A.21) can be written as

$$\begin{aligned} &\frac{\mathrm{dJ}(x, s_0, v_0)}{\mathrm{d}x} = -\mathrm{J}(x, s_0, v_0) \left(\frac{U_g}{s \, v^2 \, \mathrm{St_{char}}} + \frac{1}{v^2 \, \mathrm{Fr}} \right) \ , \\ &\text{with} \quad \mathrm{J}(x, s_0, v_0)\big|_{x=0} = 1 \ . \end{aligned} \tag{A.22}$$

The following expression for $\mathrm{J}(x, s_0, v_0)$ is then obtained from ODE (A.22) via separation of variables;

$$\mathrm{J}(x, s_0, v_0) = \exp\left[-\int_0^x \left(\frac{U_g}{s(x', s_0, v_0)\, v^2(x', s_0, v_0)\, \mathrm{St}_{\mathrm{char}}} + \frac{1}{v^2(x', s_0, v_0)\, \mathrm{Fr}}\right) dx'\right] . \tag{A.23}$$

The integral on the right-hand side of (A.23) remains to be evaluated. Relations $(\mathrm{A.8})_2$ and (A.10) allow the transformation of variables from x' to u via the identification $u = s$. The final expression of $\mathrm{J}(x, s_0, v_0)$ is then obtained through the evaluation of the integral in

$$\mathrm{J}(x, s_0, v_0) = \exp\left[-\int_{s(x,s_0,v_0)}^{s_0} \left(\frac{\beta U_g}{u} + \frac{1}{\mathrm{Ev}\,\mathrm{Fr}}\right) \frac{1}{v(u, s_0, v_0)} du\right] , \tag{A.24}$$

where $v(u, s_0, v_0)$ is the velocity given in (A.10). Knowing $s(x, s_0, v_0)$, $\mathrm{J}(x, s_0, v_0)$, the mapping $\mathbf{F}_x$ (see (A.10) and (A.13)) and specifying the boundary condition $f_0(s_0, v_0)$, $n^{KM}(x, s_1, s_2, v_1, v_2)$ can be evaluated using (A.20).

An algorithm thus allows the determination of $n^{KM}(x, s_1, s_2, v_1, v_2)$:

(i) The boundary condition $f_0(s_0, v_0)$ and with it the domain of definition for s_0 and v_0 is specified.

(ii) The variables $s(x, v_0, s_0)$ and $v(s, v_0, s_0)$ are determined for all possible values of x, s_0 and x_0 by solving relation (A.13) and using equation (A.10). When applying a numerical root finder, $s(x, s_0, v_0)$ is known at discrete points only. With computer algebra systems an analytical expression can be derived for $s(x, s_0, v_0)$.

(iii) Using the result from item (ii), the Jacobian $\mathrm{J}(x, s_0, v_0)$ is evaluated from relation (A.24).

(iv) The Jacobian, J, together with the boundary condition, f_0, allow the determination of $n^{KM}(x, s_1, s_2, v_1, v_2)$. As $s(x, s_0, v_0)$ and $\mathrm{J}(x, s_0, v_0)$ are known at discrete points only, quadrature rules have to be applied to approximate the integral in (A.17).

The results of this semi-analytical algorithm are depicted in Figures 6.2 and 6.3 (Section 6.2).

Appendix B

Uniqueness of the Sectional Method

The proof of Proposition 1 (Section 4.4) is outlined here, as it is a mathematical necessity to demonstrate the plausibility of the proposition and, because it also helps to understand the numerical algorithm that is used to compute b_k from the ratio $\mathrm{M}_k^{3/2,0,0}/\mathrm{M}_k^{0,0,0}$ ($k = 1, \ldots, N_s$). The proof is mainly following that of Dufour [43].

Proof of Proposition 1. The positive character of the strictly increasing function $s^{3/2} f(\mathbf{x}, t; \mathbf{v}, \theta, s)$ in the domain $[s_k, s_{k+1}]$ justifies the relation

$$\frac{(s_k)^{3/2} f}{\mathrm{M}_k^{0,0,0}} < \frac{(s)^{3/2} f}{\mathrm{M}_k^{0,0,0}} < \frac{(s_{k+1})^{3/2} f}{\mathrm{M}_k^{0,0,0}}, \quad \text{with} \quad s_k < s < s_{k+1} \tag{B.1}$$

which by integration of each term over $[s_k, s_{k+1})$ yields

$$(s_k)^{3/2} < \frac{\mathrm{M}_k^{3/2,0,0}}{\mathrm{M}_k^{0,0,0}} < (s_{k+1})^{3/2} \ . \tag{B.2}$$

This property of the moment ratio is true for every positive function $f(\mathbf{x}, t; \mathbf{v}, \theta, s)$ and therefore g_{I_k} (defined in (4.24)) must necessarily satisfy this relation. In Lemma 3 it is shown that this is indeed the case and g_{I_k}, which exclusively depends on $b_k \in \mathbb{R}$, is a bijective function from $\mathbb{R}$ to $[(s_k)^{3/2}, (s_{k+1})^{3/2}]$. These properties allow the inversion of g_{I_k} and so the parameter b_k is the unique solution of the algebraic equation

$$g_{I_k}(b_k) = \frac{\mathrm{M}_k^{3/2,0,0}}{\mathrm{M}_k^{0,0,0}} \ . \tag{B.3}$$

This solution ensures that $\mathrm{M}_k^{3/2,0,0}/\mathrm{M}_k^{0,0,0} = \tilde{\mathrm{M}}_k^{3/2,0,0}/\tilde{\mathrm{M}}_k^{0,0,0}$. For the infinite section I_{N_s+1} the same conclusions can be drawn, as s_{N_s+2} is equal to $+\infty$. □

Lemma 3. *Let I_k be a finite interval in $\mathbb{R}_+$, then the function $g_{I_k}(b_k)$ defined in (4.24) is strictly decreasing in $\mathbb{R}$ and exhibits the limits*

$$\lim_{b_k \to -\infty} g_{I_k}(b_k) = (s_{k+1})^{3/2} \quad \textit{and} \quad \lim_{b_k \to +\infty} g_{I_k}(b_k) = (s_k)^{3/2} \ . \tag{B.4}$$

In the infinite section, $g_{I_k}(b_k)$ is strictly decreasing on $\mathbb{R}_+$ as well, with the limit

$$\lim_{b_k \to 0^+} g_{I_k}(b_k) = (s_{N_s+1})^{3/2} \ . \tag{B.5}$$

Proof. The function $g_I(b)$, defined in (4.24), can be transformed into

$$g_I(b) = \frac{1}{1-e^{-b\Delta s}} \left(s_k^{3/2} - s_{k+1}^{3/2} e^{-b\Delta s} + \frac{3}{2b}(\sqrt{s_k} - \sqrt{s_{k+1}} e^{-b\Delta s}) \right.$$
$$\left. + \frac{3e^{-bs_k}}{2b} \int_{\sqrt{s_k}}^{\sqrt{s_{k+1}}} e^{-br^2} dr \right) , \quad \text{(B.6)}$$

where $b \neq 0$ and $\Delta s = s_{k+1} - s_k$. The limits for $b \to \pm\infty$ are obtained easily from relation (B.6).

That $g_I(b)$ is an injective and invertible function remains to be proven. The derivative of $g_I(b)$ with respect to b reads

$$g_I{}'(b) = \frac{-\int_{s_k}^{s_{k+1}} e^{-bs} ds \int_{s_k}^{s_{k+1}} s^{5/2} e^{-bs} ds + \int_{s_k}^{s_{k+1}} s^{3/2} e^{-bs} ds \int_{s_k}^{s_{k+1}} s e^{-bs} ds}{\left(\int_{s_k}^{s_{k+1}} e^{-bs} ds \right)^2} . \quad \text{(B.7)}$$

To determine the sign of $g_I{}'(b)$ the value of b is fixed and the numerator of (B.7) is written as

$$h_I(\beta) = -\int_{s_k}^{\beta} e^{-bs} ds \int_{s_k}^{\beta} s^{5/2} e^{-bs} ds + \int_{s_k}^{\beta} s^{3/2} e^{-bs} ds \int_{s_k}^{\beta} s e^{-bs} ds . \quad \text{(B.8)}$$

Differentiating this function for β yields

$$h_I{}'(\beta) = e^{-b\beta} \int_{s_k}^{\beta} \left(-s^{5/2} - \beta^{5/2} + \beta^{3/2} s + \beta s^{3/2} \right) e^{-bs} ds , \quad \text{(B.9)}$$

which reduces to

$$h_I{}'(\beta) = e^{-b\beta} \int_{s_k}^{\beta} \left(\beta^{3/2} - s^{3/2} \right) (s - \beta) e^{-bs} ds . \quad \text{(B.10)}$$

Notice that $h_I{}'(\beta) < 0$ if $\beta > s_k$ and $h_I(s_k) = 0$. So, $h_I(\beta)$ is a strictly negative function of β which allows the conclusion that $g_I{}'(b) < 0$, irrespective of the sign and value of b. Therefore, the function $g_I(b)$ is strictly decreasing on $\mathbb{R}$ and therefore it is injective and invertible. □

Appendix C

Mapping from Moments to Weights and Abscissas

The proof of Proposition 2 (Section 4.4) is necessary because it is the heart of QBSM. Even for higher real space dimensions the one-dimensional mapping from the moments in one real space direction to the respective weights and abscissas is of relevance. The considerations in this appendix are based on the explanations of Desjardins et al. [39].

Proof of Proposition 2. In one real space dimension the relations between moments in set $\bar{\mathcal{V}}_1^\dagger$ (4.38) and quadrature parameters in set $\mathcal{W}_2^\dagger$ (4.37) are

$$\begin{aligned} \bar{\mathrm{M}}_k^{3/2,0,0} &= n_k^1 + n_k^2, & \bar{\mathrm{M}}_k^{3/2,0,1} &= n_k^1 U_k^1 + n_k^2 U_k^2, \\ \bar{\mathrm{M}}_k^{3/2,0,2} &= n_k^1 (U_k^1)^2 + n_k^2 (U_k^2)^2, & \bar{\mathrm{M}}_k^{3/2,0,3} &= n_k^1 (U_k^1)^3 + n_k^2 (U_k^2)^3 \ . \end{aligned} \tag{C.1}$$

Together with the conditions (i) and (ii) in (4.41), which ensure that σ_k^p is real and non-negative, it can be checked that relations (C.1) are equivalent to

$$\begin{aligned} & n_k^1 = (\tfrac{1}{2} + x_k)\bar{\mathrm{M}}_k^{3/2,0,0}, \qquad n_k^2 = (\tfrac{1}{2} - x_k)\bar{\mathrm{M}}_k^{3/2,0,0}, \\ & (\tfrac{1}{2} + x_k)\delta U_k^1 + (\tfrac{1}{2} - x_k)\delta U_k^2 = 0, \\ & (\tfrac{1}{2} + x_k)(\delta U_k^1)^2 + (\tfrac{1}{2} - x_k)(\delta U_k^2)^2 = (\sigma_k^p)^2, \\ & (\tfrac{1}{2} + x_k)(\delta U_k^1)^3 + (\tfrac{1}{2} - x_k)(\delta U_k^2)^3 = q_k^p \ , \end{aligned} \tag{C.2}$$

where $\delta U_k^\alpha = U_k^\alpha - U_k^p$ is the deviation from the mean U_k^p and x_k still has to be determined. Solving equations $(\mathrm{C.2})_{3,4}$ for δU_k^1 and δU_k^2 yields

$$\delta U_k^1 = -\varepsilon \left(\frac{\frac{1}{2} - x_k}{\frac{1}{2} + x_k} \right)^{1/2} \sigma_k^p \ , \quad \delta U_k^2 = \varepsilon \left(\frac{\frac{1}{2} + x_k}{\frac{1}{2} - x_k} \right)^{1/2} \sigma_k^p \ , \tag{C.3}$$

with $\varepsilon = \pm 1$. Substitution of relations (C.3) into $(\mathrm{C.2})_5$ allows the specification of x_k. With (C.3), equation $(\mathrm{C.2})_5$ turns into

$$-(\tfrac{1}{2} - x_k)^2 (\varepsilon \sigma_k^p)^3 + (\tfrac{1}{2} + x_k)^2 (\varepsilon \sigma_k^p)^3 = \left(\tfrac{1}{4} - x_k^2\right)^{1/2} q_k^p \ , \tag{C.4}$$

which can easily be reduced to

$$2(\varepsilon\sigma_k^p)^3 x_k = \left(\tfrac{1}{4} - x_k^2\right)^{1/2} q_k^p \ . \tag{C.5}$$

This relation is equivalent to

$$\left(4(\varepsilon\sigma_k^p)^6 + (q_k^p)^2\right) x_k^2 = \tfrac{1}{4}(q_k^p)^2 \ , \tag{C.6}$$

which finally yields

$$x_k = \mathrm{sign}(\varepsilon)\frac{q_k^p}{2\left(4(\varepsilon\sigma_k^p)^6 + (q_k^p)^2\right)^{1/2}} \ . \tag{C.7}$$

Condition (ii) in Proposition 2 ensures that x_k is well defined and lies in $(-\frac{1}{2}, +\frac{1}{2})$ for all q_k^p. The two choices of ε yield two solutions, which are the same up to a permutation of (n_k^1, U_k^1) and (n_k^2, U_k^2). This can be checked with relations $(C.2)_{1,2,5}$ and (C.3). □

Appendix D

Linear Transformation and Translation of Moments

The mapping (cf. (4.48))

$$\boldsymbol{\phi}^* = \mathbf{L}\,(\boldsymbol{\phi} - \boldsymbol{\mu}) \tag{D.1}$$

of the vector $\boldsymbol{\phi} = (\phi_1, \phi_2)^{\mathrm{T}}$ into the vector $\boldsymbol{\phi}^* = (\phi_1^*, \phi_2^*)^{\mathrm{T}}$ can be split into a translation

$$\boldsymbol{\phi}^+ = \boldsymbol{\phi} - \boldsymbol{\mu} \tag{D.2}$$

followed by a linear transformation

$$\boldsymbol{\phi}^* = \mathbf{L}\boldsymbol{\phi}^+. \tag{D.3}$$

Let $m^*(\mathbf{k})$, $m^+(\mathbf{k})$ and $m(\mathbf{k})$ denote the moments of $\boldsymbol{\phi}^*$, $\boldsymbol{\phi}^+$ and $\boldsymbol{\phi}$, respectively, which are defined as

$$m(\mathbf{k}) := \int_{R^2} {\phi_1}^{k_1} {\phi_2}^{k_2} f(\boldsymbol{\phi}) d\boldsymbol{\phi}, \quad \text{with} \quad \mathbf{k} = (k_1, k_2)\ . \tag{D.4}$$

Then, the moment of the translated variable $\boldsymbol{\phi}^+$ can be written as

$$\begin{aligned} m^+(\mathbf{k}^+) &= \int_{R^2} (\phi_1^+)^{k_1^+} (\phi_2^+)^{k_2^+} f^+(\boldsymbol{\phi}^+) d\boldsymbol{\phi}^+ = \int_{R^2} (\phi_1 - \mu_1)^{k_1^+} (\phi_2 - \mu_2)^{k_2^+} f(\boldsymbol{\phi}) d\boldsymbol{\phi} \\ &= \sum_{t_1=0}^{k_1^+} \sum_{t_2=0}^{k_2^+} \binom{k_1^+}{t_1} \binom{k_2^+}{t_2} (-\mu_1)^{k_1^+ - t_1} (-\mu_2)^{k_2^+ - t_2} \int_{R^2} {\phi_1}^{t_1} {\phi_2}^{t_2} f(\boldsymbol{\phi}) d\boldsymbol{\phi} \\ &= \sum_{t_1=0}^{k_1^+} \sum_{t_2=0}^{k_2^+} \binom{k_1^+}{t_1} \binom{k_2^+}{t_2} (-\mu_1)^{k_1^+ - t_1} (-\mu_2)^{k_2^+ - t_2}\, m(t_1, t_2)\ . \end{aligned} \tag{D.5}$$

In line two of (D.5) the multinomial expansion [23]

$$(\phi - \mu)^k = \sum_{t=0}^{k} \binom{k}{t} (-\mu)^{k-t} \phi^t\ , \tag{D.6}$$

has been used, where

$$\binom{a}{b} = \binom{a}{a-b} := \frac{a!}{b!(a-b)!} \tag{D.7}$$

is the binomial coefficient.

The linear transformation from the variable $\boldsymbol{\phi}^+$ to the variable $\boldsymbol{\phi}^*$, using the tensor

$$\mathbf{L} = \begin{bmatrix} L_{11} & L_{12} \\ L_{21} & L_{22} \end{bmatrix} , \tag{D.8}$$

leads to a transformation of the respective moments as well, i.e.

$$\begin{aligned} m^*(\mathbf{k}^*) &= \int_{R^2} (\phi_1^*)^{k_1^*} (\phi_2^*)^{k_2^*} f^*(\boldsymbol{\phi}^*) d\boldsymbol{\phi}^* \\ &= \int_{R^2} (L_{11}\phi_1^+ + L_{12}\phi_2^+)^{k_1^*} (L_{21}\phi_1^+ + L_{22}\phi_2^+)^{k_2^*} f^+(\boldsymbol{\phi}^+) d\boldsymbol{\phi}^+ \ . \end{aligned} \tag{D.9}$$

If, again, the multinomial expansion (D.6) is used, the moment $m^*(\mathbf{k}^*)$ can be written as

$$\begin{aligned} m^*(\mathbf{k}^*) = \sum_{j_1=0}^{k_1^*} \sum_{j_2=0}^{k_2^*} \binom{k_1^*}{j_1} \binom{k_2^*}{j_2} {L_{11}}^{k_1^*-j_1} {L_{12}}^{j_1} {L_{21}}^{k_2^*-j_2} {L_{22}}^{j_2} \\ \int_{R^2} (\phi_1^+)^{k_1^*+k_2^*-j_1-j_2} (\phi_2^+)^{j_1+j_2} f^+(\boldsymbol{\phi}^+) d\boldsymbol{\phi}^+ \ . \end{aligned} \tag{D.10}$$

Introducing the Kronecker delta

$$\delta_{k,j} = \begin{cases} 1 & \text{if } k = j \ , \\ 0 & \text{else} \end{cases} \tag{D.11}$$

equation (D.10) turns into

$$\begin{aligned} m^*(k_1^*, k_2^*) = \sum_{j_1=0}^{k_1^*} \sum_{j_2=0}^{k_2^*} \binom{k_1^*}{j_1} \binom{k_2^*}{j_2} {L_{11}}^{k_1^*-j_1} {L_{12}}^{j_1} {L_{21}}^{k_2^*-j_2} {L_{22}}^{j_2} \\ \delta_{k_1^+, k_1^*+k_2^*-j_1-j_2} \, \delta_{k_2^+, j_1+j_2} \, m^+(k_1^+, k_2^+) \ . \end{aligned} \tag{D.12}$$

Letting $\mathbf{m}^*$ and $\mathbf{m}$ denote the column vectors

$$\mathbf{m}^* = \begin{bmatrix} m^*(0,0) \\ m^*(1,0) \\ m^*(0,1) \\ m^*(1,1) \\ \vdots \end{bmatrix} \quad \mathbf{m} = \begin{bmatrix} m(0,0) \\ m(1,0) \\ m(0,1) \\ m(1,1) \\ \vdots \end{bmatrix} \tag{D.13}$$

of length L, then the transformations in (D.5) and (D.12) subsumed in the tensors $\mathbf{M}_1$ and $\mathbf{M}_2$, respectively, can be written as

$$\mathbf{m}^* = \mathbf{M}_2(\mathbf{M}_1\mathbf{m}) \ . \tag{D.14}$$

It is observed that the tensors in (D.14) have the following properties

(i) $\mathbf{M}_1$ and $\mathbf{M}_2$ are of size $L \times L$.

(ii) $\mathbf{M}_1$ is a lower triangle tensor, i.e. the expression for a moment of $\boldsymbol{\phi}^*$ of order γ includes only one moment of $\boldsymbol{\phi}$ of the same order and other, lower order moments.

(iii) $\mathbf{M}_2$ is block diagonal where each square block relates the moments of the same order. The size of a block equals the number of moments of order γ.

(iv) The square sub-blocks of $\mathbf{M}_2$ are diagonal if and only if $\mathbf{L}$ in (D.8) is diagonal.

Bibliography

[1] B. Abramzon and W. Sirignano. Droplet vaporization model for spray combustion calculations. *Int. J. Heat Mass Transfer*, 32:1605–1618, 1989.

[2] P. Achim. *Simulation de collisions, coalescence et rupture des gouttes par une approche lagrangienne: application aux moteurs à propergol solide*. PhD thesis, Faculté des Sciences de l'Université de Rouen, 1999. (French).

[3] International Energy Agency. Key World Engery Statistics. available from http://www.iea.org/textbase/nppdf/free/2008/key_stats_2008.pdf (April 2009), 2008a.

[4] International Energy Agency. World energy outlook 2008. available from http://www.worldenergyoutlook.org (April 2009), 2008b.

[5] G. Ahmadi, J.F. Cao, L. Schneider, and A. Sadiki. A thermodynamical formulation for chemically active multiphase turbulent flows. *International Journal of Engineering Science*, 44:699–720, 2006.

[6] A.A. Amsden, P.J. O'Rourke, and T.D. Butler. *KIVA II: A Computer Program for Chemically Reactive Flows with Sprays*. Los Alamos Natl. Lab., 1989. LA-11560-MS.

[7] S.V. Apte, K. Mahesh, P. Moin, and J.C. Oefelein. Large-eddy simulation of swirling particle-laden flows in a coaxial-jet combustor. *Int. J. Mult. Flow*, 29:1311–1331, 2003.

[8] N. Ashgriz and J.Y. Poo. Coalescence and separation in binary collisions of liquid drops. *J. Fluid Mech.*, 221:183–204, 1990.

[9] H. Babovsky. On a simulation scheme for the Boltzmann equation. *Math. Med. Appl. Sc.*, 8:223–233, 1986.

[10] C. Baranger. Modelling of oscillations, breakup and collisions for droplets: the establishment of kernels for the T.A.B model. *Mathematical Models and Methods in Applied Sciences*, 14:775–794, 2004.

[11] G.I. Barenblatt. *Scaling*. Cambridge Texts in Applied Mathematics. Cambridge University Press, 2003.

[12] J. Bear and Y. Bachmat. *Introduction to Modeling of Transport Phenomena in Porous Media*, volume 4 of *Theory and application of transport in porous media*. Kluver Academic Publishers, 1990.

[13] G.A. Bird. *Molecular gas dynamics and the direct simulation of gas flows.* Number 42. Oxford Science Publications, 1994.

[14] B. Böhm, D. Geyer, A. Dreizler, B. Venkatesan, N.M. Laurendeau, and M.W. Renfro. Simultaneous PIV/PTV/OH PLIF imaging: Conditional flow field statistics in partially premixed turbulent opposed jet flames. In *Combustion Institute*, volume 31, pages 709–717, 2007.

[15] M. Boileau, G. Staffelbach, B. Cuenot, T. Poinsot, and C. Bérat. LES of an ignition sequence in a gas turbine engine. *Combustion and Flame*, 154(1-2):2–22, 2008.

[16] L. Boltzmann. *Vorlesungen zur Gastheorie [Lectures on gas theory].* Ambrosius Barth, Leipzig, 1898. Reprint: Boltzmann, L., 1995. Lectures on gas theory. Dover Publications Inc.

[17] J. Borée, T. Ishima, and I. Flour. The effect of mass loading and inter-particle collisions on the development of the polydispersed two-phase flow downstream of a confined bluff body. *J. Fluid Mech.*, 443:129–165, 2001.

[18] F. Bouchut. On zero pressure gas dynamics. In B. Perthame, editor, *Advances in kinetic theory and computing*, volume 22 of *Ser. Adv. Math. Appl. Sci.*, pages 171–190. World Scientific, River Edge, NJ, 1994.

[19] F. Bouchut, S. Jin, and X. Li. Numerical approximations of pressureless and isothermal gas dynamics. *SIAM J. Numer. Anal.*, 41:135–158, 2003.

[20] R.M. Bowen. Theory of Mixtures, part I. In A.C. Eringen, editor, *Continuum Physics III*, pages 2–127. Academic Press, 1976.

[21] F. Brandt. *Brennstoffe und Verbrennungsrechnung.* Vulkan Verlag, Essen, 1999. (German).

[22] P.R. Brazier-Smith, S.G. Jennings, and J. Latham. The interaction of falling water drops: coalescence. *Proceedings of the Royal Society, London*, 326:393–408, 1972.

[23] I.N. Bronstein, K.A. Semendjajew, G. Musiol, and H. Mühlig. *Taschenbuch der Mathematik.* Verlag Harri Deutsch, fifth edition, 2000. (German).

[24] C. Cercignani. *The Boltzmann Equation and Its Applications*, volume 67 of *Applied Mathematical Sciences.* Springer, 1988.

[25] P. Chadwick. *Continuum Mechanics - Concise Theory and Problems.* Dover Publications, Inc., 1976.

[26] S. Chapman and T.G. Cowling. *The Mathematical Theory of Non-Uniform Gases.* Cambridge University Press, Cambridge, England, 1970.

[27] G.-Q. Chen and H. Liu. Formation of δ-shocks and vacuum states in the vanishing pressure limit of solutions to the Eulerian equations for isotropic fluids. *SIAM J. Math. Anal.*, 34:925–938, 2003.

[28] R. Clift, J.R. Grace, and M.E. Weber. *Bubbles, Drops and Particles.* Adademic Press, New York, 1978.

[29] Personal communication with S. Bareiss, 2009. EKT, Technische Universität Darmstadt.

[30] C.B.B. Costa, M.R.W. Maciel, and R.M. Filho. Considerations on the crystalliztion modeling: Population balance solution. *Computers & Chemical Engineering*, 31: 206–218, 2006.

[31] O. Coussy. *Poromechanics.* John Wiley & Sons, 2004.

[32] S.C. Cowin, editor. *Bone Mechancis Handbook.* CRC Press, London, second edition, 2001.

[33] C.T. Crowe, M. Sommerfeld, and Tsuji Yutaka. *Multiphase Flows with Droplets and Particles.* CRC Press, 1998.

[34] S. de Chaisemartin, F. Laurent, M. Massot, and J. Reveillon. Evaluation of Eulerian multi-fluid versus Lagrangian methods for the ejection of polydisperse evaporating sprays by vortices. *submitted to J. Comput. Phys.*, 2008. available from http://hal.archives-ouvertes.fr (April 2009).

[35] E. de Villiers, A.D. Gosman, and H.G. Weller. Large eddy simulation of primary diesel spray atomization. *SAE International*, (2004-01-0100), 2004.

[36] F.-X. Demoulin, P.-A. Beau, G. Blokkeel, A. Mura, and R. Borghi. A new model for turbulent flows with large density fluctuations: Application to liquid atomization. *Atomization Sprays*, 17:315–345, 2007.

[37] S. Descombes and M. Massot. Operator splitting for nonlinear reaction-diffusion systems with an entropic structure: singular perturbation and order reduction. *Numerische Mathematik*, 97:667–698, 2004.

[38] O. Desjardins, R.O. Fox, and P. Villedieu. A quadrature-based moment method for the Williams spray equation. In *Proceedings of the Summer Program.* Center for Turbulence Research, 2006.

[39] O. Desjardins, R.O. Fox, and P. Villedieu. A quadrature-based moment method for dilute fluid-particle flows. *J. Comput. Phys.*, 227:2514–2539, 2008.

[40] O. Desjardins, V. Moureau, and H. Pitsch. An accurate conservative level set/ghost fluid method for simulating turbulent atomization. *J. Comput. Phys.*, 227:8395–8416, 2008.

[41] K. Domelevo. The kinetic-sectional approach for noncolliding evaporating sprays. *Atomization and Sprays*, 11(3):291–303, 2001.

[42] D.A. Drew and S.L. Passman. *Theory of Multicomponent Fluids*, volume 135 of *Applied Mathematical Sciences.* Springer, 1999.

[43] G. Dufour. *Modélisation multi-fluide Eulérienne pour les écoulements diphasiques à inclusions dispersées.* PhD thesis, L'Université Toulouse, 2005. (French).

[44] G. Dufour and P. Villedieu. The sectional method revisited for evaporating sprays. *Mathematical Modelling and Numerical Analysis*, 39:931–963, 2005.

[45] J.K. Dukowicz. A particle-fluid numerical model for liquid sprays. *J. Comput. Phys.*, 35(2):229–253, 1980.

[46] J. Eggers and E. Villermaux. Physics of liquid jets. *Rep. Prog. Rhys.*, 77(036601), 2008.

[47] J.-P. Estrade. *Etude expérimentale et modélisation de la collision de gouttelettes.* PhD thesis, Ecole Nationale Supérieure de l'Aéronautique et de l'Espace, Toulouse, 1998. (French).

[48] R. Fan and R.O. Fox. Segregation in polydisperse fluidized beds: Validation of a multi-fluid model. *Chem. Eng. Sci.*, 63:272–285, 2008.

[49] R. Fedkiw, T. Aslam, B. Merriman, and S. Osher. A non-oscillatory Eulerian approach to interfaces in multimaterial flows (the ghost fluid method). *J. Comput. Phys.*, 152:457–492, 1999.

[50] J.H. Ferziger and M. Peric. *Computational Methods for Fluid Dynamics.* Springer, third edition, 2001.

[51] P. Février, O. Simonin, and K.D. Squires. Partitioning of particle velocities in gas-solid turbulent flows into a continuous field and a spatially uncorrelated random distribution: theoretical formalism and numerical study. *J. Fluid Mech.*, 533:1–46, 2005.

[52] K.W. Fong, T.H. Jefferson, T. Suyehiro, and L. Walton. *Guide to the SLATEC Common Mathematical Library.* Sandia, Los Alamos, Air Force Weapons Laboratory Technical Exchange Committee, 1993. available from http://www.netlib.org/slatec/ (April 2009).

[53] R.O. Fox. *Computational Models for Turbulent Reacting Flows.* Cambrdige University Press, 2003.

[54] R.O. Fox. Bivariate direct quadrature method of moments for coagulation and sintering of particle populations. *Journal of Aerosol Science*, 37:1562–1580, 2006.

[55] R.O. Fox. *Multiphase reacting flows: modelling and simulation*, chapter Introduction and Fundamentals of Modeling Approaches for Polydisperse Multiphase Flows. Number 492 in CISM International Centre for Mechanical Sciences. Springer, 2007.

[56] R.O. Fox. A quadrature-based third-order moment method for dilute gas-particle flows. *J. Comput. Phys.*, 227:6313–6350, 2008.

[57] R.O. Fox. Optimal moment sets for multivariate direct quadrature method of moments. *Int. Eng. Chem. Res.*, 2008. DOI:10.1021/ie801316d.

[58] R.O. Fox. Higher-order quadrature-based moment methods for kinetic euquations. *submitted to J. Comput. Phys.*, 2008.

[59] R.O. Fox, F. Laurent, and M. Massot. Numerical simulation of spray coalescence in an Eulerian framework: direct quadrature method of moments and multi-fluid method. *J. Comput. Phys.*, 227:3058–3088, 2008.

[60] M. Friedrich and B. Weigand. Eulerian multi-fluid simulation of polydisperse dense liquid sprays by the direct quadrature method of moments. In *ICLASS, Kyoto, Japan*, number ICLASS06-121, 2006.

[61] N. Garcia Rosa, P. Villedieu, J. Dewitte, and G. Lavergne. A new droplet-wall interaction model. In *ICLASS, Kyoto, Japan*, number ICLASS06-167, 2006.

[62] N. Garcia Rosa, P. Villedieu, and Lavergne G. A statistical model for droplet-wall interaction. In *2nd colloque INCA*, October 2008.

[63] F. Gelbard, Y. Tambour, and J.H. Seinfeld. Sectional representations for simulating aerosol dynamics. *J. Colloid Interface Sci.*, 76:541–556, 1980.

[64] D. Geyer, A. Kempf, A. Dreizler, and J. Janicka. Turbulent opposed-jet flame: A critical benchmark experiment for combustion LES. *Combustion and Flame*, 143: 524–548, 2005.

[65] S. Ghosal and M. Herrmann. Modeling sprays by the method of Laplace transforms. In *Proceedings of the Summer Program*. Center for Turbulence Research, 2006.

[66] V. Giovangigli. *Multicomponent Flow Modeling*. Birkhäuser, 1999.

[67] R.G. Gordon. Error bounds in equilibrium statistical mechanics. *I. Math. Phys.*, 9: 655–663, 1968.

[68] J.B. Greenberg, D. Albagli, and Y. Tambour. An opposed jet quasi-monodisperse spray diffusion flame. *Combust. Sci. Technol.*, 50:255–270, 1986.

[69] J.B. Greenberg, I. Silverman, and Y. Tambour. On the origin of spray sectional conservation equations. *Combust. Flame*, 93:90–96, 1993.

[70] R. Greve. *Kontinuumsmechanik - Ein Grundkurs*. Springer, 2003. (German).

[71] R. Groll. *Numerische Modellierung der Verdunstung turbulenter Zwei-Phasen-Strömungen mittels eines Euler/Euler-Verfahrens*. PhD thesis, Technische Universität Darmstadt, 2002. (German).

[72] R. Grosch, H. Briesen, and W. Marquardt. Generalization and numerical investigation of QMOM. *Process Systems Engineering*, 53:207–227, 2007. DOI:10.1002/aic.11041.

[73] M. Hage, A. Dreizler, and J. Janicka. Flow fields and droplet diameter distributions of water and n-heptane sprays at varied boundary conditions in a generic gas turbine combustor. Number GT-2007-27108. ASME Turbo Expo: Power for Land, Sea and Air, 2007.

[74] F. Hahn, C. Olbricht, and J. Janicka. Large eddy simulation of an evaporating spray based on an Eulerian-Lagrangian approach. In *ILASS Europe*, pages 2–9, 2008.

[75] F. Ham, S.V. Apte, G. Iaccarino, X. Wu, M. Herrmann, G. Constantinescu, K. Mahesh, and P. Moin. Unstructured LES of reacting multiphase flows in realistic gas turbine combustors. Technical report, Center for turbulence research, Stanford, 2003.

[76] M. Herrmann. A balanced force refined level set grid method for two-phase flows on unstructured flow solver grids. *J. Comput. Phys.*, 227:2674–2706, 2007.

[77] D. Hill. *The Computer Simulation of dispersed two-phase flows.* PhD thesis, University of London, 1998.

[78] A.C. Hindmarsh. *Brief Description of ODEPACK – A Systematized Collection of ODE Solvers Double Precision Version.* Lawrence Livermore National Laboratory, 2001. available from http://www.netlib.org/odepack/ (April 2009).

[79] L.-P. Hsiang and G.M. Faeth. Near limit drop deformation and secondary breakup. *Int. J. Multiphase Flow*, 18:635–652, 1992.

[80] K. Hutter and K. Jöhnk. *Continuum Methods of Physical Modeling.* Springer, 2004.

[81] F. John. *Partial Differential Equations.* Springer, 1991.

[82] S. Kahn Ribeiro, S. Kobayashi, M. Beuthe, J. Gasca, D. Greene, D.S. Lee, Y. Muromachi, P.J. Newton, S. Plotkin, D. Sperling, R. Wit, and P.J. Zhou. *Climate Change 2007: Mitigation. Contribution of Working Group III to the Fourth Assessment Report of the Intergovernmental Panel on Climate Change*, chapter Transport and its infrastructure. Cambridge University Press, 2007.

[83] A. Kaufmann. *Towards Eulerian-Eulerian large eddy simulation of reactive two-phase flows.* PhD thesis, Institute National Polytechnique de Toulouse, 2004.

[84] A. Kaufmann, M. Moreau, O. Simonin, and J. Helie. Comparison between Lagrangian and mesoscopic Eulerian modelling approaches for inertial particles suspended in decaying isotropic turbulence. *J. Comput. Phys.*, 227:6448–6472, 2008.

[85] C. Kemfert. *Die andere Klima Zukunft; Innovation statt Depression.* Murmann, 2008. (German).

[86] M. Klein. *Direkte Numerische Simulation des primären Strahlzerfalls in Einstoffzerstäuberdüsen.* PhD thesis, Technische Universität Darmstadt, 2002. (German).

[87] J. Kowalski. *Two-Phase Modeling of Debris Flows.* PhD thesis, ETH Zürich, 2008.

[88] S.A. Krzeczkowski. Measurements of liquid droplet disintegration mechanisms. *Int. J. Multiphase Flow*, 6:227–239, 1980.

[89] O. Kyriopoulos, I.V. Roisman, T. Gambaryan-Roisman, P. Stephan, and C. Tropea. Dynamics of a liquid film produced by spray impact onto a heated target. In *ILASS Europe*, pages 13–15, Como, Italy, 2008.

[90] H. Lamb. *Hydrodynamics*. Cambridge University Press, 1932. Reprint 1997.

[91] L.D. Landau and E.M. Lifschitz. *Course of Theoretical Physics*. Butterworth Heinemann, 1987. Reprint 2002.

[92] I. Langmuir. The production of rain by a chain reaction in cumulus clouds at temperatures above freezing. *Journal of Meteorology*, 5:175–192, 1948.

[93] J.C. Lasheras, E. Villermaux, and E.J. Hopfinger. Break-up and atomization of a round water jet by a high-speed annular air jet. *J. Fluid Mech.*, 357:351–379, 1998.

[94] C. Laurent. *Développement et Validation de Modèles d'évaporation Multi-composant*. PhD thesis, L'Institut Supérieur de l'Aéronautique et de'Espace, Toulouse, 2008. (French).

[95] F. Laurent. Numerical analysis of Eulerian multi-fluid models in the context of kinetic formulations for dilute evaporating sprays. *M2AN Math. Model. Numer. Anal.*, 40:431–468, 2006.

[96] F. Laurent and M. Massot. Multifluid modelling of laminar poly-dispersed spray flames: origin, assumptions and comparison of sectional and sampling methods. *Combust. Theory and Modelling*, 5:537–572, 2001.

[97] F. Laurent, M. Massot, and P. Villedieu. Eulerian multifluid modelling for the numerical simulation of coalescence and polydisperse dense liquid sprays. *J. Comput. Phys.*, 194:505–543, 2004.

[98] F. Laurent, V. Santoro, M. Noskov, A. Gomez, M.D. Smooke, and M. Massot. Accurate treatment of size distribution effects in polydisperse spray diffusion flames: multi-fluid modeling, computations and experiments. *Combust. Theor. Model.*, 8: 385–412, 2004.

[99] N. Le Lostec, R.O. Fox, O. Simonin, and P. Villedieu. Numerical description of dilute particle-laden flows by a quadrature-based moment method. In *Proceedings of the Summer Program*. Center of Turbulence Research, Stanford, 2008.

[100] A.H. Lefebvre. *Atomization and Sprays*. Hemisphere Publishing Corporation, 1989.

[101] R.J. LeVeque. *Numerical Methods for Conservation Laws*. Lectures in Mathematics, ETH Zürich. Birkhäuser, 1992.

[102] R.J. LeVeque. *Finite Volume Methods for Hyperbolic Problems*. Cambridge Texts in Applied Mathematics. Cambridge University Press, 2002.

[103] S.P. Lin. *Breakup of Liquid Sheets and Jets.* Cambridge University Press, 2003.

[104] J. Madsen. *Computational and Experimental Study of Sprays from the Breakup of Water Sheets.* PhD thesis, Engineering and Science, Aalborg University, 2006.

[105] C. Marchioli and A. Soldati. Mechanisms of particle transfer and segregation in a turbulent boundary layer. *J. Fluid Mech.*, 468:283–315, 2002.

[106] D.L. Marchisio and R.O. Fox, editors. *Multiphase reacting flows: modelling and simulation.* Number 492 in CISM International Centre for Mechanical Sciences. Springer, 2007.

[107] D.L. Marchisio and R.O. Fox. Solution of population balance equations using the direct quadrature method of moments. *J. Aerosol Sci.*, 36:43–73, 2005.

[108] D.L. Marchisio, R.O. Vigil, and R.O. Fox. Quadrature method of moments for aggregation-breakage processes. *Journal of Colloid and Interface Science*, 258:322–334, 2003.

[109] R. McGraw. Description of aerosol dynamics by the quadrature method of moments. *Aerosol Sci. Technol.*, 27:255–265, 1997.

[110] T. Menard, S. Tanguy, and A. Berlemont. Coupling level set/VOF/ghost fluid methods: Validation and application to 3d simulation of the primary break-up of a liquid jet. *Int. J. Multiphase Flow*, 33:510–524, 2007.

[111] G.P. Merker, C. Schwarz, G. Stiesch, and F. Otto. *Simulating Combustion.* Springer, 2006.

[112] J.-P. Minier and E. Peirano. The pdf approach to turbulent polydisperse two-phase flows. *Physics Reports*, 352:1–214, 2001.

[113] H.K. Nanbu. Direct simulation scheme derived from the Boltzmann equation. I. Monocomponent gas. *J. Phys. Soc. Jap.*, 49:2042–2049, 1980.

[114] R.I. Nigmatulin. *Dynamics of multiphase media.* Hemisphere, Washington D.C., 1991.

[115] N. Nora Okong'o, A. Leboissetier, and J. Bellan. Detailed characteristics of drop-laden mixing layers: Large eddy simulation predictions compared to direct numerical simulation. *Phys. Fluids*, 20(10):103305, 2008. DOI:10.1063/1.2990758.

[116] M. Ochs. *Verdunstung monodisperser frei beweglicher Brennstoff-Tropfen in einer turbulenten Heissluftströmung.* PhD thesis, Eidgenössische Technische Hochschule, Zürich, 1999. (German).

[117] Commission of the European Communities. Results of the review of the community strategy to reduce CO2 emissions from passenger cars and light-commercial vehicles. available from http://eur-lex.europy.eu (April 2009), February 2007. COM(2007) 19 final.

[118] Commission of the European Communities. Limiting global climate change to 2 degrees celsius the way ahead for 2020 and beyond. available from http://eur-lex.europy.eu (April 2009), January 2007. COM(2007) 2 final.

[119] P.J. O'Rourke. *Collective drop effects on vaporizing liquid sprays*. PhD thesis, Los Alamos National Laboratry, 1981.

[120] P.J. O'Rourke and A. Amsden. The TAB method for numerical calculation of spray droplet breakup. Technical Report 87545, Los Alamos National Laboratory, 1987.

[121] C.W. Oseen. Über die Stokessche Formel und über eine verwandte Aufgabe in der Hydrodynamik. *Arkiv f. Math., Astro. och Fysik*, 6(29), 1911. (German).

[122] S. Osher and R. Fedkiw. *Level Set Methods and Dynamic Implicit Interfaces*. Springer, 2003.

[123] M.G. Pai. *Probability density function formalism for multiphase flows*. PhD thesis, Iowa State University, Ames, 2007.

[124] S.L. Passman, J.W. Nunziato, and E.K. Walsh. *Rational Thermodynamics*, chapter A Theory of Multiphase Mixtures, pages 286–325. Springer, second edition, 1984.

[125] M. Pilch and C.A. Erdman. Use of breakup time data and velocity history data to predict the maximum size of stable fragments of acceleration-induced breakup of a liquid drop. *Int. J. Multiphase Flow*, 13:741–757, 1987.

[126] T. Poinsot and D. Veynante. *Theoretical and Numerical Combustion*. R.T. Edwards, Inc., second edition, 2005.

[127] B.E. Poling, J.M. Prausnitz, and J.P. O'Connell. *The Properties of Gases and Liquids*. Mcgraw-Hill Professional, fifth edition, 2001.

[128] S.B. Pope. *Turbulent Flows*. Cambridge University Press, 2000.

[129] W.H. Press, S.A. Teukolsky, W.T. Vetterling, and B.P. Flannery. *Numerical recipes in Fortran 77: The art of scientific computing*. Cambridge University Press, 1992.

[130] J. Qian and C.K. Law. Regimes of coalescence and separation in droplet collision. *J. Fluid Mech.*, 331:59–80, 1997.

[131] V. Raman, H. Pitsch, and R.O. Fox. Eulerian tranported probability density function sub-filter model for large-eddy simulations of turbulent combustion. *Combustion Theory and Modeling*, 10:439–458, 2006.

[132] D. Ramkrishna. *Population Balances*. Academic Press, 2000.

[133] M. Reeks. On a kinetic equation for the transport of particles in turbulent flows. *Phys. Fluids A*, 3:446–456, 1991.

[134] N.C. Reis, R.F. Griffiths, and J.M. Santos. Numerical simulation of the impact of liquid droplets on porous surfaces. *J. Comput. Phys.*, 198:747–770, 2004.

[135] J. Reveillon. *Multiphase Reacting Flows: Modelling and Simulation*, chapter Direct numerical simulation of sprays: Turbulent dispersion, evaporation and combustion, pages 229–269. Number 492 in CISM courses and lectures. Springer, 2007.

[136] H.-K. Rhee, R. Aris, and N.R. Amundson. *Theory and application of hyperbolic systems of quasilinear equations: Theory and Application of Hyperbolic Systems of Quasilinear Equations.* Dover Publications, 2001.

[137] E. Riber, V. Moureau, M. Garcia, T. Poinsot, and O. Simonin. Evaluation of numerical strategies for large eddy simulation of particulate two-phase recirculating flows. *J. Comput. Phys.*, 228:539–564, 2009.

[138] R. Rioboo, M. Marengo, and C. Tropea. Time evolution of liquid drop impact onto solid, dry surfaces. *Exp. Fluids*, 33:112–124, 2002.

[139] P.L. Roe. Approximate Riemann solvers, parameter vectors, and difference schemes. *J. Comput. Phys.*, 43:357–372, 1981.

[140] I.V. Roisman and C. Tropea. Impact of a drop onto a wetted wall: description of crown formation and propagation. *J. Fluid Mech.*, 472:373–397, 2002.

[141] P. Rosin and E. Rammler. The laws governing the fineness of powdered coal. *Journal of the Institute Fuel*, 7:29–36, 1933.

[142] N. Roth, J. Schlottke, J. Urban, and B. Weigand. Simulations of droplet impact on cold wall without wetting. In *ILASS Europe*, Como, Italy, 2008. Paper ID ILASS08-9-1.

[143] D.W.I. Rouson and J.K. Eaton. Effect of preferential concentration of solid particles in turbulent chanel flow. *J. Fluid Mech.*, 428:149–169, 2001.

[144] M. Rueger, S. Hohmann, M. Sommerfeld, and G. Kohnen. Euler/Lagrange calculations of turbulent sprays: the effect of droplet collisions and coalescence. *Atomizations Sprays*, 10:47–81, 2000.

[145] A. Sadiki, M. Chrigui, J. Janicka, and M.R. Maneshkarimi. Modeling and simulation of effects of turbulence on vaporization, mixing and combustion of liquid-fuel sprays. *Flow Turbulence Combustion*, 75:105–130, 2005.

[146] P. Sagaut. *Large Eddy Simulation for Incompressible Flows.* Springer, third edition, 2006.

[147] R. Scardovelli and S. Zaleski. Direct numerical simulation of free-surface and interfacial flow. *Ann. Rev. Fluid Mech.*, 31:567–603, 1999.

[148] L. Schiller and A. Naumann. Über die grundlegenden Berechnungen bei der Schwerkraftaufbereitung. *Ver. Deut. Ing.*, 77:318, 1933. (German).

[149] H. Schlichting and K. Gersten. *Boundary-Layer Theory.* Springer, 2000.

[150] J. Schlottke and B. Weigand. Direct numerical simulation of evaporating droplets. *J. Comput. Phys.*, 227:5215–5237, 2008.

[151] L. Schneider and K. Hutter. *Solid-Fluid Mixtures of Frictional Materials in Geophysical and Geotechnical Context*. Advances in Geophysical and Environmental Mechanics and Mathematics. Springer, 2009a. in preperation.

[152] L. Schneider, A. Sadiki, and J. Janicka. A study of the Eulerian multi-fluid method for an accelerating and evaporating spray. In *ILASS Europe*, pages 2–8, 2008.

[153] L. Schneider, N. Le Lostec, P. Villedieu, and A. Sadiki. A moment method for polydisperse sprays. *Comptes Rendus Mathematique*, 2009b. in press, available from http://dx.doi.org/10.1016/j.crma.2009.03.023 (April 2009).

[154] L. Schneider, N. Le Lostec, P. Villedieu, and A. Sadiki. A moment method for splashing and evaporation processes of polydisperse sprays. *submitted to Int. J. Multiphase Flow*, 2009c.

[155] J.A. Sethian. *Level Set Methods and Fast Marching Methods*. Cambridge University Press, second edition, 1999.

[156] A.A. Shraiber, M. Podvysotsky, and V.V. Dobrovsky. Deformation and breakup of drops by aerodynamical forces. *Atomization Spray*, 6:667–692, 1996.

[157] O. Simonin. Prediction of the dispersed phase turbulence in particle-laden jets. In *Gas-Solid Flows*, volume 121, pages 197–206. ASME FED, 1991.

[158] W.A. Sirignano. *Fluid dynamics and transport of droplets and sprays*. Cambridge university press, 1999.

[159] S. Solomon, D. Qin, M. Manning, Z. Chen, M. Marquis, K.B. Averyt, M. Tignor, and H.L. Miller, editors. *IPCC, 2007: Climate Change 2007: The Physical Science Basis. Contribution of Working Group I to the Fourth Assessment Report of the Intergovernmental Panel on Climate Change*. Cambridge University Press, 2007.

[160] M. Sommerfeld and H.-H. Qiu. Detailed measurements in a swirling particulate 2-phase flow by a phase-Doppler anemometer. *International Journal of Heat and Fluid Flow*, 12:20–28, 1991.

[161] M. Sommerfeld and H.-H. Qiu. Experimental studies of spray evaporation in turbulent flows. *International Journal of Heat and Fluid Flow*, 19:10–22, 1998.

[162] J.H. Spurk. *Dimensionsanalyse in der Strömungslehre*. Springer, 1992. (German).

[163] G. Stiesch. *Modeling Engine Spray and Combustion Processes*. Springer, Heidelberg, 2003.

[164] G.G. Stokes. On the effect of the internal friction of fluids on the motion of pendulums. *Tans. Cambr. Phil. Soc.*, 9:8–106, 1856.

[165] G. Strang. On the construction and comparison of difference schemes. *SIAM J. Num. Anal.*, 5:506–517, 1968.

[166] A.H. Stroud. *Approximate Calculation of Multiple Integrals.* Prentice-Hall, Englewood Cliffs, 1971.

[167] S. Subramaniam. Statistical modeling of sprays using the droplet distribution function. *Phys. Fluids*, 13:624–642, 2001.

[168] G.I. Taylor and A.E. Green. Mechanism of the production of small eddies from large ones. *The Royal Society: Mathematical and Physical Sciences*, 158:499–521, 1937.

[169] O. Tietjens. *Strömungslehre - Bewegung der Flüssigkeit und Gase*, volume 2. Springer-Verlag, 1970. (German).

[170] C. Truesdell. Sulle basi della termodinamica delle miscele. *Rend. Accad. Naz. Lincei.*, 44(8):381–383, 1957. (Italian).

[171] C. Truesdell. *Rational Thermodynamics.* Springer, second edition, 1984.

[172] C. Truesdell and R.G. Muncaster. *Fundamentals of Maxwells's Kinetic Theory of a Simple Monatonic Gas, treated as a Branch of Rational Mechanics.* Academic Press, 1980.

[173] VDI-Gesellschaft Verfahrenstechnik und Chemieingenieurwesen, editor. *VDI-Wärmeatlas.* Springer, eighth edition, 1997. (German).

[174] M.W. Vance, K.D. Squires, and O. Simonin. Properties of the particle velocity field in gas-solid turbulent channel flow. *Phys Fluid*, 18(6):063302, 2006.

[175] M. Vanni. Approximate population balance equations for aggregation-breakage processes. *J. Colloid Interface Sci.*, 221:143–160, 2000.

[176] E. Villermaux. Fragmentation. *Annu. Rew. Fluid Mech.*, 39:419–446, 2007.

[177] J.F. Wang. *Theory of Linear Poroelasticity with Applications to Geomechanics and Hydrogeology.* Princeton University Press, 2000.

[178] K.L. Wert. A rationally-based correlation of mean fragment size for drop secondary breakup. *Int. J. Multiphase Flow*, 21:1063–1071, 1995.

[179] F.A. Williams. Spray combustion and atomization. *Phys. Fluids*, 1:541–545, 1958.

[180] J. Wilms. *Evaporation of Multicomponent Droplets.* PhD thesis, Universität Stuttgart, 2005.

[181] J. Wilms, G. Grehan, and G. Lavergne. Global rainbow refractometry with a selective imaging method. *Particle & Particle System characterization*, 25:39–48, 2008.

[182] S.-C. Wong and J.-C. Chang. Evaporation of non-dilute and dilute monodisperse droplet clouds. *Int. J. Heat Mass Transfer*, 35:2403–2411, 1992.

[183] D.L. Wright, R. McGraw, and D.E. Rosner. Bivariate extension of the quadrature method of moments for modeling simultaneous coagulation and sintering of particle populations. *J. Colloid Interface Sci.*, 236:242–251, 2001.

[184] A.L. Yarin. Drop impact dynamics: splashing, spreading, receding, bouncing... *Annual Review Fluid Mech.*, 38:159–192, 2006.

[185] D. You, F. Ham, and P. Moin. Large-eddy simulation analysis of turbulent combustion in a gas turbine engine combustor. Technical report, Center for turbulence research, Stanford, 2008.

[186] A. Zucca, D.L. Marchisio, M. Vanni, and A.A. Barresi. Validation of the bivariate DQMOM for nanoparticle processes simulation. *Aiche Journal*, 53:918–931, 2007.